

**THE WATER BUDGET OF
HETEROGENEOUS AREAS**

IMPACT OF SOIL AND RAINFALL VARIABILITY

promotor: dr ir R.A. Feddes
hoogleraar in de bodemnatuurkunde, agrohydrologie
en grondwaterbeheer

co-promotor: ir J.N.M. Stricker
universitair hoofddocent in de hydraulica

Cornelis Pieter Kim

**THE WATER BUDGET OF HETEROGENEOUS
AREAS**

IMPACT OF SOIL AND RAINFALL VARIABILITY

PROEFSCHRIFT

ter verkrijging van de graad van doctor
in de landbouw- en milieuwetenschappen
op gezag van de rector magnificus
dr C.M. Karssen
in het openbaar te verdedigen
op vrijdag 15 december 1995
des namiddags te half twee in de Aula
van de Landbouwuniversiteit te Wageningen

The research in this thesis was entirely funded by the European Community Environmental Research Program under contract numbers EPOC-CT90-0016, EPOC-CT90-0030 and EV5V-CT91-0033. The Netherlands Organization for Scientific Research (NWO) partly funded a temporary stay at the Massachusetts Institute of Technology.

BIBLIOTHEEK
LANDBOUWUNIVERSITEIT
WAGENINGEN

CIP-DATA KONINKLIJKE BIBLIOTHEEK, DEN HAAG

Kim, Cornelis Pieter

The water budget of heterogeneous areas : impact of soil and rainfall variability / Cornelis Pieter Kim. - [S.l. : s.n.]
Thesis Landbouwwuniversiteit Wageningen. - With ref. - With summary in Dutch.

ISBN 90-5485-460-X

Subject headings: hydrology / hydroclimatology.

STELLINGEN

1. 'Equivalente' bodemhydraulische parameters zijn niet alleen afhankelijk van het onderliggende heterogene veld, maar ook van de meteorologische omstandigheden en de tijdschaal waarvoor ze zijn afgeleid.
dit proefschrift.
2. Om de langdurig gemiddelde waterbalans (orde jaren) te bepalen kunnen stromingsprocessen op kleine tijdschalen (orde uren) niet worden verwaarloosd.
dit proefschrift.
3. In de noodzaak om modellen te verifiëren wordt dikwijls geen aandacht besteed aan het verschil tussen gemeten en gemodelleerde grootheden. Een voorbeeld hiervan is de studie van Vinnikov en Yeserkepova [1991] waarin de gesimuleerde vochtvoorraad in een bodemreservoir met opgelegde diepte wordt vergeleken met gemeten bodemvochtgehaltes.
Vinnikov, K.Ya., and I.B. Yeserkepova, *J. Clim.*, 4:66-79, 1991.
4. In slecht doorlatende gronden wordt evapotranspiratie beperkt door het infiltratievermogen en in goed doorlatende gronden door de snelheid van percolatie. Evapotranspiratie neemt af door heterogeniteit van bodemhydraulische eigenschappen voor slecht doorlatende gronden en neemt toe door heterogeniteit voor goed doorlatende gronden
dit proefschrift.
5. Laterale stromingsprocessen op een helling vormen een negatieve terugkoppeling die het effect van bodemheterogeniteit op de ruimtelijk gemiddelde waterbalans tegenwerkt.
dit proefschrift.
6. Bureaucratie toont een diep menselijke eigenschap: in de zucht naar controle wordt alles beheerst behalve de eigen drift.
7. Beschouw een (universitaire) organisatie als een gelijkbenige driehoek waarvan de basis de produktiekracht voorstelt en het oppervlak de organisatie-omvang. Laat nu de produktie-efficiëntie gedefiniëerd zijn als het quotiënt van de basis en het oppervlak en de bureaucratie-indicator als de hoek tussen basis en schuine zijde. Wanneer de produktiekracht verdubbelt bij ongewijzigde produktie-efficiëntie, dan volgt dat de tangens van de bureaucratie-indicator gehalveerd dient te worden. Voor niet al te grote hoeken betekent dit dat de organisatie een factor twee platter moet worden. Uit confrontatie van het bovenstaande met de realiteit blijkt dat de kennis van goniometrie bij (universitaire) bestuurskundigen gering is.

8. Nieuw beleid maakt de roep om verandering groter.
9. De financiële afhankelijkheid van klimaatonderzoekers van hun eigen onderzoeksresultaten leidt tot overschatting van het broeikaseffect.
10. De sterke op duurzaamheid en maatschappelijke relevantie gerichte ideologie van de Landbouwuniversiteit is door z'n uitsluitend karakter in strijd met een kritisch wetenschappelijke en onbevooroordeelde onderzoeksmentaliteit.
11. De hel is geen duurzame energiebron.
Maarten van Donk, 1994.
12. The nakedness of woman is the work of God.
William Blake, *The Marriage of Heaven and Hell*, 1791.
13. De bruidsschat die politici meenemen bij hun huwelijk met een partij blijkt veelal te bestaan uit hun eigen mening.
14. Een grootaandeelhouder van Shell/Koninklijke Olie is de enige permanent aanwezige in de nederlandse regering; de scheiding van Staat en Kerk is stringenter dan die van Staat en bedrijfsleven.
Rolf Latour, 1995.
15. De inrichting van de huidige maatschappij waarin de economische doctrine als eenoog heerst toont een collectieve neiging tot blindheid.
16. Het is erger door de massa te worden opgenomen dan er door verpletterd te worden.
Cornelis Verhoeven, *Filosofie Magazine*, 1995.
17. De redenen voor de onterechte oorlogen gevoerd in de naam van het vaderland liggen begraven in de tombe van de onbekende soldaat. De rottende inhoud wordt bewaakt door militairen en de stank verbrandt in de eeuwige vlam. De afwezigheid van een dergelijk monument in Nederland wijst niet op overbodigheid.

Stellingen behorend bij het proefschrift *The water budget of heterogeneous areas - impact of soil and rainfall variability* van C.P. Kim, Wageningen, 15 december 1995.

Abstract

Kim, C.P., 1995. *The water budget of heterogeneous areas - impact of soil and rainfall variability*. Ph.D. thesis, Wageningen Agricultural University, The Netherlands. 183 pp., 61 figs., 13 tables, 3 appendices.

In this thesis the heterogeneity of the soil water budget components is investigated. Heterogeneity of soil hydraulic properties and rainfall rate are taken into account by using stochastic methods. The importance of lateral groundwater flow in causing heterogeneity of the water budget components has been investigated by considering the governing physical laws. Through comparison of water budget simulations of simple soil reservoir models with numerical simulations of the governing equation for unsaturated water flow that incorporate the effect of soil heterogeneity, the importance of the lower boundary condition is revealed. The effects of the various sources of heterogeneity on the annual or long term average water budget appear to be markedly different. The dynamical behavior of spatial heterogeneity of infiltration and evapotranspiration rates on the event time scale is investigated by deriving their probability distributions and subsequently tracing their time evolution. Accounting for the influence of soil heterogeneity by means of one set of "equivalent" parameters is shown to be valid only under restricted conditions. Because of lateral groundwater flow an internal hillslope "teleconnection" is present that links the water budget of the uphill recharge and downhill discharge zones. This teleconnection establishes a negative feedback for the overall hillslope evapotranspiration since water lost as recharge uphill may reappear in the discharge zone.

Additional index words: water budget, heterogeneity, stochastic hydrology, Monte Carlo simulations.

Voorwoord

Het vertalen van gedachten naar woorden vereist stilistische vaardigheid. Wanneer die mij ten dienste stond zou dit een inleiding zijn op een meeslepende roman of enkele beklemmende gedichten. Echter, zoals vaker bij een proefschrift, een voorwoord dat voor de meesten een laatste herkenning zal zijn. Daarvoor geen excuses: iets blijft alleen de moeite waard wanneer niet iedereen toegang heeft.

Het positieve gevoel dat ik heb over de afgelopen vier en een half jaar is allereerst te herleiden tot mijn directe begeleider, Han Stricker. Zonder zijn vangsten uit de brusselse vijver en zijn betrokkenheid zouden dit onderzoek onverricht en dit boek ongeschreven zijn gebleven. Een begeleider trekt aan het sleeptouw en gooit het anker uit. Han heeft zich onderscheiden door het kiezen van de juiste momenten daarvoor. Dat tweeledige komt ook op een andere manier naar voren. Na vier jaar is me duidelijk geworden dat experiment en theorie niet als regel samenkomen in één persoon. Door met zijn groep deel te nemen aan verschillende experimenten heeft Han ervoor gezorgd dat in dit onderzoek niet ieder verband met de werkelijkheid verloren is gegaan.

Mijn promotor, Prof. Feddes bedank ik voor zijn interesse en het vertrouwen dat hij stelde in de zelfstandigheid van de Hydraulica gang. Het hoge tempo waarin de hoofdstukken verschenen in de afsluitende fase vormden geen belemmering voor een stijlvolle inhoudelijke blik.

Although not officially, I consider Dara Entekhabi to be the third member of my "promotion team". A rendez-vous at the outskirts of the Sahara initiated my stay at Parsons' lab. Learning goes with the variety and quality of people you work with and both aspects got full attention by coming to Cambridge.

De put waaruit ik niet gepubliceerde ideeën en kritiek heb gewonnen bleek dikwijls artesisch. Een kleine bronvermelding is daarom op zijn plaats: Paul Torfs voor wiskundige dwars- en noodverbanden, Remko Uijlenhoet voor lage - en hoge momenten en Margje Soet en Peter Droogers voor directe correctie en assistentie.

Het correctieve werk van drs. J.S. Drijver-de Haas is de leesbaarheid ten goede gekomen. De fraaie door Adrie van 't Veer gemaakte tekeningen vormen de visuele ondersteuning zoals die mij voor ogen stond.

Dit proefschrift gaat over water. Door water alleen als stromingsverschijnsel te zien wordt geen recht gedaan aan de veel bredere betekenis, namelijk als noodzakelijke levensvoorwaarde en inspiratiebron. In aanvulling op het schilderij 'Onweer' (1957) van Jean Bazaine (eigendom van het Van Abbe museum in Eindhoven) op de omslag, heb ik Jan-Paul Rosenberg gevraagd om daarvoor het bewijs te leveren in de vorm van het onderstaande gedicht over datgene wat in dit proefschrift onbesproken blijft: het idee van natuur als leefomgeving.

René Kim

Arnhem, september 1995

Einder

Nooit waren de elementen zó bijeen.
het einde van 'n reis, het afscheid van de dag.

Met open ogen zie je wat je achterliet:
een pad van stappen, in stormen verzand.

Vóór je ligt een broze einder open:
zee en hemel, als dieren vechtend om de zon.

Aan je voeten kneden golven rimpels van zand,
vreedzaam als in een idee.

De zon verdrinkt, de duisternis komt nader
vereent het stille land, de verre lucht, het grote water.

Contents

List of Symbols	v
1 Introduction	1
1.1 Climate	1
1.2 Climate modeling	2
1.3 Water in the climatic system	2
1.4 Land surface processes	3
1.5 Thesis objective	5
2 Rationale and Review	7
2.1 Mass and energy balance	7
2.2 Definition of the thesis' central equation	10
2.3 Length and time scales of sub-surface flow	12
2.3.1 Representative Elementary Volume ($\approx 10^{-2}$ m - 10^{-1} m)	12
2.3.2 Plot and field scale ($\approx 10^{-1}$ m - 10^2 m)	14
2.3.3 Catchment scale ($\approx 10^2$ m - 10^5 m)	15
2.4 Representation of land surface processes in climate models	19
2.4.1 Advancement of the physical description	20
2.4.2 Incorporation of spatial heterogeneity	21
2.5 Research methods	23
2.6 Thesis structure	23
3 Consistency of the water budget in simple soil reservoir models	27
3.1 Objective and methods	27
3.2 Model formulations	28
3.2.1 Multi-layer model	28
3.2.2 Formulation of the parametric models	31
3.2.3 Meaning of soil moisture in the models	34
3.2.4 Stochastic treatment of spatial heterogeneity of soil hydraulic properties	35
3.3 Specification of parameters and meteorological time series	37
3.4 Results and discussion	39

3.4.1	Effect of soil heterogeneity	39
3.4.2	Comparison of the parametric models with the multi-layer model	41
3.4.3	Implications for modeling the lower boundary	43
3.4.4	Persistence of soil moisture anomalies	44
3.5	Conclusions	45
4	The water budget considering soil and rainfall heterogeneity	47
4.1	Objective and methods	47
4.2	Problem formulation	47
4.3	Spatial heterogeneity of the water budget	51
4.3.1	Stochastic formulation	51
4.3.2	Heterogeneity of soil hydraulic properties	51
4.3.3	Heterogeneity of rainfall	51
4.3.4	Simulations	53
4.4	Results and discussion	55
4.4.1	Point scale water budget	57
4.4.2	Field scale water budget considering soil heterogeneity	58
4.4.3	Regional water budget considering rainfall heterogeneity	62
4.4.4	Regional water budget considering soil and rainfall heterogeneity	64
4.4.5	"Equivalent" soil properties	67
4.4.6	Dynamics of water storage	70
4.5	Conclusions	73
5	Analytical treatment of the soil water budget	75
5.1	Objective and methods	75
5.2	Analytical development	76
5.2.1	Soil hydraulic characteristics	76
5.2.2	Solution for storm periods	76
5.2.3	Solution for interstorm periods	79
5.3	Specification of climate and soil parameters	83
5.3.1	Climate forcing	83
5.3.2	Soil hydraulic characteristics and their spatial heterogeneity	84
5.4	Validation of the analytical solutions	85
5.5	Influence of soil parameters and their heterogeneity on the soil water budget	89
5.5.1	Sensitivity of the analytical solutions	89
5.5.2	Sensitivity of the water budget to soil heterogeneity	91
5.6	"Equivalent" soil hydraulic characteristics	93
5.6.1	Governing equations	94
5.6.2	Determination of "equivalent" soil hydraulic characteristics; an example	95

5.7	Derived distributions for heterogeneous infiltration and evapotranspiration rates	98
5.7.1	Derived distribution theory	99
5.7.2	Infiltration rate regarding spatially heterogeneous saturated hydraulic conductivity	99
5.7.3	Infiltration rate regarding spatially heterogeneous rainfall rate	105
5.7.4	Evapotranspiration rate regarding spatially heterogeneous saturated hydraulic conductivity	109
5.7.5	Evapotranspiration rate regarding spatially heterogeneous initial saturation degree	112
5.8	Conclusions	114
6	Deterministic heterogeneity on hillslopes	115
6.1	Objective and methods	115
6.2	Flow equations and initial conditions	116
6.2.1	Flow equations	116
6.2.2	Initial and boundary conditions	119
6.3	Model formulation	120
6.3.1	Numerical implementation	120
6.3.2	Analytical formulation of infiltration	120
6.3.3	Analytical treatment of the phreatic surface dynamics	121
6.3.4	Treatment of the seepage face	123
6.3.5	Treatment of convergent flow	123
6.4	Model verification	124
6.4.1	Description of the experimental site	125
6.4.2	Measured data	125
6.4.3	Model input	126
6.4.4	Verification results	127
6.5	Case studies for idealized hillslopes	129
6.5.1	Specification of climate, soil, geomorphology and vegetation properties	129
6.5.2	Case studies	131
6.6	Results of the case studies	132
6.6.1	Reference Case	133
6.6.2	Effect of climate	139
6.6.3	Effect of soil scale factor	140
6.6.4	Effect of soil depth	142
6.6.5	Effect of slope	143
6.6.6	Effect of hillslope length and convergence	143
6.6.7	Effect of rootzone depth	145
6.6.8	Effect of channel at downstream boundary	146
6.7	Conclusions	148

7 Epilogue and general conclusions	149
7.1 Investigated scale transitions	149
7.2 Investigated models as limiting cases of reality	151
7.3 Principal conclusions and remaining questions	152
7.3.1 Modeling the lower boundary in one-dimensional climate- scale models	152
7.3.2 Influence of short time scale phenomena for the long-term average water budget	153
7.3.3 Existence and meaning of equivalent parameters	154
7.3.4 Characteristic spatial scales of water budget heterogeneity	154
7.3.5 Spatial heterogeneity on event time scale	155
7.3.6 Effect of simultaneous deterministic and stochastic hetero- geneity on hillslope hydrological behavior	156
A Stochastic methods	159
A.1 Random variables	159
A.2 Estimators of moments	159
A.3 Probability density and distribution functions	160
A.4 Truncation of the density function	161
A.5 Root mean square error	162
B Derivation of equation (5.30)	163
C Derivation of equation (6.30)	165
Summary	167
Samenvatting	171
Bibliography	175
Curriculum Vitae	183

List of Symbols

SYMBOL	DESCRIPTION	DIMENSION	SI UNIT
A	area	L^2	m^2
a	$\frac{2-\epsilon}{3}$ in (5.5)	-	-
a_g	shape parameter in (3.3)	L^{-1}	m^{-1}
a_s	surface albedo	-	-
B	boundary enclosing A	L	m
b	empirical constant in (3.20)	-	-
C	canopy storage	L	m
C_s	volumetric soil heat capacity	$L^{-1}MT^{-2}\Theta^{-1}$	$Jm^{-3}K^{-1}$
C_1	empirical constant in (3.18)	-	-
C_1^{sat}	empirical constant in (3.20)	-	-
C_2	empirical constant in (3.18)	-	-
C_2^{ref}	empirical constant in (3.21)	-	-
c	$\frac{2+2m}{m}$	-	-
c_p	dry air specific heat at constant pressure	$L^2 T^{-2} \Theta^{-1}$	$J kg^{-1} K^{-1}$
D	diffusivity	$L^2 T^{-1}$	$m^2 s^{-1}$
d_r	depth of reservoir	L	m
d_t	depth of embedded reservoir in (3.18)	L	m
E	evapotranspiration flux	LT^{-1}	ms^{-1}
E_c	canopy evaporation flux	LT^{-1}	ms^{-1}
E_{cp}	potential canopy evaporation flux	LT^{-1}	ms^{-1}
E_p	potential evapotranspiration flux	LT^{-1}	ms^{-1}
E_s	bare soil evaporation flux	LT^{-1}	ms^{-1}
E_t	plant transpiration flux	LT^{-1}	ms^{-1}
E_w	wet crop evapotranspiration flux in (3.25)	LT^{-1}	ms^{-1}
e	vapor pressure	$L^{-1}MT^{-2}$	Pa
e_s	saturated vapor pressure	$L^{-1}MT^{-2}$	Pa
G	soil heat flux	MT^{-3}	Wm^{-2}
g	acceleration of gravity	LT^{-2}	ms^{-2}
$g_{1..6}$	inverse relations in derived pdf		
H	sensible heat flux	MT^{-3}	Wm^{-2}
H^{in}	incoming advective sensible heat flux	MT^{-3}	Wm^{-2}
H^{out}	outgoing advective sensible heat flux	MT^{-3}	Wm^{-2}

SYMBOL	DESCRIPTION	DIMENSION	SI UNIT
H^{top}	turbulent entrainment flux of sensible heat	$M T^{-3}$	$W m^{-2}$
h	height of the phreatic surface above datum	L	m
h_c	water depth in channel	L	m
i	infiltration flux	$L T^{-1}$	$m s^{-1}$
i_h	head controlled infiltration flux	$L T^{-1}$	$m s^{-1}$
\mathbf{k}	hydraulic conductivity tensor	$L T^{-1}$	$m s^{-1}$
k	hydraulic conductivity	$L T^{-1}$	$m s^{-1}$
k_s	saturated hydraulic conductivity	$L T^{-1}$	$m s^{-1}$
k_s^w	saturated conductivity in (3.14)	$L T^{-1}$	$m s^{-1}$
l	shape parameter in (3.4)	-	-
m	pore size distribution index	-	-
N	number of Monte Carlo realizations	-	-
n	empirical constant in (3.14)	-	-
n_1	shape parameter in (3.3)	-	-
n_2	$1 - n_1^{-1}$	-	-
P	precipitation or rainfall rate	$L T^{-1}$	$m s^{-1}$
p	pressure	$L^{-1} M T^{-2}$	Pa
Q^{in}	incoming advective water vapor flux	$L T^{-1}$	$m s^{-1}$
Q^c	catchment outflow	$L^3 T^{-1}$	$m^3 s^{-1}$
Q^{out}	outgoing advective water vapor flux	$L T^{-1}$	$m s^{-1}$
Q_s	saturated lateral flow	$L^2 T^{-1}$	$m^2 s^{-1}$
Q^{top}	downward entrainment dry air flux	$L T^{-1}$	$m s^{-1}$
Q_u	unsaturated lateral flow	$L^2 T^{-1}$	$m^2 s^{-1}$
q	soil water flux	$L T^{-1}$	$m s^{-1}$
\mathbf{q}	soil water flux vector	$L T^{-1}$	$m s^{-1}$
q^{in}	lateral incoming soil water flux	$L T^{-1}$	$m s^{-1}$
q^{out}	lateral outgoing soil water flux	$L T^{-1}$	$m s^{-1}$
q_{ie}	infiltration excess surface runoff flux	$L T^{-1}$	$m s^{-1}$
q_p	percolation flux	$L T^{-1}$	$m s^{-1}$
q_r	recharge flux	$L T^{-1}$	$m s^{-1}$
q_s	surface runoff flux ($q_{ie} + q_{se}$)	$L T^{-1}$	$m s^{-1}$
q_{se}	saturation excess surface runoff flux	$L T^{-1}$	$m s^{-1}$
q_{sf}	flux through seepage face	$L T^{-1}$	$m s^{-1}$
R_a	anisotropy ratio in (6.3)	-	-
R_c	convergence ratio in (6.21)	-	-
R_l^{down}	downwelling longwave radiation flux	$M T^{-3}$	$W m^{-2}$
R_l^{up}	downwelling longwave radiation flux	$M T^{-3}$	$W m^{-2}$
R_n	net radiation flux	$M T^{-3}$	$W m^{-2}$
R_s	incoming shortwave radiation flux	$M T^{-3}$	$W m^{-2}$
r	exponent in transpiration function (5.19)	-	-
r_a	aerodynamic resistance	$L^{-1} T$	$s m^{-1}$
r_s	stomatal resistance	$L^{-1} T$	$s m^{-1}$

SYMBOL	DESCRIPTION	DIMENSION	SI UNIT
\mathbf{S}	vector with soil hydraulic parameters		
S	sorptivity	$L T^{-\frac{1}{2}}$	$m s^{-\frac{1}{2}}$
S_r	defined in (5.8)	$L^{\frac{1}{2}}$	$m^{\frac{1}{2}}$
S_y	specific yield	-	-
s	degree of saturation	-	-
s_0	initial degree of saturation	-	-
T_a	air temperature	Θ	K
T_s	soil temperature	Θ	K
t	time	T	s
t_b	duration of interstorm period	T	s
t_c	compression time in (5.12)	T	s
t_d	duration of storm period	T	s
t_e	equivalent time in (5.9)	T	s
t_p	ponding time in (5.11)	T	s
U	root water uptake	T^{-1}	s^{-1}
u	wind speed	$L T^{-1}$	$m s^{-1}$
V	volume	L^3	m^3
W	water storage in column	L	m
x	lateral coordinate	L	m
x_L	hillslope length	L	m
x_{sf}	length of the seepage face	L	m
z	vertical coordinate (positive upwards)	L	m
z_a	atmospheric screening height	L	m
z_b	elevation of channel bottom	L	m
z_c	lower boundary of the soil column	L	m
z_h	height of atmospheric boundary layer	L	m
z_r	lower boundary of root zone	L	m
z_s	location of the land surface	L	m
z_0	roughness length	L	m
α	scale factor	-	-
β_F	transpiration efficiency Feddes	-	-
β_W	transpiration efficiency Warrilow	-	-
γ	psychrometric constant	$L^{-1} M T^{-2} \Theta^{-1}$	$Pa K^{-1}$
Δ	$\frac{de_s}{dT_a}$	$L^{-1} M T^{-2} \Theta^{-1}$	$Pa K^{-1}$
δ_{ij}	Kronecker delta (1 if $i = j$ else 0)	-	-
δz	height of hydrostatic region	L	m
ϵ_a	atmospheric thermal emissivity	-	-
ϵ_s	surface thermal emissivity	-	-
θ	volumetric moisture content	-	-
θ_c	critical moisture content	-	-
θ_e	effective moisture content in (3.22)	-	-
θ_l	small value to prevent zero division in (3.21)	-	-

SYMBOL	DESCRIPTION	DIMENSION	SI UNIT
θ_r	residual moisture content	-	-
θ_s	saturated moisture content	-	-
θ_t	moisture content embedded layer in (3.18)	-	-
θ_w	wilting point moisture content	-	-
θ_0	initial moisture content	-	-
ϑ	atmospheric potential temperature	Θ	K
κ	rainfall fractional area	-	-
Λ	transient lateral flow ratio in (6.29)	-	-
λ	latent heat of vaporization	$L^2 T^{-2}$	$J kg^{-1}$
ν	atmospheric specific humidity	$M M^{-1}$	$g kg^{-1}$
ρ_a	density of air	$L^{-3} M$	$kg m^{-3}$
ρ_w	density of water	$L^{-3} M$	$kg m^{-3}$
ζ	soil parameter in (6.17)	-	-
τ	diurnal period	T	s
ϕ	hillslope angle	rad	rad
ψ	soil matric head (< 0 if soil is unsaturated)	L	m
ψ_s	air entry value	L	m
ψ_0	initial soil matric head	L	m
$\psi_{1..4}$	transition points in Fig. 3.1	L	m

OPERATOR	DESCRIPTION	DIMENSION	UNIT
$F_{\omega}(\omega)$	cumulative distribution function of ω	-	-
$f_{\omega}(\omega)$	probability density function of ω	dim [ω^{-1}]	unit [ω^{-1}]
$m_e[\omega]$	median of ω	dim [ω]	unit [ω]
$\widehat{m}_e[\omega]$	estimator of median of ω	dim [ω]	unit [ω]
$m_o[\omega]$	mode of ω	dim [ω]	unit [ω]
$\widehat{m}_o[\omega]$	estimator of mode of ω	dim [ω]	unit [ω]
$\mu[\omega]$	mean of ω	dim [ω]	unit [ω]
$\widehat{\mu}[\omega]$	estimator of mean of ω	dim [ω]	unit [ω]
$\sigma[\omega]$	standard deviation of ω	dim [ω]	unit [ω]
$\widehat{\sigma}[\omega]$	estimator of standard deviation of ω	dim [ω]	unit [ω]
$\bar{\omega}$	time average of ω	dim [ω]	unit [ω]
$\langle \omega \rangle$	spatial average of ω	dim [ω]	unit [ω]
$\mathcal{R}[\omega]$	root mean square error	dim [ω]	unit [ω]

SUPERSCRIPIT	DESCRIPTION
a	annual value
cum	cumulative value
int	integration time
max	maximum value
min	minimum value
ref	scaled average or reference value

Chapter 1

Introduction

1.1 Climate

The climatic system consists of the earth's atmosphere together with its adjoining systems: the hydrosphere, including oceans, groundwater, lakes and rivers, the cryosphere formed by the snow and ice masses on the earth, the underlying lithosphere and the biosphere, consisting of the marine and terrestrial biosystems [72, Peixoto and Oort 1992]. Climate is defined as the mean physical state of the climatic system. The increasing awareness that human activities may exert influence on climate has greatly stimulated the study of the climatic system.

Throughout history, climate has shown variations on time scales ranging from years to glacial periods. This climate variability can be expressed in terms of forced and free variations. Forced variations are changes in external forcing, e.g. the intensity of solar radiation, the atmosphere's chemical composition and changes of the land-surface. Free variations are due to internal feedbacks. As an example, the diurnal and seasonal cycle of the atmospheric state are related to astronomical factors and are therefore forced variations. In contrast, day to day or year to year weather variations that take place independently of changes in external forcing, are considered free variations. If the climatic system were linear, the periodic forcing of incoming solar radiation at the top of the atmosphere would lead to a periodic response of the climatic system of the same frequency. The wide range of time and space scales within the climatic system and the non-linear interactions between them, however, results in variabilities ranging from planetary and interdecadal down to turbulence dissipation scales (centimeters and seconds).

Due to variations in external forcings and internal feedbacks, different regimes prevail in the course of climate evolution [51, Lorenz 1969]. Hence, climate depends on the averaging time interval. Using an interval of thirty years, as determined by the World Meteorological Organization, the ice ages may be regarded as different from the current climate, but when using the no less arbitrary interval

of one hundred thousand years, however, ice ages can be considered to be part of the climate. Restricting ourselves to the atmospheric part of climate solely, it is clear that climate and weather differ fundamentally, although both are governed by the same physical laws. Slowly varying boundary conditions can often be neglected when studying weather, since on small time scales the atmosphere is almost inert. Clearly this is not the case for climate so that its study is therefore more complex.

1.2 Climate modeling

The need for prognostic tools has encouraged the development and elaboration of climate models. An overview of the various types of climate models, ranging from zero-dimensional to three-dimensional, can be found in Peixoto and Oort [72, 1992]. The class of models that initiated this study consists of the three-dimensional General Circulation Models (GCMs), that in many perspectives can be regarded as approaching reality as close as possible. Despite many simplifications, the first attempt to model the general circulation [75, Phillips 1956] demonstrated the feasibility of numerical simulation in the study of the atmosphere. Since then, great progress has been made, resulting in the complex GCMs currently used. In GCMs, the primitive equations that govern the fluid dynamical motion of the atmosphere and the oceans in response to pressure gradients, heating, rotation of the Earth and friction, are solved numerically by (coarsely) discretizing time and space. The global circulation patterns obtained in this way are reasonably realistic. Opposed to these so called "dynamics", the physical description of predominantly one-dimensional processes like radiative transfer, cloud formation, convection and land surface-atmosphere interactions is to a great extent inadequate, largely because of a gap in present knowledge. Besides the coarse spatial resolution of GCMs, the insufficient representation of physical processes explains the poor quality of continental climate predictions.

1.3 Water in the climatic system

Water in all three phases plays a dominant role in the climatic system. The large amounts of energy associated with phase transitions cause the vast quantities of water that are continuously carried around to transport enormous amounts of energy. The global hydrological cycle can be divided into the oceanic, the terrestrial and the atmospheric branch. The oceans store 97.5 % of all water and thus constitute by far the largest reservoir. Of the remaining fraction, 74 % of the water is stored in glaciers, 25 % in groundwater and the remainder in lakes and rivers [71, Peixoto 1993]. The amounts of water stored in the biosphere

and the atmosphere are extremely small ($< 0.005\%$). The average residence time of water within a reservoir is inversely proportional to the storage. For atmospheric water vapor the average residence time is about nine days and for water stored in the oceans this figure is of the order of thousands of years [71, Peixoto 1993]. Although volumetrically the atmosphere stores little water, the transport of energy associated with it is large because of the intensive mixing and fast renewal of water vapor.

Water that leaves the terrestrial branch either as runoff or evapotranspiration, serves as input to the oceanic and atmospheric branch respectively. Alternatively, water leaving the atmospheric branch as precipitation, comprises the input of the oceanic and terrestrial branches. The hydrological cycle thus links the land, ocean and atmosphere.

1.4 Land surface processes

This thesis concerns the hydrological processes at the land surface. Because of the large amounts of energy involved in the phase transitions of water (latent heats), the exchanges of water and energy are intrinsically coupled. This is reflected by the presence of the evapotranspiration term in both the energy and the water budget equations, as will be shown in detail in Chapter 2. Thus, in order to realistically simulate the climatic system, a proper representation of the water budget of the land surface is indispensable.

The water budget of the land surface describes the change in water storage at the land surface in relation to the incoming and outgoing fluxes. Precipitation falling on the land surface is partitioned into interception, infiltration and surface runoff. Intercepted water either falls on the land surface or evaporates back into the atmosphere. The infiltrated water may return to the atmosphere through evapotranspiration or percolate to deeper layers. Percolated water may return to the land surface from where it either evaporates or is discharged through the surface water system. Besides on the atmospheric conditions and the characteristics of the land surface (soil, vegetation and topography), the partitioning of water into the various terms strongly depends on the moisture state of the land surface. On average, 63 % of the precipitation falling on the continents returns to the atmosphere through evapotranspiration [71, Peixoto 1993]. The remainder is discharged as runoff into the oceans. These fractions, however, vary considerably over the earth.

Coupled hydrological-atmospheric behavior integrates phenomena over a wide range of time and space scales. As a general rule, these processes are nonlinear and there are many feedbacks between them. It is intuitive that the strength of the coupling between the land surface and the atmosphere depends on the

spatial scale considered. Generally, the increasing amounts of water being exchanged strengthen the coupling between the land surface and the atmosphere with increasing scale. To illustrate this, for a certain land surface type on a small spatial scale ($< 10^4$ m), evapotranspiration from the land surface into the atmosphere does not significantly change the atmospheric precipitable water content. Precipitation out of the atmosphere is thus effectively an independent boundary condition for hydrological processes (one-way coupling). In contrast, on larger scales ($> 10^4$ m) the atmospheric water content is affected by evapotranspiration from the land surface so that precipitation on the land surface can no longer be regarded as an independent boundary condition (two-way coupling).

An example of hydrological behavior that changes with scale is presented in Fig. 1.1. Depending on the region, the mean annual runoff per unit area in-

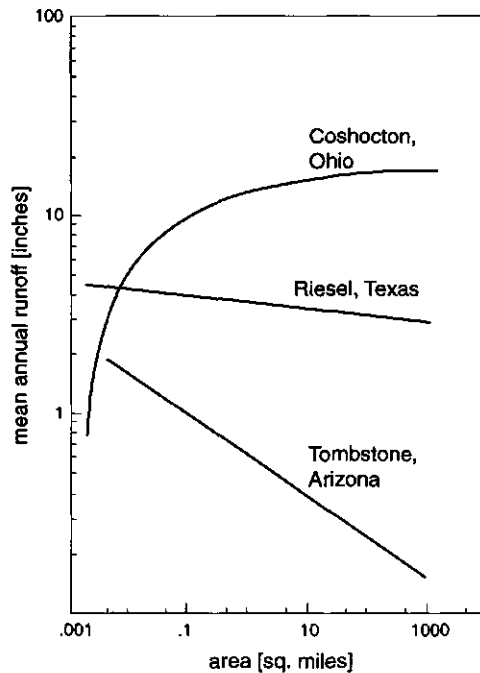


Figure 1.1: Mean annual runoff per unit area versus the drainage area for three regions (after Glymph and Holtan [40, 1969]).

increases, decreases or remains constant with increasing area. This shows that inference of large-scale hydrological behavior from well understood phenomena at smaller scales is complicated. The various sources of heterogeneity of the land surface and the atmosphere further complicate the understanding of large-scale hydrological processes. It is therefore not surprising that a universal technique to

pass hydrologic information from smaller to larger scales (or vice versa) has not been found yet.

1.5 Thesis objective

The main objective of this thesis is to obtain quantitative insight into the effect of upscaling spatially heterogeneous hydrological processes that constitute the water budget of the land surface. The spatial scales considered in this thesis (mostly $\leq 10^4$ m) are small enough to regard the atmospheric conditions as boundary conditions. Hence, the coupling between land surface and atmosphere is not considered. This is discussed in more detail in Chapter 2.

Also in Chapter 2, the scale dependence of the water budget components is discussed extensively. It is shown that a tremendous discrepancy exists between the scales at which the physical processes are sufficiently *understood* ($< 10^0$ m) and the scales at which the processes need to be *represented* ($> 10^4$ m).

In Chapters 3 - 5 the water budget components in the presence of spatial heterogeneity of soil properties and rainfall rate are studied. Because of the complexity of soil and rainfall heterogeneity, a statistical approach is applied: soil parameters and rainfall rate are viewed as random variables with associated probability distribution functions.

In Chapter 6 the hydrological processes in sloping areas are investigated. Water transport from higher to lower elevations is governed by well understood physical laws. Thus, in contrast to Chapters 3 - 5, the heterogeneity that is investigated here has a deterministic origin.

The objectives and contents of Chapters 3 - 6 are discussed in greater detail at the end of Chapter 2 since they rely heavily on the review given there. Finally, in Chapter 7 the insights and the conclusions arrived at are summarized and some remaining questions are highlighted.

Chapter 2

Rationale and Review

2.1 Mass and energy balance

As mentioned in the first chapter, the land surface and the atmosphere exchange water and energy. These exchange processes are subject to the conservation principle which states that no mass or energy can be generated or lost. Now consider the cross-section of soil, with lower boundary z_c , and the overlying atmospheric boundary layer, with time variable height z_h , in Fig. 2.1.

The time evolution of the vertically average state variables soil water content θ , atmospheric specific humidity ν , soil temperature T_s and atmospheric potential temperature ϑ can be derived by formulating the water and energy budget equations. Since the purpose here is to demonstrate the coupling between the land surface and the atmosphere, only the dependencies of the fluxes on the four state variables are indicated

$$\frac{d\theta}{dt} = \frac{1}{|z_c|} \left\{ P(\nu) - q_s(\theta, P) - q_p(\theta) - E(\theta, \nu, \vartheta) + q^{in} - q^{out} \right\} \quad (2.1)$$

$$\frac{d\nu}{dt} = \frac{\rho_a g}{p(z_s) - p(z_h(t))} \left\{ Q^{in} - Q^{out} - Q^{top} - P(\nu) + E(\theta, \nu, \vartheta) \right\} \quad (2.2)$$

$$\frac{dT_s}{dt} = \frac{1}{C_s(\theta) |z_c|} \left\{ [1 - a_s(\theta)] R_s + [1 - \epsilon_a(\nu)] R_i^{down} - R_i^{up}(T_s) - H(T_s, \vartheta) - \rho_w \lambda E(\theta, \nu, \vartheta) - G(\theta, T_s) \right\} \quad (2.3)$$

$$\frac{d\vartheta}{dt} = \frac{g}{c_p [p(z_s) - p(z_h(t))]} \left\{ H^{in} - H^{out} + H^{top} + H(T_s, \vartheta) + (R_i^{down} + R_i^{up}(T_s)) \epsilon_a(\nu) \right\} \quad (2.4)$$

where t denotes time, z the vertical coordinate (positive upwards), P the precipitation flux, q_s the surface runoff flux, q_p the percolation flux to deeper soil layers, E the evapotranspiration flux, q^{in} and q^{out} the incoming and outgoing soil water

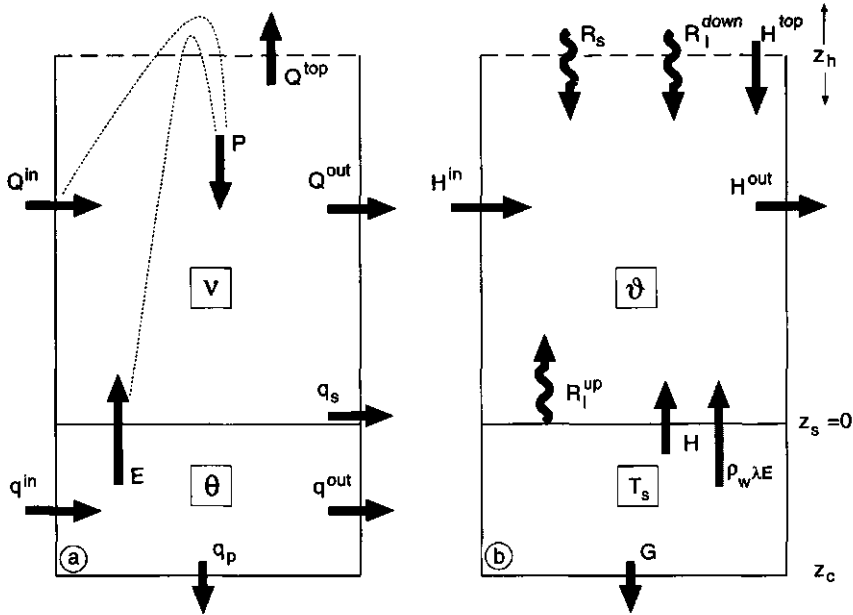


Figure 2.1: Cross-section of the land surface and the overlying atmospheric boundary layer. (a) water budget and (b) energy budget. Fluxes are positive in the direction of the arrows.

fluxes, ρ_a the air density, g the acceleration of gravity, p the pressure, Q^{in} and Q^{out} the lateral advective fluxes of water vapor, Q^{top} the downward entrainment flux of dry air, C_s the volumetric soil heat capacity, a_s the surface albedo, R_s the incoming shortwave radiation flux density, ϵ_a the atmospheric emissivity, R_l^{down} the downwelling longwave radiation flux density, R_l^{up} the upwelling longwave radiation flux density, H the sensible heat flux, λ the latent heat of vaporization of water, G the soil heat flux, c_p the dry air specific heat at constant pressure, H^{in} and H^{out} the lateral advective fluxes of sensible heat and H^{top} the turbulent entrainment flux of sensible heat.

It must be emphasized here that the four state variables change with vertical position. For a realistic representation of the processes one should consider the actual profiles rather than the vertically average values as is done in (2.1) - (2.4). For example, the sensible heat flux H and upwelling longwave radiation R_l^{up} depend on the surface temperature $T_s(z_s)$ rather than on the average soil temperature. The time dependence of z_h reflects that the height of the boundary layer is governed by the magnitude of the turbulent fluxes. Condensation is assumed to occur above the boundary layer and the term $\rho_w \lambda E$ in the soil energy budget equation (2.3) is not balanced by a $\rho_w \lambda P$ term in (2.4). The influence of the atmospheric

conditions on the incoming shortwave radiation R_s is assumed to be negligible.

Despite the omission of many dependencies, it is evident that the four conservation equations constitute a coupled system. The soil water and the energy budget equations, (2.1) and (2.3) respectively, share the evapotranspiration term. The dependence of C_s , a_s and G on the state variable θ ties the two budget equations even closer. Similar interdependencies can be seen for other combinations of (2.1) - (2.4).

An elegant model to study the nonlinear dynamics of water and energy exchanges within the land-atmosphere system, based on the four coupled equations, was proposed by Brubaker and Entekhabi [13, 1994]. A lucid, highly simplified illustration of the coupled nature of water and energy exchange at the land surface is given in Fig. 2.2. The arrows indicate some pathways through which an initial

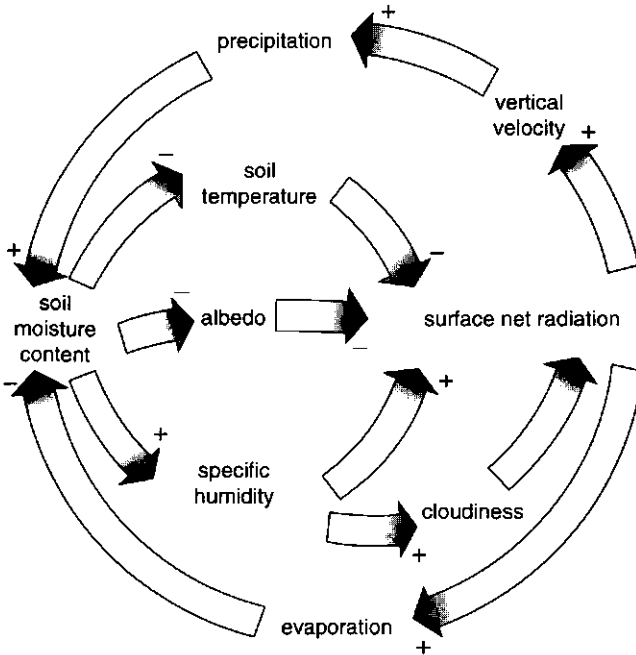


Figure 2.2: Feedback processes related to a change in soil water content (O’Kane based on a discussion by Rowntree [81, 1984]).

change in soil water content may be damped (-) or amplified (+). Both positive and negative feedbacks can be identified.

The crucial implication of the above-stated is that a proper representation of the water budget of the land surface is indispensable in climate models as it affects

both the atmospheric water and the energy budget. This is confirmed by various studies using both observations and numerical climate models (e.g. Shukla and Mintz [90, 1982], Mahfouf *et al.* [52, 1987], and Meehl and Washington [59, 1988])

2.2 Definition of the thesis' central equation

Atmospheric and sub-surface water and energy transport differ fundamentally with respect to their characteristic time and space scales. In the soil, transport occurs in a virtually static medium. The high impedance causes low transport velocities with little mixing as a result. Atmospheric flow is usually turbulent and the medium itself becomes intensively blended. The characteristic time and space scales of atmospheric flow are therefore short and large respectively when compared to sub-surface flow.

In principle, the conservation equations (2.1) - (2.4) are valid regardless of the horizontal space scale considered. However, the dependencies of the fluxes in the budget equations on the relevant state variables change with scale, due to various sources of heterogeneity. This necessitates the aggregation (disaggregation) of processes at one scale to a larger (smaller) one. These scale transitions are generally complicated by nonlinear dependencies, in many cases across scales.

Considering all this, it is logical that the strength of the two-way coupling between the atmospheric and sub-surface states changes with scale. At small space scales the sub-surface system may be considered to be forced by atmospheric conditions and modification of these by fluctuating sub-surface processes can be safely neglected. At very large space scales the signature of the land surface becomes clearly visible. For example, the typical features of continental climates reflect the influence of land-atmosphere interactions over large scales. Similarly, the short time scale dynamical behavior of the sub-surface system is generally limited and the influence on the atmospheric system is small. It is only over longer periods that fluctuations of sub-surface processes are substantial enough to affect the overlying atmosphere. The importance of sub-surface and hydrological processes will therefore be far greater in climate models than in weather models, in which the influence of the sub-surface is essentially limited to the specification of the initial condition.

An example of the relatively long time scales of sub-surface flow is found in Fig. 2.3, which shows the propagation of rainfall anomalies (i.e. deviations from the long time average) through a cascade of sub-surface reservoirs: soil moisture and groundwater, and the corresponding fluxes: surface runoff and streamflow. Because of the storage associated with the reservoirs, the sub-surface essentially acts as a low-pass filter [34, Entekhabi 1994] adding memory to the system. Since the time scale of an anomaly "moving down" in Fig. 2.3 is of the same order as

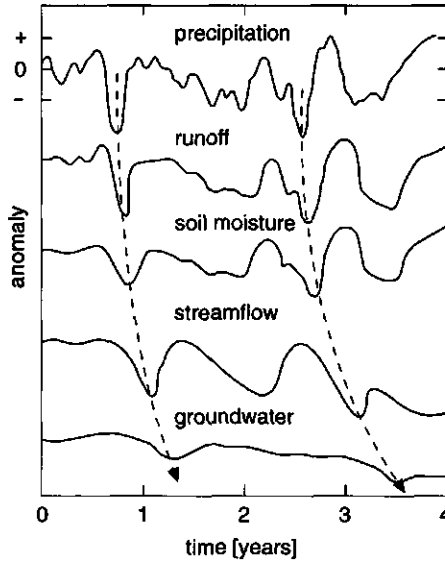


Figure 2.3: Propagation of rainfall anomalies through sub-surface reservoirs (after McNab [58, 1989]).

that of an anomaly “moving up” (not shown), it is evident that the sub-surface may affect the atmosphere over long time scales, as indicated by Delworth and Manabe [24, 1989] and Rodriguez-Iturbe *et al.* [77, 1991].

In this thesis the dependence of the atmospheric state variables ν and ϑ on the sub-surface system is not considered. In other words, the sub-surface system is assumed not to affect its own boundary conditions, that are prescribed accordingly. The focal point is the aggregation of (2.1) rather than the system represented by (2.1) and (2.3). Therefore, the dependencies of a_s and R_t^{up} on θ and T_s respectively are omitted by introducing the net incoming radiation flux density:

$$R_n = [1 - a_s(\theta)] R_s + [1 - \epsilon_a(\nu)] R_t^{down} - R_t^{up}(\epsilon_s, T_s) \quad (2.5)$$

where ϵ_s denotes the surface thermal emissivity. The energy budget equation (2.3) now basically serves as a means to limit the evapotranspiration in (2.1) to its potential value E_p , which depends on ν, ϑ, R_n, u and vegetation resistance under unlimited water availability r_s^{min} .

In conclusion, central in this thesis is the water budget equation:

$$\frac{d}{dt} \int_{z_c}^{z_s} \theta(z) dz = P - q_s(\theta(z_s), P, \mathbf{S}(z_s)) - q_p(\theta(z_c), \mathbf{S}(z_c)) - E(\theta(z), E_p, \mathbf{S}(z)) \quad (2.6)$$

where $E_p = E_p(\nu, \vartheta, R_n, u, r_s^{min})$ and \mathbf{S} denotes the vector containing the parameters that describe the soil hydraulic properties that will be discussed in Section

2.3.1. Rather than the vertically average value θ , in (2.6) the vertical profile $\theta(z)$ is considered. The incoming and outgoing lateral soil water fluxes are not included in (2.6) for reasons of brevity.

As previously mentioned, due to heterogeneity, the relationships between the fluxes in (2.6) and the state variable θ depend on the spatial space scale at which they are considered. A brief review of the water budget and the various sources of heterogeneity at different scales is given following section.

2.3 Length and time scales of sub-surface flow

The water budget equation incorporates processes with a variety of length and time scales. From (2.6) it is evident that these scales relate to the characteristics of rainfall, potential evapotranspiration and soil hydraulic properties. In this section an overview is presented of the water budget at hydrologically different scales.

2.3.1 Representative Elementary Volume ($\approx 10^{-2}$ m - 10^{-1} m)

The most important equation in soil physics, Darcy's law, states that flow within an isotropic porous medium occurs owing to a head gradient, at a rate governed by the conductivity of the medium

$$\mathbf{q} = -\mathbf{k}(\theta)\nabla(\psi + z) \quad (2.7)$$

Here the vector \mathbf{q} contains the water flux in three dimensions, \mathbf{k} is the hydraulic conductivity tensor and ψ the soil matric head and z the elevation head.

The soil matric head is the equivalent of the pressure potential on weight basis relative to atmospheric pressure (where $\psi = 0$). In an unsaturated medium, water is held against gravity by matric forces and ψ is negative accordingly. For a particular soil the following applies: the smaller the water content, the smaller the pores the water resides in, the stronger the matric forces and the smaller (i.e. more negative) the soil matric head. This mechanism is expressed by means of the soil water retention curve, $\theta(\psi)$. Similarly, when the water content becomes smaller, the area available to flow and, accordingly, the conductivity decreases, which is expressed by a $k(\theta)$ relationship. The vector \mathbf{S} in (2.6) contains the parameters of the $\theta(\psi)$ and $k(\theta)$ relationships. Of the many parametric forms for the $\theta(\psi)$ and $k(\theta)$ relationships that have been suggested, the ones of Brooks and Corey [12, 1966] and Van Genuchten [102, 1980] are frequently used in this thesis and are presented later.

Essentially, the Darcy flow equation contains the volume average effects of flow phenomena at smaller scales. These cannot be resolved explicitly because of the

unknown geometry of the porous medium and the hardly understood flow processes at lower moisture contents. The averaging volume (if existent) for which (2.7) applies is called the representative elementary volume (REV). The size of the REV is selected such that the soil hydraulic parameters in \mathbf{S} are independent of the size of the REV:

$$\left(\frac{\partial \mathbf{S}}{\partial V} \right)_{V=\text{REV}} = 0 \quad (2.8)$$

The concept of a time and space invariant REV that is valid for all physical properties in \mathbf{S} has been questioned by Baveye and Sposito [4, 1984], yet it remains the fundament of the description of water flow processes in porous media.

Obviously, no mass can be lost or generated, which for a fixed volume can be expressed by means of the conservation equation

$$\frac{\partial \theta}{\partial t} = -\nabla \cdot \mathbf{q} \quad (2.9)$$

Combination of (2.9) with the Darcy flow equation (2.7) yields the governing equation of non-stationary flow phenomena in porous media

$$\frac{\partial \theta}{\partial t} = \nabla \cdot \mathbf{k}(\theta) \nabla (\psi + z) \quad (2.10)$$

Throughout this thesis, the one-dimensional form of (2.10), commonly called Richards' equation, is used for vertical unsaturated flow. After addition of a sink term U that represents root water uptake, Richards' equation reads

$$\frac{\partial \theta}{\partial t} = \frac{\partial}{\partial z} \left(k_z(\theta) \left[\frac{\partial \psi}{\partial z} + 1 \right] \right) - U(\psi, E_p) \quad (2.11)$$

Richards' equation is highly nonlinear because of the dependence of θ , and k_z accordingly, on ψ . This nonlinear character causes upscaling to scales larger than the REV to be non trivial.

Finally, it is noted that (2.6) is obtained again by integration of (2.11) over the soil column

$$\begin{aligned} \int_{z_c}^{z_s} \frac{\partial \theta}{\partial t} dz &= \int_{z_c}^{z_s} \frac{\partial}{\partial z} \left(k_z(\theta) \left[\frac{\partial \psi}{\partial z} + 1 \right] \right) dz - \int_{z_c}^{z_s} U(\psi, E_p) dz \\ &= \underbrace{k_z(\theta) \left[\frac{\partial \psi}{\partial z} + 1 \right] \Big|_{z=z_s}}_{i - E_s} - \underbrace{k_z(\theta) \left[\frac{\partial \psi}{\partial z} + 1 \right] \Big|_{z=z_c}}_{q_p} - \underbrace{\int_{z_c}^{z_s} U(\psi(z), E_p) dz}_{E_t} \\ \iff \frac{d}{dt} \int_{z_c}^{z_s} \theta(z) dz &= P - q_s(\theta(z_s), P, \mathbf{S}(z_s)) - q_p(\theta(z_c), \mathbf{S}(z_c)) - \\ &E(\theta(z), E_p, \mathbf{S}(z)) \end{aligned} \quad (2.6)$$

where the infiltration flux $i = P - q_s$, E_s the bare soil evaporation flux across the land surface at $z = z_s$ and E_t the plant transpiration flux. Throughout this thesis only the total evapotranspiration flux $E = E_s + E_t$ is considered.

Summarizing, (2.6) is an external description of the soil of which the internal dynamics are governed by (2.11).

2.3.2 Plot and field scale ($\approx 10^{-1}$ m - 10^2 m)

The water budget of an area larger than the REV is obtained through integration of (2.6) over the considered area

$$\begin{aligned} \frac{d}{dt} \int^A \int_{z_c}^{z_s} \theta(z, \mathbf{a}) dz d\mathbf{a} = & P \cdot A - \\ & \int^A q_s(\theta(z_s, \mathbf{a}), P, \mathbf{S}(z_s, \mathbf{a})) d\mathbf{a} - \\ & \int^A q_p(\theta(z_c, \mathbf{a}), \mathbf{S}(z_c, \mathbf{a})) d\mathbf{a} - \\ & \int^A E(\theta(z, \mathbf{a}), E_p, \mathbf{S}(z, \mathbf{a})) d\mathbf{a} \end{aligned} \quad (2.12)$$

where \mathbf{a} denotes the vector with horizontal coordinates.

The difference between (2.6) and (2.12) thus arises because the vector \mathbf{S} containing the soil hydraulic parameters depends on the horizontal position. Going in the opposite direction as was done in the derivation of (2.6) from (2.11), differentiating (2.12) with respect to z leads to the equivalent of Richards' equation at the plot-scale. This "equivalent" Richards' equation is only meaningful when an "equivalent" set of soil hydraulic properties \mathbf{S}_e can be specified such that a transient behavior is obtained that is identical to that of the heterogeneous area under consideration. Optimistically stated, this may prove to be cumbersome, as will be seen later in this thesis.

For saturated flow, Dagan [20, 1982] states that the relation between the hydraulic properties at smaller and larger scales depends on the problem considered, i.e. on scale, on boundary conditions and, in the case of transient flow, on time. A sound example of this is given by Bierkens [7, 1994] who shows that the averaged Darcy equation consists of scale averages of conductivity and of hydraulic head and a closure term describing their scale average covariation.

For partially saturated media the issue becomes even more complicated. Even in case of soil homogeneity ($\theta(\psi)$ and $k_z(\theta)$ spatially uniform), the following inequality holds because of nonlinearity:

$$\langle q_z \rangle = \left\langle k_z(\theta) \left(\frac{d\psi}{dz} + 1 \right) \right\rangle \neq k_z(\langle \theta \rangle) \left(\frac{d\langle \psi \rangle}{dz} + 1 \right) \quad (2.13)$$

where $\langle \cdot \rangle$ denotes the spatial average operator.

Recapitulating, the fundamental difficulty in upscaling Richards' equation is its nonlinearity, in addition to the (co)variation of soil hydraulic properties and state variables. In terms of (2.12), this means that when the spatially average fluxes can be obtained (through measurements), this is not the case for the dependence of the average fluxes on the spatially averaged soil hydraulic parameters $\langle S \rangle$ and state variable $\langle \theta \rangle$.

A notable contribution to the spatial integration of (2.11) has been made by Chen *et al.* [15, 1993], [16, 1994]. They write (2.11) in terms of the spatial mean variables $\langle k_z \rangle$, $\langle \theta \rangle$ and $\langle \psi \rangle$ and subsequently relate them using a perturbation technique. Higher order terms are accounted for by a closure term. The resulting unknown truncation errors hamper the validity of the method for most practical situations. In accordance with the results of Dagan and Bresler [21, 1983], [11, 1983], Chen *et al.* emphasize the possibility of obtaining reliable results when using simplified point models that allow exact closure of the spatial average equation. They conclude that the relative magnitude of errors due to simplification of the governing equation tend to decrease with increasing spatial heterogeneity.

A last comment regarding the upscaling of (2.11) is of importance here. With the exception of Chapter 6, in this thesis the independent columns approach, similar to Chen *et al.* [15, 1993], [16, 1994], is frequently adopted. Representing a heterogenous area as a battery of independent soil columns does not allow for lateral links. When the phreatic surface resides deep, lateral sub-surface flow is of minor importance. However, when the rainfall intensity exceeds the infiltration capacity of the soil, surface runoff is generated as is indicated by (2.6). In reality, locally generated surface runoff may flow laterally towards a location where it (at least partly) can enter the soil. In other words, despite the local occurrence of surface runoff the area average runoff in (2.12) may well be zero (or negative when water enters from outside the plot). In that perspective, the representation of a heterogeneous area as consisting of independent columns constitutes a limiting case: surface runoff does not infiltrate elsewhere but is removed, yielding the maximum amount of surface runoff within the considered area.

2.3.3 Catchment scale ($\approx 10^2$ m - 10^5 m)

At scales larger than the plot scale, spatial aggregation of (2.6) may become increasingly difficult because of sub-surface saturated lateral flow. Additionally, at sufficiently large scales the boundary conditions P and E_p become spatially heterogenous. Similar to (2.12), the water budget of a large area can be written as:

$$\frac{d}{dt} \int^A \int_{z_c}^{z_s} \theta(z, \mathbf{a}) dz da = \int^A P(\mathbf{a}) da -$$

$$\begin{aligned}
& \int^A q_s(\theta(z_s, \mathbf{a}), P(\mathbf{a}), \mathbf{S}(z_s, \mathbf{a})) d\mathbf{a} - \\
& \int^A q_p(\theta(z_c, \mathbf{a}), \mathbf{S}(z_c, \mathbf{a})) d\mathbf{a} - \\
& \int^A E(\theta(z, \mathbf{a}), E_p(\mathbf{a}), \mathbf{S}(z, \mathbf{a})) d\mathbf{a} + \quad (2.14) \\
& \oint^B \int_{z_c}^{z_s} q^{in}(z, b) dz db - \oint^B \int_{z_c}^{z_s} q^{out}(z, b) dz db
\end{aligned}$$

where catchment boundary B encloses catchment area A .

The boundary integrals over the lateral soil water inflow and outflow q^{in} and q^{out} are included in the budget equation in order to account for lateral flow processes into and out of the catchment.

Lateral connections

Consider now a catchment for which $\oint^B \int_{z_c}^{z_s} q^{in}(z, b) dz db = 0$ (i.e. no inflow of water occurs over the catchment boundary) and lateral saturated sub-surface outflow concentrates at the catchment outlet, i.e. $\oint^B \int_{z_c}^{z_s} q^{out}(z, b) dz db = Q_s^c$. On average there is no storage change in the catchment, since accumulation and depletion have well defined upper and lower boundaries. The time average total flow through the catchment outlet, $\overline{Q^c}$, then equals:

$$\begin{aligned}
\overline{Q^c} &= \overline{Q_s^c} + \int^A \overline{q_s}(\mathbf{a}) d\mathbf{a} \\
&= \int^A (\overline{P}(\mathbf{a}) - \overline{q_p}(\mathbf{a}) - \overline{E}(\mathbf{a})) d\mathbf{a} \quad (2.15)
\end{aligned}$$

in which the overline denotes the time average and the various dependencies have been omitted for convenience.

Thus, on average, all precipitation that does not evaporate into the atmosphere or percolate towards deeper layers, leaves the catchment through the surface water system. Besides the lateral redistribution of rainfall due to surface runoff as mentioned before, water percolated to deeper layers may return at or near the surface at topographically favorable locations (such as valleys) due to groundwater flow and capillary rise. It may thus be that in (2.15) the integral over $\overline{q_p}$ is zero despite the local occurrence of percolation. The presence of lateral sub-surface (groundwater) flow prohibits the application of methods that consider an area as an ensemble of non-interacting columns, as discussed in Section 2.3.2.

Since on the time scale of a storm event the storage change cannot be neglected, the total catchment outflow is a complex function of time, $Q^c(t)$. Historically, hydrological science has focused mainly on the catchment outflow $Q^c(t)$. A broad range of strategies has been applied of which some are discussed below.

In the hydrological systems approach the physical behavior of the components in the water budget and the interactions among them are not considered. Rather, input (rainfall and sometimes potential evapotranspiration) and output (catchment outflow) are related through a mathematical relationship that is remote from the internal physical structure [14, Brutsaert 1986]. The unit hydrograph theory may serve as an example here (Sherman [88, 1932], referenced by Dooge [27, 1973]). Rodriguez-Iturbe and Valdès [79, 1979] extended the unit hydrograph concept by including geomorphological information, thereby adding physical structure to the concept.

On the other side of the catchment modeling spectrum is the physically based approach pioneered by Freeze [39, 1971], which attempts to understand the catchment-scale hydrological behavior from the governing equations at smaller scales. This leads to an elaborate numerical model containing linked processes at a variety of length and time scales. Naturally, this approach suffers from the spatial heterogeneity of the surface and sub-surface, to an even greater extent than discussed in Section 2.3.2. The limited availability and quality of data and the computational requirements often hamper its practical application. Some more recent examples of this approach are found in Abbott *et al.* [1, 1986] and in Paniconi and Wood [67, 1993].

Salvucci [83, 1994] extended the statistical dynamical water budget model of Eagleson [31, 1978] that accounts for dynamical phenomena in a statistical manner. By incorporating lateral saturated flow, Salvucci derived the long-term equilibrium state of a (two-dimensional) hillslope. This analysis clearly indicated the occurrence of spatial variation of the fluxes and moisture states along a uniform hillslope. Opposed to random variations of land surface properties, this kind of spatial variation is entirely due to lateral flow and is thus of deterministic origin.

As a last example, Beven and Kirkby [6, 1979] introduced a model that accounts for lateral connections in a rudimentary fashion. Based on an index containing topographic information, they identified locations that have identical hydrological responses. The drawback of topography as only driving force behind spatial heterogeneity is that the model breaks down in the absence of slope.

Spatial heterogeneity of rainfall and potential evapotranspiration

Whereas on small spatial scales the meteorological boundary conditions can be considered uniform (due to the intensive mixing within the atmosphere), on larger scales their spatial variation becomes a major source of hydrological variability. Traditionally, with the earlier mentioned focus on catchment outflow, the problem of spatial variation basically concerned the aggregation of atmospheric point measurements to area averages. In this thesis it is the exact opposite: the disaggregation of area averages, as obtained from numerical atmospheric models, to

values at the scale on which the flow phenomena are described. Since variation of the boundary conditions is present in both space and time, it is in fact impossible to regard spatial heterogeneity independent from time variability. For reasons of simplicity, Rodriguez-Iturbe and Mejia [78 1974] factor the space-time correlation function into a spatial and a temporal part, thus allowing separate treatment. In the following, the spatial structure of rainfall and potential evapotranspiration are briefly discussed.

Rainfall In comparison with time heterogeneity of point rainfall, the spatial rainfall structure has received considerably less attention, largely because of observational problems [33, Eagleson 1984]. A logical first step is the distinction of two sources of heterogeneity:

1. Non-stationary heterogeneity, reflecting that over an area different rainfall inducing mechanisms may be present;
2. Stationary heterogeneity, indicating that within an area covered by one mechanism the rainfall intensities are generally spatially variable.

Two examples of different rainfall types are given here as an illustration. Synoptic rainfall events often have length scales $> 10^5$ m and may exist over several days. Rainfall of convective or orographic origin is normally present on scales $< 10^4$ m with a duration of several hours at the most [105, Waymire and Gupta 1981].

High rainfall rates are generally associated with small length scales. Using rainfall measurements in The Netherlands on length scales ranging from $< 5 \cdot 10^3$ m to $> 3 \cdot 10^4$ m, Witter [106, 1984] showed that the spatial correlation between point rainfall measurements increases with increasing rainfall duration (corresponding to decreasing intensities). The spatial correlation decreases with increasing storm return periods (corresponding to higher intensities).

From this it is evident that at larger scales ($> 10^3$ m) rainfall heterogeneity must be taken into account. Since it is not the main interest in this thesis, disaggregation of rainfall is merely accomplished by specification of a probability density function of which the first moment equals the areal mean rainfall obtained from an atmospheric model.

Potential evapotranspiration Since the potential evapotranspiration rate depends on the net radiation flux density R_n , specific air humidity ν , (potential) air temperature ϑ , windspeed u and minimal vegetation resistance τ_s^{\min} , its spatial structure reflects variation of these variables. Because of the greater homogeneity of the atmosphere, the smallest scales of variation are associated with the variation of the land surface (topography and coverage) that affects the net radiation R_n (e.g. Dubayah *et al.* [30, 1990]) and local wind speed u . Here the view is taken that spatial heterogeneity of potential evapotranspiration is of less importance in

the water budget than rainfall since the latter is directly present in (2.6). For example, when evapotranspiration is limited by water availability, spatial variation of E_p is of minor importance compared to heterogeneity of soil water availability. Throughout this thesis, heterogeneity of potential evapotranspiration is therefore not considered.

2.4 Representation of land surface processes in climate models

In order to enable the long time integrations necessary for climate studies, the spatial resolution of climate models is coarse. Typically, the gridsize used in global climate models lies between $2 \cdot 10^5$ m and $5 \cdot 10^5$ m and in meso-scale climate models in between $1 \cdot 10^4$ m and $5 \cdot 10^4$ m. Besides the difficulty of the large scales at which hydrological descriptions are sought, there is the complicating fact that grid areas in climate models do not coincide with hydrologically distinguishable regions. Upscaling of hydrological processes in climate models may thus not necessarily proceed along scales that are hydrologically relevant.

This section reviews of the representation of land surface processes in climate models. The overview is structured along two lines, the degree of physical complexity and the degree of incorporated spatial heterogeneity, as is shown in Fig. 2.4.

Near the origin, both in terms of chronology and Fig. 2.4, is the so called "bucket" model of Manabe [55, 1969]. It consists of a soil reservoir that is filled by precipitation and emptied by evapotranspiration.

$$d_r \frac{d\theta}{dt} = P - q_{se}(\theta) - E(E_p, \theta) \quad (2.16)$$

In case the reservoir reaches its maximum storage capacity (the product of reservoir depth d_r and saturated moisture content θ_s), all precipitation is removed as saturation excess runoff q_{se} . Below a threshold value, evapotranspiration reduces linearly with the soil moisture content:

$$\begin{aligned} q_{se} &= P & \theta &= \theta_s, & q_{se} &= 0 & \theta < \theta_s \\ E &= E_p & \theta &\geq \frac{3}{4}\theta_s, & E &= \frac{\theta}{\theta_s} E_p & \theta < \frac{3}{4}\theta_s \end{aligned} \quad (2.17)$$

In the original formulation the product $d_r \theta_s$ was set to 0.15 m.

When comparing (2.16) and (2.6) five differences can be found:

- Percolation is not considered;

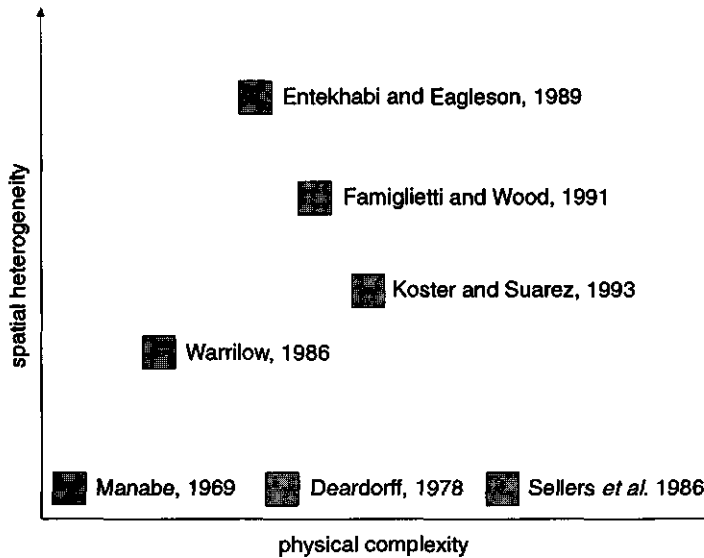


Figure 2.4: Relative location of the approaches discussed.

- Surface runoff only occurs in case of saturation and not because of rainfall exceeding the soil infiltration capacity;
- Evapotranspiration depends on the soil moisture content θ rather than the matric head ψ ;
- Transpiration does not depend on vegetation characteristics;
- Unsaturated flow within the reservoir is not considered, as indicated by the presence of only the mean moisture state rather than the soil moisture profile $\theta(z)$.

Despite its rudimentary character, inclusion of the bucket model in a global atmospheric model enabled the reproduction of gross features of the seasonal variations in the geographical distributions of precipitation, evaporation and runoff rates [56, Manabe and Holloway 1975]. Ever since this first interactive representation of land surface processes in atmospheric models, numerous approaches have been suggested, most of them modifications of the original bucket model. Structuring the discussion of the evolution of land surface schemes along the axes in Fig. 2.4 prevents the need for an exhaustive review of all developments.

2.4.1 Advancement of the physical description

Deardorff [22, 1977], [23, 1978] included an embedded top layer with a separate water budget within the original bucket and added a vegetation layer. A schematic illustration of the model can be found in Fig. 3.3 in Chapter 3, in which

the model is described in greater detail. The interaction between the embedded reservoir and the overall reservoir depends on both moisture states (force-restore method). The short time memory of the vegetation layer and the shallow top layer improve the description of dynamical processes on short time scales, such as canopy interception and evaporation and bare soil infiltration and evaporation. Plant transpiration is described using a resistance formulation, analogous to Ohm's law. The reduction of potential plant transpiration is governed by two resistances. The aerodynamic resistance depends on the foliage characteristics and decreases with increasing wind speed. The stomatal resistance reflects the opening of leaf stomata and increases with decreasing soil water content. Additionally, the stomatal resistance is related to the incoming solar radiation and is also season dependent. Noilhan and Planton [66, 1989] modified the model for use within the meso-scale climate model of the French Meteorological Service.

The inclusion of plant physiological phenomena becomes even more apparent in the schemes suggested by Dickinson *et al.* [25, 1986] (BATS) and Sellers *et al.* [85, 1986] (SiB), which are also based on resistance formulations. The two vegetation layers (canopy and ground cover) in the model of Sellers *et al.* modify the transfer of radiation, heat and water to and from the soil compartment. Three separate soil layers are distinguished, linked through a one-dimensional flow equation based on Darcy's equation (2.7). The complete formulation consists of 14 resistances, each dependent on one or several of the eight state variables (five water stores and the temperature states of the canopy, the ground surface and the soil compartment) and boundary conditions. A total of 49 parameters have to be specified, which in itself is a formidable task.

The models of Deardorff [23, 1978], Dickinson *et al.* [25, 1986] and Sellers *et al.* [85, 1986] are "big leaf" models in the sense that vegetation in a particular area or model grid is essentially represented by one big leaf with one stoma. The parameters must thus be effective at the scale to which the model is applied. Because of the intrinsic nonlinearity, of the processes this complicates the parameter specification even more since average values do not suffice, analogous to the problem defined by (2.13).

2.4.2 Incorporation of spatial heterogeneity

The assumption that the models discussed in the previous section are valid for the large spatial scales they are applied to is very severe, considering the variability present over a range of space scales (Section 2.3). In order to make a realistic representation of land surface processes for climate modeling purposes, incorporation and subsequent parameterization of this spatial variation is much needed.

A first step to account for spatial variability in a land-surface scheme was taken by Warrilow [104, 1986], who treated rainfall on a bucket as a random variable having

an exponential probability density function (pdf). By integrating the equation for infiltration over the exponential pdf, the grid average infiltration rate is obtained (the derivation is given in detail by Shuttleworth [91, 1988]). Because the point runoff increases nonlinearly with increasing rainfall intensity, the grid average infiltration rate obtained is smaller than when using the spatial mean rainfall rate. The resulting smaller amount of infiltration causes the evapotranspiration rate to be smaller as well. The inclusion of a canopy storage that can intercept and re-evaporate rain (thus effectively short-circuiting the soil water reservoir) and the incorporation of a percolation term further reduce the evapotranspiration from the reservoir.

Famiglietti and Wood [36, 1991] extended the concept of Beven and Kirkby [6, 1979] mentioned in Section 2.3.3 for use in atmospheric models. Similar to Warilow [104, 1986] they account for spatial heterogeneity by using probability density functions. The influence of soil and topographic heterogeneity is combined into a so called soils-topography index. By numerically integrating a model of the water budget over the pdfs of the spatially variable atmospheric boundary conditions (P and E_p) and soils-topography index, they derive the spatially average values of the soil moisture state and the fluxes in (2.6). The heterogeneity of soil water is implicitly prescribed however, since the local moisture state is entirely determined by the local soils-topography index and the mean moisture state. Hence, spatial variation of P and E_p affect only the mean moisture state and not its spatial distribution.

At a very large scale of aggregation, topographic effects themselves may exist as a statistical ensemble. Entekhabi and Eagleson [35, 1989] incorporate this parametrically by assuming a pdf of surface soil moisture. They obtain analytical expressions for the grid average infiltration excess and saturation excess runoff, evaporation, transpiration and percolation by integrating the governing equations for these fluxes over the pdfs of rainfall rate and surface soil moisture. Since only the grid-average water budget is maintained, it is impossible to trace the time evolution of spatial variation that must be prescribed accordingly. In other words, the model cannot be pictured as a large number of individual columns that have their own memory. Despite this shortcoming, implementation of the model in a GCM resulted in major improvements of the hydrological balance [47, Johnson *et al.* 1991].

The methods discussed so far maintain only the spatially average water budget. As an alternative, Koster and Suarez [48, 1992] divide a climate model grid in a number of independent areas, based on vegetation characteristics. For each area a simplified version of the SiB model (discussed in Section 2.4.1) is used. The grid average fluxes are obtained by simple averaging over the various areas. Since for each area the state variables are maintained, the time evolution of spatial variation can be followed. However, for a realistic treatment of sub-grid variable

land surface processes a large number of areas must be distinguished, which would greatly increase the computational demand. Hence, for practical applications only a limited degree of spatial variability can be taken into account.

2.5 Research methods

In general, simultaneous advancing of experiment and theory is preferred so that both profit from each others progress. The problem considered here is no exception. Therefore a strong international effort is ongoing conducting large-scale experiments on land-atmosphere interaction. To mention a few: the HAPEX campaigns in South-Western France [3, André *et al.* 1986] and the Sahel [41, Goutorbe *et al.* 1994], FIFE in Kansas, United States [84, Sellers, *et al.* 1988], EFEDA in Central Spain [8, Bolle *et al.* 1993] and the ongoing GEWEX campaign which covers the entire Mississippi basin. A more extensive review can be found in Shuttleworth [92, 1993].

The earlier mentioned large-scale experiments focus on the atmospheric aggregation of spatially variable fluxes at the land surface. They are conducted over large areas ($> 10^8 \text{ m}^2$) and in general on time scales shorter than three months. Given the characteristic scales of hydrological processes (Section 2.3) it can be argued that the flux data coming from these experiments are of limited value for the purpose of this thesis since their spatial resolution is too coarse and the dynamical range is too small.

In this thesis mathematical simulation is therefore frequently employed. Despite the absence of data to directly verify results (with the exception of Chapter 6), the physically based models that are used have been extensively verified at small scales. The effect of spatial heterogeneity can thus be indicated when sufficient knowledge (measurements) exists of spatial variability of soil properties and boundary conditions. Although this approach cannot replace observations of the dynamical behavior of the processes in question, it certainly provides insight in the governing mechanisms.

2.6 Thesis structure

As mentioned in Chapter I, the main objective of this thesis is to obtain quantitative insight into the water budget of areas that are heterogeneous with respect to soil hydraulic properties and rainfall. Because of the large discrepancy between the scales of process *understanding* and process *representation*, intermediate scales need to be considered to assure that the scale transitions are anchored in existing knowledge.

The specific objectives of this study are:

1. Assessment of the ability of simple models to provide a realistic description of the REV-scale water budget and the water budget of heterogeneous areas;
2. Analysis of the mechanisms through which spatial heterogeneity of soil and rainfall affect the areally average water budget;
3. Development of simple models that maintain these mechanisms;
4. Investigation of the conditions that govern the importance of spatial heterogeneity and the conditions under which "equivalent" soil properties can be expected to exist.

These four specific objectives can be considered as the thesis' backbone. Each of the following chapters focuses on at least one of them.

In Chapter 3 the emphasis is on the first, and to a lesser extent, on the second and fourth objective. The improved point water budget models of Deardorff [66, Noilhan and Planton 1989] and Warrilow [104, 1986], mentioned in Sections 2.4.1 and 2.4.2 respectively, are compared with numerical solutions of Richards' equation (2.11) that incorporate soil heterogeneity. The Deardorff and Warrilow models are chosen since their lower boundary conditions can be regarded as limiting cases.

Chapter 4 focuses on the second and fourth objective. As in Chapter 3, the point water budget is described using Richards' equation. Spatial heterogeneity of soil hydraulic properties and rainfall rate are taken into account, both in a separate and a combined fashion, using probability density functions. Since both sources of heterogeneity are manifest on different scales, the results provide insight in the areally average water budget on the typical scales of soil and rainfall variation.

The third and fourth objective are at the centre in Chapter 5. Regarding (2.6) for a soil reservoir similar to the Warrilow model [104, 1986] used in Chapter 3, analytical solutions are derived for the dynamical behavior of infiltration, evapotranspiration and percolation. These solutions are validated by comparison with the numerical solutions of Richards' equation. Using the solutions, the effect of heterogeneity of soil properties is identified for various combinations of soil and climate. The possibility of accounting for the effects of soil heterogeneity by means of a single set of equivalent parameters is investigated. Additionally, the probability distributions of infiltration and evapotranspiration rate are derived analytically, given probability distributions of saturated hydraulic conductivity, rainfall rate and saturation degree. Subsequently, using the derived distributions, the different mechanisms through which different sources of spatial heterogeneity affect the water budget on the event time scale are disentangled.

In Chapter 6 the emphasis is again on the third and fourth objective. However, in comparison to the previous chapters a completely different approach is adopted. Instead of considering heterogeneity in a statistical manner, the deterministic

mechanisms that cause spatial variation of fluxes are examined. As mentioned in Section 2.3.3, lateral connections between land surface elements complicate the spatial averaging of (2.6). A computationally efficient model of hydrological processes on the hillslope scale (10^2 m) that includes saturated lateral flow is formulated. The spatial scale considered and the fact that the model domain is a hydrological unit, enable (partial) verification using measured data. For various combinations of soil and climate the long-term average hillslope hydrological behavior is studied and the importance of lateral connections analyzed.

Finally, in Chapter 7 the insights and conclusions that were arrived at are summarized and put in perspective. The principal conclusions are presented and suggestions for further research are outlined.

Chapter 3

Consistency of the water budget in simple soil reservoir models

3.1 Objective and methods

The objective of this chapter is to investigate the ability of the simple soil reservoir or “bucket” type parameterizations of Deardorff [23, 1978] and Warrilow [104, 1986] to describe the water budget of a heterogeneous area consistently in time. Both parametric models were mentioned in Section 2.4 and will be described in detail in this chapter. From the many different available parameterizations, these frequently used models were selected because of their fundamentally different treatment of the lower boundary: the Warrilow model allows for water loss at the lower boundary, whereas the Deardorff model does not.

As mentioned in Section 2.5, direct comparison of the water budget simulations of the two models with measurements cannot be performed because of lack of suitable data. Therefore an alternative indirect approach is adopted here. Given a set of hydraulic properties within a heterogeneous region, the mean components of the water budget are determined using a detailed numerical multi-layer model based on Richards’ equation (2.11) and a scaling theory for spatially variable hydraulic properties. The multi-layer model is considered to be a closer representation of real world phenomena, since it contains fewer assumptions regarding the physics of unsaturated flow.

The ability of this method to simulate the water budget of a heterogeneous area in a realistic way was shown by Hopmans and Stricker [46, 1989] using measured data. These data can not be used here because of the presence of groundwater interaction which cannot be accounted for by the parametric models considered here. Daily average rainfall and potential evapotranspiration, derived from standard meteorological time series, constitute the conditions at the upper boundary. Given identical upper boundary conditions, the results of both parametric models and the multi-layer model can be compared objectively.

The formulations of the multi-layer model, the two parametric models and the scaling theory are presented in Section 3.2. Computations have been carried out for all combinations of the three models, with three different meteorological time series (dry, moderate and wet) and two soil types (loam and sand) that are specified in Section 3.3. In Section 3.4 the results are discussed with respect to:

1. the effect of soil heterogeneity on the water budget using the multi-layer model;
2. the ability of the parametric models to capture the time evolution of the water budget terms;
3. the implications for realistic modeling of the lower boundary;
4. the persistence of soil moisture variability and its potential effect on atmospheric variability.

3.2 Model formulations

3.2.1 Multi-layer model

In Section 2.3.1 Richards' equation for unsaturated flow (2.11) was introduced

$$\frac{\partial \theta(\psi)}{\partial t} = \frac{\partial}{\partial z} \left[k(\psi) \left(\frac{\partial \psi}{\partial z} + 1 \right) \right] - U(\psi, E_p) \quad (2.11)$$

where θ denotes the soil water content, ψ the soil matric head and k the hydraulic conductivity. U represent the water uptake by plant roots and is defined as

$$U(\psi, E_p) = \begin{cases} \beta_F(\psi, E_p) \frac{E_p}{|z_r|} & z_r \leq z \leq 0 \\ 0 & z_c \leq z < z_r \end{cases} \quad (3.1)$$

Eq. (3.1) simply states that over the depth of the rootzone $|z_r|$ roots extract water proportional to the potential evapotranspiration E_p (discussed hereafter) and a transpiration efficiency coefficient β_F . Fig. 3.1 shows the used transpiration efficiency function. Above the threshold value ψ_1 root water extraction is impossible because of oxygen deficit. For $\psi_2 \leq \psi \leq \psi_1$ the transpiration efficiency increases linearly. Transpiration occurs at its potential rate ($\beta_F = 1$) for $\psi_3 \leq \psi \leq \psi_2$ where the value of ψ_3 varies between ψ_{3a} and ψ_{3b} , linearly depending on E_p ($\psi_3 = \psi_{3a}$ for $E_p \geq 5 \text{ mm d}^{-1}$ and $\psi_3 = \psi_{3b}$ for $E_p \leq 1 \text{ mm d}^{-1}$). For $\psi \leq \psi_3$ the efficiency decreases with decreasing soil matric head since the ability of roots to extract water reduces when the water becomes more strongly bonded to the soil particles. Beyond the wilting point ψ_4 water is so strongly bonded to the soil that it can no longer be extracted by the roots. For the grass vegetation used here (see Section 3.3), the values of ψ_{3a} , ψ_{3b} , ψ_4 are set to -4 m, -6 m and -80 m respectively. In order to implicitly account for bare soil evaporation, in this study ψ_1 and ψ_2 are set to 0. Since bare soil evaporation only occurs at the soil

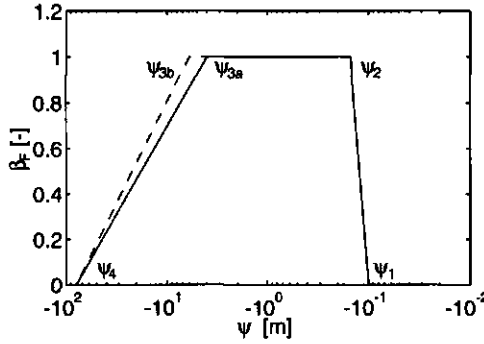


Figure 3.1: Transpiration efficiency function β_T (after Feddes *et al.* [38, 1978]). $E_p = 1$ mm d⁻¹ (dashed line) and $E_p = 5$ mm d⁻¹ (solid line).

surface it cannot, strictly speaking, be accounted for by means of a sink term over the entire rootzone (see the derivation of (2.6) from (2.11) in Section 2.3.1). However, it is assumed that over a vegetated area transpiration greatly exceeds bare soil evaporation.

Total evapotranspiration from the soil is obtained through integration of the sink term over the depth of the rootzone

$$E(\psi(z), E_p) = \int_{z_r}^0 U(\psi(z), E_p) dz \quad (3.2)$$

In order to solve (2.11), the soil hydraulic properties $\theta(\psi)$ and $k(\psi)$ and the initial and boundary conditions must be specified. Parametric descriptions of the soil hydraulic properties are given by Van Genuchten [102, 1980]:

$$s(\psi) = (1 + |a_g \psi|^{n_1})^{-n_2} \quad (3.3)$$

$$k(s) = k_s s^l \left[1 - \left(1 - s^{\frac{1}{n_2}} \right)^{n_2} \right]^2$$

$$\Leftrightarrow k(\psi) = k_s \frac{\left(1 - |a_g \psi|^{n_1-1} [1 + |a_g \psi|^{n_1}]^{-n_2} \right)^2}{[1 + |a_g \psi|^{n_1}]^{n_2 l}} \quad (3.4)$$

in which the saturation degree s is defined as:

$$s(\psi) = \frac{\theta(\psi) - \theta_r}{\theta_s - \theta_r} \quad 0 \leq s \leq 1 \quad (3.5)$$

where θ_s is the saturated water content ($\psi = 0$), θ_r the residual water content, k_s the saturated conductivity ($\psi = 0$), a_g , n_1 and l are soil specific parameters and $n_2 = 1 - n_1^{-1}$. Eqs. (3.3) and (3.4) reflect the fact that soil water content and, accordingly, hydraulic conductivity decrease with soil matric head. This can be seen in Fig. 3.5 for the loam and the sand soils that are specified in Section 3.3.

Because of the highly nonlinear nature of (2.11), analytical solutions are available only for cases with severe restrictions on the $k(\psi)$ and $\theta(\psi)$ relationships and the initial and boundary conditions. Numerical solutions are less restrictive and are therefore employed more often, although computation time can be long. Here, (2.11) is solved numerically using the SWATRE model [5, Belmans *et al.* 1983] under the following initial and boundary conditions:

$$\psi(z) = \psi_0 \quad t = 0, \quad z_c \leq z \leq 0 \quad (3.6)$$

$$\frac{\partial \psi}{\partial z} = 0 \quad t > 0, \quad z = z_c \quad (3.7)$$

$$i = -k(\psi) \left(\frac{\partial \psi}{\partial z} + 1 \right) = P(t) \quad t > 0, \quad z = 0 \quad (3.8)$$

$$E_p = E_p(t) \quad t > 0 \quad (3.9)$$

Condition ψ_0 in (3.6) implies an initially uniform water content θ_0 in a soil column with depth $|z_c|$. Condition (3.7) states that at the lower boundary water flow is entirely caused by gravity (unit gradient) and the percolation flux equals the hydraulic conductivity. This corresponds to the lower boundary condition used in the Warrilow model, as will be discussed in the next section. Condition (3.8) represents the infiltration flux boundary. Because of the low rainfall intensities, all rainfall infiltrates and the switching to a head boundary condition does not occur and has therefore been omitted. Condition (3.9) represents the time varying potential evapotranspiration and is discussed hereafter.

As stated in Section 2.2, the potential transpiration rate depends on the incoming net radiation, the atmospheric moisture and temperature state, the windspeed and the vegetation characteristics. Here the expression of Thom and Oliver [100, 1977] is used to determine E_p :

$$E_p = \frac{\Delta(R_n - G) + \frac{\rho_a c_p}{r_a} (e_s(T_a) - e)}{\rho_w \lambda \left[\Delta + \gamma \left(1 + \frac{r_s^{\min}}{r_a} \right) \right]} \quad (3.10)$$

$$r_a = \frac{4.72}{1 + 0.54u} \left[\ln \left(\frac{z_a}{z_0} \right) \right]^2 \quad (3.11)$$

where R_n is the net radiation flux density given by (2.5), G the soil heat flux through the surface $z = 0$, ρ_a the air density, c_p the dry air specific heat at constant pressure, e_s the saturated vapor pressure, e the actual vapor pressure, T_a the atmospheric temperature, Δ the slope of the saturation water vapor pressure curve, r_a the aerodynamic resistance, r_s^{\min} the minimal stomatal resistance, ρ_w the density of water, γ the psychrometric constant, λ the latent heat of vaporization, u the wind speed and z_0 the roughness length. All atmospheric variables are evaluated at the atmospheric screening height, z_a , which is 2 m.

When applied over short periods (hours), (3.10) may yield values of E_p that could never be maintained by the vegetation, regardless of the availability of soil moisture. Since (3.10) has been validated for daily values, the various measured meteorological variables were averaged to yield daily averages. In (3.10) the soil heat flux G is neglected, which on a daily basis is reasonable.

3.2.2 Formulation of the parametric models

In contrast with the multi-layer model, the bucket type models commonly used in climate modeling do not consider water flow but solely describe the transient behavior of water storage. Two bucket type models will be discussed: the modified version [66, Noilhan and Planton 1989] of the Deardorff "force-restore" model [22, 1977], [23, 1978] and the model by Warrilow [104, 1986]. The two models were selected because of their different lower boundary conditions. As mentioned in Section 2.4, these models not only describe phenomena related to the soil water budget, but also the interfacial vegetation layer between soil and atmosphere. The objective of this study, however, is to compare the soil water budget treatment and its possible implications for climate modeling. In order to compare the results objectively, the effect of the soil reservoir is isolated by using identical atmospheric conditions (rainfall and potential evapotranspiration) for the two parametric models and the multi-layer model.

Warrilow model

In the Warrilow model, the land surface is described as a simple soil reservoir of depth d_r that can be filled by precipitation and emptied by evapotranspiration and percolation (see Fig. 3.2). All precipitation is assumed to infiltrate, unless the reservoir saturates and precipitation is removed as surface runoff. Reduction of potential evapotranspiration occurs when the moisture content drops below a critical value. Percolation is described using a slightly modified formulation of the conductivity function according to Brooks and Corey [12, 1966], while assuming (3.7) at the lower boundary. The model can be stated as:

$$\frac{d\theta}{dt} = \frac{1}{d_r} [P - E(\theta) - q_p(\theta)] \quad (3.12)$$

$$E(\theta) = \beta_W(\theta)E_p = \begin{cases} 1 & \theta_c < \theta \leq \theta_s \\ \frac{\theta - \theta_w}{\theta_c - \theta_w} & \theta_w \leq \theta \leq \theta_c \\ 0 & 0 \leq \theta < \theta_w \end{cases} \quad (3.13)$$

$$q_p(\theta) = k(\theta) = k_s^w \left(\frac{\theta - \theta_w}{\theta_s - \theta_w} \right)^n \quad (3.14)$$

where θ denotes the soil reservoir moisture content, q_p is the percolation flux out of the reservoir, β_W the transpiration efficiency function, θ_c and θ_w the critical and

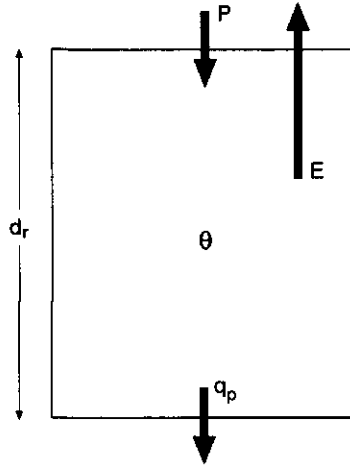


Figure 3.2: Diagram of the Warrilow model. P is the precipitation rate, E the evapo-transpiration rate, q_p the percolation flux and θ the soil moisture content.

wilting point moisture contents respectively (comparable to the threshold values of ψ_3 and ψ_4 in Fig. 3.1), k_s^w the saturated conductivity and n , an empirical constant.

Because the conductivity functions of Brooks and Corey (3.14) and Van Genuchten (3.4) differ, k_s^w and k_s are not the same, as will be explained in Section 3.3. The boundary conditions are in accordance with (3.6), (3.8) and (3.9):

$$\theta = \theta_0, \quad t = 0 \quad (3.15)$$

$$P = \begin{cases} P(t), & \theta < \theta_s \\ k_s^w, & \theta = \theta_s \end{cases} \quad t > 0 \quad (3.16)$$

$$E_p = E_p(t), \quad t > 0 \quad (3.17)$$

where θ_0 is the initial moisture content, which is given by (3.3), evaluated at ψ_0 in order to compare the results objectively. In case the reservoir is saturated, precipitation in excess of the saturated conductivity in (3.16) is removed as saturation excess runoff.

Deardorff model

Similar to the Warrilow model, the modified Deardorff model represents the soil as a reservoir. In order to improve the description near the surface, Deardorff [22, 1977] embedded a top layer, with a depth equal to the depth to which the diurnal soil moisture fluctuation extends ($d_t = 10$ cm), as shown in Fig. 3.3.

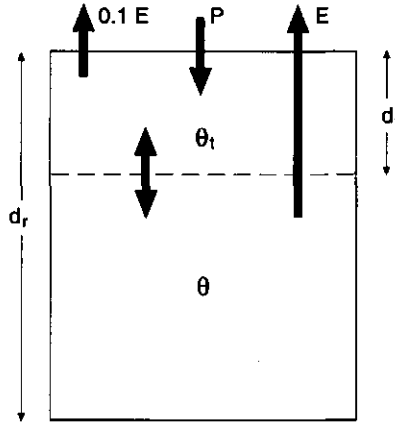


Figure 3.3: Diagram of the Deardorff model. P is the precipitation rate, E the evapotranspiration rate, q_p the percolation flux, θ the soil moisture content of the entire reservoir while θ_t indicates the soil moisture content of the embedded top layer.

The time evolution of the soil moisture states of the embedded top layer and the entire reservoir are given by

$$\frac{d\theta_t}{dt} = \frac{C_1(\theta_t)}{d_t} [P - 0.1E(\theta_e)] - \frac{C_2(\theta)}{\tau} (\theta_t - \theta) \quad (3.18)$$

$$\frac{d\theta}{dt} = \frac{1}{d_r} [P - E(\theta_e)] \quad (3.19)$$

where

$$C_1(\theta_t) = C_1^{\text{sat}} \left(\frac{\theta_s}{\theta_t} \right)^{\frac{1}{2}b+1} \quad (3.20)$$

$$C_2(\theta) = C_2^{\text{ref}} \left(\frac{\theta}{\theta_s - \theta + \theta_t} \right) \quad (3.21)$$

$$\theta_e = 0.1\theta_t + 0.9\theta \quad (3.22)$$

Here, θ_t is the volumetric moisture content of the embedded top layer, θ_e an effective moisture content for evapotranspiration, θ_t a small dummy value to prevent a zero division in case the soil reservoir saturates. C_1^{sat} , C_2^{ref} and b are empirical constants and τ the diurnal period.

The first term on the right hand side of (3.18) can be considered as a force term while the second term characterizes the diffusivity of water in the soil (restore term). Since in this study surface runoff is not present because of the low average daily rainfall intensities, the effect of the embedded top layer is minimal. Unlike

the Warrilow model, the Deardorff model does not account for percolation. Section 3.4 will show that addition of a percolation term to the Deardorff model greatly improves the results.

For the SWATRE and the Warrilow model, evapotranspiration can be written in the form of $E = \beta E_p$. In contrast, in the Deardorff model evapotranspiration is controlled by an aerodynamic and a stomatal resistance, the latter dependent on the soil moisture status:

$$E(\theta_e) = \frac{r_a}{r_a + r_s(\theta_e)} E_w \quad (3.23)$$

with r_a according to (3.11) and

$$r_s(\theta_e) = \max \left\{ 200 \left(\frac{\theta_w}{\theta_e} \right)^2, r_s^{\min} \right\} \quad (3.24)$$

$$E_w = \frac{r_s^{\min} + r_a}{r_a} E_p \quad (3.25)$$

where r_s is the stomatal resistance, E_w is the potential evapotranspiration of a wet vegetation ($r_s = 0$) and r_s^{\min} the minimum stomatal resistance of dry, well watered vegetation.

From (3.23) and (3.25) it becomes clear that when the vegetation is dry and evapotranspiration is climate controlled ($r_s = r_s^{\min}$) the actual evapotranspiration rate equals E_p according to (3.10), satisfying the requirement of identical boundary conditions. In (3.18) the fraction of total evapotranspiration extracted from the imbedded top layer represents bare soil evaporation.

Equations (3.18) and (3.19) are solved subject to the initial and boundary conditions (3.15) - (3.17). The initial value of θ_t is set equal to θ_0 .

3.2.3 Meaning of soil moisture in the models

The main difference between the multi-layer model and the parametric models discussed above is that the latter are based on the mass continuity equations (3.12) and (3.19) only, whereas the multi-layer model includes flow inside the model domain. In the parametric models, the soil moisture state greatly depends on the specification of the soil reservoir depth d_r , which specifies the amount of water available, but also the response of the system to external forcing. Therefore, the soil moisture state serves as a manipulable variable and comparison with the soil moisture state of the multi-layer model or even verification using measured data does not make sense. Hence, any comparison or verification must be solely made on the percolation and evapotranspiration fluxes.

3.2.4 Stochastic treatment of spatial heterogeneity of soil hydraulic properties

Besides treating the physics of soil moisture processes in a simplified way, generally hydrologic schemes in climate models do not account for spatial variation of the soil hydraulic properties they use (see Section 2.4). They rather assume “effective values” for the entire large-area grid. Sharma and Luxmoore [86, 1979] showed the effect spatially variable soil hydraulic properties may have on the water budget. In order to account for spatially variable soil physical properties in the multi-layer model, a stochastic approach is followed in which random fields of soil hydraulic properties are constructed within a certain soil type.

The stochastic approach is based on the similar media concept of Miller and Miller [61, 1956], who derived scaling relationships for geometrically similar soils. Soils are considered to be geometrically similar when they only differ in internal length scale and are therefore of equal porosity. This is illustrated in Fig. 3.4.

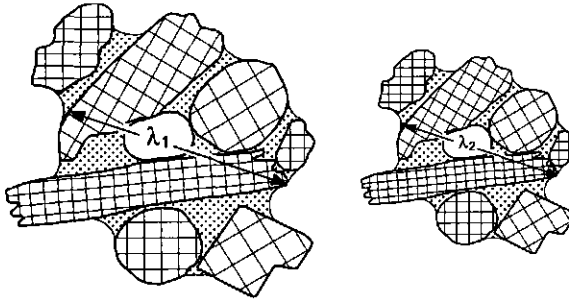


Figure 3.4: Geometrically similar media after Miller and Miller [61, 1956]. The internal length scales are indicated by λ_1 and λ_2 .

Since soils with large internal length scales have large pores it is obvious that they are less capable of binding water by capillary force. On the other hand, the conductivity in case of complete saturation is higher. Miller and Miller proved that for two similar soils with identical moisture contents, the soil matric head scales inversely and the hydraulic conductivity quadratically with the ratio α of the two internal length scales:

$$\psi_i = \alpha_i^{-1} \psi^{\text{ref}} \quad (3.26)$$

$$k_i = \alpha_i^2 k^{\text{ref}} \quad (3.27)$$

Here the superscript ref indicates a reference soil and α_i the ratio of the internal length scale for soil i and the length scale of the reference soil ($\alpha_i = \frac{\lambda_i}{\lambda^{\text{ref}}}$).

This behavior is reflected in Fig. 3.5, in which the range of soil hydraulic properties used in this study are depicted. The conductivity at saturation ($\psi = 0$) is

largest for the maximum scale factor, but decreases more rapidly with decreasing soil matric head (i.e. more negative) because of the smaller capillary tension that can be maintained, which leaves a smaller fraction of the soil available for flow.

In general, however, soil types or soil samples are not strictly geometrically similar since they do not obey the requirement of identical values of θ_s . Therefore, departing from the original theory, scaling has been performed using the degree of saturation s given in (3.3). Many studies have shown the ability of this method to characterize spatial variability of soil hydraulic properties (among others, Warrick *et al.* [103, 1977] and Hopmans [45, 1987]).

By virtue of (3.3) and (3.4) and the scaling relationships (3.26) and (3.27), it can be derived that:

$$a_{g,i} = \alpha_i a_g^{\text{ref}} \quad (3.28)$$

$$k_{s,i} = \alpha_i^2 k_s^{\text{ref}} \quad (3.29)$$

With known values for a_g^{ref} , k_s^{ref} , n_1 and l , random fields of soil hydraulic properties can be constructed through sampling of the probability density functions of α , θ_r and θ_s , respectively $f_{\underline{\alpha}}$, $f_{\underline{\theta}_r}$ and $f_{\underline{\theta}_s}$. The underline indicates a random variable, as stated in Appendix A.

Assuming vertically uniform, spatially independent soil hydraulic characteristics, no lateral soil moisture flow and independence of the density functions, the ensemble mean actual evapotranspiration is estimated as described in Appendix A.2:

$$\bar{\mu}[E(t)] = \frac{1}{N} \sum_{i=1}^N E(\alpha_i, \theta_{r,i}, \theta_{s,i}; t) \quad (3.30)$$

where $E(\alpha_i, \theta_{r,i}, \theta_{s,i}; t)$ is computed by the multi-layer model and N is the number of realizations within the random field. In accordance with Hopmans and Stricker [46, 1989] it appeared that for $N > 30$ the mean was sufficiently determined. Using the technique described by Clausnitzer *et al.* [18, 1992], the (scaled average) reference soil water retention and hydraulic conductivity functions and the corresponding scale factors have been determined for two datasets of measured soil hydraulic properties. From literature it is known that values of α and θ_s within a soil type are distributed lognormally and normally respectively (among others, Warrick *et al.* [103, 1977] and Hopmans and Stricker [46, 1989]) which is indeed the case for the soils used in this study. Both distribution functions are given in Appendix A.3.

3.3 Specification of parameters and meteorological time series

An areally uniform grass vegetation is considered that covers the soil completely. Interception is not considered. In accordance with Thom and Oliver [100, 1977], the value for r_s^{\min} in (3.10) is set at 65 s m^{-1} . The total depth for the multi-layer model, $|z_c|$, is taken as 100 cm, divided into 25 layers, increasing in thickness with depth. The depth of the rootzone, $|z_r|$, is 30 cm, consistent with the observed rooting depth of grass in the Dutch area where the meteorological time series were collected.

The soil hydraulic properties used in this study originate from samples taken near Lubbon (sand) and Castelnau (loam) in the HAPEX-Mobilhy study area [3, André *et al.* 1986]. For each sample, the multi-step outflow method [101, Van Dam *et al.* 1994] was used to determine the soil hydraulic parameters in (3.3) and (3.4). θ_s was measured separately and $f_{\theta_s}(\theta_s)$ was determined using the measured values. The values a_g^{ref} , k_s^{ref} , n_1 , l and the probability density functions $f_{\alpha}(\alpha)$ were determined using the scaling technique mentioned in Section 3.2.4. For the loam soil the variation of θ_r was small and therefore the average value is used. For the sand soil it appeared that $f_{\theta_r}(\theta_r)$ was normal and slightly dependent on θ_s (correlation coefficient 0.3). The parameter values a_g^{ref} , k_s^{ref} , n_1 , l are given in Table 3.1 and the estimate of the means $\hat{\mu}$ and standard deviations $\hat{\sigma}$ of the probability density functions $f_{\alpha}(\alpha)$ and $f_{\theta_s}(\theta_s)$ are summarized in Table 3.2.

Table 3.1: Van Genuchten parameters for the reference soil.

Soil	a_g^{ref} [m^{-1}]	k_s^{ref} [m d^{-1}]	n_1 [-]	l [-]
Loam	1.03	0.043	1.18	2.5
Sand	1.90	3.75	1.72	2.5

Table 3.2: Mean $\hat{\mu}$ and standard deviation $\hat{\sigma}$ of the distribution functions of $\ln \alpha$, θ_r and θ_s .

Soil	$\hat{\mu}[\ln \alpha]$	$\hat{\sigma}[\ln \alpha]$	$\hat{\mu}[\theta_s]$	$\hat{\sigma}[\theta_s]$	$\hat{\mu}[\theta_r]$	$\hat{\sigma}[\theta_r]$
Loam	-0.28	0.72	0.35	0.05	0.01	0
Sand	-0.31	0.80	0.40	0.07	0.05	0.03

In Fig. 3.5, the curves corresponding to the reference values of the parameters ($\alpha = 1$) and the mean values of θ_s are depicted for both soils. In order to avoid unrealistic soil hydraulic properties, the density functions were first truncated and subsequently normalized according to (A.23), such that all probability mass lies inside the finite interval $\hat{\mu}[\omega] - 2\hat{\sigma}[\omega] \leq \omega \leq \hat{\mu}[\omega] + 2\hat{\sigma}[\omega]$ where $\omega \in \{\alpha, \theta_r, \theta_s\}$. In Fig. 3.5 the effect of the scale factor on the $k(\psi)$ and $\theta(\psi)$ curves is indicated

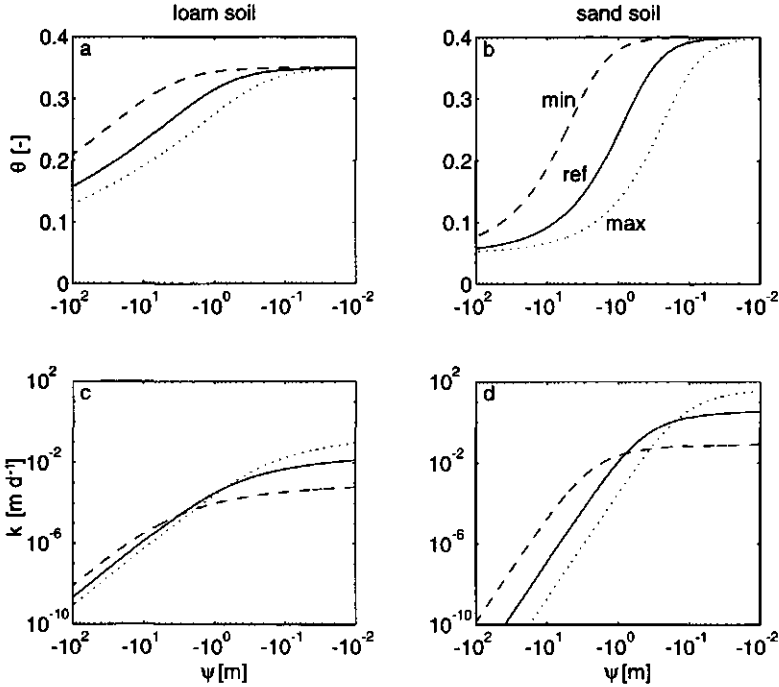


Figure 3.5: Volumetric moisture content θ and hydraulic conductivity k as function of soil matric head ψ for the loam and the sand soil. Reference curves (solid lines), minimum scale factor α (dashed lines) and maximum scale factor α (dotted lines).

for the minimum and maximum of possible α values. The initial conditions were set to $\psi_0 = -2.5$ m in accordance with the observed profiles of soil matric head in the area where the meteorological measurements were taken.

The parameter values used in the parametric models were derived from the reference soil hydraulic characteristics. The values of θ_c and θ_w in (3.13), (3.14) and (3.24) were determined using (3.3) evaluated at respectively $\psi = -5.0$ m and $\psi = -80$ m. This coincides with the ψ_3 and ψ_4 values used in the β_F function (Fig. 3.1). Values for k_s^w and n in (3.14) are derived through optimization using (3.4) in the range where percolation is important ($k > 0.01k_s$). Calibration of the constants C_1^{sat} and C_2^{ref} in (3.20) was performed according to the method described by Noilhan and Planton [66, 1989]. The constant b was determined according to Clapp and Hornberger [17, 1978]. The depth of the soil reservoir for both parametric models was set to 50 cm. Purposely, for this depth not the same value was taken as that of the rootzone in the multi-layer model. Deardorff [23, 1978] explicitly suggests $d_r = 50$ cm and Noilhan and Planton [66, 1989] indicate that d_r is deeper than the depth of the root zone $|z_r|$, which is 30 cm as mentioned

previously. Warrilow [104, 1986] suggests a slightly deeper reservoir. For objective comparison with the Deardorff model, however, the same value was chosen. The parameter values of the Warrilow and the Deardorff model are specified in Table 3.3.

Table 3.3: Parameter values for the Warrilow and Deardorff model.

Soil	Warrilow			Deardorff				Both	
	θ_c	k_s^w [m d ⁻¹]	n	C_1^{sat}	C_2^{ref}	b	d_t [m]	θ_w	d_r [m]
Loam	0.25	0.01	14.0	0.4	0.8	6.0	0.1	0.15	0.5
Sand	0.13	1.82	8.0	0.2	6.0	3.0	0.1	0.06	0.5

The meteorological data of the years 1976, 1978 and 1982, dry, wet and moderate respectively, provide the upper boundary conditions. The daily average rainfall intensities are low enough to prevent surface runoff for all models. The cumulative values of rainfall and potential evapotranspiration for the time series are given in Table 3.4.

3.4 Results and discussion

Computations were carried out for the three models, the two soil types and the three micro-meteorological time series. As the soil moisture state affects evapotranspiration most during the growing season (day 91-273), the models were compared on evapotranspiration efficiencies during that period. The cumulative evapotranspiration values are given in Table 3.4.

Table 3.4: Cumulative amounts of rainfall P^{cum} , potential evapotranspiration E_p^{cum} and model simulated actual transpiration E^{cum} , all in [mm], over the growing season for the different combinations of soil properties and meteorological boundary conditions.

Soil	Year	P^{cum}	E_p^{cum}	SWATRE		Warrilow	Deardorff	
				stoch.	ref.		no perc.	perc.
Loam	1976	197	504	241	247	232	266	264
	1978	337	373	339	341	318	356	342
	1982	244	444	304	307	281	329	313
Sand	1976	197	504	230	222	234	272	248
	1978	337	373	319	300	327	373	346
	1982	244	444	285	267	279	405	295

3.4.1 Effect of soil heterogeneity

The effect of soil heterogeneity on the water budget was analyzed by comparing the deterministic (reference soil) and the average stochastic computations (3.30)

obtained with SWATRE. Table 3.4 shows that cumulative evapotranspiration for the reference sand soil is slightly smaller than for the stochastic computations and that for the loam soil the results compare very well. The graphs in Fig. 3.6

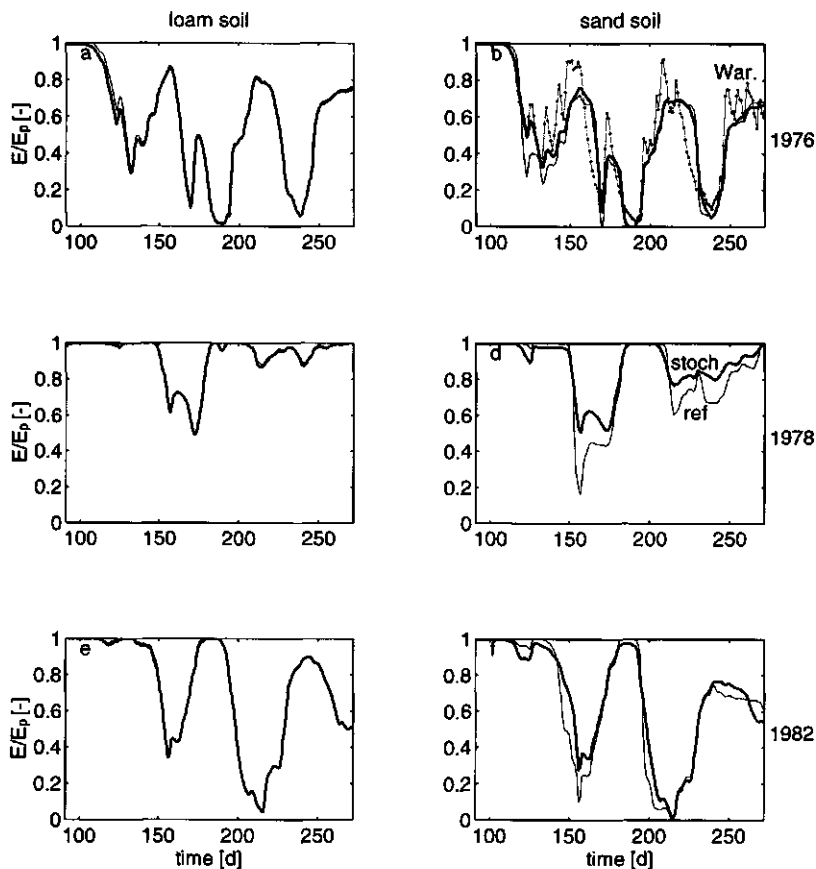


Figure 3.6: Evapotranspiration efficiency $\frac{E}{E_p}$ versus time for the mean stochastic SWATRE results (thick lines) and the SWATRE results for the scaled average reference soils (thin lines) for the loam soil (left) and the sand soil (right) and the years 1976, 1978 and 1982 (top to bottom). Line with dots in (b) indicates the Warrilow model (War.).

show the day to day course of the efficiency factor $\frac{E}{E_p}$ for the reference soil and the averaged results of the stochastic computations. The temporal behavior of $\frac{E}{E_p}$ directly reflects the influence of the soil moisture status on evapotranspiration. Within the range in which the percolation process is important in the water budget (near saturation), the $k(\psi)$ values of the loam soil are several order of

magnitude smaller than those of the sand soil (see Fig. 3.5). Since percolation depends on the hydraulic conductivity, soil heterogeneity has a much greater effect in case of the sand soil than in that of the loam soil. This phenomenon causes larger differences in soil water availability between the realizations for sand soil. Hence, the differences between the $\frac{E}{E_p}$ values for the reference and the stochastic application of SWATRE are more evident for the sand soil than for the loam soil, as can be seen in Fig. 3.6. The results allow the conclusion that the reference soil hydraulic properties describe the average water budget of the stochastic problem very well for the loam and reasonably well for the sand soil. Given the degree of spatial heterogeneity of the soil properties, the fact that the (scaled average) reference properties are so effective in describing the transient average water budget in the absence of runoff is remarkable. A similar conclusion was arrived at by Feddes *et al.* [37, 1993]. For the sand soil these results are confirmed in Chapter 4, using a half-hourly rather than a daily average meteorological forcing derived from a slightly different climate.

3.4.2 Comparison of the parametric models with the multi-layer model

Comparison of the mean stochastic results from the previous section with the results of the parametric models will indicate the ability of the Warrilow and Deardorff models to describe the soil water budget of a heterogeneous region. Any disagreement between the averaged stochastic results and the results of the parametric models should sooner be attributed to the different treatment of the physics than to the neglect of spatial variability of the various parameters. This is because of the good agreement between the deterministic and mean stochastic results shown in the previous section and the fact that the reference soils were used for the specification of the parametric models. As stated in Section 3.2.3, comparison of the soil moisture state between the multi-layer and the parametric models does not make sense. Like in the previous section the evapotranspiration efficiencies are compared since these capture the influence of the soil moisture state on the fluxes.

Warrilow model results

In Table 3.4 the cumulative evapotranspiration values are given for the three growing seasons. The Warrilow model shows only small differences when compared to the stochastic SWATRE results for the sand soil and somewhat larger differences for the loam soil. Regarding the daily evapotranspiration in Fig. 3.7a,b, however, the differences appear considerable, especially for the sand soil. Scatter increases with higher values of $\frac{E}{E_p}$. The different temporal behaviors of the two models are indicated in Fig. 3.6b for the sand soil and the meteorological conditions of 1976. They will be explained in the following. The Warrilow model

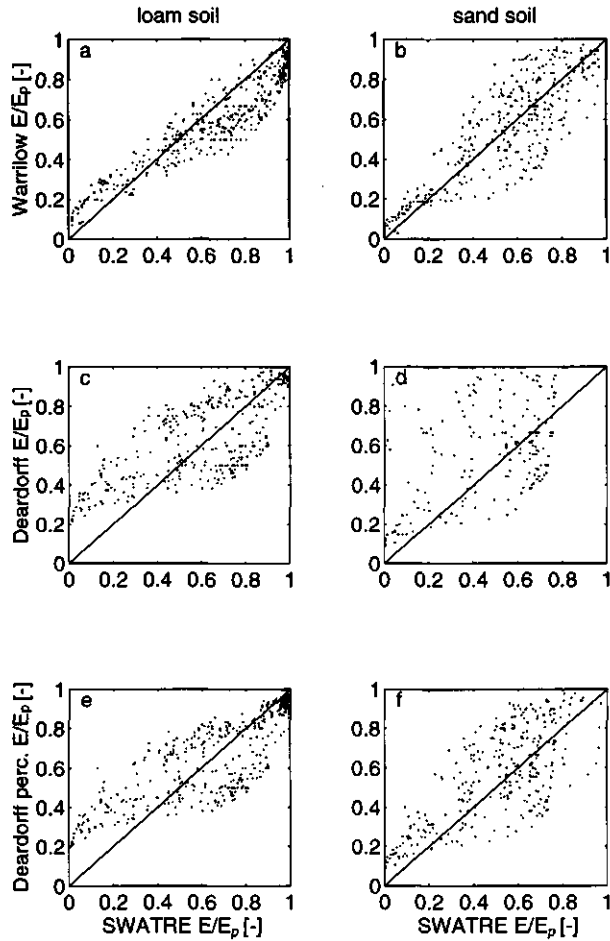


Figure 3.7: Scatter diagrams of the evapotranspiration efficiency $\frac{E}{E_p}$ of the parametric models versus the SWATRE mean stochastic results for the three years 1976, 1978 and 1982. (a) Warrilow loam soil $\mathfrak{R} = 0.15$, (b) Warrilow sand soil $\mathfrak{R} = 0.18$, (c) Deardorff loam soil $\mathfrak{R} = 0.21$ and (d) Deardorff sand soil $\mathfrak{R} = 0.40$, (e) Deardorff with percolation term loam soil $\mathfrak{R} = 0.20$ and (f) Deardorff with percolation term sand soil $\mathfrak{R} = 0.21$.

behaves more erratic than the multi-layer model, indicating its faster response to changing boundary conditions. This can largely be explained by the transient behavior of the flow processes in the multi-layer model in contrast with the instantaneous redistribution of moisture in the Warrilow model. For instance, in the Warrilow model, precipitation is redistributed directly over the entire column whereas in the multi-layer model a transient wetting front proceeds through the

profile. Another example of the smooth behavior of the multi-layer model with respect to time is the incorporation of upward capillary flow which prevents abrupt dropping of the ratio $\frac{E}{E_p}$ with time, as can be observed in Fig. 3.6a.

A good measure to express the differences in daily values between the two models is the root mean square error \mathfrak{R} defined by (A.24). Values of 0.15 and 0.18 were found for loam and sand respectively. After averaging the ratio $\frac{E}{E_p}$ over 10 days these values decrease to 0.13 and 0.15 only, indicating that in the Warrilow model the scatter due to the absence of soil moisture flow does not largely average out over a 10-day period. This would mean that there is a persistent difference in the partitioning of available energy between the Warrilow and the multi-layer model.

Deardorff model results

For the sand soil the Deardorff model greatly overestimates the evapotranspiration (see Table 3.4 and Fig. 3.7d), indicating a systematically too large water storage. This can almost entirely be explained by the absence of a percolation term in the parameterization. For the loam soil, this effect does not exist since percolation is less important so that a better result is obtained (Fig. 3.7c). However, especially for the loam soil, the Deardorff model gives higher efficiencies for dry conditions than the multi-layer model. This is caused by the different methods the models employ for the reduction of transpiration: (3.1) and (3.2) for the multi-layer model, and (3.22) and (3.23) for the Deardorff model. In the latter case, evapotranspiration is still possible at values below θ_w , at which more moisture is available to transpiration for the loam soil than for the sand soil (see Fig. 3.5).

After addition of a percolation term identical to (3.14), the Deardorff model and the Warrilow model show qualitatively the same scatter in efficiency values (see Fig. 3.7e,f). As for the Warrilow model, averaging the ratio $\frac{E}{E_p}$ over a 10 day period only slightly reduces the scatter for the Deardorff model with percolation term (\mathfrak{R} values of 0.18 and 0.19 for the loam and sand soil respectively).

3.4.3 Implications for modeling the lower boundary

Given the sensitivity of the water budget to the lower boundary condition, the question arises what condition is realistic for use in GCMs. For one-dimensional parameterizations a no-flow lower boundary can be regarded as the lower limit. Since the conditions below the reservoir are generally unknown, condition (3.7), which indicates vertical flow caused by gravity only, may be considered realistic assuming the groundwater table resides deep. However, water lost through percolation at topographically high positions may reappear in the surface layer at lower positions because of saturated lateral flow (see Section 2.3.3). In that case the areally averaged percolation is smaller than one-dimensional gravity driven

percolation. The Deardorff and the Warrilow model can therefore be regarded as the two limiting cases and a realistic description of the lower boundary must lie in between these two.

As an example, the Simple Biosphere model [85, Sellers *et al.* 1986] mentioned in Section 2.4 uses an expression similar to (3.14) multiplied by $\sin \phi$ as lower boundary condition, where ϕ is the terrain slope angle. Strictly interpreted, this term represents lateral unsaturated gravity driven flow. Note that for completely flat terrain ($\phi = 0$) it becomes a no-flow boundary similar to the Deardorff model and for a completely tilted terrain ($\phi = \pi$) it becomes identical to the Warrilow lower boundary. The parameter ϕ can thus be interpreted as a parameterization of the areally effective lower boundary condition and thus reflects the effect of lateral redistribution of soil water. In short, defining a realistic lower boundary condition for parameterizations to be used in atmospheric models essentially means that two- or three-dimensional flow processes need to be represented in a one-dimensional model. It is evident that further research on this point is needed. In Chapter 6 two-dimensional flow phenomena on a hillslope will receive much attention.

3.4.4 Persistence of soil moisture anomalies

Delworth and Manabe [24, 1989], used a closed-bottom bucket representation of the land surface to investigate the persistence of soil wetness. They state that the soil layer acts as an integrator of precipitation forcing: short time scale precipitation with a white noise spectrum is transformed into a red response spectrum with most of its variance concentrated in the lower frequencies (this can also be seen qualitatively in Fig. 2.3). Accordingly, since the soil moisture state greatly influences the partitioning of available energy over the surface heat fluxes, low frequency soil wetness variability generates low frequency atmospheric variability. It is therefore of interest to elaborate on how the results presented earlier affect the decay of soil moisture anomalies, i.e. deviations from the long-term mean state.

In a closed-bottom soil reservoir, a positive anomaly can only be erased by evapotranspiration. Inclusion of percolation will therefore further shorten the time scale of soil moisture anomalies, especially for conductive soils. Delworth and Manabe [24, 1989] note that soil moisture fluctuations in regions or seasons with a small value for the ratio of potential evapotranspiration and precipitation ($\frac{E_p}{P}$) hardly affect atmospheric variability since the actual evapotranspiration is nearly always potential. In regions or seasons with very high values for $\frac{E_p}{P}$, the persistence of soil moisture anomalies, and consequently of anomalies of the surface heat fluxes, is low. Inclusion of percolation will decrease the persistence of soil wetness and atmospheric variability. For regions or seasons with small values for $\frac{E_p}{P}$ this implicates that the influence of the soil water state on atmospheric conditions will

increase because evapotranspiration will be more frequently soil controlled.

The improvement of the Deardorff model after insertion of a percolation term may serve as an illustration of the smaller persistence of a wet anomaly caused by percolation, and the resulting decrease of evapotranspiration due to increased "soil control". For the sand soil and the meteorological conditions of 1982, the difference between the cumulative evapotranspiration values of the Deardorff model with and without percolation term (110 mm, Table 3.4) is almost entirely balanced by the cumulative amount of percolation prior to the start of the growing season (96 mm). The period prior to the growing season (day 1 to 90) has an $\frac{E_p}{P}$ ratio of 0.33 so that evapotranspiration can not balance the precipitation. During the growing season, with $\frac{E_p}{P} = 1.82$ (Table 3.4), the influence of percolation is much smaller (14 mm).

3.5 Conclusions

The reduction of evapotranspiration to a rate smaller than the potential rate, as predicted by the multi-layer SWATRE model, [5, Belmans *et al.* 1983], the adapted Deardorff model [66, Noilhan and Planton] and the Warrilow model [104, Warrilow 1986] were compared, using a sand and a loam soil, and three different years of daily average micro-meteorological data. Surface runoff did not occur because of the low precipitation intensities, resulting from the daily averaging. The following conclusions can be drawn:

1. The scaled mean soil hydraulic properties describe the average water budget and the reduction of evapotranspiration of the stochastic problem very well for the loam soil and reasonably well for the sand soil. Differences between the stochastic results of the multi-layer model and the results of the parametric models can therefore mainly be attributed to the different parameterization of the soil physics;
2. Since the Deardorff model neglects percolation, reduction of evapotranspiration is systematically underestimated compared with both the multi-layer model and the Warrilow model. Insertion of a percolation term results in a model behavior similar to the Warrilow model. For realistic situations, the lower boundary conditions used in the two parametric models may be regarded as the lower and upper limiting case respectively;
3. Both the Deardorff and the Warrilow models show large variations in daily and 10-day average evapotranspiration efficiency when compared to the multi-layer model. Of course, efficiencies over longer time periods (up to months) show less variation. This leaves the unanswered question to atmospheric modelers about the time scale on which the water budget, and by that the partitioning of energy, must be consistent and realistic.

Chapter 4

The water budget considering soil and rainfall heterogeneity

4.1 Objective and methods

In the previous chapter the influence of spatial heterogeneity of soil properties on the water budget was briefly examined. It appeared that the scaled average reference soil described the time evolution of the water budget terms reasonably accurately. However, due to the daily average meteorological forcing, phenomena that are important on shorter time scales could not be accounted for. For example, short intensive rain with a time scale of a few hours at the most, may cause ponding of water at the surface because of exceeding of the soil infiltration capacity. Time averaging of the rainfall decreases its intensity and makes ponding less likely. In case ponded water is laterally removed as infiltration excess runoff, time averaging of rainfall rate alters the partitioning of water over the various components of the water budget. Therefore, in this chapter the influence of spatial variation is investigated accounting for processes on time scales of hours. One year of half-hourly meteorological conditions resulting from a one-dimensional climate model serve as upper boundary conditions. Both variation of soil hydraulic properties and of rainfall are considered. In Chapter 2 it was already mentioned that the spatial scales at which both sources of variation are manifest, are markedly different. The results are therefore interpreted in terms of explicit spatial scales.

In Section 4.2 the model considered here is discussed. The incorporation of spatial heterogeneity of soil hydraulic characteristics and rainfall is outlined in Section 4.3 and the results of the computations are presented in Section 4.4.

4.2 Problem formulation

The model domain considered here is similar to that in the previous chapter with the exception that the water budget of the vegetation canopy is taken into

account. It is assumed that a pasture vegetation canopy perfectly covers the soil and intercepts and re-evaporates rainfall. In this study, this "short-circuiting" of the soil column is described as a combination of a step response to rainfall and a linear reservoir response to evaporation:

$$\begin{aligned}\frac{dC}{dt} &= (1 - \delta_{C,C^{\max}}) P - E_c \\ &= (1 - \delta_{C,C^{\max}}) P - \frac{C}{C^{\max}} E_{cp}\end{aligned}\quad (4.1)$$

where C is the water storage in the canopy, E_c canopy evaporation and E_{cp} potential wet canopy evaporation. The Kronecker delta $\delta_{C,C^{\max}} = 1$ when $C = C^{\max}$ and 0 otherwise. Thus, throughfall of rain only occurs when the canopy storage C is at its maximum value C^{\max} ($= 0.6$ mm). The canopy storage is assumed to be zero at the start of the simulation

$$C = 0 \quad t = 0 \quad (4.2)$$

Because of the presence of a canopy, bare soil evaporation is not considered implicitly as was done in Chapter 3. Hence, the values of ψ_1 and ψ_2 in Fig. 3.1 are set to -0.10 m and -0.15 m and the values of ψ_{3a} , ψ_{3b} and ψ_4 are taken to be identical to the values in Section 3.2.1.

The potential evapotranspiration E_p constitutes the transpiration rate at which the vegetation transpires under optimal soil water conditions. Given the atmospheric state variables and radiative fluxes, the expressions (3.10) and (3.11) of Thom and Oliver [100, 1977] were applied to determine E_p . The transient soil heat flux G in (3.10) was determined using the surface temperature given in the meteorological time series as an upper boundary condition.

In case of canopy storage, water can evaporate from the leaves as if the stomatal resistance were zero. Accordingly, the potential transpiration E_p is converted to a potential wet canopy evaporation that is used in (4.1):

$$E_{cp} = \left(1 + \frac{\gamma}{\Delta + \gamma} \frac{r_s^{\min}}{r_a} \right) E_p \quad (4.3)$$

In case of canopy storage, only a fraction of the leaves transpire water. In that case, the root extraction given by (3.1) is multiplied by the fraction of dry vegetation, $(1 - \frac{C}{C^{\max}})$.

The description of unsaturated flow and the soil hydraulic properties is similar to that in Section 3.2.1 and is therefore not repeated here. The only difference with the description in Section 3.2.1 is the possibility of infiltration switching from unponded to ponded conditions, i.e. from flux controlled to head controlled. This is due to the half-hourly meteorological forcing and the corresponding high

rainfall intensities. Accordingly, boundary condition (3.8) is replaced by

$$i = \min \left\{ \delta_{C,C^{\max}} P, -k(\psi) \left(\frac{\partial \psi}{\partial z} + 1 \right) \right\} \quad t > 0, \quad z = 0 \quad (4.4)$$

where the term $\delta_{C,C^{\max}} P$ represents the rain falling through the canopy layer.

Canopy throughfall in excess of infiltration (i.e. the water that ponds at the surface) is removed as infiltration excess runoff q_{ie}

$$q_{ie} = \begin{cases} \delta_{C,C^{\max}} P - i & t > 0, \quad \delta_{C,C^{\max}} P > i \\ 0 & t > 0, \quad \delta_{C,C^{\max}} P \leq i \end{cases} \quad (4.5)$$

In this study (2.11) and (4.1) are solved using a finite element model [26, Dirksen *et al.*]. The initial and lower boundary conditions and the potential evapotranspiration are identical to (3.6), (3.7) and (3.9) respectively, where $\psi_0 = -2.5$ m. The infiltration is given by (4.4). In a soil column, 200 layers of 1 cm depth are considered ($|z_c| = 2$ m) and the time discretization varies depending on the magnitude of soil matric head gradients within the column with a maximum of 0.5 hour. As in Chapter 3, the depth of the rootzone $|z_r|$ is set to 0.3 m, a typical value for pasture used in the generation of the meteorological time series.

With the Single Column Model (SCM) of the United Kingdom Meteorological Office [50, Lean 1992], a one-year time series (January 1 - December 31) was generated consisting of half-hourly values of rainfall (convective and stratiform type), wind speed, net radiation and atmospheric state variables at a height of 2 m above the surface. The SCM is a one-dimensional version of the three-dimensional General Circulation Model (GCM) used for climate predictions. Apart from the atmospheric dynamics that are generated statistically or taken from observations, the SCM contains all physical processes that are included in the GCM. These processes range from cloud-radiation interaction to convection. Therefore even a brief description of the model is beyond the scope of this study. The advantage of a one-dimensional climate model is that the effects of the various physical processes can be assessed better because they are not obscured by large-scale feedback mechanisms. In this study the SCM was statistically forced at its boundaries with lateral fluxes of momentum, heat and water vapor, considering the climatology of southern England as described by Dooge *et al.* [28, 1994].

The vegetation used in the generation of the time series was pasture for which in the SCM the minimal stomatal resistance $r_s^{\min} = 79 \text{ s m}^{-1}$ and the roughness length $z_0 = 0.02$ m. As the SCM distinguishes between different soils, the loam and sand soils introduced in Section 3.3 were used to generate the two atmospheric time series. Fig. 4.1 shows the cumulative grid average rainfall and potential evapotranspiration, derived from the micro-meteorological time series for both the loam (L) and the sand (S) soil. Since the generated time series are identical

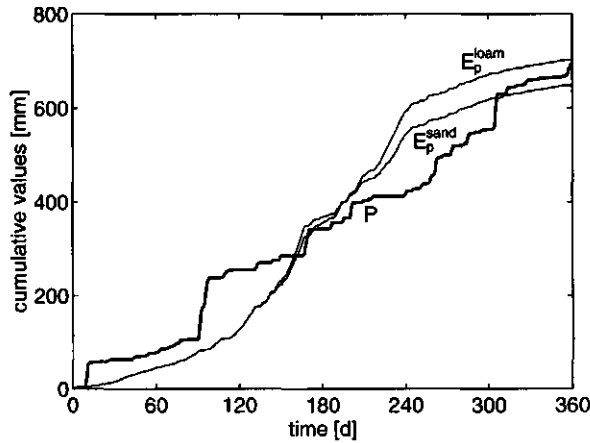


Figure 4.1: Cumulative rainfall P and potential evapotranspiration E_p of the micro-meteorological time series for the loam soil and the sand soil.

for rainfall and differ only slightly for potential transpiration, it is evident that the lateral atmospheric forcing dominates the model climate.

The annual potential transpiration (Fig. 4.1) is very high for southern England conditions, due to the low specific humidities present in the SCM simulations. Since this study aims at studying effects rather than describing the behavior of a specific area, the time series are sufficient for the purpose of this study. In fact, the high value of annual potential evapotranspiration enhances the influence of soil moisture and thereby soil heterogeneity on the evapotranspiration.

Similar to what was done in Section 2.3.1, (2.11) was integrated over the soil column. Addition of (4.1) then yields the total water budget of the soil column and the canopy reservoir

$$\mathbf{V}(t) \cdot \mathbf{e} = P(t) - q_{ie}(t) - q_p(t) - E_t(t) - E_c(t) - \frac{dW(t)}{dt} - \frac{dC(t)}{dt} = 0 \quad (4.6)$$

where

$$W(t) = \int_{z_c}^0 \theta(z, t) dz \quad (4.7)$$

\mathbf{V} is the vector containing the components of the water budget and \mathbf{e} indicates the vector $(1 -1 -1 -1 -1 -1 -1)$. The actual plant transpiration E_t is obtained from (3.2). The vector notation is introduced to simplify the discussion on the treatment of spatial heterogeneity in the next section.

4.3 Spatial heterogeneity of the water budget

4.3.1 Stochastic formulation

As mentioned in Section 2.3, heterogeneity of soil hydraulic characteristics and rainfall induces differences in the water budget terms summarized in \mathbf{V} . Heterogeneity of soil hydraulic properties is taken into account using the scaling theory of Miller and Miller [61, 1956] that was outlined in detail in Section 3.2.4. Because of notational reasons, hereafter, a random variable is indicated by an underline (see Appendix A).

The annual values of the fluxes in vector \mathbf{V} for soil column i are obtained by

$$\mathbf{V}_i^a(\mathbf{S}_i) = \int_0^{t^{\text{int}}} \mathbf{V}(\mathbf{S}_i, P_i(t)) dt \quad (4.8)$$

where the integration time t^{int} is 360 days (the length of the meteorological time series). \mathbf{S} denotes the vector with parameters specifying the soil hydraulic properties as in (2.8) and $P_i(t)$ is the time series of rainfall for soil column i which is generated through consequent sampling of the probability density function describing spatially heterogeneous rainfall, as will be discussed in Section 4.3.3. The estimators of the ensemble mean $\hat{\mu}$ and variance $\hat{\sigma}^2$ of \mathbf{V}^a are determined as described in detail in Appendix A:

$$\hat{\mu}[\mathbf{V}^a] = \frac{1}{N} \sum_{i=1}^N \mathbf{V}_i^a(\mathbf{S}_i) \quad (4.9)$$

$$\hat{\sigma}^2[\mathbf{V}^a] = \frac{1}{N-1} \sum_{i=1}^N [\mathbf{V}_i^a(\mathbf{S}_i)]^2 - (\hat{\mu}[\mathbf{V}^a])^2 \quad (4.10)$$

In order to avoid unrealistic values, the density functions of the soil parameters and the rainfall intensity are truncated according to (A.23).

4.3.2 Heterogeneity of soil hydraulic properties

The soils considered here are the loam and sand soils introduced in Section 3.3. All information on the soil hydraulic properties and their heterogeneity is summarized in Tables 3.1 and 3.2. The range of employed soil hydraulic properties is shown in Fig. 3.5 in which the water retention and hydraulic conductivity functions are depicted corresponding to the reference, minimum and maximum values of scale factor α for both the loam and the sand soil.

4.3.3 Heterogeneity of rainfall

The density function of spatially heterogeneous rainfall intensity within the size of a grid depends on the amount and type of rainfall. The area affected by convective

type rainfall for example, is usually smaller than for the stratiform type. Within the affected area, it is unlikely that the rain rate is uniform (see Section 2.3.3). A widely used method for the spatial disaggregation of rainfall intensity is sampling from an exponential density function of point rainfall within the affected fraction κ (e.g. Warrilow [104, 1986]; Entekhabi and Eagleson [35, 1989]). For the two different types of rainfall that are generated by the SCM, the exponential densities are

$$f_{P_t > 0}(P_t) = \frac{\kappa_t}{\mu[P_t]} \exp\left(-\frac{\kappa_t P_t}{\mu[P_t]}\right) \wedge \Pr[P_t = 0] = 1 - \kappa_t \quad (4.11)$$

where the subscript t indicates the type of rainfall, i.e. stratiform (s) and convective (c).

The half-hourly mean values μ for both types of rainfall are given in the meteorological time series. κ depends on the type of rainfall as well as on the gridsize under consideration, the latitude and the mean rainfall [19, Collier 1993]. Consistent with the SCM, $\kappa_s = 1.0$ and $\kappa_c = 0.3$. For every change in boundary conditions, a new random field of rainfall intensities is generated using the actual mean values, assuming both rainfall types to be independent. The total half-hourly point precipitation, P , is taken to be the sum of the realized stratiform rainfall (P_s) and convective rainfall (P_c) at that point. When time dependence is not taken into account this results in an erratic point rainfall pattern which constitutes a limiting case. It leads to small variation in the annual rainfall amounts.

The other limiting case can be constructed by generating rainfall time series assuming perfect temporal correlation. At the onset of a storm period (t_0) a rainfall field is constructed similar as discussed before. For all subsequent times t within the storm, rainfall intensities for both the convective and the stratiform type are related as follows:

$$P_t(t) = \frac{P_t(t_0)}{\mu[P_t(t_0)]} \mu[P_t(t)] \quad (4.12)$$

From (4.12) it is clear that the autocorrelation of each rainfall time series is identical to the autocorrelation of the grid mean rainfall since they only differ by a time-independent factor. For convective rainfall this procedure implies that a location remains dry throughout the entire storm period when that particular location does not receive any rainfall at the start the storm period. In summary, this approach distributes storm rainfall amounts rather than half-hourly amounts. It leads to large variation in the annual rainfall as will be seen later.

For one particular stratiform storm event, Fig. 4.2 shows typical examples of the rainfall time series generated with and without considering temporal correlation.

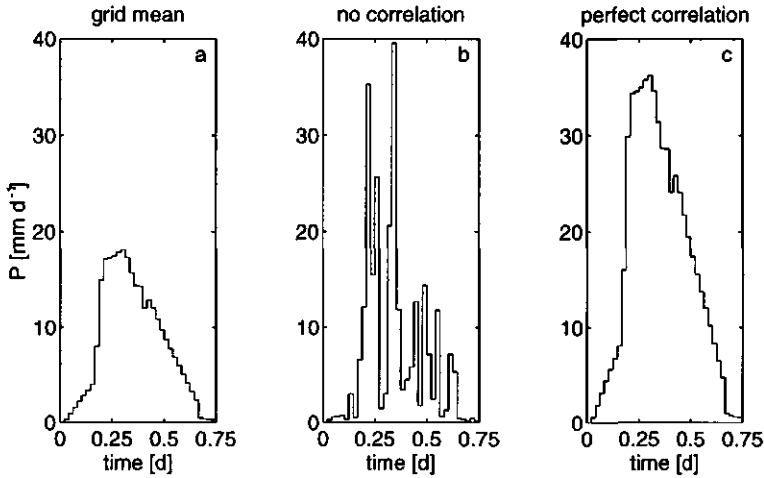


Figure 4.2: Typical time series in meteorological forcing of half-hourly stratiform point rainfall for the grid mean and the two methods of spatial disaggregation.

4.3.4 Simulations

Since the soil hydraulic characteristics corresponding to the values α_g^{ref} and k_s^{ref} in Table 3.1 are the scaled mean characteristics of the measured samples, it is logical to simulate the water budget of a soil column using the reference hydraulic properties. The influence of the different sources of heterogeneity on the water budget terms is studied by comparing the average results of the Monte Carlo simulations with the deterministic results of the single reference soil column and/or uniform rainfall. The considered deterministic and stochastic cases, summarized in Table 4.1, need some explanation.

In order to interpret the ensemble mean (4.9) and variance (4.10) as spatial mean and variance respectively (i.e. assuming ergodicity), the area must be large enough. More specifically, the typical scale of the considered area has to be much larger than the correlation length scales of the various fluxes, which in turn are proportional to the correlation length scales of soil hydraulic properties and rainfall. The larger the variance of soil hydraulic properties and rainfall are, the larger the area must be. Typically, the correlation length scale of soil hydraulic properties is of the order of $10^0 - 10^1$ m. A reasonable spatial scale associated with the computations containing heterogeneity of soil hydraulic properties is therefore of the order of 10^2 m. Similarly, realistic correlation length scales for rainfall are of the order of $10^3 - 10^4$ m (see Section 2.3.3), leading to spatial scales for computations that consider rainfall heterogeneity of about $10^4 - 10^5$ m. Keeping these scales in mind, Table 4.1 can be interpreted either according the idea of represented scales or according to that of meso-scale subgrid heterogeneity.

Table 4.1: Considered deterministic and stochastic problems. Rain rate and soil hydraulic parameters are taken to be uniform or spatially heterogeneous (heterog.). (u) indicates temporally uncorrelated and (c) temporally correlated. N is the number of realizations. Interpretation of the cases in terms of spatial scales is given in the text.

Case	Soil	P	α	θ_s	θ_r	N
L1	loam	uniform	uniform	uniform	uniform	1
L2	loam	uniform	heterog.	uniform	uniform	400
L3	loam	uniform	heterog.	heterog.	uniform	400
L4	loam	heterog. (u)	uniform	uniform	uniform	200
L5	loam	heterog. (c)	uniform	uniform	uniform	400
L6	loam	heterog. (u)	heterog.	heterog.	uniform	400
L7	loam	heterog. (c)	heterog.	heterog.	uniform	700
S1	sand	uniform	uniform	uniform	uniform	1
S2	sand	uniform	heterog.	uniform	uniform	400
S3	sand	uniform	heterog.	heterog.	heterog.	400
S4	sand	heterog. (u)	uniform	uniform	uniform	200
S5	sand	heterog. (c)	uniform	uniform	uniform	400
S6	sand	heterog. (u)	heterog.	heterog.	heterog.	400
S7	sand	heterog. (c)	heterog.	heterog.	heterog.	700

Following the idea of represented scales, the Cases L1/S1 are point scale processes. Cases L2/S2 and L3/S3 are linked to areas of $10^{-2} - 10^0 \text{ km}^2$ with uniform rainfall. The remaining cases represent large areas ($10^2 - 10^4 \text{ km}^2$) where spatial variation of rainfall can be expected. The areas can be seen to have either homogeneous soils or areal "effective" hydraulic properties (L4/S4 and L5/S5) or to exhibit realistic variation of hydraulic properties (L6/S6 and L7/S7).

Following the idea of meso-scale subgrid heterogeneity, the Cases L1/S1 will show results at gridsize when no subgrid spatial variation exists, or when this has been averaged out beforehand. Cases L2/S2 and L3/S3 yield results at gridsize for the single effect of subgrid soil heterogeneity, while Cases L4/S4 and L5/S5 do so for subgrid rainfall heterogeneity. Finally, L6/S6 and L7/S7 represent the most realistic cases, having spatial heterogeneity of rainfall and soil hydraulic properties at the meso scale. Obviously, the subgrid heterogeneity of soil hydraulic properties does not include the possibility of different soil types occurring within the grid, i.e. the reference soil hydraulic properties and the corresponding density functions are stationary.

Summarizing, there is a certain hierarchy in Table 4.1, either in spatial scales or in the complexity of subgrid heterogeneity, and the expectation is that the simulations will reveal some of the effects of scale or subgrid complexity. As already indicated, effects caused by spatial interaction (e.g. topography) are not

included.

The number of simulations N statistically required to get representative first and second moments for the simulated water budget components cannot be derived in a straightforward manner from theory in the case of spatial rainfall heterogeneity. The number of time series that can be constructed by either uncorrelated 30 min or correlated event-based sampling is so overwhelming that one has to resort to experiment for selection of N . For the Cases L2/S2 and L3/S3 a smaller value of N could have been chosen to establish reliable values of the lower moments. In order to obtain enough points for the scatter diagrams that are presented in the next section, however, the redundant simulations are maintained.

4.4 Results and discussion

The annual values of the water budget terms (indicated by the superscript a) of the considered cases will be discussed first. The effect of the different sources of heterogeneity on these terms for the two soils are dealt with separately. This will be followed by a discussion on the possibility of specifying “equivalent” soil properties and the dynamics of the water storage.

Because of the small canopy storage ($C^{\max} = 0.6$ mm), \underline{E}_c^a is only a small fraction of the plant transpiration (< 10 %), despite the frequent filling and emptying of the canopy. Moreover, \underline{E}_c^a shows negligible variation between the various realizations. Therefore the total evapotranspiration $\underline{E}^a = \underline{E}_t^a$ and \underline{E}_c^a is considered here.

The change of soil moisture storage over the year is dW^a . The annual change in water storage of the canopy, dC^a , is neglected since it is very small ($\leq C^{\max}$). Ideally, the simulation is repeated until equilibrium, i.e. for every Monte Carlo realization $dW^a = 0$. However, because of the prohibitive computational effort this was not feasible. How the results are likely to change in case the annual soil water storage is zero will be indicated for the various calculations.

The annual cumulative values of the various fluxes are obtained according to (4.8). For those cases that consider spatial heterogeneity of soil hydraulic properties and/or rainfall intensities, it has been verified that the estimations of mean ($\hat{\mu}$), standard deviation ($\hat{\sigma}$), median (\hat{m}_e) and mode(s) (\hat{m}_o) of the distribution of annual fluxes are more or less insensitive to enlarging the number of Monte Carlo realizations. Although this does not necessarily imply that the underlying probability density functions are sufficiently known, one can get a good indication of important features like skewness and bimodality of the distribution. For example, $\hat{\mu} = \hat{m}_e = \hat{m}_o$ points to a symmetric distribution and $\hat{\mu} > \hat{m}_e > \hat{m}_o$ relates to a positively skewed distribution. Table 4.2 summarizes these statistical

Table 4.2: Statistical quantities of the annual values of the water balance terms. μ the mean, σ standard deviation, m_e median, m_o mode, all in [mm]. Bimodality is marked by two values of m_o .

Flux	Case	$\hat{\mu}$	$\hat{\sigma}$	\widehat{m}_e	\widehat{m}_o	Case	$\hat{\mu}$	$\hat{\sigma}$	\widehat{m}_e	\widehat{m}_o
$\underline{P^a}$	L1	694	-	-	-	S1	694	-	-	-
$\underline{q_{ie}^a}$		21	-	-	-		0	-	-	-
$\underline{q_p^a}$		116	-	-	-		191	-	-	-
$\underline{E^a}$		471	-	-	-		452	-	-	-
$\underline{dW^a}$		86	-	-	-		51	-	-	-
$\underline{P^a}$	L2	694	-	-	-	S2	694	-	-	-
$\underline{q_{ie}^a}$		121	127	65	0		0	0	0	0
$\underline{q_p^a}$		78	55	88	10, 140		214	34	198	180
$\underline{E^a}$		443	32	462	470		462	25	460	460
$\underline{dW^a}$		52	46	77	-30, 90		18	58	29	7
$\underline{P^a}$	L3	694	-	-	-	S3	694	-	-	-
$\underline{q_{ie}^a}$		125	126	79	0		0	0	0	0
$\underline{q_p^a}$		75	55	77	10, 140		216	37	203	200
$\underline{E^a}$		442	33	457	470		462	27	460	460
$\underline{dW^a}$		52	46	73	-30, 90		16	60	27	80
$\underline{P^a}$	L4	693	27	691	690	S4	695	28	693	690
$\underline{q_{ie}^a}$		171	21	170	170		0	0	0	0
$\underline{q_p^a}$		30	4	30	30		194	24	193	200
$\underline{E^a}$		431	7	431	430		445	10	445	450
$\underline{dW^a}$		61	6	61	60		56	3	57	60
$\underline{P^a}$	L5	661	179	632	630	S5	683	193	626	62
$\underline{q_{ie}^a}$		141	123	106	10		0	0	0	0
$\underline{q_p^a}$		61	39	53	20		251	172	187	130
$\underline{E^a}$		406	41	406	410		396	40	393	400
$\underline{dW^a}$		53	34	55	60		36	30	32	30
$\underline{P^a}$	L6	690	28	689	690	S6	693	29	693	690
$\underline{q_{ie}^a}$		208	121	216	not def.		0	0	0	0
$\underline{q_p^a}$		40	37	21	30		222	42	215	210
$\underline{E^a}$		410	36	418	430		458	28	455	460
$\underline{dW^a}$		32	53	32	-30, 90		13	61	17	50
$\underline{P^a}$	L7	671	170	640	640	S7	689	200	630	64
$\underline{q_{ie}^a}$		203	189	165	20		2	17	0	0
$\underline{q_p^a}$		55	71	20	20		281	169	225	220
$\underline{E^a}$		388	49	386	380		411	53	403	410
$\underline{dW^a}$		25	71	22	-40, 100		-5	80	0	30

quantities for the annual fluxes of the various cases. Since the mode of a discrete density function cannot be determined accurately, it must be interpreted as an indication, rather than an accurate number.

4.4.1 Point scale water budget

The results in this section were obtained using the reference soil hydraulic properties and the grid mean rainfall time series. In term of point scale processes, differences between the two soil types can be observed.

L1 ($P, \alpha, \theta_s, \theta_r$ uniform)

Table 4.2 shows that only a very small fraction of the annual rainfall does not infiltrate into the soil but is removed as infiltration excess runoff. Therefore, virtually all rainfall is partitioned over percolation, evapotranspiration and storage change. Obviously, any increase in infiltration excess runoff, due to spatially variable soil properties and/or rainfall intensity, reduces the magnitude of the other water budget terms as will be shown later.

Continuation of the simulation until equilibrium (no annual storage change) caused an increase in percolation from 116 to 196 mm. Surface runoff increased very little, from 21 to 27 mm, and evapotranspiration did not change at all. This is not surprising since infiltration excess runoff is largely dominated by the soil hydraulic properties and much less by the initial moisture status. On the other hand, since the percolation flux is equal to the unsaturated conductivity on the lower boundary (3.7), it is highly sensitive to the initial condition. Because the simulation starts at January 1, evapotranspiration is low because of the low potential evapotranspiration. By the time the potential evapotranspiration becomes significant, the effect of the initial condition is largely removed and evapotranspiration becomes dominated by the intermitting wetting and drying events.

S1 ($P, \alpha, \theta_s, \theta_r$ uniform)

The absence of infiltration excess runoff causes all rainfall to be partitioned over percolation, evapotranspiration and storage change. The actual evapotranspiration is slightly lower compared to the deterministic loam soil (L1) but, as shown in Fig 4.1, the potential evapotranspiration is slightly lower too, resulting in an approximately identical value of $\frac{E_a}{E_p}$ (≈ 0.7). The higher unsaturated conductivity of the sand soil causes annual percolation to be higher than for the loam soil.

Continuation of the simulation until equilibrium reveals that the positive storage change is entirely added to the annual percolation while the evapotranspiration remains unchanged. The explanation is the same as for the loam soil.

4.4.2 Field scale water budget considering soil heterogeneity

In this section the results of the Cases L2/L3 and S2/S3 are presented. As mentioned in Section 4.3.4, the characteristic area for which these results are valid is of the order of 10^{-2} - 10^0 km² or the field scale. In terms of subgrid heterogeneity the results indicate the effects due to soil heterogeneity. Fig 4.3a,b indicate the annual values of the water budget components as a function of the soil scale factor α , for both the loam and the sand soil. Note that in these graphs the results of the Cases L1 and S1 are on the vertical line $\ln \alpha = 0$.

L2 (P uniform, α heterogeneous, θ_s and θ_r uniform)

Spatial variation of the scale factor induces spatial variation of the infiltration rates. In Fig. 3.5b,d shows that the saturated conductivity increases with the soil scale factor, which explains the pattern in Fig. 4.3a. Going from left to right along the curves in Fig. 4.3a that connect the N points of the Monte Carlo simulation, at first ($\ln \alpha < -0.75$) infiltration excess runoff decreases with increasing saturated conductivity. Because the unsaturated conductivity is small, percolation is close to zero. The resulting decreasing infiltration excess runoff is counterbalanced by increasing evapotranspiration and storage change. As $\ln \alpha$ increases, the higher saturated conductivity causes smaller amounts of infiltration excess runoff and higher amounts of percolation since the larger unsaturated conductivity allows more wetting fronts to reach the lower boundary. Finally, for $\ln \alpha > 0.3$ all rainfall infiltrates and the distribution of water over evapotranspiration, percolation and storage change remains almost constant. Since the distribution of $\ln \alpha$ is normal around -0.28 (Table 3.2), most realizations have lower scale factors than the reference soil ($\ln \alpha = 0$) and by virtue of (3.29) lower saturated conductivities. This explains the increase in spatial mean infiltration excess runoff relative to L1, and the decrease in spatial mean percolation, evapotranspiration and storage change (Table 4.2).

At this point it is interesting to investigate how the results would change if the simulations were to be continued until equilibrium for every realization ($dW^a = 0$). For large scale factors the present positive storage change will be partitioned over infiltration excess runoff, percolation and evapotranspiration. The infiltration excess runoff is dominated by saturated conductivity. Hence, changes in its annual value are expected to be small, especially above the previously mentioned threshold value of $\ln \alpha$, when no infiltration excess runoff occurs. Percolation depends far more on the initial condition than evapotranspiration (as discussed for Case L1). It is therefore likely that percolation increases most. For small scale factors the annual percolation is very close to zero and since the lower boundary condition (3.6) allows no upward flow, the annual infiltration excess runoff and evapotranspiration have to decrease in case the storage change would

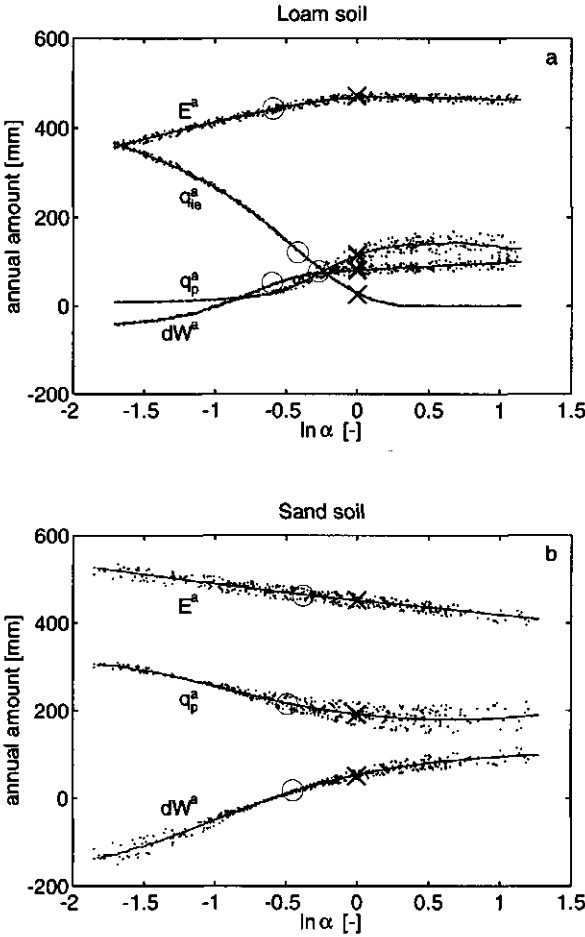


Figure 4.3: Diagrams summarizing the annual results for the (a) the loam soil and (b) the sand soil. Solid lines correspond with the results of Cases L2 and S2, dots represent the results of Cases L3 and S3. The results for Cases L1 and S1 are indicated by (x) and the “equivalent” soil properties are represented by (o).

become zero (i.e. increases relative to the current simulation). Because the dependence of infiltration excess runoff on the moisture profile is small, it is likely that evapotranspiration decreases more than infiltration excess runoff.

In summary, because for $\ln \alpha \approx -1$ the storage change is already zero, continuation of the simulations until equilibrium for every realization will mainly yield a decrease in evapotranspiration for soils where $\ln \alpha < -1$ and an increase in percolation for soils where $\ln \alpha > -1$. For the minimum, maximum and reference

(L1) values of the scale factor the simulations were continued. The results confirmed the hypothesis. In Fig. 4.3a the dependence of the annual values on $\ln \alpha$ thus becomes more pronounced at equilibrium (i.e. larger variances of the annual values).

It is interesting to remark that soils showing a positive storage change in the simulations take only one year to reach equilibrium, whereas soils with a negative storage change take much longer. This because an initial condition that is too wet is largely lifted by percolation, which is a slow process for soils corresponding with small scale factors.

L3 (P uniform, α and θ_s heterogeneous, θ_r uniform)

In Fig. 4.3a the scatter points indicate the results obtained when both α and θ_s are spatially variable. The scatter appears to be normally distributed around the lines that indicate the univariate dependence on soil scale factor α for the average value of θ_s (Case L2). When considering two sets of soil hydraulic functions with identical soil hydraulic parameters except for θ_s and the same initial condition of soil matric head ψ_0 , two differences can be found. Firstly, the amount of water available to root extraction and percolation is greater for high values of θ_s . Secondly, infiltration of the same amount of water causes the moisture content to become closer to saturation when θ_s is small. The resulting unsaturated conductivity is therefore larger for the soil with the small value of θ_s , yielding a higher percolation rate. Analysis of the scatter in Fig. 4.3a reveals that larger percolation amounts correspond to smaller values of θ_s , indicating dominance of the second mechanism. The scatter caused by heterogeneity of θ_s hardly becomes manifest in the values of annual infiltration excess runoff because the infiltration process is dominated by the saturated conductivity. Comparing the results for L2 and L3 in Table 4.2, allows the conclusion that heterogeneity of θ_s has little effect on the statistical indicators of the water budget terms. Thus, although heterogeneity of θ_s affects individual calculations, the effects largely cancel out after averaging. Continuing the simulation until equilibrium will yield similar results as those discussed in the previous section.

S2 (P uniform, α heterogeneous, θ_s and θ_r uniform)

Even for the smallest scale factor (i.e. smallest saturated conductivity) no infiltration excess runoff occurs. For all realizations, rainfall is therefore partitioned over evapotranspiration, percolation and storage change only. Going from small to large scale factors in Fig. 4.3b, the general trend is decreasing values of evapotranspiration and percolation and increasing storage changes. Decreasing evapotranspiration rates are explained by the fact that the unsaturated conductivity (Fig. 3.5d) in the range of small soil matric heads (high moisture contents) is

large for high values of the soil scale factor. As a result, wetting fronts associated with rainfall move faster through the rootzone ($z = z_r$), thereby reducing the possibility of water uptake and subsequent transpiration back into the atmosphere. Comparison of the water retention curves for the scale factors indicated in Fig. 3.5d shows that at the initial condition ($\psi_0 = -2.5$ m) both water storage and unsaturated conductivity become smaller for higher scale factors. Therefore, percolation (at $z = z_c$) decreases with $\ln \alpha$ whereas storage changes increases.

The absence of infiltration excess runoff causes the mean annual fluxes to deviate much less from the deterministic case in comparison with the loam soil. The main difference caused by heterogeneity of the scale factor is the small increase of evapotranspiration and percolation at the expense of annual storage change. This comes as no surprise considering the fact that since $\ln \alpha$ has a normal probability density with a mean of -0.31 , most realizations have scale factors smaller than the reference soil ($\ln \alpha = 0$) and thus higher annual evapotranspiration and percolation (Fig. 4.3b). The approximately linear dependence of annual evapotranspiration on $\ln \alpha$ forces its density function to be normal as well (as is indicated in Table 4.2 by the fact that $\hat{\mu}[E^a] = \hat{m}_e[E^a] = \hat{m}_o[E^a]$).

If the simulations were to be continued until equilibrium the results would change as follows. For small scale factors ($\ln \alpha < -0.6$) the smaller amount of available water corresponding to a zero annual storage change would mainly induce smaller annual percolation and have much less influence on annual evapotranspiration. This is because evapotranspiration is largely determined by the intermittent filling and emptying of the rootzone corresponding to storm and interstorm events. By the same token, large scale factors ($\ln \alpha > -0.6$) would mainly bring about increased annual percolation and, to a much smaller extent, higher annual evapotranspiration. In short, at equilibrium the annual percolation would increase rather than decrease with scale factor, while the annual evapotranspiration pattern largely remains unchanged. This is confirmed by continuing the simulations for the minimum, maximum and reference (Case S1) value of $\ln \alpha$ for a second year. Thus, in contrast with Case L2 the dependence of annual values of $\ln \alpha$ becomes less pronounced (i.e. smaller variance of the annual values).

S3 (P uniform, α , θ_s and θ_r heterogeneous)

The scatter points in Fig. 4.3b show the results for heterogeneous α and θ_s . As with the loam soil, it appears that the scatter is normally distributed around the lines that indicate the dependence of the fluxes on scale factor α when using the average value of θ_s . The effects of varying the saturated moisture content, while the other parameters remain unchanged, were mentioned in the discussion under L3. For very small scale factors it appears that a small saturated moisture content limits the amount of water that can move downwards and therefore causes

smaller percolation rates. For higher scale factors, small θ_s values cause higher percolation rates.

Similar to the loam soil, the influence of heterogeneity of saturated moisture content on the ensemble average water budget is marginal (Table 4.2). Because of the similarity with Case S2, continuation of the simulations until equilibrium will yield the same results as discussed under S2.

4.4.3 Regional water budget considering rainfall heterogeneity

As mentioned in Section 4.3.4, the spatial scale associated with the results presented in this section is of the order of $10^2 - 10^4$ km², or the meso scale. In order to investigate the effects caused by rainfall heterogeneity only, it is assumed that the soil hydraulic properties are either uniform over the area or can be regarded as areally "effective". Both temporally uncorrelated and correlated rainfall are considered (L4/L5 and S4/S5 respectively).

L4 (*P* heterogeneous (no correlation), α , θ_s and θ_r uniform)

Analogous to distributing soil hydraulic characteristics, spatial heterogeneity of rainfall causes variation of infiltration rates. Compared to Case L1 on average this causes higher infiltration excess runoff fluxes, again counterbalanced by lower values of the other budget terms. Generation of the rainfall intensity field does not take into account correlation in time, yielding small variances of the annual rainfall values. By virtue of the central limit theorem, the annual values of rainfall are normally distributed. Analysis reveals that the density functions of the various fluxes are also normal, as is partly indicated by the fact that the mean, median and mode of the various fluxes are very close to each other (Table 4.2). Note that because identical values of annual rainfall may arise for different time series, a scatterplot of the annual fluxes versus P^a does not result in a clear pattern as is the case for the dependence on $\ln \alpha$ in Fig. 4.3a. Comparing the standard deviations of the fluxes, it appears that variation of annual rainfall volumes is mainly transformed into variation of infiltration excess runoff. Continuation of the simulations until equilibrium for a few different rainfall time series results in virtually identical annual runoff and evapotranspiration values and a significant increase in percolation.

L5 (*P* heterogeneous (perfect correlation), α , θ_s and θ_r uniform)

Distributing rainfall intensities, taking into account temporal correlation, results in much more variation of the annual rainfall compared to Case L4. As indicated in Section 4.3.2, this procedure spatially distributes rainfall events rather than

individual intensities. Table 4.2 suggests that the corresponding density function is slightly positively skewed ($\hat{\mu}[P^a] > \bar{m}_e[P^a] > \bar{m}_o[P^a]$). A heuristic explanation may be that the sum of a number of identical exponentially distributed random variables yields a gamma distribution. In this study the annual rainfall reflects the sum of a number of different exponentially distributed random variables, namely the event rainfall amounts. Note that when sampling a longer time series (i.e. a time series containing more rainfall events), the central limit theorem predicts a normal distribution of the annual rainfall amount. A scatter plot of the annual fluxes versus P^a would result in an even less clear pattern than that for L4 because of the large scatter. Despite the very different rainfall patterns obtained by considering time correlation, the mean values of the annual fluxes in Table 4.2 are not very different from those obtained when neglecting any time correlation. It must be noted, however, that there is a slight bias in the results since the mean annual rainfall differs about 3 cm between Cases L4 and L5. This bias results from the truncation of the exponential density function of rainfall intensity in order to avoid unrealistically high cumulative amounts per event. Because of the higher variation in annual rainfall amounts, the standard deviation of the annual values of the various fluxes is higher as well. Similar to Case L4, most of the variation in annual rainfall manifests itself as variation in infiltration excess runoff as is expressed by the value of the standard deviation in Table 4.2. From the same table it is clear that the skewness in the annual rainfall manifests itself most clearly in the cumulative runoff and to a lesser extent in the cumulative percolation.

S4 (P heterogeneous (no correlation), α , θ_s and θ_r uniform)

Contrary to the loam soil, compared to Case S1, the heterogeneity of rainfall intensity hardly affects the annual budget terms (Table 4.2). The obvious reason for this is that no infiltration excess runoff occurs because of the high saturated conductivity and that for all realizations more or less the same amount of water is partitioned over evapotranspiration, percolation and storage change. Similar to Case L4 the annual rainfall is normally distributed by virtue of the central limit theorem. The results presented in Table 4.2 suggest that the three water budget terms are normally distributed too, because of the symmetry of the density functions. The largest part of the variation in annual rainfall manifests itself as variation of annual percolation as is clear from comparison of the standard deviations.

S5 (P heterogeneous (perfect correlation), α , θ_s , θ_r uniform)

As discussed in detail for Case L5, heterogeneity of rainfall taking into account temporal correlation leads to a positively skewed density function of annual rainfall. The greater variation of event cumulative rainfall amounts produces a considerable variation in the sharpness of wetting fronts in the soil. Sharp wetting

fronts propagate rapidly and cause an increase in percolation and a corresponding decrease in mean annual evapotranspiration and storage change compared to both Cases S1 and S4. The density function of annual percolation resembles the large standard deviation and positive skew present in the density function of annual rainfall.

4.4.4 Regional water budget considering soil and rainfall heterogeneity

The results in the previous section assumed spatially uniform or "effective" soil hydraulic properties. They revealed effects caused by spatial heterogeneity of rainfall on the water budget. In this section the effects of soil and rainfall heterogeneity are examined jointly. Since the characteristic scales of soil and rainfall heterogeneity differ by several orders of magnitude, the spatial variation of the water budget terms that will arise is of a "nested" nature. To imagine this, consider a representative number of realized rainfall time series (i.e. a situation like the one discussed in the previous section) each of them with a representative number of soil hydraulic properties (i.e. a situation similar to L3/S3). It appeared that the statistical indicators in Table 4.2 stabilize for $N > 700$. The results are presented in Fig. 4.4 in which the results of the Cases L4/L5 and S4/S5 are depicted also (on the line $\ln \alpha = 0$).

L6 (P heterogeneous (no correlation), α , θ_s heterogeneous, θ_r uniform)

From Table 4.2 it appears that the effect of spatial heterogeneity of both soil hydraulic properties and temporally uncorrelated rainfall, is an increase in the average runoff compared with the cases in which either soil heterogeneity (L3) or rainfall heterogeneity (L4) are considered. The increase in infiltration excess runoff is counterbalanced by a decrease in the other budget components. The standard deviations are of the same order as in the cases with only soil heterogeneity. The fact that the standard deviations of Case L4 are small indicates that heterogeneity of the budget components occurs mostly at the field scale. The curves through the scatter in Fig. 4.4a indicate the splines that yield the minimum sum of squares. The curve for infiltration excess runoff lies anywhere above the curve in Fig. 4.3a (Cases L2 and L3). Hence there is no threshold value of $\ln \alpha$ above which no infiltration excess runoff occurs is not present. Even for the highest realization of soil scale factor α , infiltration excess runoff occurs occasionally, because of heterogeneity of rainfall intensity.

On the whole, prolonging the computations until equilibrium for every realization will have the same effects on the partitioning of water over the various water budget components as mentioned for Case L2.

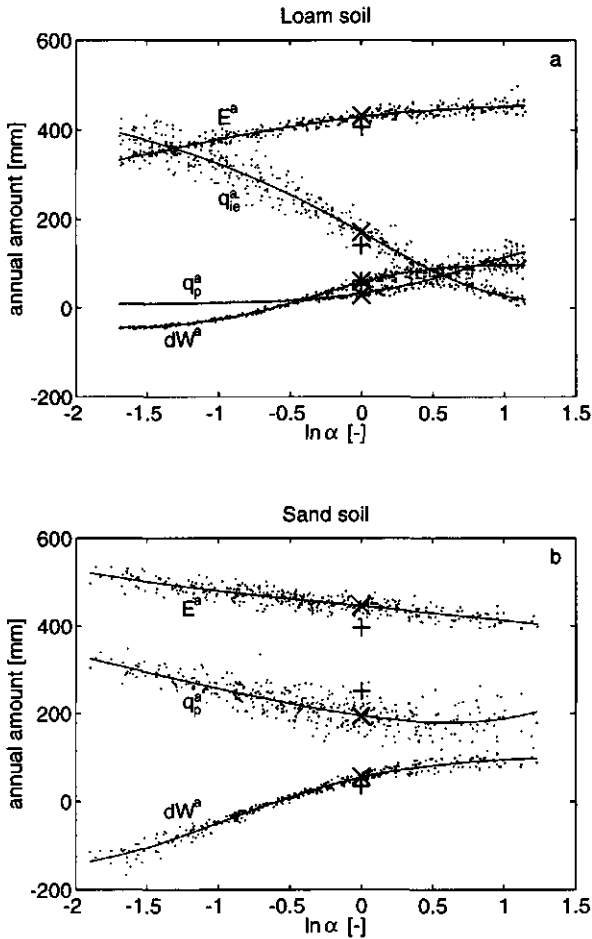


Figure 4.4: Diagrams summarizing the annual results for (a) the loam soil and (b) the sand soil. Solid lines correspond with the best fit spline through the dots that represent the results of Cases L6 and S6. The results for L4 and S4 are indicated by (x) and for Cases L5 and S5 by (+). Cases L7 and S7 are not shown.

L7 (P heterogeneous (perfect correlation), α and θ_s heterogeneous, θ_r uniform)

Temporal correlation in the spatial heterogeneity of rainfall induces a positively skewed probability distribution for the annual rainfall amounts with large standard deviation, as was previously shown for Case L5. Unlike in Case L6, the multivariate dependence (on $\ln \alpha$, θ_s and P^a) of the water budget terms does not approximately collapse into a univariate dependence on $\ln \alpha$ and are therefore

not shown in Fig. 4.4.

A striking result in Table 4.2 is that for the Cases L6 and L7 the mean values of the annual amounts of the water budget terms do not differ much. When considering the mean annual fluxes as a fraction of the mean annual rainfall (to account for the bias in annual rainfall, as discussed under L5), percolation is somewhat more and storage change somewhat less important compared to Case L6. This relates to the fact that due to the larger variation in event scale rainfall, the wetting fronts associated with large rainfall amounts travel faster through the soil column. Qualitatively, the differences in mean annual fluxes between Cases L6 and L7 are the same as between L4 and L5 in which there was no heterogeneity of soil hydraulic properties. Obviously, the standard deviations are somewhat higher for Case L7 since the variation of the annual rainfall is much higher. Unlike for Case L6, in which there was mainly heterogeneity of the fluxes at the field scale, for this case heterogeneity occurs at both the field scale and the meso scale. This can be inferred from the fact the standard deviations of the annual fluxes are higher in comparison to the two cases that considered soil or rainfall heterogeneity only (L3 and L5 respectively).

S6 (P heterogeneous (no correlation), α , θ_s , θ_r heterogeneous)

Comparison of the scatterplots in Figs. 4.3b and 4.4b reveals that heterogeneity of temporally uncorrelated rainfall intensities in addition to heterogeneity of soil hydraulic properties does not cause significant differences in the overall pattern. The best-fit spline curve through the data points in Fig. 4.4b almost exactly coincides with the lines drawn in Fig. 4.3b. Thus, in contrast with the loam soil (Cases L6 and L3), the effect of distributing (temporally uncorrelated) rainfall is negligible. The results obtained after continuation of the simulations until equilibrium can be expected to match those discussed under S2.

S7 (P heterogeneous (perfect correlation), α , θ_s and θ_r heterogeneous)

Heterogeneity of temporally correlated rainfall intensities in addition to heterogeneity of soil hydraulic properties leads to a great increase in scatter compared to the Case S6. As a result, the influence of heterogeneity of P^a cannot be approximately "mapped" around dependence on $\ln \alpha$ and is therefore not depicted. The results in Table 4.2 show that the annual percolation increases compared to the cases with heterogeneity of the soil hydraulic properties only (S3) or temporally correlated rainfall only (S5). From the small standard deviation of annual percolation for Case S3 and the similar values of S5 and S7, it can be concluded that the heterogeneity of percolation is mainly due to rainfall heterogeneity and thus manifests itself at the meso scale. For the few realizations that have both a small soil scale factor as well as a high annual rainfall, a small amount of runoff occurs.

4.4.5 "Equivalent" soil properties

Following Milly and Eagleson [62, 1982], "equivalent" soil hydraulic properties must yield the same water budget as the mean water budget corresponding to a random field of soil hydraulic properties. After insertion of the areally averaged annual values of infiltration excess runoff, percolation, evapotranspiration and storage change of the Cases L2 and S2 in the corresponding scatterplots in Fig. 4.3a and 4.3b, it appears that a unique value of $\ln \alpha$ can be approximately found for the sand soil but not for the loam soil. Sharma and Luxmoore [86, 1979] already concluded that the spatial average water budget behavior of a random field of geometrically similar soils could not be obtained using the mean, median or mode of the distribution, the median being the best estimate. For the sand soil qualitatively this agrees with the fact that the soil corresponding to $\ln \alpha \approx -0.4$ describes the mean annual water budget rather well. This value is close to $\bar{\mu}[\ln \underline{\alpha}]$ (see Table 3.2) and thus $\ln(\overline{m_e}[\underline{\alpha}])$. With the exception of a small period after the initialization of the model, the transient behavior of the water budget using the equivalent soil is remarkably similar to the ensemble mean water budget, as is shown in Fig. 4.5. Obviously, this greatly increases the practical value of the equivalent soil hydraulic properties, since they capture the influence of soil heterogeneity on the dynamical behavior of the field scale water budget accurately. With respect to the curves drawn in Fig. 4.3b it can be seen that they are not far from being point symmetrical around the intersection of the curves with the line $\ln \alpha = -0.4$. Since the distribution of $\ln \underline{\alpha}$ factors is also approximately symmetrical around this value, it clarifies why this point possesses the equivalent property for the annual values. This reasoning does not explain however why the equivalent transient behavior agrees so well, but an important condition seems to be that no infiltration excess runoff happens and hence that all columns receive the same amount of rainfall.

From Fig. 4.3a it is clear that one cannot define an equivalent loam soil that is valid for the different water budget components. In other words, the equivalent homogeneous soil for the annual water budget (if it exists) cannot be found in the set of soils that can be constructed using the values a_g^{ref} , k_s^{ref} and the corresponding probability density function of scale factors. Although the range of α values corresponding to the ensemble mean annual fluxes is rather narrow, any soil within this range yields an unrealistic dynamic behavior of the water budget. This is illustrated in Fig. 4.6 for the transient percolation and transpiration efficiency associated with $\ln \alpha = -0.4$. In Fig. 4.3a it is seen that for this scale factor the annual percolation is underestimated while the annual values of infiltration excess runoff and evapotranspiration are almost the same as the ensemble mean of the Monte Carlo simulation. Although the transient results for percolation differ greatly between the equivalent soil and the ensemble mean, the transpiration efficiencies correspond quite well. It is important to note that even the soil that yields the same amount of annual percolation as the ensemble

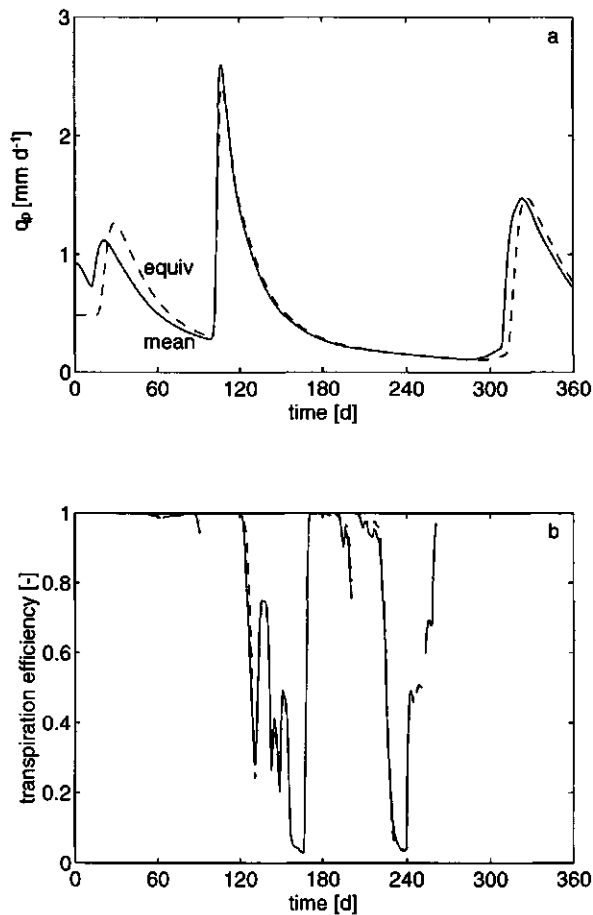


Figure 4.5: Transient behavior of (a) percolation rate q_p and (b) transpiration efficiency $\frac{E}{E_p}$ for the ensemble mean of Case S2 (solid lines) and the “equivalent” soil ($\ln \alpha = -0.4$, dashed lines). Discontinuities in the transpiration efficiency occur when $E_p = 0$.

mean ($\ln \alpha \approx -0.25$) does not reproduce the transient percolation of the ensemble mean.

A probable explanation for the absence of an equivalent soil is that the various soil columns of the Monte Carlo simulation do not all receive the same amount of infiltration and thus do not have a comparable water budget. Furthermore, since the occurrence of infiltration excess runoff depends critically on the specific rainfall pattern, it is inevitable that possible equivalent soil hydraulic characteristics

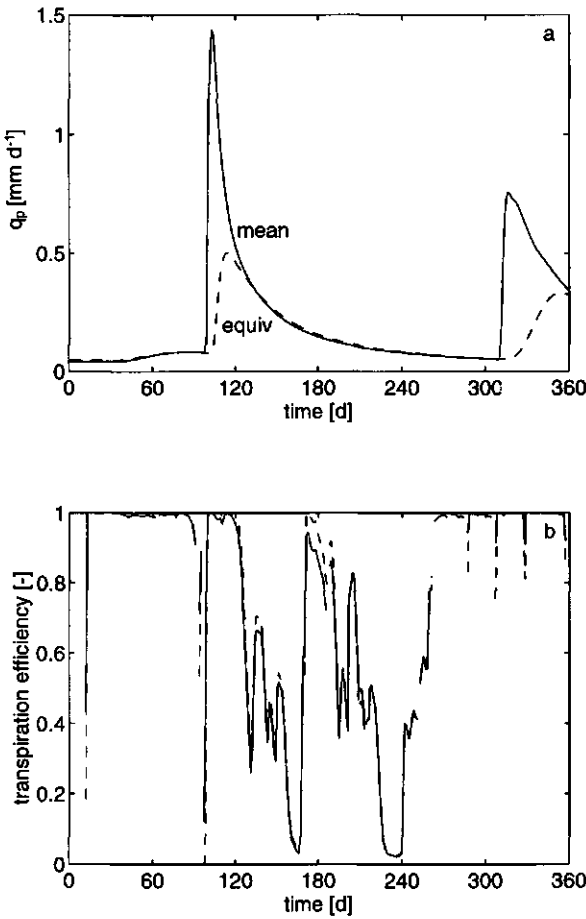


Figure 4.6: Transient behavior of (a) percolation rate q_p and (b) transpiration efficiency $\frac{E}{E_p}$ for the ensemble mean of Case L2 (solid lines) and the soil corresponding to $\ln \alpha = -0.4$ (dashed lines). Discontinuities in the transpiration efficiency occur when $E_p = 0$.

depend on the boundary conditions. Therefore they will have little significance as they cannot be derived from measurements of soil hydraulic characteristics on scales smaller than those on which the equivalent properties are valid. The existence of equivalent soil hydraulic properties will be studied in more detail in Chapter 5.

4.4.6 Dynamics of water storage

The dynamical behavior of water storage in the soil profile reflects the transient behavior of the fluxes q_{ie} , q_p and E . Figs. 4.7 and 4.8 summarize the effect of distributing soil hydraulic properties or rainfall intensity on the water storage dynamics for the loam and the sand soil respectively. The cases in which both soil hydraulic properties and rainfall intensities are spatially heterogeneous are not included in order to focus on the individual mechanisms rather than on the combined effects. Figs. 4.7a and 4.8a show the relative storage, i.e. the ratio of the mean water storage in the soil column, of some stochastic cases and the water storage of the deterministic case. The graphs in Figs. 4.7b and 4.8b show the temporal behavior of the standard deviation of water storage.

Loam soil

From the discussion of the annual values it is clear that both heterogeneous soil hydraulic properties and rainfall intensities enhance the infiltration excess runoff production relative to the deterministic case. Any severe storm event therefore causes the ratio $\frac{\bar{W}}{\bar{W}(L1)}$ to decrease. This is illustrated in Fig. 4.7a. Similar to the average annual values, it appears that heterogeneity of the saturated moisture content in addition to a spatially variable scale factor has only little effect.

The similarity between the Cases L4 and L5 is quite remarkable considering the very different nature of the time series of rainfall with and without temporal correlation respectively (see Fig. 4.2). Because the soil hydraulic properties of L4 and L5 are identical to the deterministic case, initially the ratio equals 1. During periods of drying the ratio tends to return to this value.

The temporal behavior of the standard deviation of storage $\hat{\sigma}[W]$ is less obvious. The main difference is the decrease in $\hat{\sigma}[W]$ after a rainfall event for cases with spatial variation of soil hydraulic properties and the increase for cases with spatial heterogeneity of rainfall (Fig. 4.7b). Of course the increase relates to the different amounts of rainfall each column receives as a result of rainfall heterogeneity. Since the variation of total storm rainfall amount is greatest when temporal correlation is taken into account, the increase in $\hat{\sigma}[W]$ is most significant for Case L5. The decrease in $\hat{\sigma}[W]$ for the Cases L2 and L3 can be explained regarding Fig. 3.5a,b. Soils corresponding to small scale factors store more water but have a smaller saturated conductivity than soils corresponding to large scale factors. During a rainfall event most infiltration therefore occurs for soils that have the least water stored, thereby reducing the variation of water storage between the columns. The spatial heterogeneity of the saturated moisture content in L3 causes $\hat{\sigma}[W]$ to be higher and less temporally variable compared to that in L2.

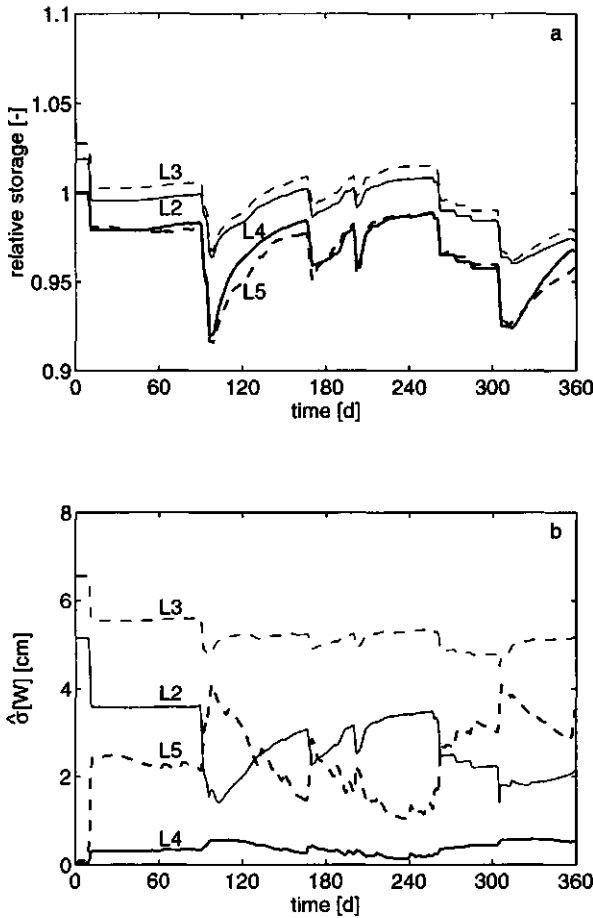


Figure 4.7: Temporal behavior of mean and standard deviation of daily values of soil water storage for the loam soil. (a) relative storage ratio $\frac{\hat{\mu}[W]}{W(L)}$ and (b) standard deviation $\hat{\sigma}[W]$ for the stochastic Cases L2 (thin solid lines), L3 (thin dashed lines), L4 (thick solid lines) and L5 (thick dashed lines).

Sand soil

For the sand soil no infiltration excess runoff occurs and all rainfall is partitioned over evapotranspiration, percolation and storage change. Differences between the realizations are therefore due to the water storage capacity and the velocity of wetting fronts in the soil. The uniform soil properties used in Cases S4 and S5 imply that differences in wetting front velocities in the soil are entirely due to the

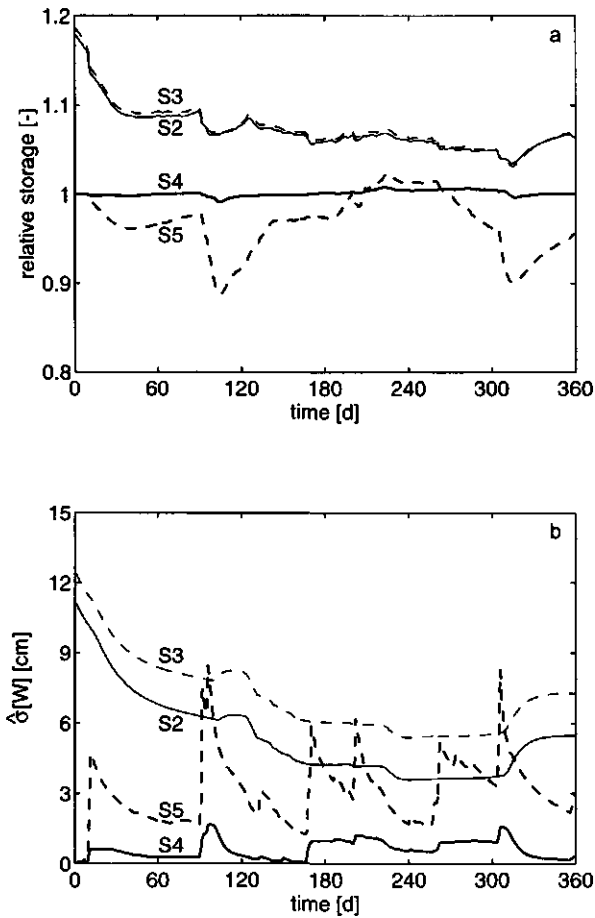


Figure 4.8: Temporal behavior of mean and standard deviation of daily values of soil water storage for the sand soil. (a) relative storage ratio $\frac{\hat{W}[W]}{W(S1)}$ and (b) standard deviation $\hat{\sigma}[W]$ for the stochastic Cases S2 (thin solid lines), S3 (thin dashed lines), S4 (thick solid lines) and S5 (thick dashed lines).

different amounts of water delivered by storms. The sharp wetting fronts induced by large rainfall amounts travel faster than less pronounced fronts. Accordingly, the decrease in $\frac{\hat{W}[W]}{W(S1)}$ for S5 in Fig. 4.8a relates to realizations that receive a large amount of rainfall which is subsequently routed downwards and lost as percolation. This effect is almost absent in S4 because the neglect of temporal correlation makes extreme amounts of storm rainfall less likely than for S5. The standard deviations of the storm rainfall amounts, small for S4 and high for S5

respectively, explain the transient behavior of $\hat{\sigma}[W]$ in Fig. 4.8b.

Cases S2 and S3 behave similar, again illustrating how small the effect of heterogeneity of the saturated moisture content is. The largest decrease in $\frac{\hat{\mu}[W]}{\hat{W}(S1)}$ occurs immediately after the start of the calculations (Fig. 4.8a). At the initial condition ($\psi_0 = -2.5$ m) in Fig. 3.5a it can be seen that both the unsaturated conductivity and the water storage increase with decreasing values of scale factor. As a result initially wet profiles dry faster, which explains the decrease in both $\frac{\hat{\mu}[W]}{\hat{W}(S1)}$ in Fig. 4.8a and $\hat{\sigma}[W]$ for S2 and S3 in Fig. 4.8b. After the effect of the initial condition has largely been removed, one can see that major rainfall events slightly decrease $\frac{\hat{\mu}[W]}{\hat{W}(S1)}$ for S2 and S3. In Fig. 4.8b it is demonstrated that only large rainfall events (day 95 and day 305) result in a modest increase in the standard deviation. This is related to the fact that only the sharp wetting fronts corresponding to those events reach the lower boundary and induce spatial variation of the percolation rates. This also explains why the increase in the standard deviation for soil heterogeneity lags behind the increase caused by spatially variable amounts of rainfall.

4.5 Conclusions

The influence of spatial heterogeneity of soil hydraulic characteristics and rainfall intensity, both separately and combined, was investigated using Monte Carlo simulation. The soil columns were assumed to be laterally independent and vertically uniform and there was no interaction with groundwater. Two limiting cases regarding the temporal correlation of spatial heterogeneous rainfall were explored. Apart from rainfall, the atmospheric conditions were assumed to be spatially uniform.

Because of the different spatial scales at which soil heterogeneity and rainfall heterogeneity become manifest, the water budgets corresponding to soil and rainfall heterogeneity are associated with distinct spatial scales. For soil heterogeneity this is the field scale ($\approx 10^{-2} - 10^0$ km²) and for rainfall heterogeneity the meso scale ($\approx 10^2 - 10^4$ km²). The main conclusions of this chapter are:

1. The occurrence of infiltration excess runoff strongly dominates the effect of spatial heterogeneity of the soil scale factor on components of the water budget. Therefore, heterogeneity of soil hydraulic properties on the components of the annual water budget has a stronger effect for the loam soil than for the sand soil;
2. Heterogeneity of the saturated moisture content has a negligible effect on the annual water budget components for both the loam and the sand soil, nor does it induce different variances;

3. In general, for the loam soil, rainfall heterogeneity with and without temporal correlation yields similar mean water budgets, that differ greatly in variance however. For the sand soil, heterogeneity of rainfall without temporal correlation yields a mean water budget that are virtually identical to the deterministic case. Introduction of temporal correlation of rainfall significantly increases percolation at the expense of evapotranspiration;
4. Because soil heterogeneity has a great influence, for the loam the heterogeneity of the water budget occurs mostly at the field scale and to a lesser extent the meso scale. For the sand soil most of the water budget variation arises due to temporally correlated rainfall and thus occurs at the meso scale;
5. A homogeneous "equivalent" loam soil which yields the same annual water budget as a stationary random field of soil hydraulic properties does not exist. For the sand soil, the properties corresponding to the median of the distribution of scale factors are close to the equivalent soil. This equivalent sand soil captures the transient behavior of the (field scale) spatially variable water budget remarkably well. The occurrence of infiltration excess runoff seems a crucial factor governing the presence of equivalent properties.

Chapter 5

Analytical treatment of the soil water budget

5.1 Objective and methods

In the previous chapter the effects of spatial heterogeneity of soil hydraulic properties and rainfall intensity on the areally average water budget were revealed. Flow phenomena governed by the highly nonlinear Richards' equation (2.11) in spatially heterogeneous soils possess many subtle features that complicate the analysis of the results however. In this chapter a simplified system is defined that allows analytical treatment of soil water processes. It allows a more rigorous inspection of the mechanisms through which spatial heterogeneity affects the water budget. Also, the *computational efficiency of this approach enables investigation of more combinations of climate and soil for longer periods than in Chapter 4.*

The essence of the method applied here is the omission of redistribution within the unsaturated zone. In that sense the model is similar to that of Warrilow [104, 1986] discussed in section 3.2.2, since only the dynamics of total water storage are considered. Transient infiltration during storms is described analytically using the solution of Philip [74, 1957] and the time compression approximation, and will be discussed in detail. A new solution is derived for simultaneous evapotranspiration and percolation during interstorms. During storm periods, percolation is assumed to be zero.

The analytical development of the solutions is presented in Section 5.2. The parameters of three climate and three soil types are specified in Section 5.3 and in Section 5.4 a comparison with the numerical model used in Chapter 4 is performed for all combinations of climate and soil. In Section 5.5 the influence of spatial variation of some soil parameters is further explored. The existence of an "equivalent" soil is subsequently investigated in Section 5.6. Finally, in Section 5.7, the probability density functions of infiltration and evapotranspiration rate are derived analytically for some special cases of the initial conditions on the

time scale of one (inter)storm event. The time evolution of the density functions shows the different effects of heterogeneity of saturated conductivity, rain rate and saturation degree on the water budget.

Throughout this chapter the results are not interpreted in terms of explicit spatial scales. The scales associated with heterogeneity of soil hydraulic properties and rainfall rate were extensively discussed in section 4.3.4.

5.2 Analytical development

5.2.1 Soil hydraulic characteristics

For reasons of analytical tractability, in this chapter the Brooks and Corey [12, 1966] relationships for soil water retention and unsaturated conductivity characteristics are preferred over the formulations (3.3) and (3.4) used in the preceding chapters:

$$s(\psi) = \begin{cases} \left(\frac{\psi}{\psi_s}\right)^{-m} & \psi < \psi_s \\ 1 & \psi_s \leq \psi \leq 0 \end{cases} \quad (5.1)$$

$$k(s) = k_s s^{\frac{2+3m}{m}} \quad (5.2)$$

$$s = \frac{\theta}{\theta_s} \quad 0 \leq s \leq 1 \quad (5.3)$$

Here s is the degree of saturation identical to (3.5) with $\theta_r = 0$, ψ the soil matric head, ψ_s the air entry value and m (> 0) the pore size distribution index. In general, when the soil becomes sandier, ψ_s becomes less negative, and k_s and m become larger. Although the soil parameters will be specified later, one can obtain an impression of the behavior of (5.1) and (5.2) from Fig. 5.3.

5.2.2 Solution for storm periods

After the onset of rainfall, infiltration i will occur at a rate equal to the rainfall intensity P , which is assumed constant for a storm event

$$i(t) = P \quad (5.4)$$

When the rainfall intensity exceeds the saturated hydraulic conductivity of the soil, eventually the soil will no longer be able to maintain an infiltration rate equal to the rainfall intensity, and water will pond at the surface. Mathematically this means that the flux boundary condition changes to a head boundary condition at ponding time $t = t_p$.

The infiltration flux corresponding to a head boundary condition, i_h , can be described for short time t using the first two terms of a series expansion in t obtained by Philip [74, 1957]

$$i_h(t) = \frac{1}{2}S(s_0)t^{-\frac{1}{2}} + ak_s \quad (5.5)$$

where S is the sorptivity and s_0 the initial vertically uniform saturation degree. The constant a can be expressed as $\frac{2-\zeta}{3}$ [69, Parlange *et al.* 1982] in which ζ ($0 \leq \zeta \leq 1$) depends on the behavior of the unsaturated conductivity near saturation. When the conductivity is approximately constant near saturation $\zeta = 0$, which corresponds to the Green and Ampt [42, 1911] limit. For real soils ζ is commonly close to 1, indicating that near saturation the conductivity varies rapidly [69, Parlange *et al.* 1982]. In reality, the infiltration rate approaches k_s for $t \rightarrow \infty$ and evidently (5.5) breaks down when using $a \neq 1$.

S in (5.5) represents sorptivity and is determined here following Smith and Parlange [98, 1978]

$$S^2(\theta_0) = 2(\theta_s - \theta_0) \int_{\theta_0}^{\theta_s} D(\theta) d\theta \quad (5.6)$$

where the diffusivity D is defined as

$$D(\theta) = k(\theta) \frac{d\psi}{d\theta} \quad (5.7)$$

Solving (5.6) and writing in terms of the initial saturation degree s_0 yields

$$\begin{aligned} S(s_0) &= \left(\frac{2\theta_s(1-s_0)\psi_s}{1+3m} \left[s_0^{\frac{1+3m}{m}} - 1 \right] \right)^{\frac{1}{2}} k_s^{\frac{1}{2}} \\ &= S_r k_s^{\frac{1}{2}} \end{aligned} \quad (5.8)$$

where S_r is introduced for notational convenience.

More advanced analytical representations of soil controlled infiltration may be used (e.g. Haverkamp *et al.* [43, 1990]) but the present model contains the essence of the infiltration process and allows simple analytical derivation of the switching from flux to head controlled infiltration, shown hereafter.

Mein and Larsson [60, 1973] outline the time compression approximation (TCA) originally introduced by Sherman [89, 1943] to match (5.4) and (5.5). The method is illustrated in Fig. 5.1 and outlined hereafter. Physically, ponding occurs when the infiltration flux becomes equal to the rainfall intensity. Equating (5.4) and (5.5) and solving for time yields the equivalent time t_e

$$t_e = \frac{S_r^2 k_s}{4(P - ak_s)^2} \quad P > ak_s \quad (5.9)$$

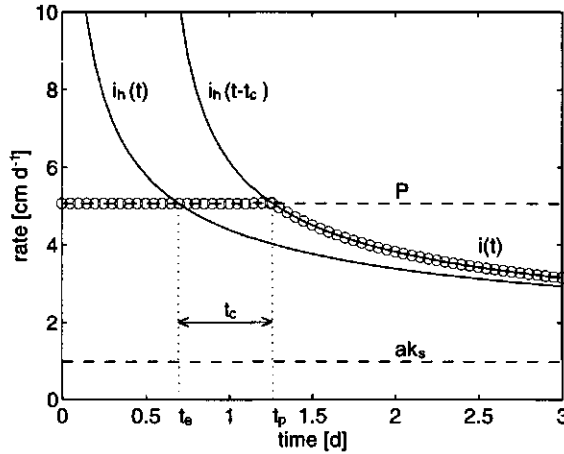


Figure 5.1: Illustration of the time compression approximation (TCA) for the infiltration rate. $i(t)$ is given by (5.13) and indicated by (o). All symbols are explained in the text.

Since after the start of a storm event $P \leq i_h$, the soil's capacity to absorb water decreases slower than i_h and the actual time to ponding is longer than t_e . An expression for ponding time t_p is obtained by equating the cumulative infiltration resulting from flux controlled infiltration to the cumulative infiltration that would result from head controlled infiltration up to t_e

$$\int_0^{t_p} P dt = \int_0^{t_e} i_h(t) dt \quad (5.10)$$

Essentially, the time compression approximation thus means that cumulative infiltration serves as a surrogate for time. Using (5.5) and solving (5.10) for t_p yields

$$t_p = \begin{cases} \frac{S_r^2 k_s (2P - ak_s)}{4P(P - ak_s)^2} & P > ak_s \\ \infty & P \leq ak_s \end{cases} \quad (5.11)$$

As anticipated, (5.11) shows that ponding time t_p decreases with increasing rain rate P and/or decreasing saturated conductivity k_s .

After ponding, infiltration is assumed to occur according to (5.5) with $t > t_e$. This necessitates a shift of the time axis by an amount t_c :

$$\begin{aligned} t_c &= t_p - t_e \\ &= \frac{S_r^2 k_s}{4P(P - ak_s)} \quad P > ak_s \end{aligned} \quad (5.12)$$

The subscript c is used to adhere to the somewhat confusing but often used term "compression" or "condensation". The resulting formulation for infiltration rate

now becomes

$$i(t) = \begin{cases} P & t \leq t_p \\ i_h(t - t_c) & t > t_p \end{cases} \quad (5.13)$$

Cumulative infiltration i^{cum} up to time t can be derived by integrating (5.13) which yields

$$i^{\text{cum}}(t) = \begin{cases} Pt & t \leq t_p \\ Pt_p + \int_{t_p}^t i_h(\tau - t_c) d\tau & t > t_p \end{cases} \quad (5.14)$$

The right hand side of (5.14) for $t > t_p$ can be obtained easily using (5.5) and $t_e = t_p - t_c$

$$i^{\text{cum}}(t) = Pt_p + S_r k_s^{\frac{1}{2}} \left((t - t_c)^{\frac{1}{2}} - t_e^{\frac{1}{2}} \right) + ak_s(t - t_p) \quad t > t_p \quad (5.15)$$

The time compression approximation is discussed in more detail by Sivapalan and Milly [93, 1989]. Dooge and Wang [29, 1993] showed that TCA is an excellent approximation under most circumstances, although not necessarily exact.

Now consider a soil reservoir of depth d_r . During rainfall, at any time t the soil moisture state in the soil reservoir is given by

$$s(t) = s_0 + \frac{i^{\text{cum}}(t)}{d_r \theta_s} \quad (5.16)$$

The total amount of infiltration excess runoff up to time t is given by

$$q_{ie}^{\text{cum}}(t) = Pt - i^{\text{cum}}(t) \quad (5.17)$$

The reservoir may (super)saturate ($s \geq 1$) because during rainfall it cannot lose water. When this occurs the amount of saturation excess runoff generated up to time t equals

$$q_{se}^{\text{cum}}(t) = d_r \theta_s [s(t) - 1] \quad (5.18)$$

5.2.3 Solution for interstorm periods

During an interstorm period, evapotranspiration E is assumed to occur according to

$$E(s) = E_p s^r \quad (5.19)$$

where the exponent r determines the shape of the transpiration efficiency.

In reality, as indicated in detail in section 3.2.1, there is a threshold value of s above which evapotranspiration occurs at its potential rate. In (5.19) however, such a threshold value is not taken into account in order to keep the formulation analytically tractable. Furthermore r is set to 1 since any other value prohibits an analytical solution. As clarified by Brubaker and Entekhabi [13, 1994], the linear shape of the evapotranspiration efficiency function overestimates the coupling

between the water and energy budgets under humid conditions since evapotranspiration is always soil controlled (i.e. moisture limited). Under dry conditions evapotranspiration is overestimated since in reality plants cannot extract water beyond wilting point (as illustrated for soil matric head ψ_4 in Fig. 3.1).

By assuming downward water flow due to gravity only like in (3.7), the percolation flux q_p at the lower boundary of the soil reservoir equals the hydraulic conductivity (5.2)

$$q_p = k_s s^{\frac{2+3m}{m}} \quad (5.20)$$

The evolution of the moisture state of the soil reservoir introduced before is given by the differential equation

$$\begin{aligned} \frac{ds}{dt} &= -\frac{q_p + E}{d_r \theta_s} \\ &= -\frac{s}{d_r \theta_s} (k_s s^c + E_p) \end{aligned} \quad (5.21)$$

where $c = \frac{2+2m}{m}$. Hereafter, (5.21) is first solved for two limiting cases: evapotranspiration only and percolation only, followed by the derivation of the general solution.

Solutions for two limiting cases

By setting k_s to 0 in (5.21) one obtains the limiting case for water loss due to evapotranspiration only and a linear reservoir is obtained in the sense that the rate of depletion is linear with storage. Using the initial condition $s(t) = s_0$ at time $t = 0$ yields the limiting solution $s_1(t)$

$$s_1(t) = s_0 \exp \left[-\frac{E_p}{d_r \theta_s} t \right] \quad (5.22)$$

Setting E_p to 0 in (5.21) yields the second limiting case, i.e. water loss is entirely due to percolation. Using the change of variables $u = s^{-c}$ and the same initial condition as in (5.22) results in the limiting solution $s_2(t)$

$$s_2(t) = s_0 \left(1 + \frac{ck_s}{d_r \theta_s} s_0^c t \right)^{-\frac{1}{c}} \quad (5.23)$$

General solution for interstorm behavior

In reality, evapotranspiration and percolation occur simultaneously and water recession from the soil reservoir occurs at a rate that is always higher than either of the limiting solutions (5.22) and (5.23). Upon introducing the substitution

$$\begin{aligned} v(t) &= \frac{E(s) + q_p(s)}{q_p(s)} \\ &= 1 + \frac{E_p}{k_s} s^{-c} \end{aligned} \quad (5.24)$$

(5.21) reduces to the simple linear differential equation

$$\begin{aligned}\frac{dv(t)}{dt} &= \frac{cE_p}{d_r\theta_s} \left(1 + \frac{E_p}{k_s} s^{-c}\right) \\ &= \frac{cE_p}{d_r\theta_s} v(t)\end{aligned}\quad (5.25)$$

The solution of (5.25) reads

$$v(t) = v_0 \exp\left(\frac{cE_p}{d_r\theta_s} t\right) \quad (5.26)$$

where $v_0 = v(0)$. Back substitution yields the general solution of (5.21)

$$s(t) = \left(\left[s_0^{-c} + \frac{k_s}{E_p} \right] \exp\left[\frac{cE_p}{d_r\theta_s} t \right] - \frac{k_s}{E_p} \right)^{-\frac{1}{c}} \quad (5.27)$$

From (5.27) it can readily be seen that $s(t) = s_1(t)$ when $k_s = 0$. A little more effort reveals that $\lim_{E_p \downarrow 0} s(t) = s_2(t)$.

Now let ϵ ($0 \leq \epsilon \leq 1$) denote the ratio of the evapotranspiration flux over the rate of total water loss

$$\begin{aligned}\epsilon(t) &= \frac{E(s)}{q_p(s) + E(s)} \\ &= 1 - \frac{1}{v(t)} \\ &= 1 - (1 - \epsilon_0) \exp\left[-\frac{cE_p}{d_r\theta_s} t\right]\end{aligned}\quad (5.28)$$

where $\epsilon_0 = \epsilon(0)$. Substitution of (5.22) and (5.28) into (5.27) yields

$$s(t) = s_1(t) \left(\frac{\epsilon_0}{\epsilon(t)} \right)^{\frac{1}{c}} \quad (5.29)$$

From (5.28) it follows that $\lim_{t \rightarrow \infty} \epsilon(t) = 1$. Hence $\frac{\epsilon_0}{\epsilon(t)}$ in (5.29) decreases from 1 at $t = 0$ to ϵ_0 when $t \rightarrow \infty$. This shows that the depletion of $s(t)$ is indeed more rapid than that of $s_1(t)$.

The expression for the cumulative amount of evapotranspiration up to time t is derived in Appendix B and reads:

$$E^{\text{cum}}(t) = d_r\theta_s s_0 \epsilon_0^{\frac{1}{c}} \left(1 - \frac{s_1(t)}{s_0} + \sum_{n=1}^{\infty} \frac{\left[1 - \left\{ \frac{s_1(t)}{s_0} \right\}^{nc+1} \right] [1 - \epsilon_0]^n}{n(nc+1) B(c^{-1}, n)} \right) \quad (5.30)$$

where the beta function B is given by (B.5). The series in (5.30) converges quite rapidly under most circumstances. In general its contribution is relatively minor. Omission of the series term in (5.30) leads to a first order approximation of $E^{\text{cum}}(t)$ in terms of the cumulative evapotranspiration $E_1^{\text{cum}}(t)$ that is derived from (5.22)

$$E^{\text{cum}}(t) \approx \epsilon_0^{\frac{1}{c}} E_1^{\text{cum}}(t) = \left(\frac{E_p}{E_p + k_s s_0^c} \right)^{\frac{1}{c}} E_1^{\text{cum}}(t) \quad (5.31)$$

Eq. (5.31) states that to a first-order approximation, the cumulative evapotranspiration from a soil reservoir that also loses water due to percolation is proportional to the cumulative evapotranspiration from a bottom-closed reservoir and a reduction factor that depends on the climate and soil properties and the initial condition. From (5.31) it is clear that $E^{\text{cum}}(t) = E_1^{\text{cum}}(t)$ when $k_s = 0$ and that $E^{\text{cum}}(t) = 0$ for $k_s \rightarrow \infty$.

The cumulative percolation can be readily obtained from mass conservation considerations

$$q_p^{\text{cum}}(t) = d_r \theta_s [s_0 - s(t)] - E^{\text{cum}}(t) \quad (5.32)$$

In summary, the above framework of solutions enables efficient computation of the time evolution of the water budget terms. The cumulative amounts of infiltration on the one hand and evapotranspiration and percolation on the other can be determined considering only the transition points (t_1, t_2, t_3, \dots) from storm to interstorm periods and vice versa, as illustrated in Fig. 5.2.

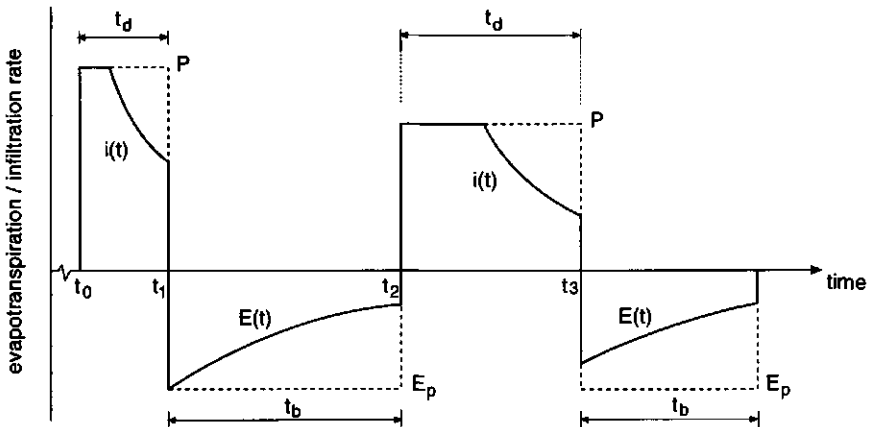


Figure 5.2: Diagram of the Poisson rectangular pulses model that constitutes the meteorological forcing. Computations are only performed at the times t_1, t_2, t_3 etc.

5.3 Specification of climate and soil parameters

Throughout this chapter, the depth of the soil reservoir d_r is taken as 50 cm. In order to run the model, a time series of rainfall and potential evapotranspiration as well as the soil hydraulic properties need to be defined. In the following, the parameters from which time series can be constructed and the soil hydraulic properties are specified for three different climates and three different soil types.

5.3.1 Climate forcing

The solutions derived in Section 5.2 require that the rain rate P remains constant over a storm period and that the potential evapotranspiration intensity E_p is constant during an interstorm period. Therefore, the meteorological forcing is modeled after Eagleson [32, 1978] as a Poisson arrival process of rectangular rainfall pulses with exponentially distributed rainfall intensity P and duration t_d . The durations of interstorm periods t_b are exponentially distributed and the potential evapotranspiration E_p is assumed to be time independent. In Fig. 5.2 a schematic picture of the meteorological forcing is shown. From the definition of the exponential distribution in (A.16), it follows that a climate is completely defined by the mean values $\mu[P]$, $\mu[t_d]$, $\mu[t_b]$ and E_p . Obviously, this simple model is a very crude representation of climate, but it nevertheless captures the hydrologically important intermittency of rainfall events. In Table 5.1 the parameters are given

Table 5.1: Parameters of the Poisson rectangular pulses model for rainfall and potential evapotranspiration for the arid, semi-humid and humid climate according to Hawk and Eagleson [44, 1992].

Parameter	Arid (A)	Semi-humid (SH)	Humid (H)
$\mu[P]$ [mm d ⁻¹]	29.9	50.7	16.1
$\mu[t_d]$ [d]	0.48	0.25	0.72
$\mu[t_b]$ [d]	6.46	3.44	3.77
E_p [mm d ⁻¹]	4.1	3.3	1.9
\overline{P} [mm d ⁻¹]	2.0	3.3	2.6
$\overline{E_p}$ [mm d ⁻¹]	3.8	3.1	1.6

that determine the three climates used here: arid (A), semi-humid (SH) and humid (H). Indicated in the same table are the long-term averages of daily rainfall \overline{P} and potential evapotranspiration $\overline{E_p}$. As expected,

$$\begin{aligned}
 \overline{E_p} &= \frac{1}{t^{\text{int}}} \int_0^{t^{\text{int}}} E_p(t) dt \\
 &= \frac{\mu[t_b]}{\mu[t_d] + \mu[t_b]} E_p
 \end{aligned}
 \tag{5.33}$$

The analytical expression for \bar{P} was derived by Eagleson [32, 1978]. Throughout this chapter, the analytical model is integrated over a period $t^{\text{int}} = 15$ years. It has been verified that for this period the mean values of the three climates in Table 5.1 are reproduced.

5.3.2 Soil hydraulic characteristics and their spatial heterogeneity

In order to cover a wide range of soil hydraulic properties, three soils have been selected: clay (C), loam (L) and sand (S). The parameter values are taken from Bras [10, 1990] and are given in Table 5.2. The corresponding water retention and hydraulic conductivity functions are presented in Fig. 5.3.

Table 5.2: Brooks and Corey parameters for the three soils (after Bras [10, 1990]).

Parameter	Clay (C)	Loam (L)	Sand (S)
k_s [cm d ⁻¹]	2.94	29.4	294
ψ_s [cm]	-90	-45	-25
θ_s [-]	0.45	0.35	0.25
m [-]	0.44	1.2	3.3
c [-]	6.5	3.7	2.6

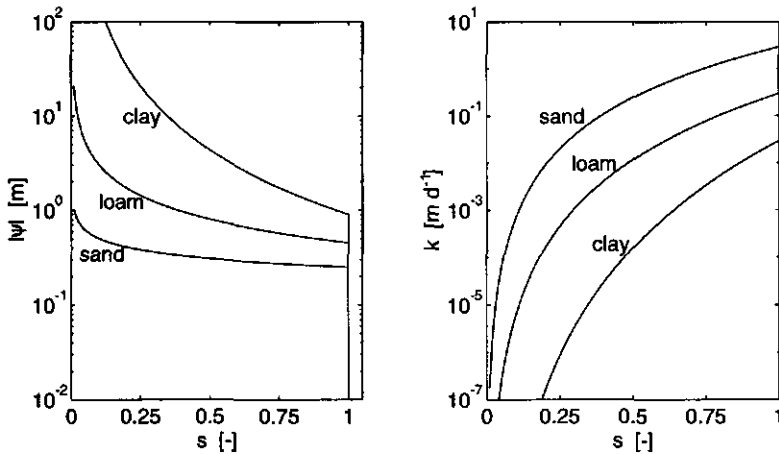


Figure 5.3: Absolute soil matric head $|\psi|$ in (5.1) and hydraulic conductivity k in (5.2) as functions of saturation degree s corresponding to the parameters of the clay, loam and sand soil in Table 5.2.

The constant $a = \frac{2-\zeta}{3}$ in (5.5) is set to $\frac{1}{3}$ since for real soils ζ is close to 1. In accordance with Smith and Parlange [98, 1978], the results appear not very sensitive for a .

In reality the parameters exhibit considerable spatial (co)variation that must be accounted for in water budget modeling. As in the previous chapters the scaling theory of Miller and Miller [61, 1956] is used, which was explained in detail in Section 3.2.4. Combination of (3.26), (3.27) and (5.1), (5.2) yields the following relationships:

$$\psi_{s,i} = \alpha_i^{-1} \psi_s^{\text{ref}} \quad (5.34)$$

$$k_{s,i} = \alpha_i^2 k_s^{\text{ref}} \quad (5.35)$$

where α is the soil scale factor and the subscript i denotes all possible realizations.

Although strictly speaking the geometrically similar media concept only applies to soils with identical saturated moisture contents θ_s and exponents m , in practice these parameters are found to be heterogeneous as well. It will be seen later that the sensitivity of the water budget to θ_s is small. Spatial variability of θ_s is therefore not considered.

As mentioned in Chapters 3 and 4, it is well a established fact that the soil scale factor is lognormally distributed random variable (see Appendix A.3). Brakensiek *et al.* [9, 1981] and Russo and Bresler [82, 1981] found that within a textural class the exponent m can be represented by a lognormal distribution as well. Correlation between the scale factor α and the exponent m is not considered here, although it may be easily incorporated.

5.4 Validation of the analytical solutions

The two major simplifications introduced in the derivation of the solutions are the omission of unsaturated flow within the reservoir and the impossibility of upward capillary flow through the lower boundary. To check the validity of these simplifications, the analytical solutions are compared with the numerical model based on Richards' equation [26, Dirksen *et al.* 1993] used in Chapter 4. To that end, the numerical model is slightly modified here such that the evapotranspiration formulation is identical to (5.19). The unit gradient lower boundary condition (3.7) corresponds with the condition that results in (5.20). The soil water retention characteristic in the numerical model is given by (3.3) according to Van Genuchten [102, 1980], and was determined by nonlinear regression versus the curves specified by the parameters in Table 5.2 in the range $0.1 < s \leq 1$. This results in small deviations between the soil water retention characteristics in the analytical solutions and the numerical model. The hydraulic conductivities in the analytical and numerical model are identical.

When locating the lower boundary of the numerical model at 50 cm below the soil surface ($z_c = -50$ cm), the same model domain is obtained as for the soil reservoir with depth $d_r = 50$ cm. Differences between the analytical and the numerical model are then mainly due to the absence of unsaturated redistribution fluxes within the analytical solutions. The severity of the second simplification, upward capillary water flow into the zone of root extraction, is investigated by locating the lower boundary at 150 cm below the soil surface in the numerical model ($z_c = -150$ cm). Fig. 5.4 summarizes the long-term mean water budgets

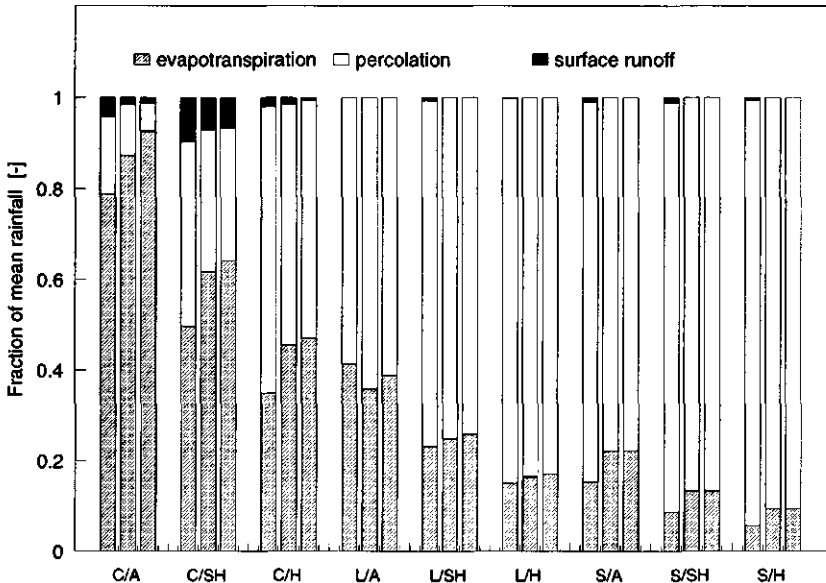


Figure 5.4: Comparison of the 15 year average water budget according to the analytical solutions (left bars), and numerical solutions of Richards' equation for $z_c = -50$ cm (middle bars) and $z_c = -150$ cm (right bars) for all nine combinations of climate and soil listed in Tables 5.1 and 5.2.

(15 years) from the analytical model and the numerical model (both for $z_c = -50$ cm and $z_c = -150$ cm) for all nine combinations of climate and soil type listed in Tables 5.1 and 5.2. The differences in the partitioning of water over the budget terms (as a fraction of rainfall) between the analytical and the numerical model with $z_c = -50$ cm are due to the omission of redistribution in the analytical model. Although redistribution certainly affects the partitioning, the agreement between the analytical and the numerical model is satisfactorily. As could be expected beforehand, for both models the fraction of evapotranspiration decreases when the climate becomes more humid and/or the soil becomes sandier. The analytical model captures surface runoff quite well, despite its small fraction of the

water budget. The occurrence of runoff for nearly all cases in the analytical model relates to occasional saturation of the reservoir and disappears for a deeper soil reservoir. With the exception of the loam soil with arid climate (C/A), evapotranspiration is underestimated by the analytical model, for reasons explained later on.

The importance of upward capillary flow can be inferred from comparing the numerical results obtained using $z_c = -50$ cm and $z_c = -150$ cm. Not surprisingly, the magnitude of upward capillary flow is largest for the clay soil and the arid climate. In general, the contribution of capillary flow is relatively minor, which justifies the omission of deeper layers in the analytical model. It is important to note that when a groundwater table is maintained at the lower boundary rather than allowing for free drainage, the contribution of upward capillary flow cannot be neglected.

In Fig. 5.5, the transient behavior of the saturation degree for a 200 day period of the analytical and the numerical model ($z_c = -50$ cm) are depicted using the loam soil and the semi-humid climate (L/SH). The depletion of soil water after a

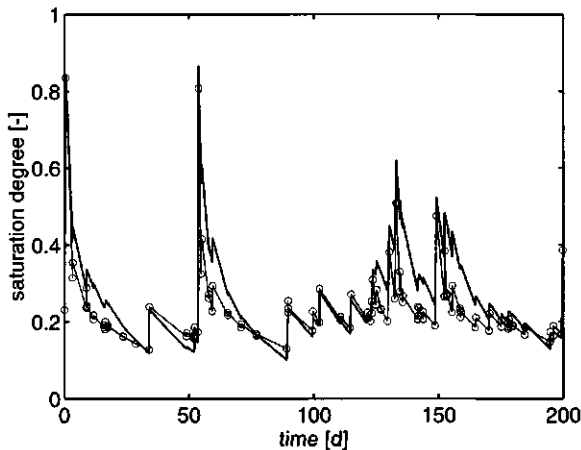


Figure 5.5: Transient saturation degree for the loam soil and the semi-humid climate (L/SH) corresponding to the analytical model (o) and the numerical model using $z_c = -50$ cm (solid line).

rainfall event is faster for the analytical model in comparison with the numerical model. The explanation is that in the analytical solution infiltrated water becomes equally available for both evapotranspiration and percolation. Percolation therefore starts immediately after rainfall has ceased. This is in contrast with the numerical model in which a wetting front propagates through the soil column and percolation comes into effect with some delay. Since at high saturation degrees percolation is much more efficient in removing water than evapotranspiration, the

above reasoning also explains the underestimation of mean evapotranspiration in Fig. 5.4 (with the exception of the loam soil with arid climate).

Finally, the event cumulative evapotranspiration of the numerical model and the analytical solutions for all interstorms during a 5 year simulation are shown in Fig. 5.6. The results are close to the 1:1 line. The bias in the analytical model

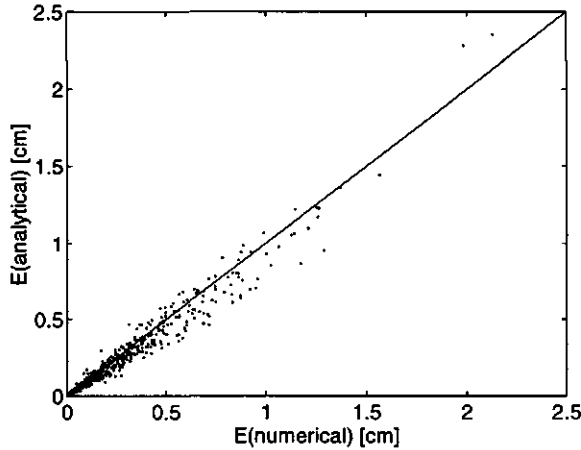


Figure 5.6: Cumulative evapotranspiration E^{cum} for all interstorm periods during a 5 year period for the loam soil and the semi-humid climate (L/SH) as simulated by the analytical model and the numerical model with $z_c = -50$ cm. The root mean square error \mathfrak{R} defined by (A.24) is 0.27 cm.

towards too low evapotranspiration amounts can be observed. The overestimation of the analytical model for very high evapotranspiration amounts is associated with very long interstorm periods. As can be seen in Fig. 5.5, for a long interstorm period (e.g. day 50 - 90), the soil water depletion rate becomes smaller for the analytical model compared to the numerical model. This also explains the slight overestimation of the long-term mean evapotranspiration for the loam soil and the arid climate (L/A) in Fig. 5.4, since the mean interstorm duration $\mu[\underline{t}_b]$ of the arid climate is long (Table 5.1).

The agreement with numerical results indicates that the presented framework of analytical solutions represents the intermittent wetting and drying of the soil reservoir satisfactorily. Therefore, this framework allows analysis of some fundamental questions. Its computational efficiency enables the study of the sensitivity of the fluxes to the various soil hydraulic and climate parameters and the effects of spatial variability of these parameters for long time integrations.

5.5 Influence of soil parameters and their heterogeneity on the soil water budget

5.5.1 Sensitivity of the analytical solutions

A logical first step in analyzing the behavior of the suggested solutions is to consider their sensitivities to the soil parameters k_s, ψ_s, θ_s and m and the reservoir depth d_r . Using the scaling relationships (5.34) and (5.35) the influences of k_s and ψ_s are investigated simultaneously using the soil scale factor α and the relationships (5.34) and (5.35) and are thus assumed to be perfectly correlated.

Sensitivity of the soil water budget to θ_s and d_r

From (5.16), (5.30) and (5.32) it follows that the product of θ_s and d_r determines the storage of the soil reservoir and that the corresponding model sensitivities for both parameters are identical, with the exception that θ_s also slightly affects i^{cum} through (5.8) and (5.15). It appears that the sensitivity of the long-term mean (15 years) water budget terms to the reservoir storage is small. This can be readily explained with Fig. 5.7. Given a certain amount of water in the reservoir w ,

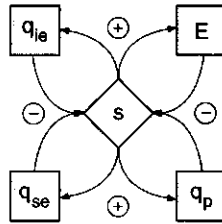


Figure 5.7: Diagram of the feedbacks between soil moisture saturation degree s and the fluxes in the water budget: infiltration excess runoff (q_{ie}), saturation excess runoff (q_{se}), evapotranspiration (E) and percolation (q_p).

increasing either d_r or θ_s results in a smaller value of s (here $\frac{w}{d_r \theta_s}$). This causes all four fluxes to become smaller because of their positive dependence on s , which in return increases the filling up and decreases the depletion of the reservoir. Hence, except for very small values of $d_r \theta_s$, the system tries to restore itself towards an “equilibrium” value of s and the overall feedback is strongly negative. The dependence of i^{cum} on θ_s works in the same direction (an increase in θ_s leads to an increase in S_r through (5.8) and to an increase in i^{cum} through (5.15)) and thus enhances the negative feedback.

These results are in line with the small dependence of the annual water budget on θ_s as found in Chapter 4 and reported by Milly and Eagleson [62, 1987]. It is important to note that although the long-term mean water budget is not very sensitive to the reservoir storage, this is not the case for the transient behavior.

Sensitivity of the water budget to α and m

Infiltration is dominated by the value of k_s , which is determined by the value of the soil scale factor α and the scaled average value k_s^{ref} . The exponent m only slightly influences the infiltration rate through (5.8). The partitioning of infiltrated water over evapotranspiration and percolation is governed by both α and m . The latter determines the rate at which percolation declines in (5.20). Thus on the time scale of one (inter)storm the soil scale factor governs the infiltration amount whereas the partitioning of infiltrated water over evapotranspiration and percolation is determined by both α and m . However, because the initial condition of a storm period is determined by the processes during the interstorm period and vice versa, the sensitivity of the long-term mean water budget to α and m is more complex.

Fig. 5.8 shows the sensitivity the ratio $\frac{\bar{E}}{\bar{P}}$ to scale factor α and exponent m for all nine combinations of soil and climate. For $\alpha = 1$ and the values of m in Table 5.2,

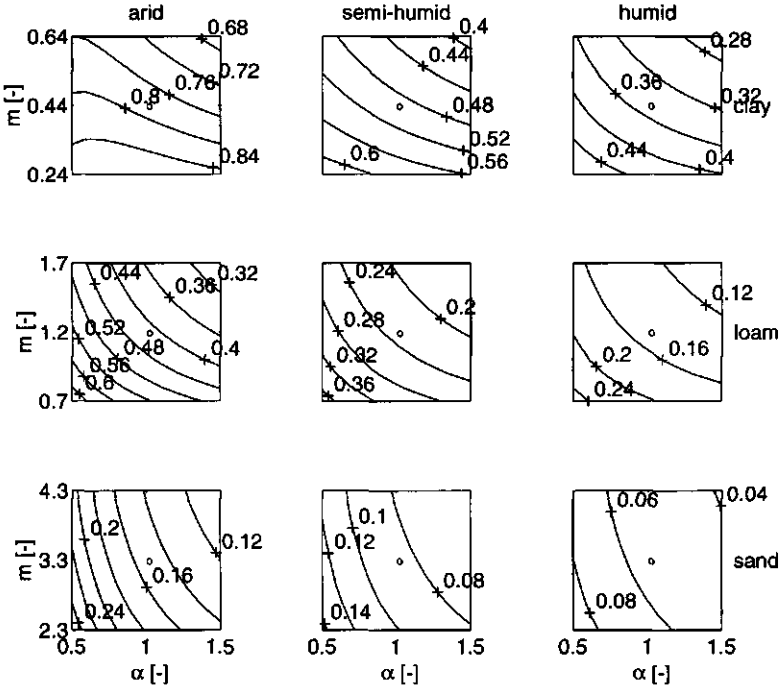


Figure 5.8: Sensitivity of the ratio $\frac{\bar{E}}{\bar{P}}$ on scale factor α and exponent m for all 9 combinations of climate and soil listed in Tables 5.1 and 5.2. The contour lines are indicated by (+). Results of Fig. 5.4 are indicated by (o).

the cases corresponding to Fig. 5.4 are obtained. The general trend in Fig. 5.8 is that the ratio $\frac{\bar{E}}{\bar{P}}$ decreases with increasing values of α and m . This can be

explained by (5.20): the percolation becomes larger with increasing values of k , (and α accordingly) and m . Only for the arid climate and the clay soil, $\frac{\bar{E}}{P}$ decreases for small values of α . This reflects the fact that small infiltration rates limit the recharging of the reservoir. Thus for evapotranspiration an “infiltration limited” ($\alpha \rightarrow 0$) and a “percolation limited” ($\alpha \rightarrow \infty$) regime can be distinguished. The two regimes are more clearly visible in Fig. 5.9, to be discussed in the following section.

5.5.2 Sensitivity of the water budget to soil heterogeneity

In Chapter 4 it was shown that soil heterogeneity, represented by a distribution function of the soil scale factor, increased the areally average surface runoff due to the less permeable soil columns that are more frequent in the lognormal distribution. As a consequence, the water availability for evapotranspiration and percolation was reduced. Spatial heterogeneity of the water budget was thus mainly caused by variation in infiltration, which is mostly governed by the saturated conductivity or, accordingly, the soil scale factor. In addition to variability of α , here spatial variation of m is regarded as well. As was clarified in the previous section, the exponent m mainly affects the partitioning of water over evapotranspiration and percolation.

In order to analyze the effect of simultaneous variation of α and m on the areally average ratio $\frac{\hat{\mu}[E]}{P}$ quantitatively, computations were carried out as illustrated in Fig. 5.9. The ratio $\frac{\hat{\mu}[E]}{P}$ is determined as described in Appendix A.2:

$$\frac{\hat{\mu}[E]}{P} = \frac{1}{NP} \sum_{i=1}^N \bar{E}(\alpha_i, m_i) \quad (5.36)$$

where the 15 year average ratio $\frac{\bar{E}}{P}$ as a function of α and m is shown in Fig. 5.9c.

For all nine combinations of soil and climate, 121 evenly spaced points in the $\mu[\underline{\alpha}] - \mu[\underline{m}]$ plane were selected. For each point, 250 realizations (N) were made. The values $\sigma[\ln \underline{\alpha}]$ and $\sigma[\ln \underline{m}]$ were set to 1.0 and 0.4 respectively and the values $\mu[\ln \underline{\alpha}]$ and $\mu[\ln \underline{m}]$ were determined using (A.13). It must be borne in mind that changing the value of $\mu[\ln \underline{\alpha}]$ is equivalent to changing the reference soil hydraulic properties k_s^{ref} and ψ_s^{ref} . The ratio of $\sigma[\ln \underline{\alpha}]$ and $\sigma[\ln \underline{m}]$ is in accordance with Milly and Eagleson [62, 1986], but, as they state, is of no universal significance. Note that $\sigma[\underline{\omega}]$ in (A.14) depends on $\sigma[\ln \underline{\omega}]$ and $\mu[\ln \underline{\omega}]$ and thus on $\mu[\underline{\omega}]$. Since both $\sigma[\ln \underline{\alpha}]$ and $\sigma[\ln \underline{m}]$ are assumed constant, the standard deviations of α and m depend on the particular values of $\mu[\underline{\alpha}]$ and $\mu[\underline{m}]$. The graphs in Fig. 5.10 show the ensemble mean ratio $\frac{\hat{\mu}[E]}{P}$ as a function of $\mu[\underline{\alpha}]$ and $\mu[\underline{m}]$. The differences between ratio $\frac{\bar{E}}{P}$ in Fig. 5.8 and ratio $\frac{\hat{\mu}[E]}{P}$ in Fig. 5.10 are due to soil

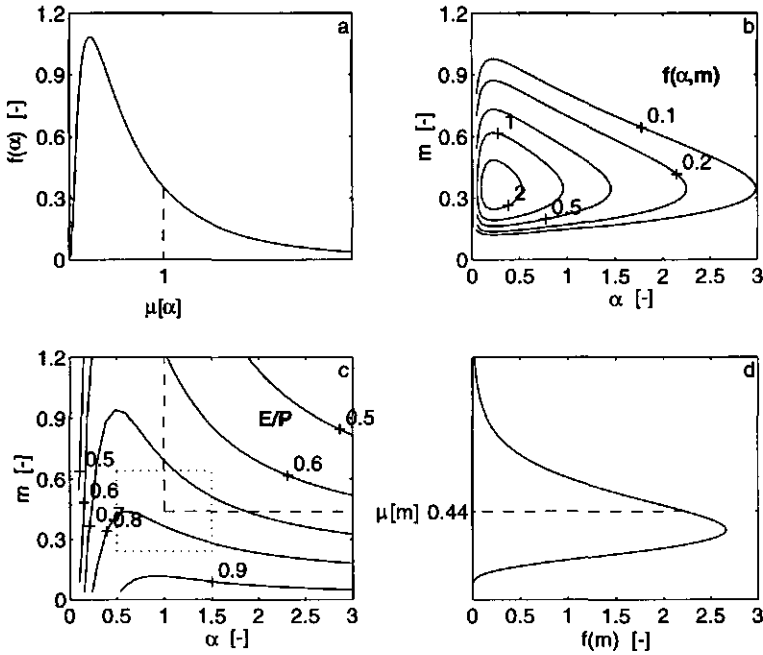


Figure 5.9: Diagram illustrating the determination of the ensemble mean ratio $\frac{\hat{\mu}[E]}{P}$ for $\mu[\alpha] = 1$ and $\mu[m] = 0.44$ for the arid climate. 250 (α, m) points are randomly selected according to their joint density function $f_{\alpha, m}(\alpha, m)$ in b. For each point the ratio $\frac{E}{P}$ is determined from panel c. The dotted box in c. is identical to Fig. 5.8a. Because α and m are independent, $f_{\alpha, m}(\alpha, m) = f_{\alpha}(\alpha) \cdot f_m(m)$. The marginal density functions of α and m are shown in a. and d. respectively.

heterogeneity. Compared to ratio $\frac{\bar{E}}{P}$ in Fig. 5.8, ratio $\frac{\hat{\mu}[E]}{P}$ in Fig. 5.10 is smaller for the clay soil with the semi-humid climate and even more so for the clay soil with the arid climate. This can be readily explained when looking at Fig. 5.9. Most of the probability mass of $f_{\alpha, m}(\alpha, m)$ is located in the region $\alpha < \mu[\alpha]$ and $m < \mu[m]$ (see Fig. 5.9b) which corresponds to smaller ratios $\frac{E}{P}$ in Fig. 5.9c. For all other combinations $\frac{\hat{\mu}[E]}{P}$ increases relative to $\frac{\bar{E}}{P}$ due to heterogeneity. Because all of the rain infiltrates, the lognormal distribution of α causes the percolation of most realizations to be smaller than the spatial mean as most of the probability mass is associated with saturated conductivities smaller than the mean. This was already discussed in Chapter 4. Additionally, the conductivity decreases more rapidly with saturation degree because the lognormal distribution of m causes most realizations to have smaller m values than $\mu[m]$. This enhances the decrease in spatial average percolation. Thus under infiltration limited regime, soil hetero-

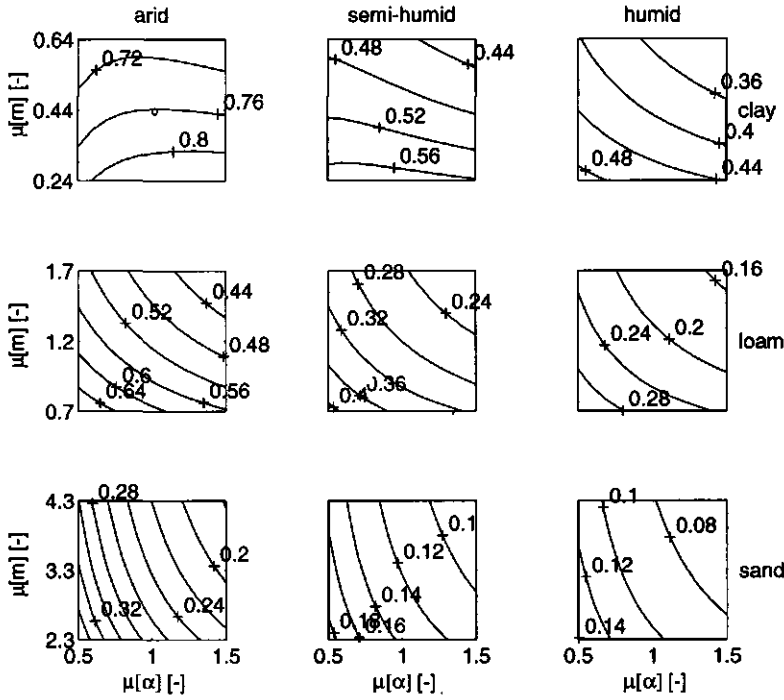


Figure 5.10: Sensitivity of the ensemble average ratio $\frac{\mu[E]}{P}$ on the mean scale factor $\mu[\alpha]$ and the mean exponent $\mu[m]$ for all 9 combinations of climate and soil listed in Tables 5.1 and 5.2. Differences with Fig. 5.8a are due to soil heterogeneity. The contour lines are indicated by (+). The result of the computations illustrated in Fig. 5.9 is indicated by (o).

generity reduces evapotranspiration and under "percolation limited" regime the soil heterogeneity increases evapotranspiration.

In contrast with what was said above, Milly and Eagleson [62, 1987] state that soil heterogeneity causes infiltration to increase rather than decrease for soils of low average permeability. Because most of the probability mass is associated with smaller scale factors than $\mu[\alpha]$, in the present solution such a situation will only occur when the increase in surface runoff is significantly less for smaller scale factors α than the decrease for larger scale factors.

5.6 "Equivalent" soil hydraulic characteristics

When the influence of soil heterogeneity can be taken into account through simulations using one "equivalent" soil, the need for computationally demanding

Monte Carlo simulations shown in Fig. 5.10 can be prevented. In Chapter 4 the presence of equivalent soil properties has already been briefly touched on. It appeared that for the sand soil used equivalent soil properties existed unlike for the loam soil. Here the issue of equivalent soil properties will be investigated in greater detail. Next, first the equation for an equivalent set of soil hydraulic parameters is derived. Afterwards the derivation of an equivalent set of soil properties is illustrated for the clay soil and the three climates.

5.6.1 Governing equations

When the proposed solutions are integrated over a certain time, the time average output of the model can be written as

$$\mathbf{F} = \mathbf{M}(\mathbf{H}, \mathbf{U}, \mathbf{C}) \quad (5.37)$$

where vector \mathbf{F} contains all non-zero and independent time average fluxes from \bar{q}_{se} , \bar{q}_{ie} , \bar{E} and \bar{q}_p , \mathbf{H} is a vector with the spatially heterogeneous soil parameters, \mathbf{U} contains the spatially uniform parameters, \mathbf{C} comprises the climate parameters and \mathbf{M} indicates the relationships between the time average fluxes in \mathbf{F} and the soil hydraulic and climatic parameters (i.e. the analytical solutions integrated over time). The conditions for \mathbf{F} reflect that the sum of all fluxes is equal to \bar{P} , yielding a maximum of three independent fluxes (or degrees of freedom). However, in case time average fluxes are 0 there are fewer degrees of freedom, for example, when all rainfall infiltrates, $\bar{q}_{se} = \bar{q}_{ie} = 0$ and there is only one independent flux, since for given \bar{P} knowledge of \bar{E} determines \bar{q}_p or vice versa.

Following Milly and Eagleson [62, 1987], an equivalent homogeneous set of parameters \mathbf{H}_e for any flux satisfies

$$\mu[\mathbf{F}] = \mathbf{M}(\mathbf{H}_e, \mathbf{U}, \mathbf{C}) \quad (5.38)$$

Approximation of (5.38) by the first two terms of a Taylor expansion around the mean parameter set $\mu[\mathbf{H}]$ yields

$$\mu[\mathbf{F}] = \mathbf{M}(\mu[\mathbf{H}], \mathbf{U}, \mathbf{C}) + \frac{\partial \mathbf{M}(\mu[\mathbf{H}], \mathbf{U}, \mathbf{C})}{\partial \mathbf{H}} (\mathbf{H}_e - \mu[\mathbf{H}]) + O^2 \quad (5.39)$$

where $\frac{\partial \mathbf{M}(\mu[\mathbf{H}], \mathbf{U}, \mathbf{C})}{\partial \mathbf{H}}$ denotes the Jacobian matrix.

Similarly, expanding (5.37) in a Taylor series around the mean parameter set $\mu[\mathbf{H}]$ and taking the expected value yields

$$\mu[\mathbf{F}] = \mathbf{M}(\mu[\mathbf{H}], \mathbf{U}, \mathbf{C}) + \frac{1}{2} \sum_{i=1}^n \sum_{j=1}^n \frac{\partial^2 \mathbf{M}(\mu[\mathbf{H}], \mathbf{U}, \mathbf{C})}{\partial H_i \partial H_j} R_{ij} + O^3 \quad (5.40)$$

with the covariance matrix $\mathbf{R} = \mu[(\mathbf{H} - \mu[\mathbf{H}])(\mathbf{H} - \mu[\mathbf{H}])^T]$ and n the dimensionality of the vector \mathbf{H} .

When the inverse of the matrix $\frac{\partial \mathbf{M}(\mu[\mathbf{H}], \mathbf{U}, \mathbf{C})}{\partial \mathbf{H}}$ exists (i.e. the dimensionality of \mathbf{M} and \mathbf{H} are equal) and is non-singular, the right hand sides of (5.39) and (5.40) can be solved for \mathbf{H}_e :

$$\mathbf{H}_e = \mu[\mathbf{H}] + \left(\frac{\partial \mathbf{M}(\mu[\mathbf{H}], \mathbf{U}, \mathbf{C})}{\partial \mathbf{H}} \right)^{-1} \left(\frac{1}{2} \sum_{i=1}^n \sum_{j=1}^n \frac{\partial^2 \mathbf{M}(\mu[\mathbf{H}], \mathbf{U}, \mathbf{C})}{\partial H_i \partial H_j} R_{ij} \right) \quad (5.41)$$

It is important to note that the omission of higher order terms only holds for small variances of the parameters.

From (5.41) it follows directly that an equivalent set of parameters depends on the specific climate and the spatially uniform parameters, in addition to the obvious dependence on the mean, variance and covariance of the spatially variable parameters. The equal dimensionality of \mathbf{M} and \mathbf{H} implies that the number of equivalent parameters is equal to the number of independent fluxes. As mentioned before, from the four fluxes at the most three are independent.

5.6.2 Determination of "equivalent" soil hydraulic characteristics; an example

As an example, the equivalent properties are determined using (5.41) for the clay soil and the three climates in Table 5.1 and the integration time of 15 years. Soil heterogeneity is due to variation of the scale factor α and the exponent m that are assumed to be independent (off diagonal terms in the covariance matrix \mathbf{R} are 0). The simultaneous determination of two equivalent parameters requires exactly two independent time average fluxes. Because q_{se} is absent or very small for most combinations of α and m , here \bar{q}_{ie} and \bar{E} are taken as independent and $\bar{q}_p = \bar{P} - \bar{q}_{ie} - \bar{E}$.

In Fig. 5.11 the equivalent parameters α_e and m_e are shown as a function of $\mu[\alpha]$ and $\mu[m]$ taking $\sigma[\alpha] = 0.5$ and $\sigma[m] = 0.2$. For the arid and semi-humid climate the results correspond to intuition. The α_e values are smaller than the mean values $\mu[\alpha]$ since the lognormal distribution is positively skewed and most of the probability mass is associated with α values smaller than $\mu[\alpha]$. In general, the dependencies of α_e on $\mu[m]$ and, vice versa, α_e on $\mu[\alpha]$ are small. The not entirely smooth behavior of the contour lines is due to the limited numerical accuracy in the determination of the Jacobian matrix. The strange result for the humid climate can be explained by the occasional occurrence of saturation excess runoff q_{se} and the small magnitude of infiltration excess runoff q_{ie} which cause (5.41) to be ill posed. From Fig. 5.11 it is clear that the equivalent parameters α_e and m_e depend on the climate under consideration.

In order to investigate the validity of (5.41), the water budget associated with the equivalent parameters α_e and m_e for $\mu[\alpha] = 1$ and $\mu[m] = 0.44$ in Fig. 5.11 is com-

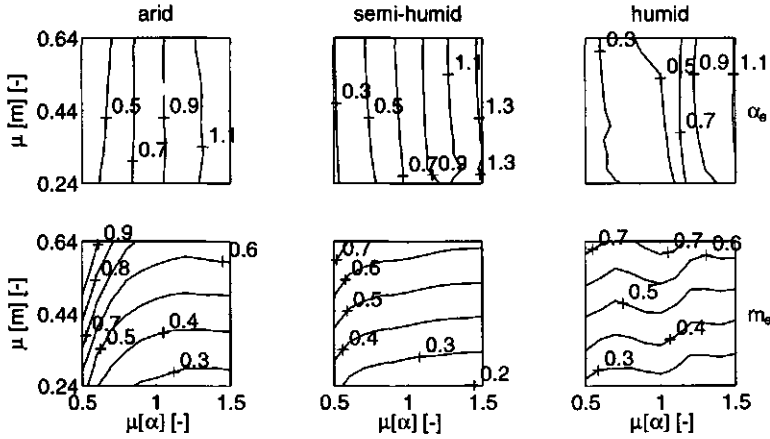


Figure 5.11: Equivalent parameters α_e and m_e according to (5.41) as a function of $\mu[\underline{\alpha}]$ and $\mu[\underline{m}]$ for the clay soil and the three climates. Contour lines are indicated by (+). $\sigma[\underline{\alpha}] = 0.5$ and $\sigma[\underline{m}] = 0.2$.

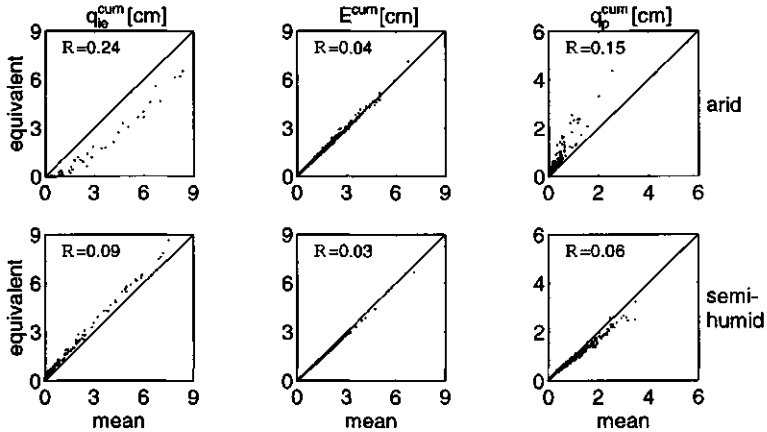


Figure 5.12: Areally mean and equivalent cumulative infiltration excess runoff (q_e^{cum}), evapotranspiration (E^{cum}) and percolation (q_p^{cum}) for all (inter)storm periods during a 15 year simulation for the arid and the semi-humid climate. $\mu[\underline{\alpha}] = 1$ and $\mu[\underline{m}] = 0.44$. The values of the root mean square error \mathfrak{R} [cm] according to (A.24) are indicated.

pared with the corresponding mean water budget derived by Monte Carlo simulation. The cumulative amounts of infiltration excess runoff, evapotranspiration and percolation over all (inter)storm periods during a 15 year simulation are shown in Fig. 5.12 for the arid and semi-humid climate. In Fig. 5.12 it can be seen that the water budget components using the equivalent parameters agree

reasonably well with the areally mean values for the semi-humid climate but not for the arid climate. Because of the bias in the q_{ie}^{cum} and q_p^{cum} values, the 15 year average equivalent and spatially mean water budget are different. Apparently, the omission of higher order terms in (5.41) is not justified for the arid climate and the values applied for $\sigma[\underline{\alpha}]$ and $\sigma[\underline{m}]$. This can be visualized by considering Fig. 5.8. For the clay soil and the arid climate the derivatives $\frac{d\bar{E}}{d\alpha}$ and $\frac{d\bar{E}}{dm}$ evaluated for $\alpha = 1$ and $m = 0.44$ differ greatly from the derivatives for smaller α and m values, with respect to magnitude as well as sign. The differences are much smaller for the semi-humid climate. Note that when \bar{E} is a linear function of α and m , the derivatives $\frac{d\bar{E}}{d\alpha}$ and $\frac{d\bar{E}}{dm}$ remain constant and higher order derivatives are zero. In that case (5.41) and the resulting equivalent parameters are exact.

Since infiltration excess runoff increases with decreasing values of scale factor α whereas percolation decreases, the cumulative interstorm evapotranspiration values associated with the Monte Carlo simulations and the equivalent parameters agree very well. This is in agreement with the temporal behavior of evapotranspiration of the equivalent soils in Figs. 4.5 and 4.6. When the interest is mainly on reliable estimates of evapotranspiration fluxes, as is the case in climate modeling, this is an important result.

Because of the opposing effects of soil scale factor α on infiltration excess runoff and percolation, for the arid climate undoubtedly better equivalent parameters could be found through inverse modeling. This, however, requires a priori knowledge of the effect of soil heterogeneity on the water budget (i.e. information of the kind present in Fig. 5.10). This is in contrast with (5.41) for which only the sensitivity of the water budget components to changing parameters needs to be known (i.e. information like present in Fig. 5.8).

It is important to note that even when equivalent parameters would describe the long-term average water budget perfectly, this is not necessarily true for shorter time scales, as illustrated for infiltration i using the simple diagram in Fig. 5.13. Shown are the transient infiltration rates for two geometrically similar clay soils with α values of $2^{-\frac{1}{2}}$ and $2^{\frac{1}{2}}$. An equivalent soil has to behave identical to the average of the two curves $\mu[\underline{i}]$, which is also shown. The two ponding times cause the average curve to be non-differentiable at two points, which can never be the case for one (equivalent) soil. Since for $t \rightarrow \infty$ the infiltration in (5.5) goes to ak_s , the mean infiltration rate approaches $a\mu[k_s]$. By virtue of (5.35) this corresponds with $\alpha = (\mu[\underline{\alpha}^2])^{1/2}$ for which the infiltration rate is depicted as well in Fig. 5.13.

Fig. 5.13 allows the conclusion that representing the areally average transient infiltration by means of an equivalent soil is most problematic when the area is partly ponded and partly unponded. Unfortunately, rainfall duration is hardly ever long enough to cause ponding over an extended area. Likewise, the appealing concept of accounting for soil heterogeneity through one equivalent soil has only limited validity.

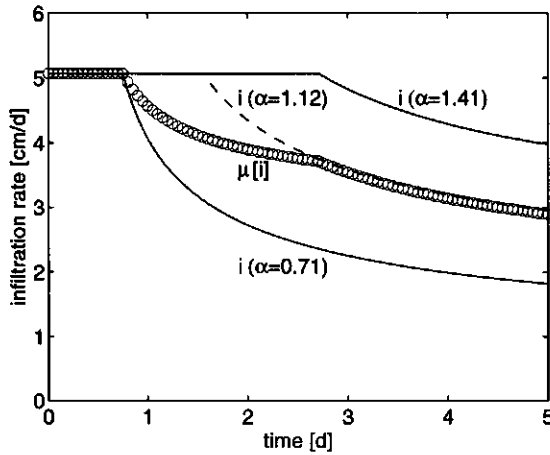


Figure 5.13: Infiltration rate vs. time. Mean infiltration $\mu[i]$ (o) for two clay soils with $\alpha = 2^{-\frac{1}{2}} \approx 0.71$ and $\alpha = 2^{\frac{1}{2}} \approx 1.41$ and the infiltration rate using $\alpha = (\mu[\alpha^2])^{1/2} \approx 1.12$. Rainfall $P = 5.07 \text{ cm d}^{-1}$.

5.7 Derived distributions for heterogeneous infiltration and evapotranspiration rates

So far, the focus has been on the effects of soil heterogeneity on the areally average water budget. In the following the distributions of spatially varying infiltration and evapotranspiration rates on the time scale of a storm event are derived analytically. The distribution functions provide much information on the nature of heterogeneity of the water budget components. Although the distribution function may easily be approximated through Monte Carlo simulation, the advantage of the analytical expressions discussed below is the direct physical insight that is obtained. Furthermore, the inevitable sampling errors in Monte Carlo simulation are avoided and the accuracy can easily be increased at almost no computational cost. The main drawback is that the distribution functions can only be derived for certain highly idealized conditions and that their time evolution can not be traced when boundary conditions change. In Table 5.3 the assumptions used in the derivation of the distributions are summarized.

Maller and Sharma [53, 1981] investigated the distribution $F_{\frac{1}{2}}(i|S, k_s)$ where sorptivity S and saturated conductivity k_s are assumed to be bivariate lognormally distributed. Thus, any functional dependence between S and k_s , like in (5.8), was not considered. Furthermore, they did not obtain analytical expressions. Sivapalan and Wood [94, 1986] obtained approximate expressions for the first two moments of $F_{\frac{1}{2}}(i|k_s)$ and implicit expressions for the first two moments of $F_{\frac{1}{2}}(i|P)$.

Table 5.3: Summary of the assumptions in the derivation of the probability density and distribution functions. $F_{\underline{y}}(y|\omega)$ denotes the distribution function of the variable y (infiltration i or evapotranspiration E) given the distribution of parameter ω .

Distribution	k_s	m	s_0	P	E_p
$F_{\underline{i}}(i k_s)$	lognormal	constant	constant	constant	-
$F_{\underline{i}}(i P)$	constant	constant	constant	lognormal	-
$F_{\underline{E}}(E k_s)$	lognormal	constant	constant	-	constant
$F_{\underline{E}}(E s_0)$	constant	constant	beta	-	constant

5.7.1 Derived distribution theory

In the following, frequent use is made of the derived distribution theory which is therefore briefly explained here. The essence of the theory is that given the process $y = g(\omega)$, the cumulative distribution function (cdf) and the probability density function (pdf) of \underline{y} are derived from the cdf and pdf of the random variable $\underline{\omega}$.

Consider the process $\underline{y}=g(\underline{\omega})$, where $g(\omega)$ is a monotonous function. For the cumulative distribution function (cdf) of \underline{y} the following holds [68, Papoulis 1991]:

$$\begin{aligned}
 F_{\underline{y}}(y) &= \Pr[\underline{y} \leq y] \\
 &= \Pr[\underline{\omega} \leq g^{-1}(y)] \\
 &= F_{\underline{\omega}}(g^{-1}(y))
 \end{aligned}
 \tag{5.42}$$

Here $g^{-1}(y)$ denotes the inverse relation of $g(\omega)$. For the probability density function (pdf) it follows that

$$\begin{aligned}
 f_{\underline{y}}(y) &= \frac{dF_{\underline{y}}(y)}{dy} \\
 &= \left| \frac{dg^{-1}(y)}{dy} \right| f_{\underline{\omega}}(g^{-1}(y))
 \end{aligned}
 \tag{5.43}$$

Although the equations in the sections that follow may look complex at a first glance, they can all be reduced to (5.42) or (5.43). The apparent complexity is due to the various inverse relations g^{-1} . From here onwards these will be indicated by $g_{1..6}$ for notational convenience.

5.7.2 Infiltration rate regarding spatially heterogeneous saturated hydraulic conductivity

In this section the saturated conductivity k_s is a lognormally distributed random variable. From (5.34), (5.35) and (5.8) it can be deduced that for geometrically similar soils, the sorptivity S scales with $\alpha^{\frac{1}{2}}$ rather than with α as is implicitly

assumed by accounting for heterogeneity of k_s only (and thus omitting heterogeneity of ψ_s). However, because the aim here is to obtain qualitative insight into the nature of heterogeneity for highly simplified situations, this inconsistency is not considered too severe.

In reality, the initial saturation degree at the onset of a storm event s_0 is spatially heterogeneous. Hence, in addition to the saturated conductivity, the variable S_r in (5.8) exhibits heterogeneity as well. Except for high saturation degrees, however, the functional dependence of S_r on s_0 is not too strong and is omitted here to allow explicit solutions. Furthermore, the contribution of the sorptivity term on the infiltration rate in (5.13) vanishes with increasing time. It should be noted though that the distribution of infiltration given the distribution of s_0 and spatially uniform saturated conductivity and rainfall rate can be derived explicitly, but is not included in this thesis for reasons of brevity. The behavior of

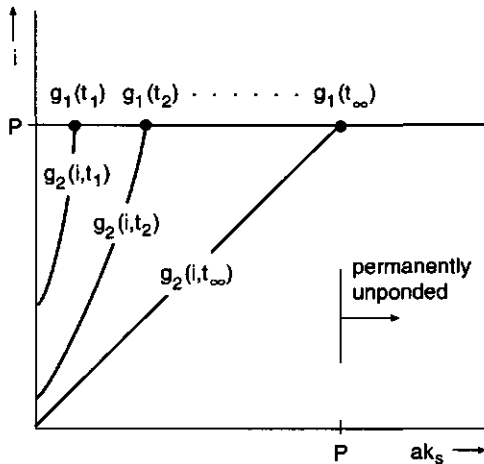


Figure 5.14: Diagram indicating the infiltration rate i versus the ak_s . The function $g_1(t)$ indicates the value of ak_s for which ponding occurs at t . The function $g_2(i, t)$ indicates the value of ak_s for which at time t infiltration occurs at a rate i .

the infiltration rate as a function of k_s for spatially uniform rainfall is illustrated in Fig. 5.14, where the infiltration rate i is depicted as a function of ak_s for different times t . When $t = 0$, infiltration is unponded everywhere and $i = P$ regardless of the value of ak_s . As time proceeds, ponding will occur for increasing values of ak_s , except for $ak_s \geq P$ where infiltration remains unponded. The value of ak_s for which ponding occurs at time t is indicated by $g_1(t)$ in Fig. 5.14. In the same figure, the function $g_2(i, t)$ indicates the value of ak_s for which ponded infiltration at time t occurs at a rate i . Ponded infiltration occurs at a rate smaller than P and approaches ak_s for $t \rightarrow \infty$. As previously mentioned, this behavior is an

artifact resulting from (5.5), which is only valid for short times as was mentioned upon its introduction. In reality the infiltration rate approaches the saturated conductivity k_s (i.e. $a = 1$). Despite the fact that unless $a = 1$ (5.5) does not hold for $t \rightarrow \infty$ the following expressions describe the governing mechanisms qualitatively correct.

Given the very different nature of ponded and unponded infiltration in (5.13), first the pdf and cdf of the ponded fraction are derived. Inverting (5.11) yields $g_1(t_p)$ which indicates the saturated conductivity of the soil that ponds at time t_p (see Fig. 5.14)

$$g_1(t_p) = \frac{P}{a} \left(1 - \frac{S_r}{(4Pt_p - S_r^2)^{\frac{1}{2}}} \right) \quad (5.44)$$

The associated derivative with respect to t_p reads

$$\frac{dg_1(t_p)}{dt_p} = \frac{2P^2 S_r}{a(4Pt_p - S_r^2)^{\frac{3}{2}}} \quad (5.45)$$

Using (5.43) and (A.11), the pdf of ponding time reads

$$f_{t_p}(t_p) = \left| \frac{dg_1(t_p)}{dt} \right| \frac{1}{(2\pi)^{\frac{1}{2}} \sigma [\ln k_s] g_1(t_p)} \exp \left(- \left[\frac{\ln g_1(t_p) - \mu [\ln k_s]}{2^{\frac{1}{2}} \sigma [\ln k_s]} \right]^2 \right) \quad (5.46)$$

At a certain time t_p the fraction $F(t_p)$ of the total area where k_s values are smaller than $g_1(t_p)$ will have ponded. Using (A.12) this can be expressed as

$$\begin{aligned} F_{t_p}(t_p) &= \int_0^{g_1(t_p)} f_{k_s}(k) dk \\ &= F_{k_s}(g_1(t_p)) \\ &= \frac{1}{2} \left[1 + \operatorname{erf} \left(\frac{\ln g_1(t_p) - \mu [\ln k_s]}{2^{\frac{1}{2}} \sigma [\ln k_s]} \right) \right] \end{aligned} \quad (5.47)$$

The relations (5.46) and (5.47) were derived by Sivapalan and Wood [94, 1986].

In order to derive the pdf and cdf of the ponded infiltration rate, the inverse relation, $g_2(i, t)$, of (5.13) for $t > t_p$ has to be obtained. By omitting the dependence of $(t - t_c)^{-\frac{1}{2}}$ on k_s in (5.12), the approximate inversion of (5.13) and its derivative with respect to i can be expressed explicitly as

$$g_2(i, t) = \frac{i}{a} + \frac{S_r^2}{8a^2(t - t_c)} \left(1 - \left[\frac{16ia(t - t_c)}{S_r^2} + 1 \right]^{\frac{1}{2}} \right) \quad (5.48)$$

$$\frac{dg_2(i, t)}{di} = \frac{1}{a} \left(1 - \left[\frac{16ia(t - t_c)}{S_r^2} + 1 \right]^{-\frac{1}{2}} \right) \quad (5.49)$$

The meaning of $g_2(i, t)$ is indicated in Fig. 5.14. Insertion of (5.48) and (5.49) into (5.43) yields the pdf of the infiltration rate for the ponded area.

$$f_{\dot{i}}(i; t) = \left| \frac{dg_2(i, t)}{di} \right| \frac{1}{(2\pi)^{\frac{1}{2}} \sigma [\ln k_s] g_2(i, t)} \exp \left(- \left[\frac{\ln g_2(i, t) - \mu [\ln k_s]}{2^{\frac{1}{2}} \sigma [\ln k_s]} \right]^2 \right) \quad (5.50)$$

Over the unponded area the infiltration rate is equal to the rainfall rate and has a probability of $1 - F_{\dot{i}_p}(t)$, where $F_{\dot{i}_p}(t)$ is given by (5.47)

$$\Pr [\dot{i}(t) = P] = \frac{1}{2} \left[1 - \operatorname{erf} \left(\frac{\ln g_1(t) - \mu [\ln k_s]}{2^{\frac{1}{2}} \sigma [\ln k_s]} \right) \right] \quad (5.51)$$

Substituting (5.48) and (A.12) into (5.42) and accounting for the infiltration in the unponded area results in the cdf

$$F_{\dot{i}}(i; t) = \frac{1}{2} \left[1 + \operatorname{erf} \left(\frac{\ln g_2(i, t) - \mu [\ln k_s]}{2^{\frac{1}{2}} \sigma [\ln k_s]} \right) \right] + \frac{H(i - P)}{2} \left[1 - \operatorname{erf} \left(\frac{\ln g_1(t) - \mu [\ln k_s]}{2^{\frac{1}{2}} \sigma [\ln k_s]} \right) \right] \quad (5.52)$$

where the Heaviside function $H(x) = 1$ for $x \geq 0$ and 0 otherwise. The first term in (5.52) represents the probability density for the ponded fraction, the second part the probability mass associated with the unponded fraction.

The most important constraint when using the approximate relation (5.48) is that $F_{\dot{i}}(P; t)$ has to integrate to 1, so that no probability mass is lost or generated. It is clear from (5.52) that this can be enforced by equating $g_1(t)$ and $g_2(P, t)$ using the term t_c as a closure term. Application of (5.44) and (5.48) yields

$$t_c(t) = t - \frac{S_r^2 g_1(t)}{4(P - a g_1(t))^2} \quad (5.53)$$

Because of this closing procedure t_c becomes a function of time. When comparing (5.53) and (5.9) it follows that $t - t_c(t)$ is similar to the definition of the equivalent time t_e . This is not surprising because $g_1(t)$ indicates the saturated conductivity of the soil that ponds at time t and because of (5.12) it holds that $t - t_c(t) = t_e$.

It can be shown that $t_c(t)$ is always larger than the real compressed time t_c according to (5.12). Overestimation of t_c means that the time axis in Fig. 5.1 is shifted further backwards so that the estimated infiltration rates are always higher than the actual rates. However, for most times this bias is small because the compression time t_c is small relative to t .

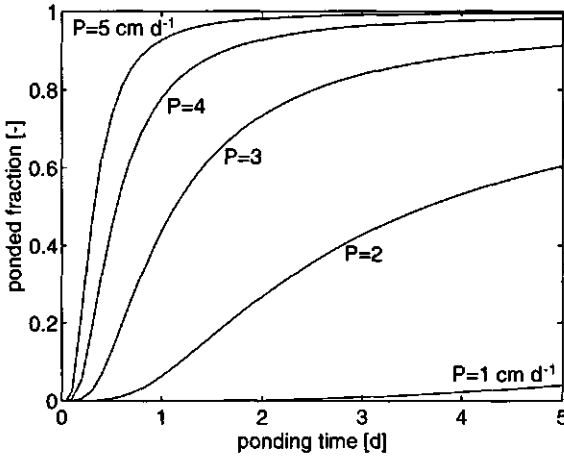


Figure 5.15: Poned fraction $F_{I_p}(t_p)$ in (5.47) as a function of ponding time for different rainfall rates for the clay soil with heterogenous saturated conductivity. $\mu [k_s] = 2.94 \text{ cm d}^{-1}$, $\sigma [k_s] = 1.57 \text{ cm d}^{-1}$ and the initial saturation degree $s_0 = 0.5$.

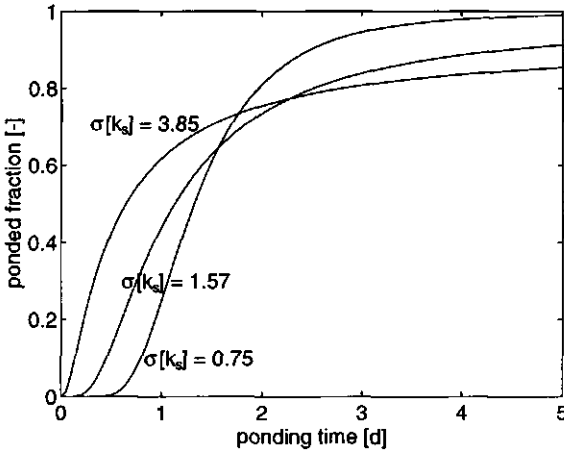


Figure 5.16: Poned fraction $F_{I_p}(t_p)$ in (5.47) as a function of ponding time for the clay soil with heterogenous saturated conductivity with different values of $\sigma [k_s]$. $\mu [k_s] = 2.94 \text{ cm d}^{-1}$, $P = 3 \text{ cm d}^{-1}$ and the initial saturation degree $s_0 = 0.5$.

In Fig. 5.15 the poned fraction is plotted as a function of time for different rainfall rates P . As could have been expected beforehand, the poned fraction increases faster for higher rainfall rates and approaches a higher value asymptotically. The behavior of the relations described above is illustrated for the clay

soil taking $\mu[\ln k_s] = 0.953$ and $\sigma[\ln k_s] = 0.5$. By virtue of (A.13) and (A.14) this results in $\mu[k_s] = 2.94 \text{ cm d}^{-1}$ and $\sigma[k_s] = 1.57 \text{ cm d}^{-1}$ which corresponds to the values in Table 5.2. The initial saturation degree $s_0 = 0.5$. Fig. 5.16 illustrates the influence of the degree of heterogeneity on the transient behavior of the ponded fraction for $\sigma[\ln k_s]$ values of 0.25, 0.5 and 1.0 (corresponding to $\sigma[k_s]$ values of 0.75, 1.57 and 3.85 cm d^{-1} respectively), while maintaining $\mu[k_s] = 2.94 \text{ cm d}^{-1}$ and $P = 3 \text{ cm d}^{-1}$. Because of the higher variance, the probability mass for both small and large values of k_s increases. Therefore, the ponded fraction increases faster with increasing $\sigma[k_s]$, but asymptotically approaches a smaller value. Note that when $\sigma[k_s] = 0$, the soil is uniform and the entire area ponds at

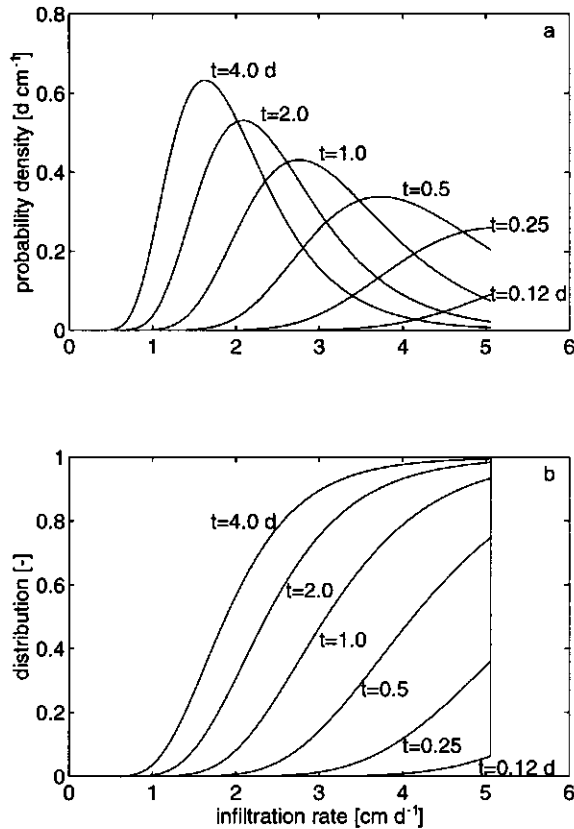


Figure 5.17: Time evolution of (a) the probability density function $f_1(i; t)$ in (5.50) and (b) the cumulative distribution function $F_1(i; t)$ in (5.52) for the clay soil with heterogeneous saturated conductivity. $\mu[k_s] = 2.94 \text{ cm d}^{-1}$, $\sigma[k_s] = 1.57 \text{ cm d}^{-1}$, rainfall rate $P = 5.07 \text{ cm d}^{-1}$ and initial saturation degree $s_0 = 0.5$.

the same time. In that case, $f_{\underline{P}}(t_p)$ would become a Dirac function with a spike of probability at t_p .

In Fig. 5.17 the probability density function $f_{\underline{i}}(i; t)$ in (5.50) and the cumulative distribution function $F_{\underline{i}}(i; t)$ in (5.52) are depicted for rainfall rate $P = 5.07 \text{ cm d}^{-1}$, corresponding to $\mu[\underline{P}]$ for the semi-humid climate in Table 5.1. At $t = 0$ (not shown) all probability mass lies at $i = P$ since no soil has ponded yet. When time proceeds, soils with low saturated conductivities start to pond and probability mass moves towards smaller infiltration rates. Because of (5.5), in the ponded region $i(\infty) = ak_s$ and, accordingly, $f_{\underline{i}}(i; \infty) = \frac{1}{a} f_{k_s}(\frac{k_s}{a})$. From this it is clear that for $a = 1$ the pdf of the infiltration rate approaches the pdf of saturated conductivity.

5.7.3 Infiltration rate regarding spatially heterogeneous rainfall rate

In this section it is assumed that the saturated conductivity is spatially homogeneous and that the rainfall rate is a lognormally distributed random variable. Fig. 5.18 illustrates that this situation is fundamentally different from the pre-

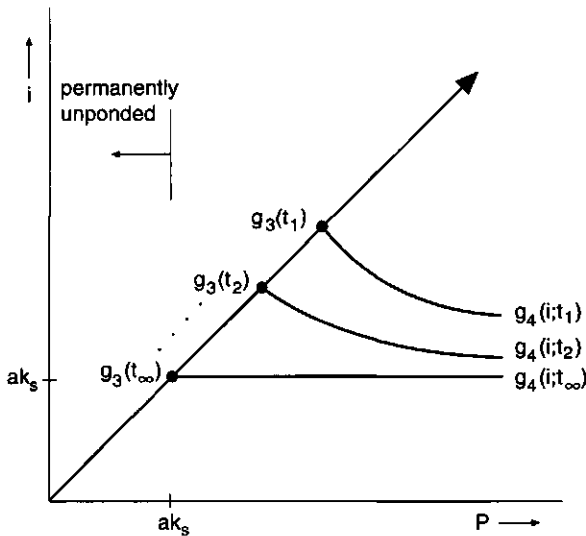


Figure 5.18: Diagram indicating the infiltration rate i versus the rain rate P . The function $g_3(t)$ indicates the value of P for which ponding occurs at time t . The function $g_4(i, t)$ indicates the value of P for which at time t infiltration occurs at a rate i .

vious case of heterogeneous saturated conductivity. When $t = 0$, infiltration is unponded regardless of the value of P . With increasing time, ponding occurs first

for the highest rainfall rates. This is indicated by $g_3(t)$ which represents the value of P for which ponding occurs at time t . Note that the maximum infiltration intensity decreases with time and is always equal to the rainfall rate that causes ponding. For $t \rightarrow \infty$ infiltration remains unponded when $P \leq ak_s$. The function $g_4(i, t)$ in Fig. 5.18 represents the value of P for which at time t infiltration occurs at a rate i . For $t \rightarrow \infty$ and $P > ak_s$ the infiltration rate i approaches ak_s . It is important to realize that for $t > 0$ any infiltration rate $ak_s < i < g_3(t)$ occurs for two different rainfall rates P : one in the ponded region and one in the unponded fraction.

Following the same procedure as before, first the pdf and cdf of ponding time t_p are derived. In order to do so, the inverse of (5.11), $g_3(t_p)$, has to be derived. In essence this means solving a third order polynomial in P . Of the three possible inverse relations only one is physically realistic:

$$g_3(t_p) = 2 \left(\frac{-\zeta}{3} \right)^{\frac{1}{2}} \cos \left(\frac{1}{3} \arccos \left(\left[\frac{27\xi^2}{-4\zeta^3} \right]^{\frac{1}{2}} \right) \right) + \frac{2}{3} ak_s \quad (5.54)$$

where

$$\zeta = -\frac{(ak_s)^2}{3} - \frac{S_r^2 k_s}{2t_p}$$

$$\xi = \frac{2(ak_s)^3}{27} - \frac{a(S_r k_s)^2}{12t_p}$$

The inverse relation $g_3(t_p)$ indicates the rainfall rate for which ponding occurs at time t_p and is the highest infiltration rate present over the area as shown in Fig. 5.18. Ponded infiltration occurs for $P \geq g_3(t_p)$ and the expression for the ponded fraction thus becomes

$$F_{t_p}(t_p) = 1 - \int_0^{g_3(t_p)} f_P(P) dP$$

$$= \frac{1}{2} \left[1 - \operatorname{erf} \left(\frac{\ln g_3(t_p) - \mu[\ln P]}{2^{\frac{1}{2}} \sigma [\ln P]} \right) \right] \quad (5.55)$$

In the ponded area the infiltration rate is given by (5.13) of which the inverse reads

$$g_4(i, t) = \frac{1}{2} \left(ak + \left[(ak)^2 + \frac{4S_r^2 k_s}{4t - \frac{S_r^2 k_s}{(i-ak_s)^2}} \right]^{\frac{1}{2}} \right) \quad (5.56)$$

Fig. 5.18 visualizes the meaning of $g_4(i, t)$. The derivative of $g_4(i, t)$ with respect to i reads

$$\frac{dg_4(i, t)}{di} = 2S_r^4 k_s^2 (i - ak_s)^{-3} \left(4t - \frac{S_r^2 k_s}{(i - ak_s)^2} \right)^{-2} \left((ak_s)^2 + \frac{4S_r^2 k_s}{4t - \frac{S_r^2 k_s}{(i-ak_s)^2}} \right)^{-\frac{1}{2}} \quad (5.57)$$

Substituting (5.56) and (5.57) into (5.43), the combined pdf for unponded and ponded infiltration is obtained:

$$f_{\dot{i}}(i; t) = \frac{H(g_3(t) - i)}{(2\pi)^{\frac{1}{2}} \sigma [\ln P]} \left[\frac{1}{i} \exp \left(- \left[\frac{\ln i - \mu [\ln P]}{2^{\frac{1}{2}} \sigma [\ln P]} \right]^2 \right) + \frac{H(i - ak_s)}{g_4(i, t)} \left| \frac{dg_4(i, t)}{di} \right| \exp \left(- \left[\frac{\ln g_4(i, t) - \mu [\ln P]}{2^{\frac{1}{2}} \sigma [\ln P]} \right]^2 \right) \right] \quad (5.58)$$

where again the Heaviside function $H(x) = 1$ for $x \geq 0$ and 0 otherwise.

The interpretation of (5.58) is straightforward when considering Fig. 5.18. Firstly, as stated before, at any time t , the highest infiltration rate is equals the rainfall rate that causes ponding and there is no probability assigned to infiltration rates higher than $g_3(t)$. This explains the presence of $H(g_3(t) - i)$. Secondly, in the unponded area the infiltration rate is equal to the rainfall rate and so that the pdf of the infiltration rate is identical to the pdf of the rainfall rate (the first term within the brackets). Finally, the second term within the brackets indicates that in the ponded area infiltration occurs at a rate higher than ak_s , which explains the $H(i - ak_s)$ term. For sake of completeness, the cdf is given also:

$$F_{\dot{i}}(i; t) = 1 + \frac{1}{2} \left[\operatorname{erf} \left(\frac{\ln i - \mu [\ln P]}{2^{\frac{1}{2}} \sigma [\ln P]} \right) - \operatorname{erf} \left(\frac{\ln g_4(i, t) - \mu [\ln P]}{2^{\frac{1}{2}} \sigma [\ln P]} \right) \right] \quad (5.59)$$

An example of the behavior of (5.55), (5.58) and (5.59) is given for the clay soil. The mean rainfall rate, $\mu [\ln P] = 1.50$ and the standard deviation $\sigma [\ln P] = 0.5$. Through (A.13) this corresponds with $\mu [P] = 5.07 \text{ cm d}^{-1}$, the value for the semi-humid climate in Table 5.1. By virtue of (A.14) $\sigma [P] = 2.70 \text{ cm d}^{-1}$. In Fig. 5.19 the ponded fraction $F_{i_p}(t_p)$ given by (5.55) is shown as a function of time for different values of the saturated conductivity k_s . Obviously, the ponded fraction increases faster and towards a higher asymptotic value for small values of k_s . By again using $\mu [P] = 5.07 \text{ cm d}^{-1}$ and $k_s = 4 \text{ cm d}^{-1}$, the influence of the variance $\sigma [\ln P]$ is shown in Fig. 5.20. The probability mass associated with small and large values of P increases with $\sigma [P]$. Therefore, as in Fig. 5.16, the more frequent high values of P cause the ponded fraction to increase faster with time and the more frequent small P values explain the lower asymptotic limit. In Fig. 5.21 the probability density function $f_{\dot{i}}(i; t)$ in (5.58) and the distribution function $F_{\dot{i}}(i; t)$ in (5.59) are shown for the saturated hydraulic conductivity of the clay soil in Table 5.2, $k_s = 2.94 \text{ cm d}^{-1}$. The graphs show that for $t = 0$ the distribution of infiltration rate is identical to the distribution of rainfall rate. With increasing time, probability mass moves from the unponded into the ponded area. This is indicated by the growth of the peak in the right tail of the pdf. For $t \rightarrow \infty$, everywhere in the ponded region, the infiltration rate approaches ak_s and there is a spike of probability at $i = ak_s$. The maximum infiltration rate decreases with time as ponding occurs for lower rainfall rates. Hence, the standard deviation

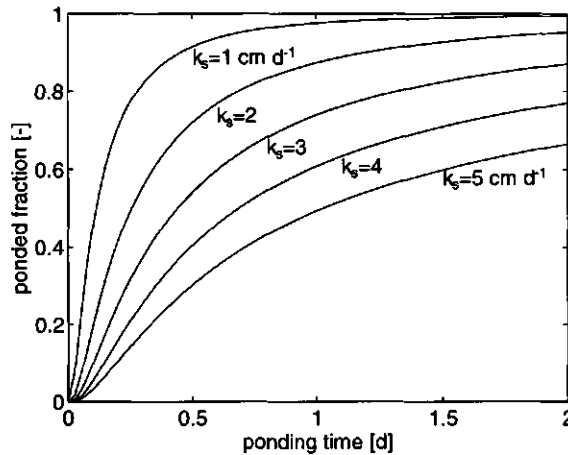


Figure 5.19: Ponded fraction $F_{tp}(t_p)$ in (5.55) as a function of ponding time for different saturated hydraulic conductivities with heterogeneous rainfall rate. $\mu[P] = 5.07 \text{ cm d}^{-1}$, $\sigma[P] = 2.70 \text{ cm d}^{-1}$ and the initial saturation degree $s_0 = 0.5$.

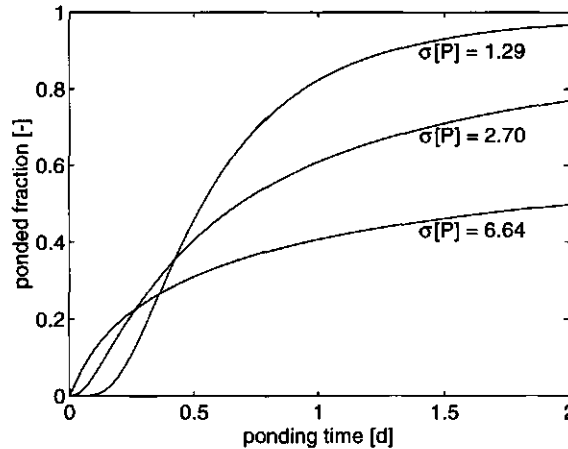


Figure 5.20: Ponded fraction $F_{tp}(t_p)$ in (5.55) as a function of time for heterogeneous rainfall rate with different values of $\sigma[P]$. $\mu[P] = 5.07 \text{ cm d}^{-1}$, $k_s = 4 \text{ cm d}^{-1}$ and the initial saturation degree $s_0 = 0.5$.

$\sigma[z]$ decreases monotonically which confirms the finding of Sivapalan and Wood [94, 1986]. As mentioned in the previous section, the short time expansion (5.5) breaks down for large t since infiltration should approach k_s rather than ak_s . However, qualitatively, the behavior described above remains correct.

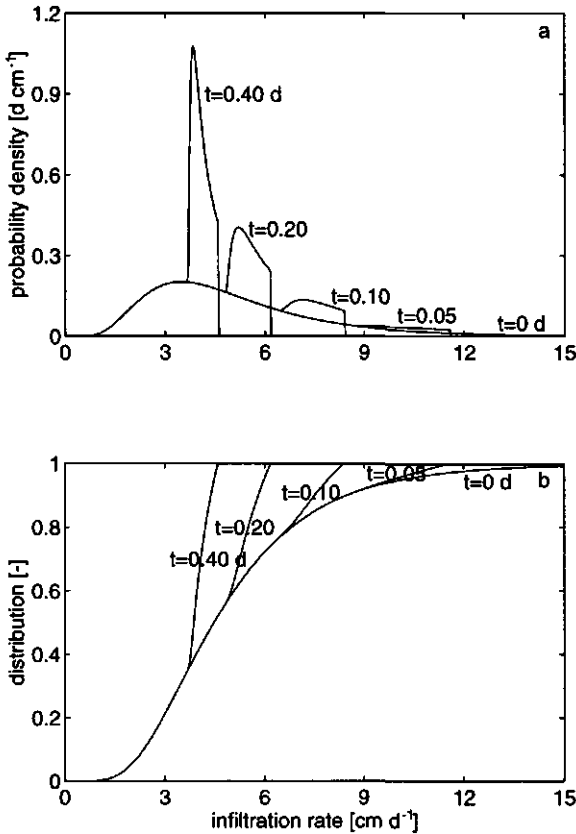


Figure 5.21: Time evolution of (a) the probability density function $f_{\frac{1}{2}}(i; t)$ in (5.58) and (b) the cumulative distribution function $F_{\frac{1}{2}}(i; t)$ in (5.59) for the clay soil and heterogeneous rainfall rate P . $\mu[\mathcal{L}] = 5.07 \text{ cm d}^{-1}$, $\sigma[\mathcal{L}] = 2.70 \text{ cm d}^{-1}$, saturated hydraulic conductivity $k_s = 2.94 \text{ cm d}^{-1}$ and the initial saturation degree $s_0 = 0.5$.

5.7.4 Evapotranspiration rate regarding spatially heterogeneous saturated hydraulic conductivity

The depletion of a soil water reservoir by simultaneous percolation and evapotranspiration is given by (5.27). Since the saturated hydraulic conductivity governs the percolation rate and hence the evapotranspiration rate, spatial heterogeneity of k_s induces heterogeneity of evapotranspiration. In this section the pdf of evapotranspiration rate will be derived, again assuming k_s to be lognormally distributed.

At any time t , the evapotranspiration rate is found by inserting (5.27) into (5.19).

Inverting this relation yields $g_5(E, t)$, the value of k_s for which at time t evapotranspiration occurs at a rate E

$$g_5(E, t) = \frac{E_p \left(\left[\frac{E}{E_p} \right]^{-c} - \left[s_0 \exp \left(-\frac{E_p}{d_r \theta_s} t \right) \right]^{-c} \right)}{\exp \left(\frac{c E_p}{d_r \theta_s} t \right) - 1} \quad (5.60)$$

The derivative of $g_5(E, t)$ with respect to the evapotranspiration rate is easily obtained

$$\frac{dg_5(E; t)}{dE} = \frac{c \left(\frac{E}{E_p} \right)^{-(c+1)}}{\exp \left(\frac{c E_p}{d_r \theta_s} t \right) - 1} \quad (5.61)$$

Inserting (5.60) and (5.61) into (5.43) results in the pdf of evapotranspiration rate

$$f_{\underline{E}}(E; t) = \left| \frac{dg_5(E, t)}{dE} \right| \frac{1}{(2\pi)^{\frac{1}{2}} \sigma [\ln k_s] g_5(E, t)} \exp \left(- \left[\frac{\ln g_5(E, t) - \mu [\ln k_s]}{2^{\frac{1}{2}} \sigma [\ln k_s]} \right]^2 \right) \quad (5.62)$$

At any time t the highest evapotranspiration rate corresponds to the smallest saturated conductivity. The cdf of the evapotranspiration rate thus becomes:

$$\begin{aligned} F_{\underline{E}}(E; t) &= 1 - F_{k_s}(g_5(E, t)) \\ &= \frac{1}{2} \left[1 - \operatorname{erf} \left(\frac{\ln g_5(E, t) - \mu [\ln k_s]}{2^{\frac{1}{2}} \sigma [\ln k_s]} \right) \right] \end{aligned} \quad (5.63)$$

Two limits of (5.62) are of special interest here. When starting at saturation ($s_0 = 1$), for $t = 0$ evapotranspiration occurs everywhere at its potential rate so that $\sigma[\underline{E}] = 0$. For $t \rightarrow \infty$ evapotranspiration ceases entirely because the water storage is completely exhausted, regardless of the value of saturated conductivity, so that $\sigma[\underline{E}] = 0$ again. The implication of this is that after the onset of evapotranspiration the standard deviation will increase. However, as time progresses, the standard deviation has to decrease again in order to arrive at the limiting value for $t = \infty$.

Because the influence of k_s on the evapotranspiration rate is more pronounced for the loam soil than for the clay soil, the behavior of (5.62) and (5.63) is illustrated in Fig. 5.22 for the loam soil with the semi-humid climate. The mean and standard deviation of $\ln k_s$ are set to 2.88 and 1.0 respectively which by virtue of (A.13) corresponds to $\mu[k_s] = 29.4 \text{ cm d}^{-1}$, being the value for the loam soil in Table 5.2. Through (A.14) $\sigma[k_s] = 38.5 \text{ cm d}^{-1}$. The potential evapotranspiration rate of the semi-humid climate in Table 5.1 is 0.33 cm d^{-1} . The initial condition is at saturation ($s_0 = 1$).

In Fig. 5.22, the increase of the variance for short times and the decrease for long times are easily identified. For short times the distribution has a negative skew,

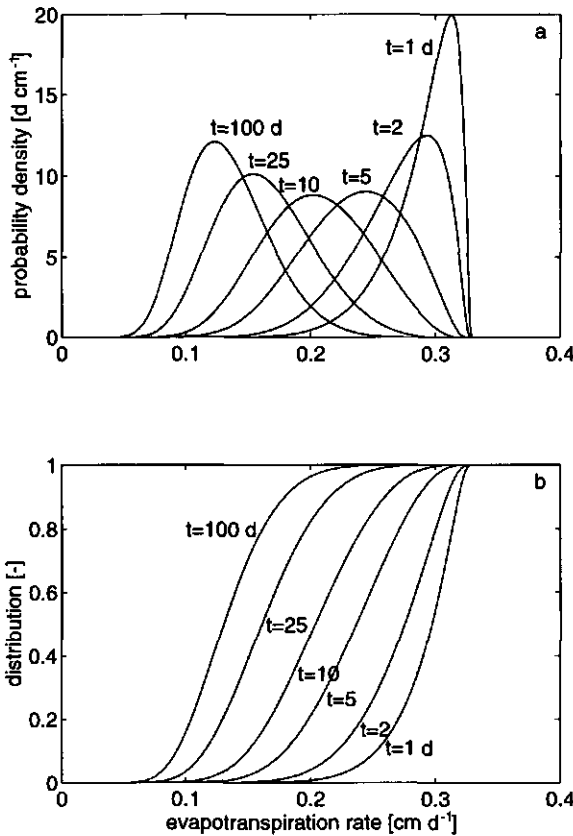


Figure 5.22: Time evolution of (a) the probability density function $f_E(E; t)$ in (5.62) and (b) the cumulative distribution function $F_E(E; t)$ in (5.63) for the loam soil and heterogeneous saturated hydraulic conductivity. $\mu [k_s] = 29.4 \text{ cm d}^{-1}$, $\sigma [k_s] = 38.5 \text{ cm d}^{-1}$, $E_p = 0.33 \text{ cm d}^{-1}$ and the initial saturation degree $s_0 = 1$.

caused by the positive skew of the density function of k_s (a large k_s corresponds to a high percolation rate and hence a low evapotranspiration rate). For long times the skewness becomes positive because evapotranspiration decreases faster for the higher saturation degrees that correspond to the smaller values of k_s .

As mentioned upon introduction of (5.19), the fact that evapotranspiration is always soil controlled is not in accordance with reality where above a certain threshold s_c evapotranspiration occurs at the potential rate (as in the original “bucket” formulation of Manabe [55, 1969] in Section 2.4 and the model of Warilow [104, 1986] in Section 3.2.2). For realistic situations, the behavior illustrated in Fig. 5.22 corresponds to a spatially uniform initial condition of $s = s_c$. Of

course, such a situation is unlikely to occur. Nevertheless, Fig. 5.22 gives a qualitative indication of the effect of spatially variable k_s on the evapotranspiration rate.

5.7.5 Evapotranspiration rate regarding spatially heterogeneous initial saturation degree

In this section, the influence of heterogeneity of the initial saturation degree at the start of an interstorm event, s_0 , on the evapotranspiration rate is investigated. The probability density and distribution functions of evapotranspiration rate are derived assuming that s_0 has a beta distribution. This distribution has the advantage that it is defined on the finite interval $[0,1]$ and that it is highly flexible. The beta probability density and distribution functions are given by (A.19) and (A.20) respectively.

The inverse relation $g_6(E; t)$ and its derivative with respect to E are obtained analogous to (5.60):

$$g_6(E, t) = \left(\left[\left(\frac{E}{E_p} \right)^{-c} + \frac{k_s}{E_p} \right] \exp \left(-\frac{cE_p t}{d_r \theta_s} \right) - \frac{k_s}{E_p} \right)^{-\frac{1}{c}} \quad (5.64)$$

$$\begin{aligned} \frac{dg_6(E, t)}{dE} &= \left(\left[\left(\frac{E}{E_p} \right)^{-c} + \frac{k_s}{E_p} \right] \exp \left(-\frac{cE_p t}{d_r \theta_s} \right) - \frac{k_s}{E_p} \right)^{-\frac{c+1}{c}} \\ &\quad \left(\frac{E}{E_p} \right)^{-(c+1)} \exp \left(-\frac{cE_p t}{d_r \theta_s} \right) \frac{1}{E_p} \end{aligned} \quad (5.65)$$

Using (5.42) and (5.43) again, the probability density and distribution functions of evapotranspiration rate \underline{E} become:

$$f_{\underline{E}}(E; t) = \left| \frac{dg_6(E, t)}{dE} \right| \frac{1}{B(\nu, \nu)} (g_6(E, t))^{\nu-1} (1 - g_6(E, t))^{\nu-1} \quad (5.66)$$

$$F_{\underline{E}}(E; t) = \int_0^{g_6(E, t)} \frac{1}{B(\nu, \nu)} w^{\nu-1} (1 - w)^{\nu-1} dw \quad (5.67)$$

The incomplete beta function in (5.67) has been extensively tabulated and algorithms exist for numerical evaluation (for example Press *et al.* [76, 1986]). In Fig. 5.23 the pdf (5.66) and cdf (5.67) are depicted for the loam soil ($k_s = 29.4 \text{ cm d}^{-1}$) and the semi-humid climate ($E_p = 0.33 \text{ cm d}^{-1}$) for the parameters $\nu = \nu = 2$. By virtue of (A.21) and (A.22), these values correspond with $\mu[s_0] = 0.5$ and $\sigma[s_0] = 0.224$. For $t = 0 \text{ d}$ the pdf of the evapotranspiration rate exactly follows the pdf of initial soil saturation degree, scaled by the value

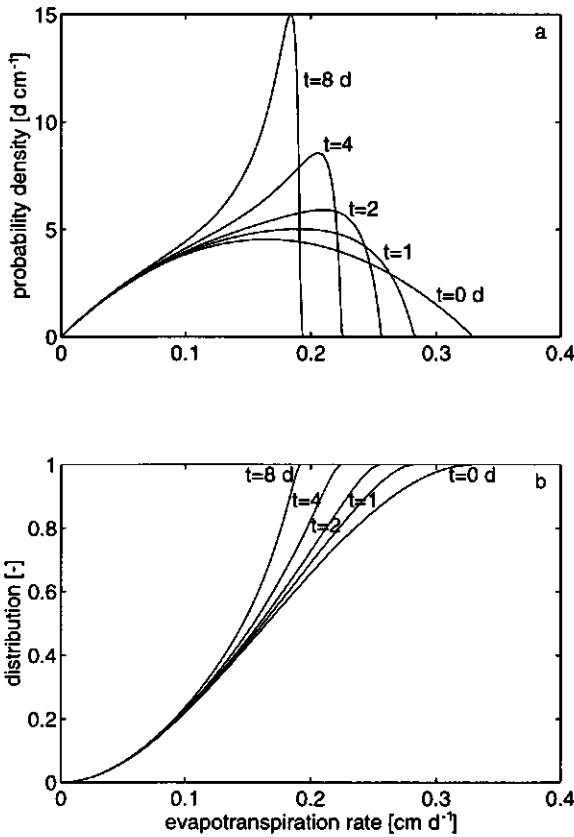


Figure 5.23: Time evolution of (a) the probability density function $f_E(E; t)$ in (5.66) and (b) the cumulative distribution function $F_E(E; t)$ in (5.67) for the loam soil and the semi-humid climate. $\mu [s_0] = 0.5$, $\sigma [s_0] = 0.224$, $k_s = 29.4 \text{ cm d}^{-1}$ and $E_p = 0.33 \text{ cm d}^{-1}$.

$E_p = 0.33 \text{ cm d}^{-1}$. When time increases, probability mass moves from higher to smaller evapotranspiration rates. This is because in the wet region percolation and evapotranspiration deplete the soil moisture reservoir much faster. Obviously, when $t \rightarrow \infty$, all probability mass will be located at $E = 0$.

Because the soil hydraulic properties are assumed to be uniform, the heterogeneity of s_0 considered here may be thought of as the result of rainfall heterogeneity. Not surprisingly, over such a region the variation in evapotranspiration becomes smaller with time because wet regions dry faster than dry ones.

5.8 Conclusions

This chapter presented an analytical framework for the description of the water budget of a soil reservoir. In the derivation of the various solutions, redistribution of water in the unsaturated zone was omitted. The framework was validated against numerical solutions of Richards' equations and subsequently used to investigate the influence of soil heterogeneity, to analyze the existence of equivalent soil properties and to analytically derive some probability density and distribution functions of the infiltration and evapotranspiration rate. The main conclusions of this chapter are:

1. The suggested framework of analytical solutions captures the hydrological phenomena related to intermittent wetting and drying events satisfactorily when compared to numerical solutions of Richards' equation (see Section 5.4);
2. The sensitivity of the long-term mean water budget components to the maximum soil water storage is small (Section 5.5);
3. For highly conductive soils, heterogeneity of the soil scale factor α and the exponent m according to lognormal distributions increases the magnitude of the evapotranspiration rate relative to the uniform situation with the mean values of α and m . In contrast, for less conductive soils the decreasing infiltration rates due to heterogeneity of α cause the evapotranspiration rate to be smaller (Section 5.5);
4. The number of "equivalent" soil parameters that can be determined is equal to the number of independent fluxes. For the four fluxes that are potentially present (infiltration and saturation excess runoff, evapotranspiration and percolation), the maximum number of equivalent parameters is three (Section 5.6);
5. The equivalent parameters depend on not only the soil hydraulic parameters and their heterogeneity but also on the considered climate and the spatially uniform parameters (Section 5.6);
6. The areally average infiltration excess runoff and percolation corresponding to Monte Carlo simulations and "a priori" determined equivalent soil hydraulic properties compare reasonably well for the semi-humid climate but not for the arid climate (Section 5.6). Due to the opposite effect of soil scale factor α on infiltration excess runoff and percolation, the equivalent properties behave much better for evapotranspiration;
7. "Equivalent" parameters derived for the long term average water budget are not valid for transient behavior (Section 5.6);
8. From the derived distribution functions it appears that the mechanisms by which heterogeneity of the saturated conductivity and rainfall rate affect heterogeneity of the water budget components are markedly different (Section 5.7).

Chapter 6

Deterministic heterogeneity on hillslopes

6.1 Objective and methods

In Chapters 3 - 5 the emphasis was on the heterogeneity of the water budget components induced by spatial heterogeneity of soil hydraulic parameters and rainfall. Because of the complexity of these sources of heterogeneity, stochastic methods were applied. Typically, an area was regarded as an ensemble of independent soil columns in which one-dimensional vertical flow was considered. Each of the columns had its own soil hydraulic properties and/or rainfall time series.

As mentioned in Section 2.3.3, heterogeneity of the water budget may also arise because of lateral flow processes and thus be of deterministic rather than stochastic origin. Insight into the mechanisms of how climate, soil hydraulic properties, topography and vegetation affect hillslope hydrological response is considered to be essential in scaling up hydrological processes to catchment-scale for at least two reasons.

Firstly, because of the high degree of nonlinearity of hillslope flow processes, for a time-varying spatially average or "equivalent" hydrological state to be defined such that it resembles the actual transient behavior, is even less likely than for the one-dimensional situation described in Section 5.6. Secondly, internal redistribution of water affects the time span over which the water may be released into the atmosphere by evapotranspiration. As an example, consider the downhill riparian zones (e.g. Penman [73, 1951] referenced in [49, Kühnel *et al.* 1991]) that transpire at the potential rate long after cessation of rainfall, owing to delayed uphill water delivery. Salvucci [83, 1994] showed some other examples of lateral redistribution of water along hillslopes. In this study the equilibrium hydrological state of a hillslope was derived using a statistical dynamical method in which transient phenomena were represented in a statistical manner.

The scope of this chapter is to gain insight into the deterministic structure of the

variability of fluxes and soil water content at and near the land surface. To that end, a fully transient mixed analytical-numerical model of coupled unsaturated-saturated flow on a hillslope is developed. Its computational efficiency allows the analysis of the long-term water budget of a hillslope.

A similar approach was taken by Smith and Hebbert [97, 1983] who used kinematic wave theory to describe downward unsaturated flow. Since kinematic waves travel in one direction only, their model does not account for upward capillary flow from the ground water. Although well suited to the study of runoff producing storm events, the model of Smith and Hebbert is less applicable for analyzing the long-term water budget on a hillslope where the intermittency of wetting and drying events is crucial.

Below, Section 6.2 presents the unsaturated and saturated flow equations that constitute the backbone of the model as well as the initial and boundary conditions. The numerical methods and the analytical treatment of the processes that are computationally most demanding are outlined in Section 6.3. In Section 6.4 a limited verification of the model is performed, using measured data from an experimental hillslope in New-Zealand. In order to explicitly address the influence of climate, soil hydraulic properties, geomorphology and vegetation on hillslope behavior, 16 case studies are defined in Section 6.5 of which the results will be discussed in Section 6.6.

6.2 Flow equations and initial conditions

6.2.1 Flow equations

The hillslope shown in Fig. 6.1 consists of an unsaturated and a saturated domain separated by the phreatic surface. The soil surface and the impermeable layer are the upper and lower boundaries of the unsaturated and saturated zone respectively. The coordinate system has an x -direction parallel to the impermeable layer and a z -direction normal to it. The origin is taken at the most downhill location of the impermeable layer. The soil depth is indicated by z_s and may vary with x . Note that only the position of the zero-plane $z = 0$ and not the direction of the vertical coordinate differs in comparison to Chapters 3 and 4. In the model, fluxes towards the origin are taken as being positive, as illustrated in Fig. 6.1.

Unsaturated domain

Using the Darcy equation (2.7), the fluxes in the x and z direction for an isotropic unsaturated medium take the form

$$q_x = k(\theta) \left(\frac{\partial \psi}{\partial x} + \sin \phi \right) \quad (6.1)$$

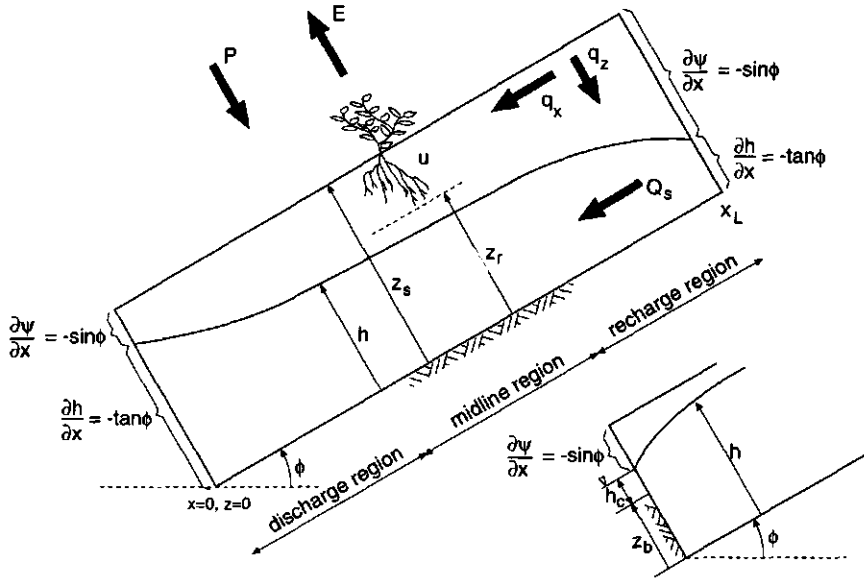


Figure 6.1: Schematic overview of the hillslope model domain and boundary conditions. The inset shows the lower boundary in case of a channel. The symbols are outlined in the text.

$$q_z = k(\theta) \left(\frac{\partial \psi}{\partial z} + \cos \phi \right) \quad (6.2)$$

Anisotropy can be accounted for by distinguishing between k_x and k_z . The anisotropy ratio R_a is a parameter in the model and is defined as the ratio of the saturated conductivities in the x and z direction:

$$R_a = \frac{k_{s,x}}{k_{s,z}} \quad (6.3)$$

Through substitution of (6.1) and (6.2) into (2.9), the two dimensional Richards' equation is obtained which, after addition of a sink term U for water uptake by plant roots, is written as

$$\frac{\partial \theta(\psi)}{\partial t} = -\frac{\partial}{\partial x} \left[k(\theta) \left(\frac{\partial \psi}{\partial x} + \sin \phi \right) \right] - \frac{\partial}{\partial z} \left[k(\theta) \left(\frac{\partial \psi}{\partial z} + \cos \phi \right) \right] - U(\theta) \quad (6.4)$$

The soil hydraulic characteristics $\theta(\psi)$ and $k(\theta)$ are described according to Van Genuchten [102, 1980] and are given by (3.3) and (3.5). Water uptake by roots is described as in Chapters 3 and 4.

$$U(\theta) = \begin{cases} \beta(\theta) \frac{E_p}{z_s - z_r} & z_r \leq z \leq z_s \\ 0 & 0 \leq z < z_r \end{cases} \quad (6.5)$$

$$\beta(\theta) = \begin{cases} 1 & \theta_c < \theta \leq \theta_s \\ \frac{\theta - \theta_w}{\theta_c - \theta_w} & \theta_w \leq \theta \leq \theta_c \\ 0 & 0 \leq \theta < \theta_w \end{cases} \quad (6.6)$$

The transpiration efficiency in (6.6) is identical to (3.13). Because the principal state variable of the model is the volumetric moisture content, the transpiration efficiency is expressed in terms of θ rather than ψ . The root density is assumed to be uniform over the depth of the root zone ($z_s - z_r$), but other distributions may be easily implemented. The total evapotranspiration is obtained through integration of the water uptake U over the depth of the rootzone, as denoted in (3.2).

Saturated domain

When neglecting saturated flow in the z -direction (Dupuit assumption), one-dimensional saturated lateral flow in the x -direction, Q_s , is given by the Boussinesq equation

$$Q_s = k_s h \cos \phi \left(\frac{\partial h}{\partial x} + \tan \phi \right) \quad (6.7)$$

where h is the height of the phreatic surface above the impermeable layer as depicted in Fig. 6.1. Irregularities of the impermeable layer can easily be taken into account by replacing h in (6.7) with $h - z_b$ where z_b indicates a local deviation from the $z = 0$ level.

Applying the continuity principle, the time rate of change of the phreatic surface is given by

$$S_y(t) \frac{\partial h}{\partial t} = q_r - \frac{\partial}{\partial x} \left(k_s h \cos \phi \left[\frac{\partial h}{\partial x} + \tan \phi \right] \right) \quad (6.8)$$

where S_y stands for the specific yield, i.e. the empty pore space available to water storage and q_r is the recharge, given by

$$\begin{aligned} q_r &= q_z(z = h) \\ &= k_z(\psi) \left(\frac{\partial \psi}{\partial z} + \cos \phi \right) \Big|_{z=h} \end{aligned} \quad (6.9)$$

From these governing equations, it is evident that the saturated and unsaturated zones are coupled through the recharge flux (6.9). Since the strongest flow inducing gradients are vertical in the unsaturated zone, lateral variations in hydrological conditions are mainly governed by saturated lateral flow (6.7) and the coupling in (6.9). Therefore, realistic treatment of the spatial heterogeneity of hydrological response in sloping areas requires the consideration of the entire coupled saturated-unsaturated system represented by the governing equations (6.1) through (6.9).

6.2.2 Initial and boundary conditions

In order to solve the flow equations of the unsaturated and saturated system, initial and boundary conditions need to be specified. Unless the initial conditions are exactly known, they are chosen arbitrarily and the model is allowed to “warm-up” to ensure that their effect is diminished. The closer the initial conditions are to a physically realistic state of the system, the shorter the warming-up period.

In case of a rainfall event, the upper boundary condition for the unsaturated domain switches from flux to head controlled infiltration whenever the soil surface saturates and is no longer capable of completely absorbing the rain falling on it. From that time onwards a water layer develops at the surface, running downhill (infiltration excess runoff q_{ie}). If the phreatic surface reaches the surface it acts as an impervious layer and all rain falling on it is removed as saturation excess overland flow q_{se} . Mathematically, the infiltration rate i is thus given by

$$i(x, t) = \begin{cases} P(t) & \psi(x, z_s, t) < 0 \\ k_s \left(\frac{\partial \psi}{\partial z} + \cos \phi \right) \Big|_{z=z_s} & \psi(x, z_s, t) = 0 \\ 0 & h(x, t) = z_s(x) \end{cases} \quad (6.10)$$

In order to accurately resolve the infiltration process using a numerical solution of (6.10), high resolutions in space and time would be necessary. An analytical treatment of infiltration has therefore been adopted which will be discussed in Section 6.3.2.

The lower boundary condition for the unsaturated flow domain, which makes up the upper boundary condition for the saturated domain, is the atmospheric pressure at the phreatic surface

$$\psi = 0 \quad z = h(x) \quad (6.11)$$

The last two boundary conditions for the unsaturated flow domain are the no-flow conditions at the vertical uphill (divide) and downhill (valley) boundaries

$$\frac{\partial \psi}{\partial x} = -\sin \phi \quad \begin{cases} h(0) < z \leq z_s(0) \\ h(x_L) < z < z_s(x_L) \end{cases} \quad (6.12)$$

As for the unsaturated zone, no saturated flow is allowed at the divide and, because of hillslope symmetry, in the valley:

$$\frac{\partial h}{\partial x} = -\tan \phi \quad x = 0, \quad x = x_L \quad (6.13)$$

When at the downhill boundary a channel with an elevation z_b is present in which a water level h_c is maintained (see inset Fig. 6.1), (6.13) is replaced by

$$h = z_b + h_c \quad x = 0 \quad (6.14)$$

Adjacent to the downhill boundary a seepage face is present when the groundwater reaches the soil surface. The uphill boundary of the seepage face depends on the transient flow conditions:

$$h = z_s(x) \quad 0 < x \leq x_{sf}(t) \quad (6.15)$$

where x_{sf} is the most uphill position where the seepage face is present. The numerical treatment of the seepage face is discussed in Section 6.3.4.

6.3 Model formulation

The objective for the construction of the model requires two conflicting conditions to be satisfied. Accurate numerical solution of the system of transient nonlinear equations can only be achieved by using a high resolution in both space and time. A high resolution discretization, however, is computationally intensive and would prohibit long time integrations of the model. To compromise both requirements, the computationally most demanding processes, transient infiltration (6.10) and movement of the phreatic surface (6.8) are treated analytically while the other processes are solved numerically.

6.3.1 Numerical implementation

The fluxes in (6.1), (6.2) and (6.7) are approximated using their finite difference form. Interblock conductivities for the unsaturated fluxes are taken as the geometric mean of the neighboring cells and for the saturated fluxes the arithmetic mean is used. Zaidel and Russo [107, 1993] present a more accurate estimation of the unsaturated interblock conductivities which improves the accuracy of numerical solutions, especially for infiltration into dry soils. In the present model, however, the infiltration is treated analytically, thereby reducing the possible improvements of using more advanced weighing schemes. Solution of (6.4) uses an explicit finite difference scheme in time, whereas (6.8) is treated analytically, as will be explained shortly.

6.3.2 Analytical formulation of infiltration

The infiltration fluxes at the soil surface are determined using the method of Smith *et al.* [96, 1993]. This method is preferred over others because of its ability to account for intervals of low rain rates, during which a ponded surface temporarily unponds and soil moisture redistributes. In the following, the treatment of switching from unponded to ponded infiltration is outlined. For the derivation of the equations and further details on the determination of infiltration parameters

after soil moisture redistribution (which in the model is computed numerically), the reader is referred to the paper of Smith *et al.* [96, 1993].

As indicated in (6.10), when the phreatic level reaches the surface ($h = z_s$) all rainfall is removed as saturation excess runoff q_{se} . Otherwise, given a vertically uniform moisture content θ_i at the beginning of a rainfall event t_i , the method predicts the ponding time t_p at which the boundary condition (6.10) switches from flux controlled to head controlled. Mathematically, the infiltration flux is

$$i(t) = \begin{cases} \min \{P(t), i_h(t)\} & h < z_s \\ 0 & h = z_s \end{cases} \quad (6.16)$$

where the head controlled infiltration i_h rate given by

$$i_h(t) = k_s \left(1 + \varsigma \left[\exp \left(\frac{2\varsigma [i^{\text{cum}}(t) - k(\theta_i)t] k_s}{S^2(\theta_i)} \right) - 1 \right]^{-1} \right) \quad (6.17)$$

of which the sorptivity $S(\theta_i)$ is given by (5.6) and in which $i^{\text{cum}}(t)$ denotes the cumulative infiltration since the beginning of the storm event. Except for very high initial moisture contents, $k(\theta_i)t \ll i^{\text{cum}}$ and might as well be neglected.

In (6.16) infiltration i^{cum} accumulates from any pattern $P(t)$ ($P > k_s$) until the rainfall rate encounters the curve $i_h(t)$ (at $t = t_p$), after which i^{cum} accumulates from $i_h(t)$. This behavior resembles the time compression approximation introduced in Section 5.2.2. As was stated then, the time compression approximation is essentially tantamount to using cumulative infiltration as a surrogate for time, which is explicit in (6.17). The meaning of the parameter ς in (6.17) was given in Section 5.2.2, and, as was done there, ς is set at 1 from here onwards. Smith *et al.* [96, 1993] show that the infiltration rate and ponding time predicted by (6.17) become relatively insensitive to ς when the rain rate is much higher than the saturated conductivity.

Due to the transient nature of the model, the condition of a uniform initial profile is generally not met. Water uptake by roots, however, tends to homogenize the moisture profile in the root zone, thereby relaxing the severity of the assumption. In the model, sorptivity S is determined using the soil moisture status of the grid cell closest to the soil surface.

6.3.3 Analytical treatment of the phreatic surface dynamics

The height of the groundwater table determines to a great extent the lateral saturated fluxes as well as the moisture profile and fluxes in the unsaturated zone above it. Hence, the location of the phreatic surface needs to be determined with considerable accuracy. In order to keep accurate track of the phreatic surface

while using a coarse vertical discretization, a simple analytical treatment has been adopted that allows for subgrid movement. The method described below replaces the numerical solution of (6.8).

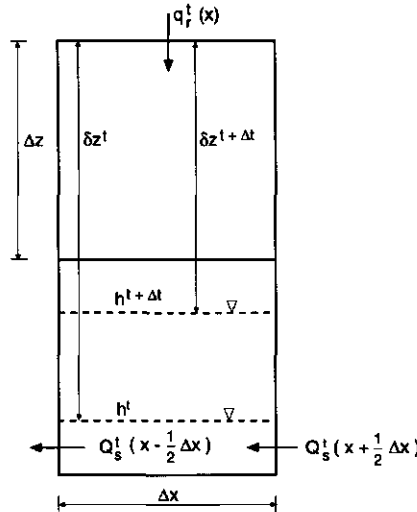


Figure 6.2: Diagram explaining the updating of the phreatic surface going from t to $t + \Delta t$. The height of the hydrostatic region is indicated by δz .

Consider the vertical cross-section in Fig. 6.2. A region above the phreatic surface of height δz is assumed to be in hydrostatic equilibrium with the groundwater table, i.e. $\psi = h - z$. Any flux going into or out of this region is assumed to equilibrate instantaneously with the phreatic surface. The height of the hydrostatic region ($\Delta z < \delta z < 2\Delta z$) at any location x at time $t + \Delta t$ can be solved implicitly by formulating the mass balance at time t for the two grid cells containing the phreatic surface and the hydrostatic zone:

$$\begin{aligned} (2\Delta z - \delta z^{t+\Delta t}) \theta_s + \int_{-\delta z^{t+\Delta t}}^0 \theta(\psi) d\psi &= (2\Delta z - \delta z^t) \theta_s + \int_{-\delta z^t}^0 \theta(\psi) d\psi \\ &+ \left(\frac{Q_s^t(x + \frac{1}{2}\Delta x) - Q_s^t(x - \frac{1}{2}\Delta x)}{\Delta x} \right) \Delta t \\ &+ q_r^t \Delta t \end{aligned} \quad (6.18)$$

As indicated in Fig. 6.2, the recharge flux q_r^t is determined at the top of the hydrostatic zone rather than right at the phreatic surface as suggested by (6.9).

In case the hydrostatic zone moves into another grid cell, $\delta z^{t+\Delta t}$ can be determined implicitly by formulating the mass balance for three grid cells. Since no analytical integration of $\theta(\psi)$ in (3.3) is possible, $\theta(\psi)$ is assumed to be linear for

$-\delta z \leq \psi \leq 0$:

$$\int_{-\delta z}^0 \theta(\psi) d\psi \approx \frac{\theta_s + \theta(-\delta z)}{2} \delta z$$

This assumption is close to reality as long as δz is smaller than the height of the capillary fringe, the zone above the water table that can be considered to be effectively saturated. Because $\delta z < 2\Delta z$, the error in the above linearization is thus small when the vertical grid distance Δz is chosen to be smaller than half the height of the capillary fringe.

The rise of the phreatic surface is determined by the length of the time step Δt . To prevent large changes of the phreatic surface, the length of a time step is restricted. For the time steps used for the computations in this chapter (< 10 min) the movement of the phreatic surface is small in comparison to the height of a grid cell.

When the phreatic surface comes close to the soil surface ($h > z_s - 2\Delta z$), the hydrostatic zone is assumed to extend up to the soil surface. The limited empty pore space available for water storage causes the phreatic surface to react in a very pronounced way to small amounts of water that are either extracted or supplied. When the phreatic surface reaches the soil surface, a seepage face develops.

6.3.4 Treatment of the seepage face

Flow out of the seepage face is described as the divergence of the lateral saturated flow minus the actual evapotranspiration over the seepage face:

$$q_{sf}(x) = \frac{Q_s(x + \frac{1}{2}\Delta x) - Q_s(x - \frac{1}{2}\Delta x)}{\Delta x} - E(x) \quad (6.19)$$

In case the hillslope has a rectangular layout (as is the case for the 16 case studies discussed in Section 6.5), the Dupuit assumption in (6.7) causes divergence of the saturated lateral flow $\frac{dQ_s}{dx} = 0$. Accordingly, over a seepage face of length $x_{sf} = n\Delta x$ (where $n \geq 1$), water only seeps out at the most downhill grid ($n = 1$). When averaged over the entire hillslope, the seepage outflow amounts to

$$q_{sf} = \frac{Q_s(x_{sf}) - Q_s(0) - \sum_{i=0}^{n-1} E\left(\left(i + \frac{1}{2}\right)\Delta x\right) \Delta x}{x_L} \quad (6.20)$$

where the summation represents the total evapotranspiration that occurs over the seepage face.

6.3.5 Treatment of convergent flow

To partly overcome the two-dimensionality of the model, uniform convergence of the flow domain can be included. This is effected by specifying the convergence

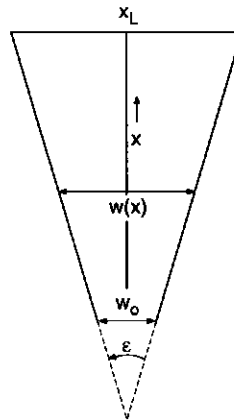


Figure 6.3: Diagram explaining the incorporation of convergence of the model domain. x denotes the uphill position, ϵ the convergence angle, $w(x)$ the hillslope width at x and $w_0 = w(0)$.

angle ϵ and the width of the downhill boundary of the hillslope w_0 as shown in Fig. 6.3. All lateral fluxes are multiplied with the ratio of local hillslope width over the downstream width:

$$R_c(x) = \frac{w(x)}{w_0} = 1 + \frac{2x}{w_0} \tan \frac{\epsilon}{2} \quad (6.21)$$

Values of $R_c < 1$ relate to divergent hillslopes.

6.4 Model verification

The proposed transient model aims at studying the long-term hillslope hydrological behavior by time integration over long periods. This assures that processes acting on short time scales (of the order of hours) exert their influence on the long-term mean state. Before doing so, however, model simulations have to be compared against measured data in order to verify the model's ability to realistically reproduce observed phenomena. In a similar effort, Stephenson and Freeze [99, 1974] concluded that a mathematical model that

'previously experienced only the coddled simplicity of carefully devised hypothetical cases [.once,] introduced to the perils of the real world [...] proved to be a valuable aid to a unified interpretation of field measurements.'

The correspondence between the simulated results and the measured data was neither particularly good nor particularly bad but

'probably representative of what can be attained when a fully deterministic mathematical model is applied to a field site with a fairly complete, but as always imperfect, set of field measurements.'

Stephenson and Freeze state that one of the main impediments to better results is the mathematical development of the model which, by definition, implies a major simplification of reality. The scarcity of the data they mention relates especially to information about the geomorphological structure and the soil hydraulic properties that are difficult to obtain and vary greatly over short distances. Bearing this in mind, the suggested model is validated for an intensively measured experimental hillslope in the Maimai catchment at South Island, New Zealand. The data collected in the catchment have been extensively documented by Mosley [64, 1979], Pearce *et al.* [70, 1986], Sklash *et al.* [95, 1986] and McDonnell [57, 1990]. The data of the last study are used here.

6.4.1 Description of the experimental site

The Maimai M8 catchment is located in the Tawhai State Forest in New Zealand (45°05'S, 171°48'E). The mean annual rainfall is approximately 2600 mm, producing approximately 1550 mm runoff from the 1950 mm net rainfall [80, Rowe, 1979] (referenced in [70, Pearce *et al.*, 1986]). The area is thus highly responsive to rainfall. Mosley [64, 1979] states that the catchment is underlain by a layer that is 'effectively impermeable'. The slopes are short (< 30 m) and steep (mean 34°) and the soil depth varies greatly (mean 0.6 m, range 0.2-1.8 m) [57, McDonnell, 1990]. The mineral soils are overlain by a thick humic horizon with a minimum saturated conductivity of 250 mm h⁻¹ which prevents the occurrence of infiltration excess runoff. A digital terrain model of the surface elevation data is shown in Fig. 6.4 in which the Pit 5 location for which the model is verified, is indicated.

6.4.2 Measured data

At Pit 5, located on a midslope hollow (see Fig. 6.4), soil was excavated down to the underlying impermeable bedrock. This was carried out over a length of several meters to prevent convergence of flow lines towards the pit [64, Mosley 1979]. The data of 19 tensiometers, ranging from 108 cm to 15 cm below the soil surface and from 1.10 m to 7.60 m uphill from the pit, were used to monitor the dynamics of the soil matric head and the phreatic surface. The validation is performed for the response of the phreatic surface to the storm event of October 29, 1987, for which 10 min rainfall data are available. The lack of accurate soil hydraulic information prohibits comparison with the soil matric head measurements.

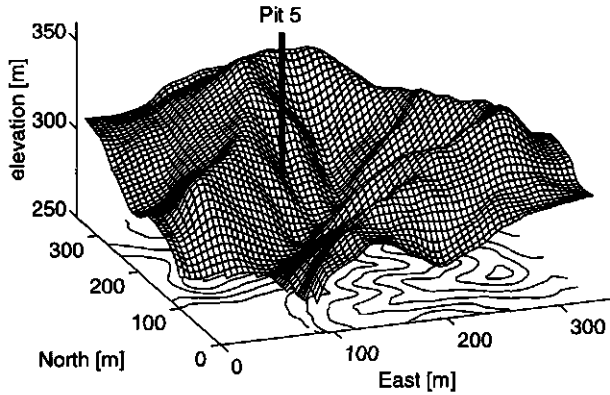


Figure 6.4: Digital elevation model of the Maimai M8 catchment. The location of the Pit 5 site for which the verification is performed, is indicated.

6.4.3 Model input

Geomorphological hillslope layout

McDonnell [57, 1990] indicates that at Pit 5 the slope angle is 34° and the soil depth is 1.5 m. From the digital elevation data, the length of the hillslope was determined to be approximately 25 m. Data regarding the soil depth along the hillslope are given by Mosley [64, 1979]. Although highly variable, according to the general trend, the soil depth decreases in uphill direction. Therefore, a uniformly decreasing soil depth from 1.5 m at the downhill boundary $x = 0$ to 0.4 m at the divide $x = 25$ m was assumed, as shown in Fig. 6.5. Convergence of the flow

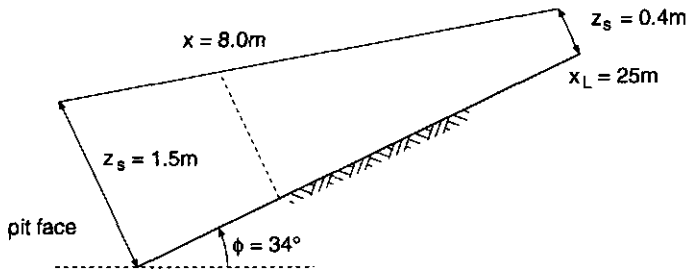


Figure 6.5: Idealized geomorphological layout used for the verification simulation of the hillslope uphill from Pit 5. The hillslope length $x_L = 25$ m and the slope $\phi = 34^\circ$. The soil depth decreases from 1.5 m at the pitface to 0.4 m at $x = x_L$. The dotted line at $x = 8.0$ m indicates the uphill distance below which the tensiometric measurements were performed.

domain has not been taken into account due to lack of data. The horizontal and vertical node distances were set at 50 cm and 10 cm respectively. The time step used was 2.5 min.

Soil hydraulic properties

According to McDonnell [57, 1990], the soil hydraulic properties show considerable variation and little information about them is available. The saturated conductivity of the mineral soil ranges from 70 to 700 cm d^{-1} . Here the average value $k_s = 400 \text{ cm d}^{-1}$ is used. Parameters θ_s , α and n in (3.3) were determined using the average soil water retention data ($-100 \text{ cm} \leq \psi \leq 0 \text{ cm}$) provided by McDonnell and assuming $\theta_r = 0.05$. Finally, parameter l in (3.4) was set to the frequently used value 0.5 [65, Mualem 1976].

Initial conditions

An accurate initial condition is not available. To overcome this problem, the storm event of October 24 has been included in the simulation. Consistent with McDonnell's observation [57, 1990], the model results indicate that the downhill outflow through the pit face had fully recovered from this event before October 29. The model state of the hillslope prior to the October 29 event was rather wet but completely unsaturated, which is qualitatively in agreement with the high value of the antecedent precipitation index reported by McDonnell.

6.4.4 Verification results

The transient behavior of the simulated phreatic surface at the locations $x = 1.0 \text{ m}$, $x = 4.5 \text{ m}$ and $x = 7.5 \text{ m}$ in relation to the rainfall pattern is shown in Fig. 6.6. It can be seen that the most uphill position reacts faster to the storm event. This is explained by the decreasing soil depth in uphill direction and the corresponding smaller unsaturated storage capacity. The phreatic level of the downhill location recedes slowest because of moisture delivery from uphill.

The small jumps that show clearly in the recession limb of the $x = 1.0 \text{ m}$ location in Fig. 6.6 occur every 10 cm of phreatic level drop. This is caused by the analytical treatment of the phreatic surface dynamics explained in Fig. 6.2 and happens whenever the phreatic surface moves into a lower grid. In Fig. 6.7 the phreatic surface is shown for a cross section of the hillslope for four different times. For $t = 1.71 \text{ d}$ the phreatic level given by McDonnell [57, 1990] is depicted as well. The phreatic surface appears and disappears rapidly, in agreement with McDonnell's observation. The model does not entirely capture the behavior of the phreatic level near the pit face. This is not surprising because the Dupuit approximation does not apply to groundwater flow near a seepage face.

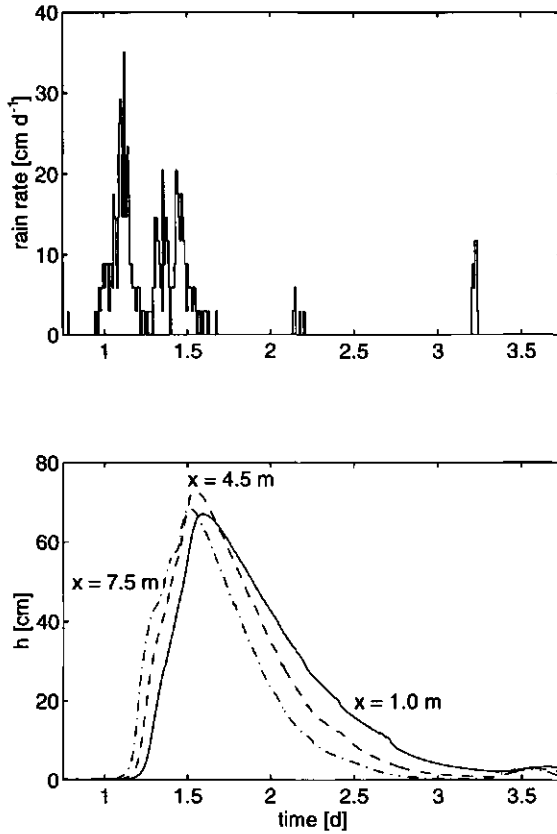


Figure 6.6: Rain rate of the October 29 storm event and the response of the height of the phreatic surface h above the bedrock for the uphill locations $x = 1.0$ m, $x = 4.5$ m and $x = 7.5$ m at the Pit 5 location.

The above verification is rather limited, with respect to the time period considered (one event) and the parts of the model that were verified. Nevertheless, the analytical treatment of the phreatic surface, which often plays a governing role in the response of sloping areas, was found to reproduce the timing and magnitude of the groundwater response to a storm event satisfactorily. Preferably, verification would include processes acting on longer time scales and checks on other simulated state variables and fluxes. Notwithstanding the need for a more elaborate verification, the introductory results shown here permit the use of the model to analyze of the mechanisms that control hillslope hydrological behavior.

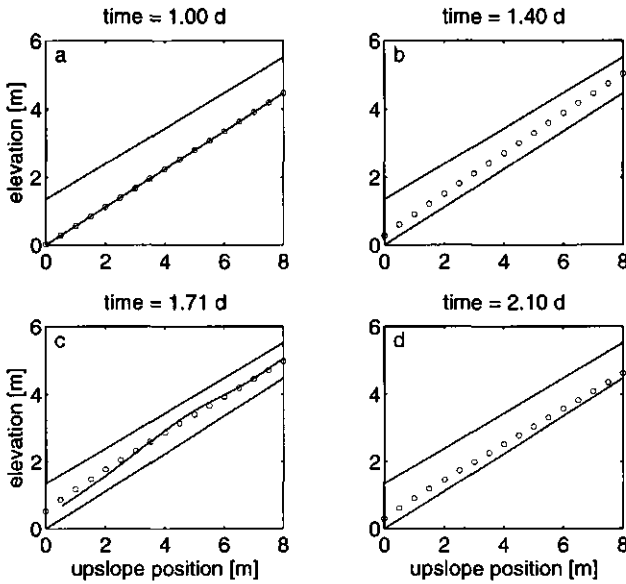


Figure 6.7: Hillslope cross section at the Pit 5 location showing the phreatic surface at different times during the October 29 storm event. The simulated values at the grid points are indicated by (o). The drawn line in c. is the measured phreatic surface given by McDonnell [57, 1990].

6.5 Case studies for idealized hillslopes

Hillslope hydrological behavior arises because of the complex interaction of many processes. In the remainder of this chapter, the influences of climate, soil hydraulic properties, geomorphology and vegetation on hillslope hydrological behavior are investigated. The hillslope configuration and the various climates and soil properties used will be described first, followed by a description of the different cases for which simulations have been carried out.

6.5.1 Specification of climate, soil, geomorphology and vegetation properties

Simulation of the hillslope hydrological behavior using the proposed model requires specification of the initial and meteorological boundary conditions, the soil hydraulic parameters, the geomorphological layout and the vegetation characteristics. The initial conditions were chosen arbitrarily and the model was integrated for one year prior to the collection of the simulation diagnostics. By varying the parameters or boundary conditions, the influence of climate, soil, geomorphology

and vegetation are examined. In the following, these four groups will be discussed separately.

Climate forcing

Like in Chapter 5, the atmospheric forcing is modeled as a Poisson arrival process of rectangular rainfall pulses with in between periods of constant potential evapotranspiration intensity. This procedure has been outlined in detail in Section 5.3.1. The arid, semi-humid and humid climates mentioned in Table 5.1 are used here again since they cover a wide range of different climatic conditions.

Soil hydraulic parameters

The loam soil specified in Table 3.1 and shown in Fig. 3.5a,c is used again in this chapter. The effect of (spatially uniform) soil hydraulic properties is investigated simply by using the scaling theory outlined in Section 3.2.4. Different soils are constructed by selecting different values of soil scale factor α .

Geomorphological parameters

It is to be expected that the geomorphological configuration of the hillslope greatly affects its hydrological behavior. For the purpose of simplicity, the analysis in this paper uses an idealized hillslope, like the one shown in Fig. 6.1. It consists of a rectangle of soil on top of impermeable bedrock. The soil depth z_s is constant over the entire domain, as is the slope angle ϕ . The hillslope is supposed to form half of a symmetrical valley, such that the boundary at $x = 0$ can be taken as a no-flow boundary. Unless a channel is present, no significant water depth is maintained in the valley in the case of seepage outflow. Uniform convergence can be included by multiplying the lateral subsurface fluxes with the ratio R_c in (6.21). To determine the average water budget of the hillslope, the vertical fluxes must then be weighed by the planar surface through which they flow.

Note that for the rectangular hillslope layout and the Dupuit assumption in (6.7), seepage flow can only occur at the most downhill grid. The average seepage flow out of the hillslope is then given by (6.20). In reality the flow is two-dimensional and the groundwater flow lines bend towards the surface and the seepage flow is not restricted to the downhill grid only.

Vegetation parameters

Root extraction in (6.5) and (6.6) is completely defined by the depth of the rootzone ($z_s - z_r$) and the values of θ_c and θ_w . The vegetation fully covers the

soil surface. Bare soil evaporation is not treated explicitly, assuming transpiration to dominate the total evapotranspiration loss of water. The values of $(z_s - z_r)$ used in this study are 0.1, 0.2 and 0.3 m. The values of θ_c and θ_w are given by (3.3) evaluated at ψ values of -5 m and -160 m respectively. This implies that the amount of water potentially available to transpiration depends on the soil hydraulic properties. The ψ values are identical to the ψ_3 and ψ_4 values in Fig. 3.1.

6.5.2 Case studies

An arbitrary Reference Case and 15 additional cases were selected, each differing in one aspect from the Reference Case only. Table 6.1 describes the various cases

Table 6.1: List of the input parameters of the Reference Case. The additional cases are identical to the Reference Case with the exception of the indicated parameter.

Case	Climate	α	R_a	z_s [m]	$\sin \phi$	x_L [m]	$R_c(x_L)$	$z_s - z_r$ [m]	z_b [m]
Ref	SH	2	1	2	0.1	75	1	0.2	2
1a	A								
1b	H								
2a		1							
2b		3							
3			$2\frac{1}{4}$						
4a				1.5					
4b				4.0					
5a					0.05				
5b					0.15				
6						150			
7							15		
8a								0.1	
8b								0.3	
9a									1.25
9b									0.75

that differ with respect to climate, soil scale factor, anisotropy, soil depth, slope, hillslope length, convergence, rootzone depth and the presence of a channel at the downhill boundary. The horizontal node spacing $\Delta x = 1$ m is used for all cases except for the extended hillslope (Case 6) where $\Delta x = 2$ m. The vertical node spacing is taken as $\Delta z = 0.1$ m. The time step $\Delta t = 6$ min was chosen to prevent significant mass balance errors. The results presented here reflect time integrations over ten year, excluding a one year “warming-up” period to eliminate the effect of the arbitrarily chosen initial conditions. The storage change over

this period is very small compared to the other terms in the water budget and is therefore neglected.

6.6 Results of the case studies

The results of the Reference Case will be presented first and some characteristics of transient flow phenomena on hillslopes are highlighted. The discussion on Cases 1a - 9b is structured around three returning graphic panels. Two of these panels show the average evapotranspiration and recharge fluxes (both normalized for rainfall) along the hillslope while the third panel features the relative contribution of transients to the lateral groundwater flow.

Table 6.2 summarizes the hillslope average partitioning of rainfall over evapotranspiration, infiltration excess and saturation excess runoff, groundwater discharge through the seepage face and the discharge into the channel (if present) for all cases. Prior to discussing the various cases in detail, a few remarks about

Table 6.2: 10 year average water budget components as fractions of average rainfall integrated over the hillslope of the various cases. \bar{E} denotes evapotranspiration, \bar{q}_{ie} infiltration excess runoff, \bar{q}_{se} saturation excess runoff, \bar{q}_{sf} the flux through seepage face, \bar{q}_c the flux into channel and m.e. the mass balance error.

Case	\bar{E}	\bar{q}_{ie}	\bar{q}_{se}	\bar{q}_{sf}	\bar{q}_c	m.e.
Ref	0.737	0.013	0.206	0.009	-	0.035
1a	0.902	-	0.085	-	-	0.013
1b	0.587	-	0.344	0.061	-	0.008
2a	0.694	0.242	0.048	-	-	0.016
2b	0.740	-	0.180	0.055	-	0.025
3	0.731	0.013	0.190	0.044	-	0.022
4a	0.738	0.013	0.210	0.005	-	0.034
4b	0.729	0.013	0.171	0.050	-	0.037
5a	0.740	0.013	0.210	0.002	-	0.035
5b	0.730	0.013	0.190	0.031	-	0.036
6	0.737	0.013	0.208	0.003	-	0.039
7	0.740	0.013	0.205	0.009	-	0.033
8a	0.677	0.011	0.266	0.012	-	0.034
8b	0.773	0.014	0.175	0.007	-	0.031
9a	0.731	0.013	0.186	-	0.034	0.036
9b	0.717	0.013	0.168	-	0.069	0.033

some general features in Table 6.2 will be made. Comparison of the results for the Reference Case and the Cases 1a and 1b, shows that the most pronounced effect on the hillslope average water budget is caused by climatic forcing. The effect

of soil hydraulic properties (Cases 2a and 2b) and depth of the rootzone (Cases 8a and 8b) is less pronounced. The results of the other cases are very similar, in spite of the fact that the distribution of fluxes along the hillslope differ greatly, as will be shown later in this section. The mass error as a fraction of the mean rainfall is smaller than 0.04 for all cases.

6.6.1 Reference Case

General features

Fig. 6.8 shows three graphs that summarize most of the hydrological phenomena

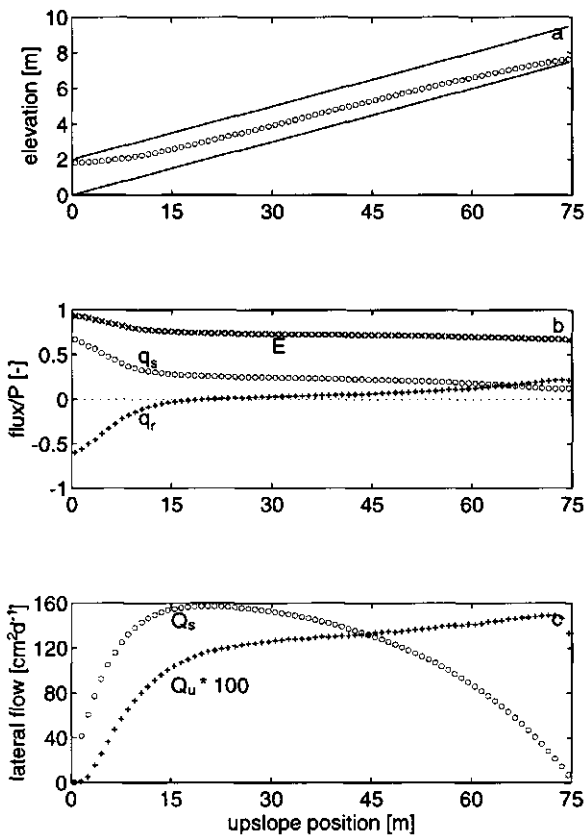


Figure 6.8: 10 year average results of the Reference Case: (a) Height of the phreatic surface h above the bedrock, (b) time average evapotranspiration \bar{E} , recharge \bar{q}_r and total surface runoff \bar{q}_s ($= \bar{q}_{se} + \bar{q}_{sc}$) fluxes normalized for rainfall and (c) magnitude of the mean lateral saturated flux \bar{Q}_s and the mean lateral unsaturated flux \bar{Q}_u .

acting on the hillslope defined in the Reference Case. The top panel shows the average position of the water table over the integration period of ten years. The second panel pictures the magnitude of average evapotranspiration, recharge and surface runoff fluxes, normalized by the average rainfall. The third panel shows the lateral saturated and unsaturated flow. Going from the divide in downhill direction to the valley, three regions can be distinguished.

In the uphill region ($\pm 30 \text{ m} \leq x \leq 75 \text{ m}$) the water table resides at relatively great depth, which prevents significant capillary rise and causes large storage capacity in the unsaturated zone. As a result, evapotranspiration and surface runoff fluxes are relatively small, resulting in a net recharge flux to the saturated zone (see Fig. 6.8a). This recharge causes the groundwater flow to increase in downhill direction which in turn forces the water table to rise relative to the bedrock. Note that the mean evapotranspiration as a fraction of the mean rainfall \bar{P} is 0.70, equivalent to a fraction of the mean potential evapotranspiration \bar{E}_p of 0.75. On average this points to considerable soil control over this region.

The midslope region ($\pm 15 \text{ m} \leq x < \pm 30 \text{ m}$) is characterized by a groundwater table being nearly parallel to the surface ($\frac{\partial h}{\partial x} \approx 0$). By virtue of (6.7), the average groundwater flow is relatively constant (see Fig. 6.8c) and the average recharge in this zone is close to zero accordingly (see Fig. 6.8a). Although significant transient negative and positive recharge fluxes do occur, on average, rainfall is partitioned mainly over evapotranspiration and surface runoff. Consistent with hydrogeological literature, this zone is called midline hereafter.

Near the valley ($0 \text{ m} < x < \pm 15 \text{ m}$), the water table approaches the surface because of the no-flow boundary condition at $x = 0$. The small storage capacity causes large surface runoff fluxes while large evapotranspiration fluxes during interstorm periods can be maintained because of capillary rise (negative recharge or discharge) from the phreatic surface (see Fig. 6.8b). In Table 6.2 the amount of groundwater discharge through the seepage face is small. The same table shows that the infiltration excess runoff mechanism is only of very little importance for this combination of climate and soil hydraulic properties and that virtually all surface runoff results from rain falling on saturated areas.

Finally, Fig. 6.8c shows the small amount of total mean unsaturated lateral flow $\bar{Q}_u = \int_h^z \bar{q}_x(z) dz$ relative to saturated lateral flow. Except for a small uphill region, where saturated flow is small, unsaturated lateral transport is nearly two orders of magnitude smaller than that in the saturated zone. In downhill direction lateral transport in the unsaturated zone decreases because the phreatic surface becomes closer to the soil surface.

Mechanisms inducing midline region

Although the presence of a midline region is more pronounced in some of the cases discussed later, the physical mechanisms initiating this region deserve attention here. Eq. (6.8) describes the dynamic behavior of the phreatic surface and is taken as a starting point for the discussion.

Following Salvucci [83, 1994], consider a steady situation $\frac{\partial h}{\partial t} = 0$. From (6.8) it follows that the recharge is then equal to the divergence of the groundwater flow, i.e. $q_r = \frac{dQ_s}{dx}$. Naturally, the recharge is positive where the water table resides deeply and negative (i.e. upward capillary water flow from the ground water) where the water table is shallow. The functional relationship between the recharge and the depth to the phreatic surface, $q_r(z_s - h)$, depends on the soil hydraulic properties and the climatic conditions. Let $z_s - h^*$ be defined by $q_r(z_s - h^*) = 0$. For the Reference Case in Fig. 6.8a $z_s - h^* \approx 100$ cm.

On a hillslope with a uniform soil, a situation where $\frac{dh}{dx} > 0$ would imply that the depth of the saturated zone increases in uphill direction and that recharge would occur downhill and discharge uphill, which is physically impossible. Hence, the depth of the saturated zone becomes smaller in uphill direction and $\frac{dh}{dx} \leq 0$ everywhere. Since over the midline region the phreatic surface runs parallel to the bedrock, i.e. $\frac{dh}{dx} = 0$, it then follows from (6.7) that

$$Q_s = k_s h \sin \phi \quad (6.22)$$

$$\begin{aligned} q_r &= \frac{dQ_s}{dx} \\ &= k_s \frac{dh}{dx} \sin \phi = 0 \end{aligned} \quad (6.23)$$

Thus over the midline the saturated lateral water transport equals $Q_s = k_s h^* \sin \phi$ which is limited by value h^* . Because of the no-flow condition at the divide x_L , the groundwater flow through the midline region is equal to the cumulative recharge uphill from position x^* where $h = h^*$:

$$k_s h^* \sin \phi = \int_{x^*}^{x_L} q_r(x) dx \quad (6.24)$$

The midline region thus acts as a restriction to the strength and the extent of the recharge zone. At the downhill boundary $x = 0$ water can only leave the hillslope through a seepage face where the phreatic surface reaches the land surface. The extent of the midline region is thus restricted by the downhill boundary. When the lateral transport capacity is large or when the hillslope is short, the uphill recharge will be restricted directly by the downhill boundary and the midline collapses to a point where $h = h^*$ but $\frac{dh}{dx} < 0$. In geohydrological literature this point is referred to as the hinge.

In summary, for steady state conditions, the midline establishes a "teleconnection" between the recharge and the discharge zone; water lost as recharge uphill

reappears in the water budget of the discharge zone, while leaving the budget of the midline unaffected.

For transient conditions the situation becomes slightly more complex. Using perturbation technique, the groundwater flow is divided into one part that is explained by the mean condition of the phreatic surface (shown in Fig. 6.8a) and another part that is caused by transient deviations from the mean state. At any time and position, the depth of the saturated zone can be written in time perturbation as:

$$h = \bar{h} + h' \quad \bar{h}' = 0 \quad (6.25)$$

where the overline indicates the time average and the prime a transient deviation from the average. Insertion of (6.25) into (6.7) and subsequently taking the time average yields

$$\bar{Q}_s = k_s \bar{h} \cos \phi \left(\frac{\partial \bar{h}}{\partial x} + \tan \phi \right) + k_s \overline{h' \frac{\partial h'}{\partial x}} \cos \phi \quad (6.26)$$

The first term on the right hand side of (6.26) represents the lateral transport explained by the mean state, whereas the second term indicates the groundwater flow due to transient deviations from the mean state. The second term can be rewritten as

$$\begin{aligned} k_s \overline{h' \frac{\partial h'}{\partial x}} \cos \phi &= k_s \text{cov} \left[h, \frac{\partial h}{\partial x} \right] \cos \phi \\ &= \frac{1}{2} k_s \frac{\partial \sigma^2 [h]}{\partial x} \cos \phi \end{aligned} \quad (6.27)$$

Because of the second term on the right hand side of (6.26) the explanation of the midline region has to be extended for transient conditions. Applying again the fact that on average the recharge over the midline is zero, it can easily be derived that

$$\frac{\partial \bar{Q}_s}{\partial x} = k_s \cos \phi \left[\frac{\partial \bar{h}}{\partial x} \left(\frac{\partial \bar{h}}{\partial x} + \tan \phi \right) + \bar{h} \frac{\partial^2 \bar{h}}{\partial x^2} + \frac{\partial \text{cov} \left[h, \frac{\partial h}{\partial x} \right]}{\partial x} \right] = 0 \quad (6.28)$$

As before, over a midline region $\frac{\partial \bar{h}}{\partial x}$ must be 0. From (6.28) then follows that the covariance term has to be spatially constant over the midline region as well. This can only be the case when for a rising or falling water table the gradient $\frac{\partial h}{\partial x}$ remains unchanged, i.e. the phreatic surface moves only normal to the bedrock. Now consider Fig. 6.9 where the phreatic surface is shown schematically for the mean state, a wet state and a dry state. In order to laterally drain the increasing water delivery from uphill during a storm event, the height h and/or the gradient of the phreatic surface $\frac{\partial h}{\partial x}$ have to increase. Since near the downhill boundary the phreatic level is closer to the soil surface, the potential increase of h is limited

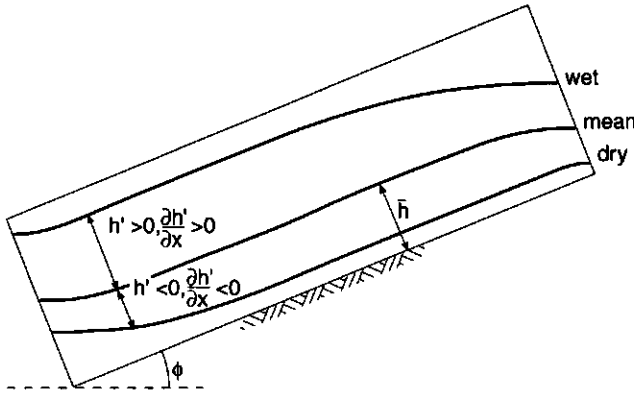


Figure 6.9: Schematic diagram of a wet, a dry and the mean state of a hillslope with a closed downhill boundary. The transient deviations from the mean height and gradient of the phreatic surface, h' and $\frac{\partial h'}{\partial x}$, are indicated.

and $\frac{\partial h}{\partial x}$ has to increase (i.e. become less negative) as well. In contrast, the reduced water delivery from uphill during a drying event forces h as well as $\frac{\partial h}{\partial x}$ to decrease. Near the divide the situation is exactly opposite as can be seen in Fig. 6.9. Hence, wetting and drying events bring about a positive correlation between h and $\frac{\partial h}{\partial x}$ near the valley and a negative correlation near the divide. Depending on the particular hillslope, a region may exist where the phreatic surface moves approximately parallel to the bedrock. Fluctuations of the phreatic surface are then mainly due to the transient behavior of recharge normal to the bedrock. A change of the water table then leaves the gradient of the phreatic surface largely unchanged and $\text{cov}\left[h, \frac{\partial h}{\partial x}\right] \approx 0$, which by virtue of (6.27) is equivalent to a spatially constant value of $\sigma^2[h]$. Thus, a necessary condition for the presence of a midline is a spatially constant zero covariance. This condition is not sufficient since a situation where $\bar{q}_r = 0$ and $\frac{\partial \bar{h}}{\partial x} \neq 0$ requires $\frac{\partial \text{cov}\left[h, \frac{\partial h}{\partial x}\right]}{\partial x} \neq 0$ in (6.28).

Since water transport from uphill down to the discharge zone would take years to decades, the teleconnection between uphill and downhill must not be interpreted as a direct recycling phenomenon. Rather, the pressure waves in the saturated zone restore and maintain an organization of the hillslope in three distinct regions.

In the discussion on the various cases indicated in Table 6.1, the relative contribution of transient deviations from the mean state to the average saturated lateral flow in (6.26) is indicated by the dimensionless ratio

$$\Lambda = \frac{k_s \text{cov}\left[h, \frac{\partial h}{\partial x}\right] \cos \phi}{Q_s} \tag{6.29}$$

In line with the above, a midline is present when over a region $\bar{q}_r = 0$ and $\Lambda = 0$.

Variance of saturated lateral flow

Because saturated lateral flow governs the teleconnection between the uphill recharge and downhill discharge area, it is interesting to look at the time variation of Q_s . In Appendix C it is shown that by neglecting third and fourth order terms the variance of saturated lateral flow can be approximated by:

$$\sigma^2 [Q_s] \approx k_s^2 \cos^2 \phi \left(\bar{h}^2 \sigma^2 \left[\frac{\partial h}{\partial x} \right] + \sigma^2 [h] \left[\frac{\partial \bar{h}}{\partial x} + \tan \phi \right]^2 + 2\bar{h} \text{cov} \left[h, \frac{\partial h}{\partial x} \right] \left[\frac{\partial \bar{h}}{\partial x} + \tan \phi \right] - \text{cov}^2 \left[h, \frac{\partial h}{\partial x} \right] \right) \quad (6.30)$$

The variance of groundwater flow can thus be explained by the patterns of mean height and gradient of the phreatic surface and their respective variances and covariance. The contribution of each term in (6.30) to the ratio $\frac{\sigma^2 [Q_s]}{k_s^2 \cos^2 \phi}$ of the Reference Case is shown in Fig. 6.10. The first term rapidly decreases in uphill

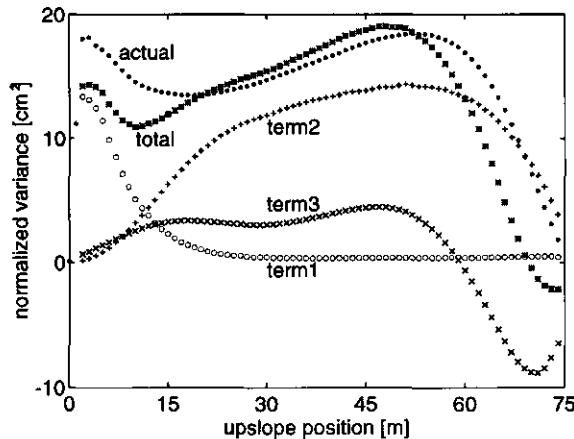


Figure 6.10: The contribution of the first three terms on the right hand side of (6.30) and their sum to the normalized variance $\frac{\sigma^2 [Q_s]}{k_s^2 \cos^2 \phi}$. Also shown is the actual value derived from the model simulations.

direction because the height of the phreatic surface decreases. Additionally, over the midline region the phreatic surface moves mainly normal to the bedrock and $\sigma^2 \left[\frac{\partial h}{\partial x} \right] \approx 0$. The second term increases in uphill direction because both the time variation and mean gradient $\frac{\partial \bar{h}}{\partial x}$ increase ($\frac{\partial \bar{h}}{\partial x} \approx 0$ over the midline). The third term closely follows the pattern of $\text{cov} \left[h, \frac{\partial h}{\partial x} \right]$. In line with the discussion on the midline in the preceding section, the third term vanishes over a midline region. The third term in Fig. 6.10 does not vanish, which indicates that a real midline is not present in the Reference Case. The contribution by the fourth term is

negligible in comparison to the first three terms and is not included therefore. The discrepancy between the actual variance of groundwater flow in the model and the approximate expression (6.30) results from the relatively small contributions of the third and fourth order terms omitted in the derivation in Appendix C.

6.6.2 Effect of climate

The results for the arid climate (Case 1a) and the humid climate (Case 1b) are presented in Fig. 6.11. Compared with the semi-humid climate of the Reference Case, the drying power, indicated by the ratio $\frac{\bar{E}_P}{\bar{P}}$ in Table 5.1, is stronger for

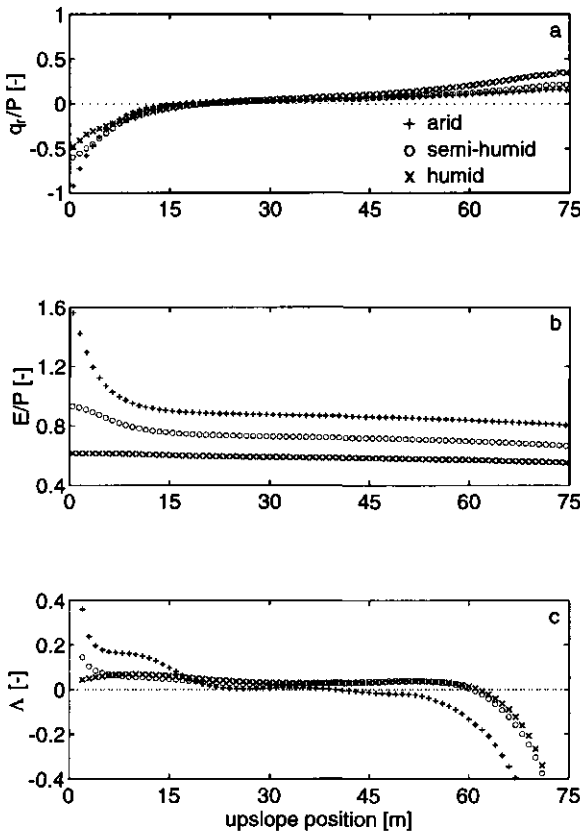


Figure 6.11: 10 year average fluxes for Case 1a (arid climate) and Case 1b (humid climate) in comparison to the Reference Case (semi-humid climate): (a) normalized recharge flux $\frac{q_r}{P}$, (b) normalized evapotranspiration flux $\frac{E}{P}$ and (c) the relative contribution of transient saturated lateral flow Λ .

the arid and weaker for the humid climate. As a result, the normalized recharge flux $\frac{\bar{q}}{P}$ is smallest for the arid and largest for the humid climate as shown in Fig. 6.11a.

In the discharge region the upward capillary flux is largest for the arid climate and is caused by the large potential evapotranspiration. The virtual absence of groundwater discharge in the arid climate in Table 6.2 shows that all water recharged uphill is lost to the atmosphere in the discharge region. The presence of a significant hillslope teleconnection is clearly illustrated in Fig. 6.11b since near the downhill boundary evapotranspiration is significantly higher than the rainfall. Obviously this would never occur when only vertical flow was considered. For the arid climate, the dryer average state of the hillslope causes saturation excess runoff q_{se} to decrease relative to the Reference Case, while the lower average rainfall rate (see Table 5.1) prevents infiltration excess runoff q_{ie} . The depth to the phreatic surface where recharge is zero, $z_s - h^*$, is greater than for the semi-humid climate. The resulting limited lateral transport capacity $k_s h^* \sin \phi$ promotes the formation of a midline (see Fig. 6.11a,c), as was explained in Section 6.6.1.

For the humid climate, the significant recharge uphill cannot be entirely balanced by evapotranspiration in the discharge region. Although evapotranspiration occurs at the potential rate on average over a 10 m region adjacent to the downhill boundary, a fraction of 0.061 of the rainfall leaves the hillslope as groundwater runoff through the seepage face. The same reasoning explains the increase in saturation excess runoff compared to the Reference Case. The fact that in Fig. 6.11c there is no region where $\Lambda = 0$ indicates that no clear midline exists. As for the arid climate, no infiltration excess occurs because of the low average rainfall rate.

6.6.3 Effect of soil scale factor

The results of changing soil scale factor α to 1 (Case 2a) and 3 (Case 2b) are shown in Fig. 6.12. Decreasing soil scale factor α results in a smaller saturated conductivity k_s and hence an increase in average infiltration excess runoff q_{ie} in Table 6.2. The smaller lateral transport capacity induces the presence of an extended midline in Fig. 6.12a,c where $\bar{q}_r = 0$ and $\Lambda = 0$ over a significant length. The smaller amount of uphill recharge causes the increase of evapotranspiration in downhill direction to be less pronounced compared to the Reference Case (Fig. 6.12b). Due to the increase in infiltration excess runoff, the saturation excess runoff decreases compared to the Reference Case. Virtually no groundwater runoff through the seepage zone occurs.

Obviously, the effects of increasing α are opposite. Infiltration excess runoff does not occur and the large lateral transport capacity causes the collapse of the midline into a (hinge) point. Uphill recharge increases relative to the Reference Case, resulting in significant increase of evapotranspiration in downhill direction. Long-term average evapotranspiration becomes even potential over the 5 m adjacent

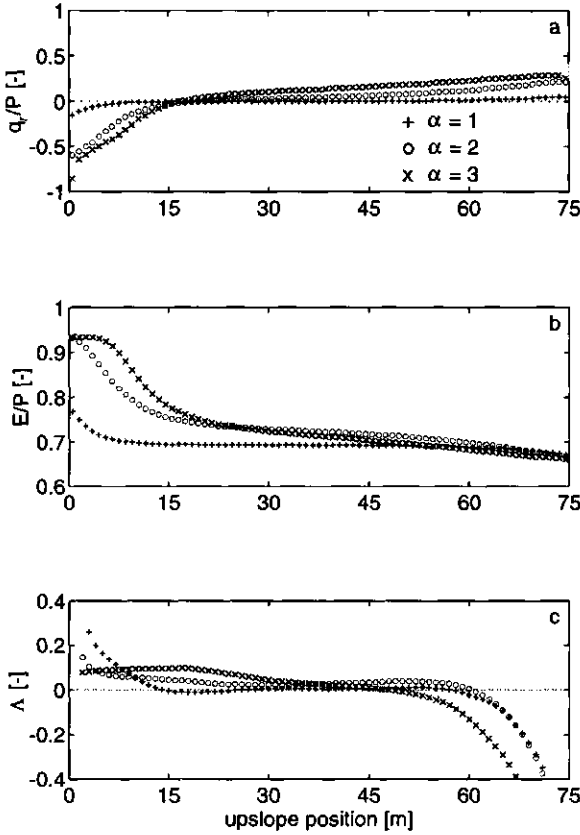


Figure 6.12: 10 year average fluxes for Case 2a ($\alpha = 1$) and Case 2b ($\alpha = 3$) in comparison to the Reference Case ($\alpha = 2$): (a) normalized recharge flux $\frac{\bar{q}}{P}$, (b) normalized evapotranspiration flux $\frac{\bar{E}}{P}$ and (c) the relative contribution of transient saturated lateral flow Λ .

to the downhill boundary. The, on average, wetter state of the hillslope near the valley increases the seepage flow, although partly at the expense of saturation excess runoff (see Table 6.2).

Not depicted in Fig. 6.12 are the simulation results for the anisotropy ratio $R_a = 2\frac{1}{4}$ (Case 3) which corresponds to the vertical conductivity of the Reference Case and the lateral conductivity of Case 2b. By and large, the results are identical to Case 2b, both for the patterns of the fluxes over the hillslope and for the hillslope average water budget in Table 6.2. This confirms the dominating role of the saturated lateral transport capacity.

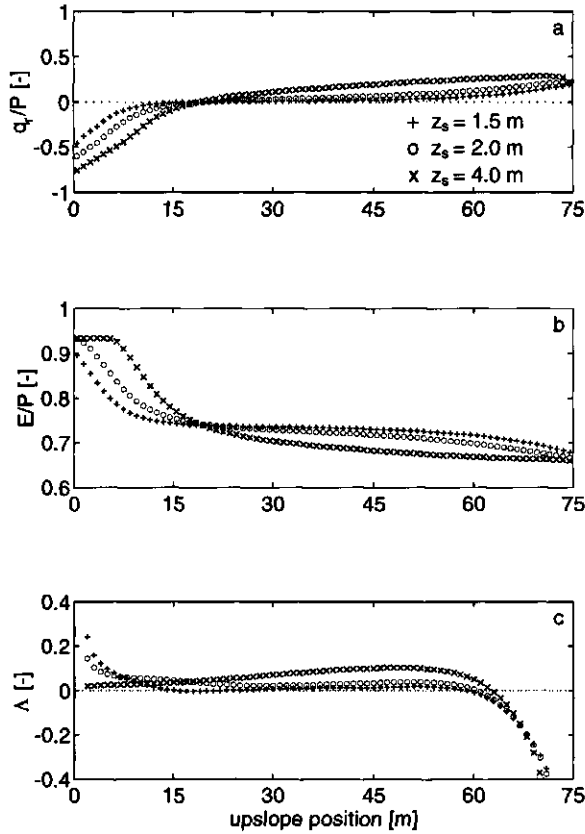


Figure 6.13: 10 year average fluxes for Case 4a ($z_s = 1.5$ m) and Case 4b ($z_s = 4.0$ m) in comparison to the Reference Case ($z_s = 2.0$ m): (a) normalized recharge flux $\frac{q}{P}$, (b) normalized evapotranspiration flux $\frac{E}{P}$ and (c) the relative contribution of transient saturated lateral flow Λ .

6.6.4 Effect of soil depth

In Fig. 6.13 the results of decreasing and increasing soil depth z_s (Cases 4a and 4b respectively), are shown. Decreasing the soil depth to 1.5 m reduces the strength of the recharge fluxes since the phreatic surface resides closer to the soil surface. Because the soil properties and the climate are identical to the Reference Case, the depth to the phreatic surface where recharge is on average zero ($z_s - h^*$), is identical as well. The lateral transport capacity thus becomes smaller since h^* has to decrease by the same amount as z_s . As a result, a clear midline develops (see Fig. 6.13a,c) that limits the extent of the recharge zone to an amount that can be laterally drained. Again, the smaller uphill recharge causes the increase

of evapotranspiration in downhill direction to be less pronounced in comparison to the Reference Case in Fig. 6.13b.

The results for the deep soil are exactly opposite. The midline collapses into a point and the connection between the uphill and downhill regions becomes stronger, illustrated by a zone of several meters downhill where evapotranspiration is potential on average.

Despite the very different partitioning of rainfall over the fluxes along the hillslope, the integrated water budgets of the Reference Case and the Cases 4a and 4b are not very different (see Table 6.2). The increase in groundwater runoff through the seepage face for the deep soil case is largely balanced by a decrease in saturation excess runoff. It must be kept in mind, however, that this conclusion holds for the long-term averages. On shorter time scales (of the order of days to weeks) the budgets are likely to differ substantially, because of the typical time scale of saturated transport.

6.6.5 Effect of slope

The results of reducing and increasing the slope (Cases 5a and 5b respectively) are presented in Fig. 6.14. As expected, the decreased lateral transport capacity for the reduced slope causes a somewhat more pronounced midline region (see Fig. 6.14a,c). Again, the smaller net recharge uphill causes evapotranspiration downhill to increase less compared to the Reference Case (see Fig. 6.14a,b). For the increased slope the results are the opposite.

The relative contribution of transients to the mean saturated lateral transport indicated in (see Fig. 6.14c) nearly vanishes for all three cases. In spite of that a midline is not present for the increased slope case $\bar{q}_r \neq 0$ in Fig. 6.14a). This emphasizes that $\Lambda = 0$ is a necessary but not a sufficient condition for a midline region.

The hillslope average water budget terms for the three cases considered here do not differ significantly (Table 6.2), the main distinction being the division of rainfall over groundwater seepage outflow and saturation excess runoff.

6.6.6 Effect of hillslope length and convergence

For Case 6 (hillslope length $x_L = 150$ m) and Case 7 (convergence ratio $R_c(x_L) = 15$) the results are shown in Fig 6.15. Because the maximum hydraulic gradient and transmissivity remain unchanged when increasing the hillslope length, the magnitude and the extent of the recharge and discharge zone do not change and the midline is expected to fill up the difference in length with the Reference Case. This can be seen indeed in Fig. 6.15 where recharge and evapotranspiration are virtually constant over a significant portion of the midline. Also, the hillslope

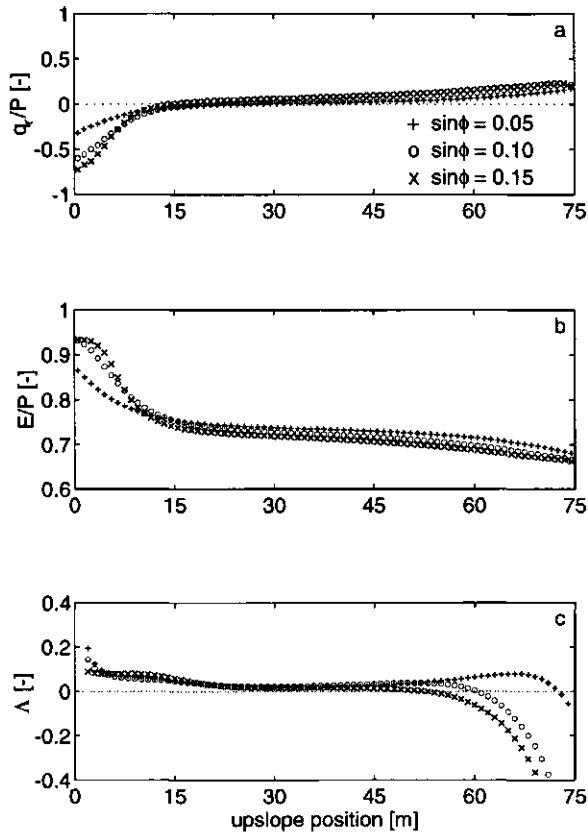


Figure 6.14: 10 year average fluxes for Case 5a ($\sin \phi = 0.05$) and Case 5b ($\sin \phi = 0.15$) in comparison to the Reference Case ($\sin \phi = 0.10$): (a) normalized recharge flux $\frac{q}{P}$, (b) normalized evapotranspiration flux $\frac{E}{P}$ and (c) the relative contribution of transient saturated lateral flow Λ .

average water budget terms in Table 6.2 almost show no difference with the Reference Case.

Convergence of the flow domain causes the depth of the saturated zone to increase faster in downhill direction in comparison to the Reference Case. This reduces the extent of the recharge zone and the disappearance of the midline region (Fig. 6.15a,c). Over the entire hillslope, evapotranspiration occurs at a higher rate relative to the Reference Case. When integrating the water budget over the hillslope, weighing the vertical fluxes by the area they flow through, the difference with the Reference Case is small, however. This is because the rather extreme convergence ratio $R_c = 15$ causes the by far largest fraction of the hillslope area

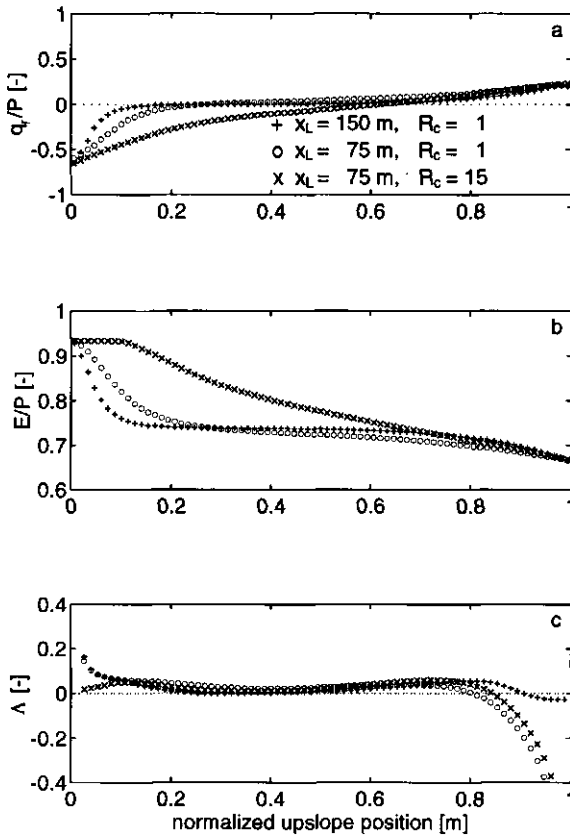


Figure 6.15: 10 year average fluxes for Case 6 ($x_L = 150$ m) and Case 7 ($R_c(x_L) = 15$) in comparison to the Reference Case: (a) normalized recharge flux $\frac{q}{P}$, (b) normalized evapotranspiration flux $\frac{E}{P}$ and (c) the relative contribution of transient saturated lateral flow Δ . The uphill position is normalized using the hillslope length x_L .

to be uphill, where the difference with the Reference Case is very small.

6.6.7 Effect of rootzone depth

Fig. 6.16 shows the results for Case 8a (depth of the rootzone $z_s - z_r = 0.1$ m) and Case 8b ($z_s - z_r = 0.3$ m). The smaller availability of water resulting from a shallower root zone reduces evapotranspiration considerably over almost the entire hillslope (see Fig. 6.16b). Evidently, the results for the deeper root zone are the opposite. The small region near the downhill boundary, where evapotranspiration is highest for the shallow root zone, is explained by the larger uphill recharge that

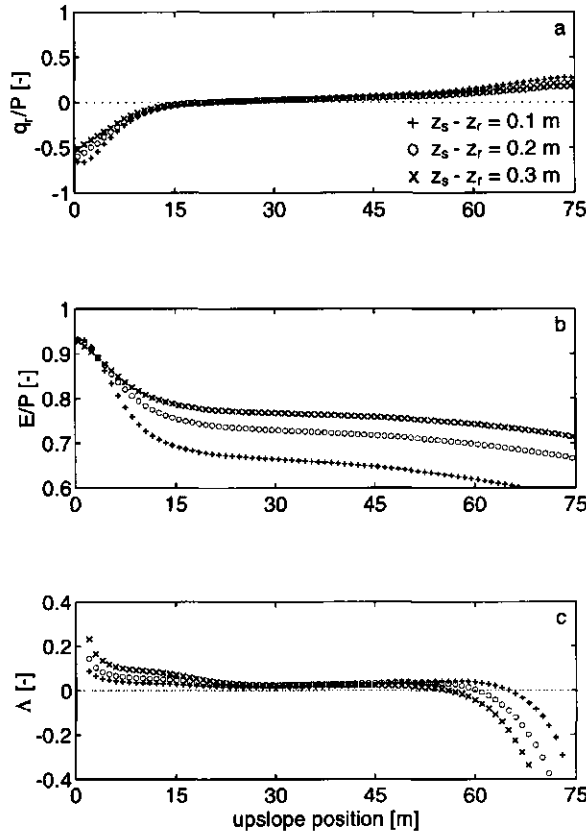


Figure 6.16: Time average fluxes for Case 8a ($z_s - z_r = 0.10$ m) and Case 8b ($z_s - z_r = 0.30$ m) in comparison to the Reference Case ($z_s - z_r = 0.20$ m): (a) normalized recharge flux $\frac{q_r}{P}$, (b) normalized evapotranspiration flux $\frac{E}{P}$ and (c) the relative contribution of transient saturated lateral flow Λ .

balances the smaller evapotranspiration, as can be seen in Fig. 6.16a. The average water budget terms of the entire hillslope in Table 6.2 differ considerably, the changes in evapotranspiration are largely balanced by the changes in saturation excess runoff.

6.6.8 Effect of channel at downstream boundary

In this section a channel with a constant water level h_c of 0.25 m serves as down-hill boundary (see inset of Fig. 6.1). Flow from the hillslope into the channel is only possible through the saturated zone and is described using the Dupuit assumption. Two different levels of the channel bottom have been used, $z_b =$

1.25 and 0.75 m (Cases 9a and 9b respectively) and the results are shown in Fig. 6.17. Not surprisingly, near the channel the phreatic surface resides deeper

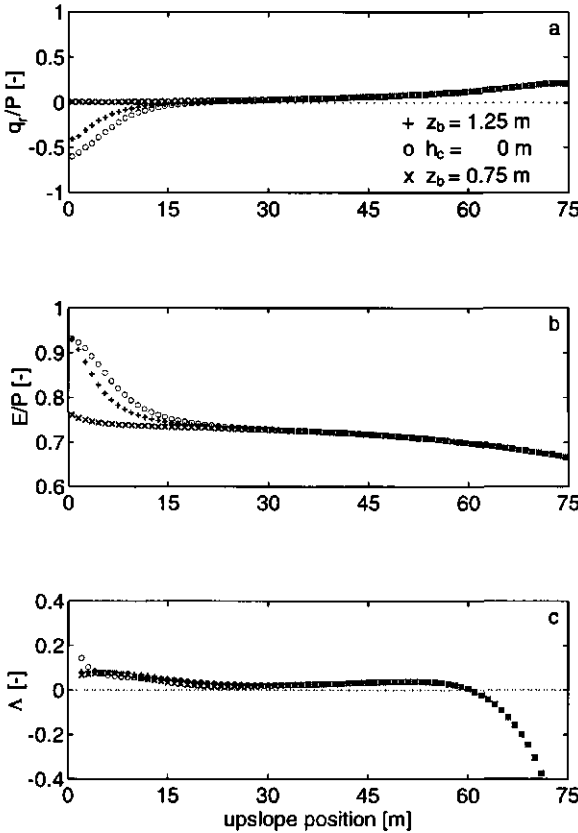


Figure 6.17: 10 year average fluxes for Case 9a ($z_b = 1.25$ m, $h_c = 0.25$ m) and Case 9b ($z_b = 0.75$ m, $h_c = 0.25$ m) in comparison to the Reference Case (no channel; $h_c = 0$ m): (a) normalized recharge flux $\frac{q_r}{P}$, (b) normalized evapotranspiration flux $\frac{E}{P}$ and (c) the relative contribution of transient saturated lateral flow Λ .

compared to the Reference Case, causing greater recharge and smaller evapotranspiration fluxes (Fig. 6.17a,b). The effect of the channel is limited to the first 30 m uphill beyond which the hillslope behaves identically to the Reference Case. This is caused by the transmissivity and gradient of the phreatic surface needed to transmit water that is recharged uphill. The hillslope average water budget terms in Table 6.2 show the discharge of water into the channel and the corresponding disappearance of flow through the seepage face. As expected, lowering of the channel bottom causes an increase in the groundwater discharge and a

decrease in evapotranspiration and surface runoff fluxes. The differences with the Reference Case are not as large as expected. If the channel bottom were located deeper, however, the flow of groundwater into the channel would be higher and the difference would become more pronounced. Another reason for the small differences is that water extraction by plant roots is very effective in limiting the amount of recharge and hence groundwater discharge.

6.7 Conclusions

A mixed analytical-numerical model of hillslope hydrological behavior is presented, partly verified and applied to explore the role of climate, soil hydraulic properties, geomorphology and vegetation on hillslope hydrological behavior. The model includes the transient effects induced by intermittent rainfall and drying events. The following conclusions can be drawn:

1. The proposed model provides a satisfactory reproduction of the measured transient response of the phreatic surface to a storm event for a catchment in New Zealand. Additional verification over much longer times is needed in the future, however;
2. The model is computationally efficient as indicated by the possibility to perform a considerable number of water budget simulations over very long times (ten year) with a high lateral resolution;
3. For most cases considered, the hillslope organizes itself into three distinct regions, a recharge and a discharge zone connected by a midline region. This division induces an internal hillslope "teleconnection" between the uphill recharge and the downhill discharge zones;
4. The magnitude of unsaturated lateral flow is very small compared to the groundwater flow. Its effect on the redistribution of water along the hillslope is minimal and can be safely neglected;
5. Despite the very different distribution of fluxes over the hillslope, the spatially average long-term water budget of many of the considered cases do not show large differences for of two reasons. First, the rectangular hillslope lay-out and the closed lower boundary do not favor the occurrence of groundwater outflow. Secondly, water extraction by roots is very efficient in preventing large recharge fluxes uphill. On event time scales, however, the behavior of the various cases differ substantially;
6. It is stressed that different combinations of climate, soil hydraulic properties, geomorphology, vegetation and lower boundary conditions are likely to bring about considerably different hillslope hydrological behavior given the high degree of nonlinearity so clearly present in all results.

Chapter 7

Epilogue and general conclusions

The water budget of the land surface incorporates hydrological processes at a wide range of space and time scales. These processes are generally nonlinear and exhibit considerable spatial variation. No universal technique is available to transfer hydrological information from one scale to another (aggregation/disaggregation). The objective of this thesis, as formulated in Chapter 1, therefore was

‘to obtain quantitative insight into the effect of spatially heterogeneous hydrological processes that constitute the water budget of the land surface.’

In this epilogue, the scale transitions investigated in this thesis will be summarized first. Subsequently, a different approach is taken in which the models are presented as limiting cases of realistic situations. Finally, the key findings are summarized and some remaining questions are discussed.

7.1 Investigated scale transitions

Because of their complex nature, spatial heterogeneity of soil hydraulic characteristics and rainfall can best be accounted for using stochastic methods. When there is no groundwater interaction, the unsaturated flow is mainly vertical so that a one-dimensional approach suffices, even for undulating topography. As was the case in Chapters 3 - 5, an area is then assumed to behave like an ensemble of independent soil columns, each with their own soil hydraulic characteristics and/or rainfall time series. When the phreatic surface is close enough to the land surface to exert a substantial effect on the water budget of the unsaturated zone, lateral groundwater flow may become an important source of spatial heterogeneity of the water budget components. An area can then no longer be represented as an ensemble of one-dimensional soil columns and the two or three-dimensional flow phenomena must be represented deterministically. This approach was followed in Chapter 6.

Table 7.1 shows for each of the Chapters 3 - 6 which sources of heterogeneity were considered and in how many dimensions flow was present. Each of the sources of heterogeneity in Table 7.1 had a characteristic length scale. It is thus possible to indicate the time and space scale transitions for each of the chapters.

Table 7.1: Scope of the four chapters as regards the presence of the four main topics in this thesis.

	Chapter 3	Chapter 4	Chapter 5	Chapter 6
soil heterogeneity	+	+	+	-
rain heterogeneity	-	+	+	-
groundwater	-	-	-	+
dimensionality	1	1	1	2

Throughout this thesis the physics of soil water movement are described at the spatial scale of a REV ($\approx 10^{-2}$ m - 10^{-1} m). The vertical length scale of the problems considered is of the order of 10^0 m over which the soil is assumed to be uniform. The boundary conditions imposed on the REV determined the characteristic time scale of the considered flow problem. With the exception of Chapter 3, where the atmospheric variables were daily averages, the time scale of the meteorological forcing was of the order of hours. Section 4.3.4 showed that the characteristic length scales associated with soil and rainfall heterogeneity were of the order of 10^2 m and 10^4 m respectively. Finally, the typical length scale of the deterministic flow processes on the hillslope scale considered in Chapter 6 were of the order of 10^2 m. Using this information, the various scale transitions in this thesis are depicted in Fig. 7.1. For each chapter a few remarks are added below to assist in the correct interpretation Fig. 7.1.

In Chapter 3 the time consistency of two parametric models for describing the annual water budget ($\approx 10^4$ h) was determined through comparison with numerical solutions of Richards' equation (2.11). Basically, the parametric "bucket" models consider only mass conservation and can therefore in principle be applied on any scale. Since they maintain only one (homogeneous) moisture state however, their associated scale of validity is comparable to the scale of the REV, although they are intended for use at very large scales (the scale of a climate modeling grid, of the order of 10^4 m and 10^5 m). The arrow in Fig. 7.1 in association with Chapter 3 relates to the stochastic simulations performed to investigate the suitability of the scaled average reference soils to account for the effects of spatial heterogeneity on the average water budget.

The scale transitions studied in Chapter 4 were related to the effect of heterogeneity of soil hydraulic characteristics and/or rainfall intensity on the areally average partitioning of rain over the components of the soil water budget for a time period of a year ($\approx 10^4$ h). The two arrows reflect that the characteristic

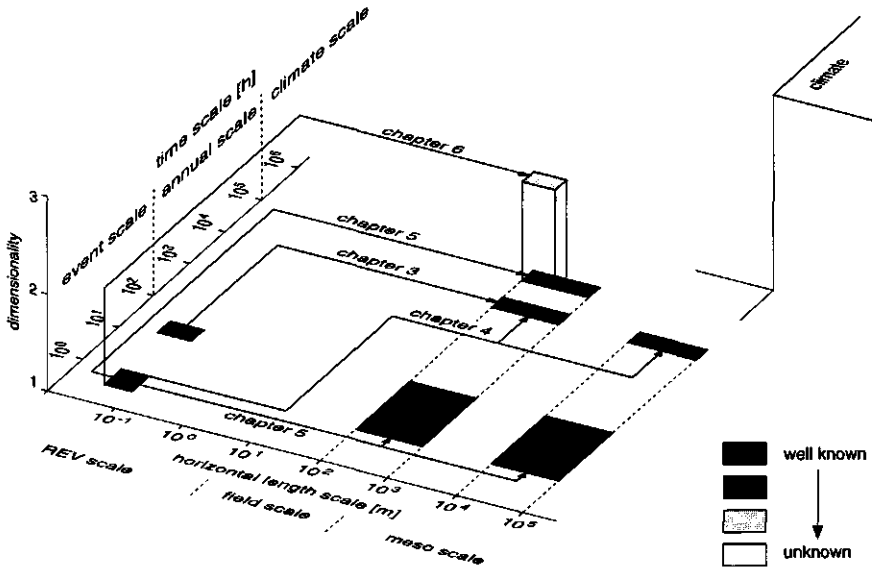


Figure 7.1: Time and space scale transitions of the chapters in this thesis.

length scale of soil and rainfall heterogeneity are disparate ($\approx 10^2$ m and $\approx 10^4$ m respectively)

In Chapter 5 a similar transition as in Chapter 4 was achieved, except that the analytic formulation of the used model allowed a longer time integration (15 year $\approx 10^5$ h). The other two transitions in Chapter 5 indicate the derived distributions of infiltration and evapotranspiration that are valid for the time scale of a storm or interstorm period ($\approx 10^0$ h - 10^2 h).

Finally, in Chapter 6 the transition in scale did not arise because of the incorporation of heterogeneity with a distinct spatial scale, but because of accounting for two-dimensional flow phenomena. The considered hillslope scale was of the order of 10^2 m and computations were carried out for 10 years ($\approx 10^5$ h)

7.2 Investigated models as limiting cases of reality

Rather than the scale transitions achieved in the previous chapters, the connection between the models addressed in the various chapters can be demonstrated.

In Table 7.2 the models that were used are indicated as limiting cases with respect to their assumptions on lateral conductivity, the conductivity at the lower boundary, the shape of the moisture profile and the presence of a slope.

Table 7.2: Scope of the various model studies as limiting cases of reality; $k^{lateral}$ denotes the lateral conductivity, k^{bottom} the conductivity at the lower boundary, k^{ug} the conductivity associated with the unit gradient condition, $\theta(z)$ the vertical distribution of moisture and ϕ the slope angle.

Model	$k^{lateral}$	k^{bottom}	$\theta(z)$	ϕ
Deardorff, Chapter 3	∞	0	uniform	0
Warrilow, Chapter 3	∞	k^{ug}	uniform	0
Analytical, Chapter 5	0	k^{ug}	uniform	0
Richards, Chapters 3, 4	0	k^{ug}	variable	0
Hillslope, Chapter 6	$[0, \infty)$	0	variable	$[0, \pi]$

The Deardorff and Warrilow models in Chapter 3 are one-dimensional and do not allow for spatial heterogeneity. Mathematically, this is equivalent to an infinitely large conductivity in the lateral direction. The application of the (homogeneous) analytical model presented in Chapter 5 can best be pictured as an ensemble of non-interacting buckets (hence $k^{lateral} = 0$), each of which is similar to the Warrilow model. In Chapter 3 and especially Chapter 4, Richards' equation was solved numerically and spatial heterogeneity was accounted for by Monte Carlo simulation of a large number of non interacting soil columns. Finally, in the hillslope model described in Chapter 6 the lateral interaction was not regarded as a limiting case, but incorporated explicitly.

7.3 Principal conclusions and remaining questions

7.3.1 Modeling the lower boundary in one-dimensional climate-scale models

In Chapter 3 it appeared that the water budget as described by the parametric Deardorff and Warrilow models was strongly affected by the conditions at the lower boundary. It was argued that the two conditions were limiting cases: a no-flow and a gravity outflow or unit gradient condition (see Table 7.2). The question that was briefly touched upon in Chapter 3 and is brought up again here is which condition can be regarded as closest to reality. When the phreatic surface resides deep enough to prevent upward capillary flow, gravity flow out of the soil reservoir is most realistic. However, the results of Chapter 6 show that

water lost by recharge at upslope locations may reappear in the water budget of downslope locations, because of lateral saturated flow. As shown in Chapter 6, the total amount of water lost by the hillslope to the surface water system depends on soil hydraulic properties, geomorphological layout of the hillslope and climate. Obviously, no simple answer is possible to the question raised, but important information may be inferred from the drainage characteristics of an area. This issue will be addressed in Section 7.3.6.

7.3.2 Influence of short time scale phenomena for the long-term average water budget

In Chapter 3 it was also concluded that the scaled average or reference soil hydraulic characteristics describe the effect of soil heterogeneity on transient unsaturated flow very well for a loam and reasonably well for a sand soil. For the latter this conclusion was partly confirmed in Chapter 4 (see Fig. 4.5), where it appeared that the median scale factor (rather than the average) may serve as an "equivalent" soil. For the loam soil, however, it was found in Chapter 4 that an equivalent soil was not present (see Fig. 4.6), not even for the annual average water budget. This discrepancy is explained by the considerably lower rainfall intensities in the daily average meteorological forcing in Chapter 3 and the resulting absence of infiltration excess runoff. This shows the importance of short-time scale transient phenomena (of the order of 10^0 h) for the long-term mean behavior.

In Chapter 5 and Chapter 6 the meteorological forcing was modeled as a Poisson arrival process of rectangular pulses of rainfall and potential evapotranspiration. Although this accounts for the critical intermittency of storm events, the diurnal and seasonal cycles of (potential) evapotranspiration were not included. The influences of the diurnal and seasonal cycle on the hydrological behavior depend on the time memory of the model considered. In the analytical model in Chapter 5, the time memory decreases with hydraulic conductivity because of the resulting lower percolation rates at the lower boundary. A completely closed lower boundary has the longest time memory, as is illustrated by the overestimation of transpiration by the Deardorff model in Chapter 3. For most realistic cases, the relatively small depth of the soil reservoir considered in Chapter 5 will result in a limited time memory and will probably prevent a large effect when seasonality is incorporated. It is likely, however, that incorporation of the diurnal cycle will affect the results more significantly. Because the various processes considered in the hillslope model in Chapter 6 cover a wider range of time scales, both the diurnal and the seasonal cycle will exert influence on the hydrological behavior. Hence, these issues deserve attention in future research.

7.3.3 Existence and meaning of equivalent parameters

The fact that in Chapter 4 equivalent properties could be derived for the sand soil but not for the loam soil relates to the fact that infiltration excess runoff is a threshold process, which, by definition, is highly nonlinear. The stronger nonlinear a process, the less likely it can be satisfactorily represented by means of a model with an equivalent parameter, or set of parameters. This was shown in detail in Chapter 5, where it appeared that equivalent clay soil parameters can be satisfactorily determined for the long-term average water budget for the semi-humid climate but not for the arid climate (see Section 5.6.2). The dependence of the water budget on the soil parameters was indeed more linear for the semi-humid climate than for the arid climate.

From the above it is also clear that an equivalent parameter set does not solely depend on soil type and heterogeneity but also on climatic conditions. By the same token, when one would attempt to describe spatial climatic heterogeneity (such as rainfall heterogeneity over a climate modeling grid) by means of equivalent quantities, these would depend on the soil and land-surface properties! Obviously this situation is undesirable, but it illustrates that the concept of equivalent parameters should be treated with great care when considering a coupled system such as the land surface-atmosphere interaction.

Chapter 5 also showed that the maximum number of equivalent parameters that can be determined is equal to the number of independent components in the water budget. Of the four components of the water budget (saturation and infiltration excess surface runoff, evapotranspiration and percolation), maximally three are independent since the fourth can be inferred from their sum and the rainfall. In case fewer fluxes are present - or observed - less equivalent parameters can be determined. Furthermore, because the nonlinearity of hydrological processes changes with the time scale on which they are considered, equivalent properties derived for the long-term mean behavior are not necessarily valid on much shorter time scales (see also Section 5.6.2).

7.3.4 Characteristic spatial scales of water budget heterogeneity

So far, the influence of heterogeneity on the areally average water budget was discussed. However, the characteristic length scale at which this heterogeneity becomes manifest may also be important. When heterogeneity is present mostly at small scales, it is not likely that it will induce spatial heterogeneity of the overlying atmosphere because of the integrating power of the boundary layer. On larger scales however, heterogeneity of the surface fluxes may give rise to local circulations on scales smaller than the climate modeling grid. This has

indeed been observed in the HAPEX campaign in South-West France in 1986 [91, Shuttleworth 1988].

Once the influence of soil and rainfall heterogeneity on the water budget is known, the disparity in scales at which both are manifest allows the characteristic scales of water budget heterogeneity to be allotted (see Fig. 7.1). The computations in Chapter 4 reveal that heterogeneity of the water budget components is for the loam soil mostly present at field scale (due to soil heterogeneity) and to a lesser extent at the meso-scale (due to either temporally correlated or uncorrelated rainfall heterogeneity). For the sand soil the heterogeneity becomes manifest mostly at the meso-scale (due to temporally correlated rainfall heterogeneity, or heterogeneity of the total storm amount).

It is important to note that heterogeneity of the water budget components for the sandy soil was entirely due to heterogeneity of the total storm amount (i.e. temporally correlated rainfall heterogeneity). In contrast, the presence of surface runoff in case of the less conductive loam soil causes heterogeneity of the rain intensity to have most influence. Hence, the influence of rainfall heterogeneity on the soil water budget depends on its origin and on the soil type.

7.3.5 Spatial heterogeneity on event time scale

In Chapter 5 the probability density and distribution functions of infiltration and evapotranspiration rate were derived for univariate heterogeneity of saturated conductivity, rainfall intensity and initial water content. By tracing the temporal evolution of the distributions, insight into the time dependence of heterogeneity of water budget components was obtained for the event time scale ($\approx 10^0$ h - 10^2 h, see Fig. 7.1). The mechanisms through which different sources of heterogeneity affect the water budget can conveniently be investigated using the obtained expressions. The concept of deriving the distributions of the fluxes can be extended to situations where two or more sources of heterogeneity are simultaneously present. It is unlikely though that explicit analytical distributions can then still be obtained. The numerical integrations that must be performed otherwise are nevertheless preferable over Monte Carlo simulations.

For the purpose of water budget computations, the derived distributions of event cumulative infiltration and evapotranspiration amounts would be of great interest and may therefore be a topic of future research. For cumulative infiltration this implies that the inverse relations $k_s(i^{\text{cum}})$ and $P(i^{\text{cum}})$ of (5.14) have to be determined. Although no explicit inversions are possible, an implicit relation still allows the derivation of a closed form distribution function. Maller and Sharma [54, 1984] presented a numerical solution for the distribution function $F(i^{\text{cum}}|S, k_s)$ where the sorptivity S and the saturated conductivity k_s are assumed to be bivariate lognormally distributed and not functionally coupled. For cumulative

event evapotranspiration, the relations $k_s(E^{\text{cum}})$ and $s_0(E^{\text{cum}})$ are inversions of the series expansion (5.30). A power series can be inverted [2, Abramowitz and Stegun 1970], but given the complexity of (5.30) it will probably involve a considerable effort. As a first approximation it would be better to use the much simpler expression (5.31), for which the inverse relation $k_s(E^{\text{cum}})$ can be expressed in an explicit form and the inverse relation $s_0(E^{\text{cum}})$ must be obtained implicitly.

7.3.6 Effect of simultaneous deterministic and stochastic heterogeneity on hillslope hydrological behavior

In this thesis, stochastic and deterministic sources of heterogeneity were considered separately. Obviously, in reality they often occur simultaneously and their individual contributions to the observable heterogeneity of water budget components become obscured by feedback processes due to the nonlinearity of the system. In the remainder of this chapter some speculations will be made about the effects of spatial heterogeneity on hillslope hydrological behavior.

Over a hillslope, flow phenomena are non-uniform, as shown in Chapter 6. Hence, upon introducing lateral soil variation on the two-dimensional hillslope illustrated in Fig. 6.1, the hydrological response will be affected by the spatial sequence of soil hydraulic properties. In other words, hillslopes that are identical in a statistical sense may yield different hydrological behaviors. The non-uniformity of the flow also causes the influence of soil heterogeneity to depend greatly on the dimensionality of the model: an impermeable vertical soil column entirely obstructs lateral flow in case saturated flow is modeled in only one dimension, whereas it can easily be surpassed when the model is two-dimensional. Hence, when incorporating spatially heterogeneous soil properties, a two-dimensional model (one vertical and one lateral direction) no longer suffices and flow in all three dimensions must be considered. Moreover, the spatial correlation structure of soil hydraulic properties that was neglected in this thesis must be taken into account as well.

Sharma *et al.* [87, 1987] considered such a problem to investigate the joint effect of soil heterogeneity and topography on the runoff production during a storm event. In that study the fact that statistically identical hillslopes may behave differently is evident because the hillslope behavior changes when tilting it backward rather than forward. Sharma *et al.* used Monte Carlo simulation with a three-dimensional hillslope model to determine the expected hydrological behavior for some particular combinations of hillslope layout and probability distribution and spatial correlation functions of the soil scale factor. It is needless to mention that undertaking such an effort on a climatic time scale and for different hillslope configurations and soil properties is virtually impossible because of the enormous computational effort it would require.

For complex problems like these, Kühnel *et al.* [49, 1991] state that partial analysis may be applied to provide plausible limits to a solution which cannot be obtained in explicit form. In the following, a rather rudimentary partial analysis is presented for hillslope hydrological behavior in the presence of soil heterogeneity.

Consider an area with heterogeneity of the soil hydraulic properties that is represented by a battery of homogeneous soil columns. Because under most circumstances lateral unsaturated flow can be safely neglected (see Chapter 6), lateral connections between the columns occur only because of the presence of a saturated zone. When the saturated conductivity in the lateral direction is zero and there is a unit gradient lower boundary conditions for all soil columns, the results of Chapter 4 are obtained (as indicated in Table 7.2). In case the lower boundaries of the soil columns are closed and the lateral saturated conductivity is infinite, the hydrological behavior is governed by the boundary condition at the drainage basis of the region (the downslope boundary for the hillslope in Chapter 6). For an entirely open drainage basis, each water particle that reaches the impermeable layer that underlies the soil columns instantaneously leaves the area, regardless of the slope of the area. This situation is very similar to Chapter 4, except that the unit gradient lower boundary condition there causes water loss to be less rapid. The results in Chapter 4 therefore provide qualitative insight in the effects of soil heterogeneity for this limiting case. In contrast, when the drainage basis is entirely closed, like the situation depicted in Fig. 6.1, the effect of soil heterogeneity will be opposed by the lateral saturated redistribution. The strength of this negative feedback greatly depends on the slope of the area. This because the phreatic surface will be completely horizontal and the steeper the area or hillslope is, the more groundwater will seep out near the drainage basis and the weaker the negative feedback will be. In the hypothetical limit of a hillslope that is completely tilted ($\phi = \pi$ in Fig. 6.1), all water that reaches the drainage basis is removed and the effect of soil heterogeneity will again be comparable to Chapter 4 (when absurdly assuming that the unsaturated flow remains directed toward the impermeable layer).

From this discussion and the results in Chapter 6 it is evident that for realistic situations, the internal hillslope "teleconnection" establishes a significant negative feedback in the hillslope average water budget: water recharged uphill may at least partly evaporate back into the atmosphere farther downhill. The strength of the negative feedback becomes weaker when the drainage basis becomes more open and/or the conductivity at the lower boundary becomes greater.

To shed more light on the above problem, future research may be directed at identifying key physical quantities or dimensionless indicators that capture the essence of hillslope hydrological behavior. For example, based on linearization of the governing equation, Zecharias and Brutsaert [109, 1988] derived an aquifer reaction factor as a characteristic time scale for the duration of groundwater

flow during recession of the phreatic surface. In an earlier study, Zecharias and Brutsaert [108, 1988] identified two parameters assimilated in the aquifer reaction factor (drainage density and average basin slope) as important geomorphological controls of groundwater discharge of nineteen watersheds. It thus seems possible to infer basin scale characteristics that are anchored in physical knowledge on the hillslope scale.

Appendix A

Stochastic methods

A.1 Random variables

For notational convenience, throughout this thesis a random variable is indicated by an underline. A specific value assigned to the random variable $\underline{\omega}$ is simply denoted as ω . Likewise, the probability density function of the random variable $\underline{\omega}$ is given by $f_{\underline{\omega}}(\omega)$.

A.2 Estimators of moments

Consider the process $\underline{y} = g(\underline{\omega})$. The mean and variance are respectively given by

$$\mu[\underline{y}] = \int_{-\infty}^{\infty} g(\omega) f_{\underline{\omega}}(\omega) d\omega \quad (\text{A.1})$$

$$\begin{aligned} \sigma^2[\underline{y}] &= \int_{-\infty}^{\infty} (g(\omega) - \mu[\underline{y}])^2 f_{\underline{\omega}}(\omega) d\omega \\ &= \int_{-\infty}^{\infty} [g(\omega)]^2 f_{\underline{\omega}}(\omega) d\omega - (\mu[\underline{y}])^2 \end{aligned} \quad (\text{A.2})$$

When the process $g(\omega)$ is complicated the integrals in (A.1) and (A.2) often do not have analytical solutions. In that case the Monte Carlo method can be fruitfully applied to estimate the mean and variance of \underline{y} . By sampling $f_{\underline{\omega}}(\omega)$, realizations ω_i of $\underline{\omega}$ are obtained. The estimators of the ensemble mean and variance then read

$$\hat{\mu}[\underline{y}] = \frac{1}{N} \sum_{i=1}^N g(\omega_i) \quad (\text{A.3})$$

$$\begin{aligned} \widehat{\sigma^2}[\underline{y}] &= \frac{1}{N-1} \sum_{i=1}^N (g(\omega_i) - \hat{\mu}[\underline{y}])^2 \\ &= \frac{1}{N-1} \sum_{i=1}^N [g(\omega_i)]^2 - (\hat{\mu}[\underline{y}])^2 \end{aligned} \quad (\text{A.4})$$

where N denotes the number of realizations. For $N \rightarrow \infty$, $\hat{\mu}[\underline{y}] \rightarrow \mu[\underline{y}]$ and $\hat{\sigma}^2[\underline{y}] \rightarrow \sigma^2[\underline{y}]$.

Consider now the process $\underline{y} = g(\omega_1, \omega_2, \dots, \omega_n)$, with the associated joint probability density function $f_{\omega_1, \omega_2, \dots, \omega_n}(\omega_1, \omega_2, \dots, \omega_n)$. The mean and variance of \underline{y} are now given by

$$\mu[\underline{y}] = \int_{\Omega} g(\omega_1, \omega_2, \dots, \omega_n) f_{\omega_1, \omega_2, \dots, \omega_n}(\omega_1, \omega_2, \dots, \omega_n) d\omega \quad (\text{A.5})$$

$$\begin{aligned} \sigma^2[\underline{y}] &= \int_{\Omega} (g(\omega_1, \omega_2, \dots, \omega_n) - \mu[\underline{y}])^2 f_{\omega_1, \omega_2, \dots, \omega_n}(\omega_1, \omega_2, \dots, \omega_n) d\omega \quad (\text{A.6}) \\ &= \int_{\Omega} [g(\omega_1, \omega_2, \dots, \omega_n)]^2 f_{\omega_1, \omega_2, \dots, \omega_n}(\omega_1, \omega_2, \dots, \omega_n) d\omega - (\mu[\underline{y}])^2 \end{aligned}$$

where Ω denotes all possible sets of the random variables $\omega_1, \omega_2, \dots, \omega_n$.

When the random variables $\omega_1, \omega_2, \dots, \omega_n$ are independent, the joint density function reduces to

$$f_{\omega_1, \omega_2, \dots, \omega_n}(\omega_1, \omega_2, \dots, \omega_n) = f_{\omega_1}(\omega_1) f_{\omega_2}(\omega_2) \dots f_{\omega_n}(\omega_n) \quad (\text{A.7})$$

In case ω_1 and ω_2 are correlated one may slightly modify (A.7) to yield

$$f_{\omega_1, \omega_2, \dots, \omega_n}(\omega_1, \omega_2, \dots, \omega_n) = f_{\omega_1}(\omega_1 | \omega_2) f_{\omega_2}(\omega_2) \dots f_{\omega_n}(\omega_n) \quad (\text{A.8})$$

When the Monte Carlo technique is used to estimate the mean and variance of \underline{y} , (A.3) and (A.4) can be easily extended.

A.3 Probability density and distribution functions

In this thesis the normal, lognormal, exponential and beta probability density functions are frequently used. The normal probability density function and distribution function are respectively given by

$$f_{\underline{\omega}}(\omega) = \frac{1}{(2\pi)^{\frac{1}{2}} \sigma[\underline{\omega}]} \exp \left[- \left(\frac{\omega - \mu[\underline{\omega}]}{2^{\frac{1}{2}} \sigma[\underline{\omega}]} \right)^2 \right] \quad (\text{A.9})$$

$$F_{\underline{\omega}}(\omega) = \frac{1}{2} \left[1 + \operatorname{erf} \left(\frac{\omega - \mu[\underline{\omega}]}{2^{\frac{1}{2}} \sigma[\underline{\omega}]} \right) \right] \quad (\text{A.10})$$

Similarly, the lognormal probability density function and distribution function read respectively

$$f_{\underline{\omega}}(\omega) = \frac{1}{(2\pi)^{\frac{1}{2}} \sigma[\ln \underline{\omega}] \omega} \exp \left[- \left(\frac{\ln \omega - \mu[\ln \underline{\omega}]}{2^{\frac{1}{2}} \sigma[\ln \underline{\omega}]} \right)^2 \right] \quad (\text{A.11})$$

$$F_{\underline{\omega}}(\omega) = \frac{1}{2} \left[1 + \operatorname{erf} \left(\frac{\ln \omega - \mu[\ln \underline{\omega}]}{2^{\frac{1}{2}} \sigma[\ln \underline{\omega}]} \right) \right] \quad (\text{A.12})$$

where

$$\mu [\underline{\omega}] = \exp \left(\mu [\ln \underline{\omega}] + \frac{\sigma^2 [\ln \underline{\omega}]}{2} \right) \tag{A.13}$$

$$\sigma^2 [\underline{\omega}] = \exp \left(2\mu [\ln \underline{\omega}] + 2\sigma^2 [\ln \underline{\omega}] \right) - \exp \left(2\mu [\ln \underline{\omega}] + \sigma^2 [\ln \underline{\omega}] \right) \tag{A.14}$$

The exponential probability density and distribution function are given by

$$f_{\underline{\omega}}(\omega) = \lambda \exp(-\lambda\omega) \tag{A.15}$$

$$F_{\underline{\omega}}(\omega) = 1 - \exp(-\lambda\omega) \tag{A.16}$$

where the associated mean and variance are given by

$$\mu [\underline{\omega}] = \lambda^{-1} \tag{A.17}$$

$$\sigma^2 [\underline{\omega}] = \lambda^{-2} \tag{A.18}$$

The beta probability density and distribution function are given by [63, Mood *et al.* 1974]

$$f_{\underline{\omega}}(\omega) = \frac{1}{B(\tau, \nu)} \omega^{\tau-1} (1 - \omega)^{\nu-1} \quad 0 \leq \omega \leq 1 \tag{A.19}$$

$$F_{\underline{\omega}}(\omega) = \frac{1}{B(\tau, \nu)} \int_0^{\omega} u^{\tau-1} (1 - u)^{\nu-1} du \quad 0 \leq \omega \leq 1 \tag{A.20}$$

where the beta function B is given by (B.5). Eq. (A.20) is the incomplete beta function. Note that for $\tau = \nu = 1$ the beta distribution reduces to a uniform distribution over the interval $[0, 1]$.

The mean and variance of the beta distribution are given by

$$\mu [\underline{\omega}] = \frac{\tau}{\tau + \nu} \tag{A.21}$$

$$\sigma^2 [\underline{\omega}] = \frac{\tau\nu}{(\tau + \nu + 1)(\tau + \nu)^2} \tag{A.22}$$

A.4 Truncation of the density function

Continuous probability density functions are defined over an infinite or semi-infinite domain. When sampling the pdf this may result in unrealistic values of the variable of interest. This can be avoided by truncating the density function below a minimum value ω^{\min} and above a maximum value ω^{\max} . In order to preserve probability mass the truncated density function has to be normalized:

$$f_{\underline{\omega}}^*(\omega) = \frac{f_{\underline{\omega}}(\omega)}{\int_{\omega^{\min}}^{\omega^{\max}} f_{\underline{\omega}}(\omega) d\omega} \tag{A.23}$$

where $f_{\underline{\omega}}^*(\omega)$ is the truncated pdf.

A.5 Root mean square error

In order to quantify the error between computed and observed values, the root mean square error \mathfrak{R} is used:

$$\mathfrak{R} = \left(\frac{1}{N} \sum_{i=1}^N [C_i - O_i]^2 \right)^{\frac{1}{2}} \quad (\text{A.24})$$

The root mean square error has the same dimension as the variable considered.

Obviously, the lower limit for \mathfrak{R} is 0, indicating that predictions and observations are identical. The root mean square error incorporates errors due to bias as well as to variation.

Appendix B

Derivation of equation (5.30)

Cumulative evapotranspiration over time t is given by integration of (5.19):

$$E^{\text{cum}}(t) = E_p \int_0^t s(\tau) d\tau \quad (\text{B.1})$$

By expressing (5.28) in terms of (5.22) and subsequent substitution in (5.29), $s(t)$ becomes

$$s(t) = s_1(t) \epsilon_0^{\frac{1}{c}} \left(1 - [1 - \epsilon_0] \left[\frac{s_1(t)}{s_0} \right]^c \right)^{-\frac{1}{c}} \quad (\text{B.2})$$

Eq. (B.2) can be written in terms of a binomial series

$$s(t) = \zeta(t) (1 - \xi(t))^{-\frac{1}{c}} \quad (\text{B.3})$$

where

$$\begin{aligned} \zeta(t) &= s_1(t) [\epsilon_0]^{\frac{1}{c}} \\ \xi(t) &= [1 - \epsilon_0] \left[\frac{s_1(t)}{s_0} \right]^c \end{aligned}$$

The binomial series expansion reads

$$\begin{aligned} (1 - \xi)^{-\frac{1}{c}} &= 1 + \sum_{n=1}^{\infty} \frac{\Gamma(c^{-1} + n)}{\Gamma(c^{-1})\Gamma(n+1)} \xi^n \\ &= 1 + \sum_{n=1}^{\infty} \frac{\Gamma(c^{-1} + n)}{n\Gamma(c^{-1})\Gamma(n)} \xi^n \\ &= 1 + \sum_{n=1}^{\infty} \frac{1}{nB(c^{-1}, n)} \xi^n \end{aligned} \quad (\text{B.4})$$

where the Beta and Gamma function are defined by respectively

$$B(\nu, \nu) = \int_0^1 \chi^{\nu-1} (1 - \chi)^{\nu-1} d\chi$$

$$= \frac{\Gamma(\nu)\Gamma(v)}{\Gamma(\nu + v)} \quad (\text{B.5})$$

$$\Gamma(v) = \int_0^\infty \chi^{v-1} \exp(-\chi) d\chi \quad (\text{B.6})$$

Now (B.3) can be rewritten, yielding

$$s(t) = s_1(t)\epsilon_0^{\frac{1}{c}} + s_0\epsilon_0^{\frac{1}{c}} \sum_{n=1}^{\infty} \frac{[1 - \epsilon_0]^n}{nB(c^{-1}, n)} \exp\left[-\frac{(nc + 1)E_p t}{d_r\theta_s}\right] \quad (\text{B.7})$$

Integration of the first part on the right hand side of (B.7) using (5.22) yields

$$\begin{aligned} \epsilon_0^{\frac{1}{c}} \int_0^t s_1(\tau) d\tau &= \epsilon_0^{\frac{1}{c}} \frac{d_r\theta_s s_0}{E_p} \left(1 - \exp\left[-\frac{E_p t}{d_r\theta_s}\right]\right) \\ &= \epsilon_0^{\frac{1}{c}} \frac{d_r\theta_s s_0}{E_p} \left(1 - \left[\frac{s_1(t)}{s_0}\right]\right) \end{aligned} \quad (\text{B.8})$$

Integration of the second part on the right hand side of (B.7) results in

$$\begin{aligned} s_0\epsilon_0^{\frac{1}{c}} \int_0^t \sum_{n=1}^{\infty} \frac{[1 - \epsilon_0]^n}{nB(c^{-1}, n)} \exp\left[-\frac{(nc + 1)E_p \tau}{d_r\theta_s}\right] d\tau &= \\ s_0\epsilon_0^{\frac{1}{c}} \sum_{n=1}^{\infty} \frac{[1 - \epsilon_0]^n}{nB(c^{-1}, n)} \int_0^t \exp\left[-\frac{(nc + 1)E_p \tau}{d_r\theta_s}\right] d\tau &= \\ s_0\epsilon_0^{\frac{1}{c}} \frac{d_r\theta_s}{E_p} \sum_{n=1}^{\infty} \frac{[1 - \epsilon_0]^n}{n(nc + 1)B(c^{-1}, n)} \left(1 - \exp\left[-\frac{(nc + 1)E_p t}{d_r\theta_s}\right]\right) &= \\ s_0\epsilon_0^{\frac{1}{c}} \frac{d_r\theta_s s}{E_p} \sum_{n=1}^{\infty} \frac{[1 - \epsilon_0]^n}{n(nc + 1)B(c^{-1}, n)} \left(1 - \left[\frac{s_1(t)}{s_0}\right]^{nc+1}\right) \end{aligned} \quad (\text{B.9})$$

Finally, substituting (B.8) and (B.9) into (B.1) yields

$$\begin{aligned} E^{\text{cum}}(t) &= E_p \int_0^t s(\tau) d\tau \\ &= d_r\theta_s s_0 \epsilon_0^{\frac{1}{c}} \left(1 - \frac{s_1(t)}{s_0} + \sum_{n=1}^{\infty} \frac{\left[1 - \left\{\frac{s_1(t)}{s_0}\right\}^{nc+1}\right] [1 - \epsilon_0]^n}{n(nc + 1)B(c^{-1}, n)}\right) \end{aligned} \quad (\text{5.30})$$

Appendix C

Derivation of equation (6.30)

In this appendix the approximate expression for $\sigma^2(Q_s)$ in (6.30) is derived.

Similar to (6.25) groundwater flow can be written as

$$Q_s = \overline{Q}_s + Q'_s \quad \overline{Q}'_s = 0 \quad (C.1)$$

Using the definition of variance from it is easily shown that

$$\sigma^2[Q_s] = \overline{(Q'_s)^2} = \overline{Q_s^2} - \overline{Q}_s^2 \quad (C.2)$$

Dupuit groundwater flow is given by (6.7) and it can be derived that

$$Q_s^2 = k_s^2 \cos^2 \phi h^2 \left[\frac{\partial h}{\partial x} + \tan \phi \right]^2 \quad (C.3)$$

Substitution of (6.25) into (C.3) and taking the time average yields

$$\begin{aligned} \overline{Q_s^2} = & k_s^2 \cos^2 \phi \left(\overline{h^2} \left[\left\{ \frac{\partial \overline{h}}{\partial x} + \tan \phi \right\}^2 + \overline{\left\{ \frac{\partial h'}{\partial x} \right\}^2} \right] + \right. \\ & \overline{(h')^2} \left\{ \frac{\partial \overline{h}}{\partial x} + \tan \phi \right\}^2 + 4 \overline{h'} \frac{\partial \overline{h'}}{\partial x} \overline{h} \left[\frac{\partial \overline{h}}{\partial x} + \tan \phi \right] + \\ & \left. 2 \overline{h'} \left[\frac{\partial h'}{\partial x} \right]^2 + 2 \overline{(h')^2} \frac{\partial \overline{h'}}{\partial x} \left[\frac{\partial \overline{h}}{\partial x} + \tan \phi \right] + \overline{(h')^2} \left[\frac{\partial h'}{\partial x} \right]^2 \right) \quad (C.4) \end{aligned}$$

The last three terms within the brackets on the right hand side of (C.4) are of third and fourth order and assumed to be small. The mean groundwater flow is given by (6.26) and accordingly

$$\overline{Q_s^2} = k_s^2 \cos^2 \phi \left(\overline{h^2} \left[\frac{\partial \overline{h}}{\partial x} + \tan \phi \right]^2 + 2 \overline{h'} \frac{\partial \overline{h'}}{\partial x} \overline{h} \left[\frac{\partial \overline{h}}{\partial x} + \tan \phi \right] + \overline{(h')^2} \left[\frac{\partial h'}{\partial x} \right]^2 \right) \quad (C.5)$$

Subtracting (C.5) from (C.4) and neglecting the third and fourth order terms yields

$$\begin{aligned} \sigma^2 [Q_s] \approx & k_s^2 \cos^2 \phi \left(\bar{h}^2 \sigma^2 \left[\frac{\partial h}{\partial x} \right] + \sigma^2 [h] \left[\frac{\partial \bar{h}}{\partial x} + \tan \phi \right]^2 + \right. \\ & \left. 2\bar{h} \text{cov} \left[h, \frac{\partial h}{\partial x} \right] \left[\frac{\partial \bar{h}}{\partial x} + \tan \phi \right] - \text{cov}^2 \left[h, \frac{\partial h}{\partial x} \right] \right) \end{aligned} \quad (6.30)$$

where

$$\sigma^2(h) = \overline{(h')^2}, \quad \sigma^2 \left(\frac{\partial h}{\partial x} \right) = \overline{\left(\frac{\partial h'}{\partial x} \right)^2}, \quad \text{cov} \left(h, \frac{\partial h}{\partial x} \right) = \overline{h' \frac{\partial h'}{\partial x}}$$

Summary

Increasing awareness of human activities being a significant force affecting the earth's climate, has stimulated the scientific study of the climatic system. Because of its large heat capacity and the vast quantities in which it is present, water is the major agent for energy transfer in the climatic system. Knowledge of the global hydrological cycle is therefore of paramount importance to understanding the causes and impacts of climatic change. The research in this thesis focuses on the water budget of the land surface that constitutes the terrestrial branch of the hydrological cycle. The length scales considered are smaller than 10^5 m.

The earth's surface water budget describes the change in water storage in relation to the incoming and outgoing fluxes (precipitation and evapotranspiration, surface runoff and percolation respectively). The processes that govern the partitioning of water over the various budget terms are only sufficiently understood at small spatial scales (of the order of centimeters). Typically, the spatial scales used in climate simulation models range from several tens to several hundreds of kilometers. Hence, a large discrepancy exists between the scales at which the processes are understood and at which they need to be represented. This necessitates the upscaling of processes at small scales to larger ones. Due to the presence of various sources of spatial heterogeneity, the aggregation of the small scale non-linear governing equations is complicated. The research reported in this thesis aims at obtaining insight into the effects of spatial heterogeneity of soil hydraulic properties and rainfall on the water budget of the land surface.

In Chapter 2 the water budget is discussed for three hydrologically different length scales: the representative elementary volume (REV) scale, the plot or field scale and the catchment scale. At REV scale ($\approx 10^{-2}$ m - 10^{-1} m) the flow processes are quite well understood and mathematically described by Richards' equation. At plot scale ($\approx 10^{-1}$ m - 10^2 m) soil heterogeneity complicates the derivation of the areally average water budget. At catchment scale ($\approx 10^2$ m - 10^5 m), apart from soil heterogeneity, lateral redistribution of soil water and, at scales $> 10^3$ m, heterogeneity of the atmospheric boundary conditions further hamper the formulation of the areally average water budget. Heterogeneity of soil hydraulic properties and atmospheric conditions has a complex spatial structure that can best be represented by stochastic methods. In contrast, lateral redistribution of

soil water is governed by well understood physical laws and is here considered as a source of deterministic heterogeneity.

In Chapter 3 the ability of two simple soil reservoir models to describe the water budget of large areas is investigated by comparison with numerical solutions of the small scale governing partial differential equation that include the effect of soil heterogeneity. The upper boundary conditions are derived from daily average meteorological conditions. It appears that the lower boundary conditions of the simple reservoir models (no flow and gravity flow) determine to a large extent the partitioning of water over the various water budget terms. Furthermore it is shown that the water budget corresponding to the scaled average or reference soil hydraulic characteristics is very similar to the areally average water budget of a random field of soil hydraulic characteristics. The reference soil hydraulic characteristics may therefore serve as areally "equivalent" properties.

In Chapter 4 the influence of spatial soil and rainfall heterogeneity is investigated both in a separate and in a joint fashion using Monte Carlo simulation. One year of half-hourly meteorological conditions generated with a one-dimensional climate model comprise the upper boundary conditions. The disparity between the scales at which both sources of heterogeneity are present, allows the results to be interpreted in terms of spatial scales: approximately 10^2 m for soil heterogeneity and approximately 10^4 m - 10^5 m for rainfall heterogeneity. For the loam soil, the low saturated conductivity causes infiltration excess runoff to increase greatly because of soil and/or rainfall heterogeneity. The effect of soil heterogeneity is smaller for the sand soil due to the absence of infiltration excess runoff. In contrast, heterogeneity of the event cumulative rainfall brings about higher percolation amounts for the sand soil. Unlike for the loam soil, it is shown that for the sand soil the effect of soil heterogeneity on the transient spatially average water budget can be accurately captured by means of equivalent soil properties. The absence of an equivalent loam soil is in contrast with the conclusion in Chapter 3. This relates to the daily average meteorological forcing used there, which precludes the occurrence of infiltration excess runoff.

In Chapter 5 a framework of analytical solutions is introduced for the water budget of a simple soil reservoir in which unsaturated water redistribution is neglected. By assuming the upper boundary conditions as rectangular pulses of rainfall with periods of constant potential evapotranspiration in between, the water budget is determined by considering only the transitions from storm to interstorm periods and vice versa. The resulting computational efficiency allows the analysis of the effect of soil heterogeneity for all possible combinations of three soil and three climate types.

Approximate expressions are presented for equivalent soil hydraulic properties that capture the effect of soil heterogeneity on the areally average water budget. Application of the expressions shows that equivalent soil properties depend on

climatic conditions and are found only under restricted conditions. Furthermore, equivalent properties valid on one time scale do not necessarily hold on other time scales. It is therefore concluded that the appealing concept of representing the effect of soil heterogeneity on the water budget terms by means of an equivalent set of parameters has only limited validity. When the interest is mainly on evapotranspiration, however, the application of equivalent properties seems to be more promising.

Also in Chapter 5, the probability distributions of infiltration and evapotranspiration rate, given spatially heterogeneous saturated conductivity, rainfall rate or initial saturation degree, are derived analytically. Although the evolution of the distribution functions can only be traced on the time scale of an (inter)storm event, it is shown that the effects of the different sources of heterogeneity are markedly different.

In Chapter 6 the emphasis is on the deterministic heterogeneity induced by lateral redistribution of water through saturated groundwater flow. The hillslope that constitutes the model domain is shown to organize itself on average into three distinct regions: a recharge zone uphill, a midline region with predominantly lateral saturated flow, and a discharge zone downhill. Water recharged uphill reappears in the water budget of the downhill region because of saturated lateral flow from uphill to downhill. Unsaturated lateral flow is shown to be of little importance. The strength of the "teleconnection" between the recharge and the discharge region greatly depends on soil hydraulic properties, geomorphological hillslope layout and climate. The long term average water budget of the entire hillslope is affected most by the climatic conditions and to a lesser extent by the depth of the rootzone. Although changing the geomorphological hillslope layout greatly alters the partitioning of rainfall over the various terms along the hillslope, the water budget of the entire hillslope does not alter drastically. Partly this is an artifact of the rectangular hillslope layout and the closed downhill boundary. It also emphasizes the importance of evapotranspiration in reducing the effect of spatial heterogeneity: part of the water recharged uphill evapotranspires downhill. The lateral water transport thus establishes a negative feedback that opposes the effect of spatial heterogeneity. The strength of this feedback depends on climate, soil properties and geomorphology.

Finally, in Chapter 7 the main conclusions of the thesis are put into perspective and discussed with respect to their implications. Also, some remaining questions are discussed.

Samenvatting

Het groeiende inzicht dat menselijk handelen een aanzienlijke invloed op het aardse klimaat zou kunnen hebben, heeft de wetenschappelijke studie van het klimaatsysteem doen toenemen. Water heeft een grote warmtecapaciteit, komt in enorme hoeveelheden voor en is bijgevolg de belangrijkste stof voor de overdracht van energie in het klimaatsysteem. Kennis van de globale hydrologische kringloop is daarom onmisbaar om de oorzaken en gevolgen van klimaatverandering te begrijpen. Centraal in dit proefschrift staat de waterbalans van het landoppervlak, het terrestrische gedeelte van de hydrologische kringloop, op ruimtelijke schalen kleiner dan 10^5 m.

De waterbalans van het landoppervlak beschrijft de verandering van de hoeveelheid geborgen water als gevolg van de in- en uitgaande fluxen (respectievelijk neerslag en evapotranspiratie, oppervlakkige afvoer en percolatie). Voldoende inzicht in de processen die de verdeling van water over de diverse waterbalanstermen reguleren, is slechts aanwezig op kleine ruimtelijke schalen (orde centimeters). De ruimtelijke schalen die in klimaatmodellen worden gebruikt variëren van enkele tientallen tot enkele honderden kilometers. Er gaapt dus een aanzienlijke kloof tussen de schalen waarop de processen bekend zijn en die waarop ze moeten worden beschreven. Het is daarom noodzakelijk om de kleinschalige processen op te schalen. De aggregatie van de kleinschalige, niet lineaire basisvergelijkingen tot de in klimaatmodellen gehanteerde ruimtelijke schalen, wordt echter bemoeilijkt door de aanwezigheid van diverse bronnen van ruimtelijke heterogeniteit op tussenliggende schalen. Het onderzoek waarvan in dit proefschrift verslag wordt gedaan, richt zich op het verkrijgen van inzicht in de invloed van ruimtelijke heterogeniteit van bodemhydraulische eigenschappen en neerslag op de waterbalans van het landoppervlak.

In Hoofdstuk 2 wordt de waterbalans besproken voor drie hydrologisch verschillende schalen: de schaal van het representatief elementair volume (REV), van een plot of een veld en van een stroomgebied. Op REV-schaal ($\approx 10^{-2}$ m - 10^{-1} m) zijn de stromingsprocessen voldoende bekend en worden zij wiskundig beschreven door middel van de Richards' vergelijking. Op plot- of veldschaal ($\approx 10^{-1}$ m - 10^2 m) wordt het opstellen van de ruimtelijk gemiddelde waterbalans bemoeilijkt door heterogeniteit van de bodem. Op de schaal van een stroomgebied ($\approx 10^2$ m -

10^5 m) vormen de laterale herverdeling van water en, op schalen $> 10^3$ m, de ruimtelijke heterogeniteit van de atmosferische randvoorwaarden extra complicaties bij de formulering van de ruimtelijk gemiddelde waterbalanstermen. De ingewikkelde ruimtelijke structuur van heterogeniteit van zowel de bodemhydraulische eigenschappen als de atmosferische omstandigheden kan het best worden weergegeven met behulp van stochastische methoden. In dit proefschrift voltrekt de laterale herverdeling van water zich als gevolg van bekende natuurkundige wetmatigheden en wordt daarom beschouwd als een bron van deterministische heterogeniteit.

In Hoofdstuk 3 worden waterbalanssimulaties met eenvoudige bodemreservoirmodellen vergeleken met numerieke oplossingen van de fundamentele partiële differentiaalvergelijking voor onverzadigde waterstroming. In de numerieke oplossingen is het effect van bodemheterogeniteit opgenomen. De bovenrandvoorwaarden zijn opgesteld uitgaande van daggemiddelde meteorologische gegevens. Uit de resultaten blijkt dat de randvoorwaarde aan de onderkant van de twee reservoirmodellen (geen uitstroming en uitstroming tengevolge van de zwaartekracht) de verdeling van water over de diverse balanstermen sterk beïnvloedt. Verder wordt aangetoond dat de waterbalans behorende bij de referentie (gemiddelde van de geschaalde) bodemhydraulische eigenschappen goed overeenkomt met de ruimtelijk gemiddelde waterbalans van een gebied met heterogene bodemhydraulische eigenschappen en daarom als ruimtelijk 'equivalent' kunnen fungeren.

In Hoofdstuk 4 wordt de invloed van bodem- en neerslagheterogeniteit, zowel afzonderlijk als gecombineerd, onderzocht door middel van Monte Carlo simulatie. De bovenrandvoorwaarden worden gevormd door een tijdreeks van een jaar bestaande uit halfuurlijkse meteorologische gegevens, gegenereerd met behulp van een één-dimensionaal klimaatmodel. De verschillende schalen waarop heterogeniteit van bodemhydraulische eigenschappen en neerslag aanwezig zijn, maken het mogelijk de resultaten te interpreteren in termen van ruimtelijke schalen: orde 10^2 m voor bodemheterogeniteit en $10^4 - 10^5$ m voor de ruimtelijke heterogeniteit van neerslag. Door de geringe doorlatendheid van de gebruikte leemgrond veroorzaakt bodemheterogeniteit een aanzienlijke toename van oppervlakkige afvoer ten gevolge van het overschrijden van het infiltratievermogen. Voor de zandgrond is het effect van bodemheterogeniteit veel geringer vanwege het uitblijven van oppervlakkige afvoer dankzij de grotere doorlatendheid. Voor de zandgrond blijkt echter dat heterogeniteit van de totale hoeveelheid neerslag van een bui grotere percolatiehoeveelheden met zich mee brengt. In tegenstelling tot de leemgrond blijkt dat voor de zandgrond het effect van bodemheterogeniteit op het tijdsverloop van de ruimtelijk gemiddelde waterbalans beschreven kan worden door middel van equivalente eigenschappen. De afwezigheid van een equivalente leemgrond is in tegenspraak met de resultaten in Hoofdstuk 3. De verklaring hiervoor is dat de daggemiddelde meteorologische gegevens gebruikt in Hoofdstuk 3 voorkomen dat oppervlakkige afvoer optreedt ten gevolge van het overschrijden

van de infiltratiecapaciteit.

In Hoofdstuk 5 wordt een aantal analytische oplossingen gepresenteerd voor de waterbalans van een eenvoudig bodemreservoir waarin de herverdeling van water wordt verwaarloosd. Door de bovenrandvoorwaarde voor te stellen als rechthoekige pulsen neerslag met daartussen perioden met constante potentiële verdamping, kan de waterbalans van een bodemreservoir worden bepaald door alleen de overgangen van neerslag- naar droge perioden en omgekeerd te beschouwen. De geringe benodigde rekentijd maakt het mogelijk om het effect van bodemheterogeniteit na te gaan voor alle combinaties van drie bodem- en drie klimaattypen.

Benaderende vergelijkingen worden gepresenteerd voor equivalente bodemhydraulische eigenschappen die het effect van heterogeniteit op de ruimtelijk gemiddelde waterbalans bevatten. Aangetoond wordt dat equivalente eigenschappen slechts onder stringente voorwaarden kunnen worden afgeleid. Bovendien zijn de equivalente eigenschappen die bepaald zijn voor een zekere tijdschaal niet noodzakelijkerwijs geldig voor andere tijdschalen. Het aantrekkelijke concept om het effect van bodemheterogeniteit op de waterbalans te representeren door middel van één equivalente set parameters, kan daarom slechts beperkt worden toegepast. Wanneer echter de interesse vooral de verdamping betreft, zoals in het geval van klimaatmodellering, lijkt de bruikbaarheid van equivalente eigenschappen groter te zijn.

In Hoofdstuk 5 worden tevens de kansverdelingen afgeleid voor de infiltratie- en verdampingsfluxen in geval van ruimtelijk heterogene verzadigde doorlatendheid, neerslagintensiteit of initiële verzadigingsgraad. Ondanks het feit dat de evolutie van de verdelingen slechts kan worden gevolgd op de tijdschaal van een neerslag- of een verdampingsperiode, wordt aangetoond dat de effecten van de verschillende bronnen van heterogeniteit zeer verschillend zijn.

In Hoofdstuk 6 ligt de nadruk op de deterministische heterogeniteit die wordt veroorzaakt door de laterale herverdeling van water tengevolge van verzadigde grondwaterstroming. Het blijkt dat op de helling die het modeldomein vormt, gemiddeld over de tijd, drie verschillende zones ontstaan: een zone waarin het grondwater wordt aangevuld (voedingsgebied) op het hoogste gedeelte, een tussenliggende zone met hoofdzakelijk laterale grondwaterstroming en een kwelzone aan de benedenstroomse zijde van de helling. Water dat in de aanvullingszone ten goede komt aan het grondwater kan door laterale verzadigde stroming terug worden gevonden in de kwelzone. Onverzadigde laterale waterstroming blijkt van ondergeschikt belang te zijn. De sterkte van de 'teleconnectie' tussen de aanvullings- en de kwelzone is sterk afhankelijk van bodemhydraulische eigenschappen, geomorfologie en klimaat. De lange termijn gemiddelde waterbalans van de gehele helling wordt het sterkst beïnvloed door de klimatologische omstandigheden en in geringere mate door de dikte van de wortelzone. Ondanks het feit dat de laterale

verdeling van waterbalanstermen sterk verandert als gevolg van wijzigingen in de geomorfologie van de helling, leidt dit niet tot aanzienlijke verschillen in de waterbalans van de gehele helling. Enerzijds is dit een artefact van het beschouwde rechthoekige modeldomein en de gesloten benedenstroomse rand. Anderzijds wijst dit op het feit dat verdamping het effect van ruimtelijke heterogeniteit afzwakt. Het laterale watertransport vormt dus een negatieve terugkoppeling die het effect van bodemheterogeniteit vermindert. De sterkte van deze terugkoppeling wordt bepaald door klimaat, bodemhydraulische eigenschappen, geomorfologie en vegetatie.

Tot slot zijn in Hoofdstuk 7 de belangrijkste conclusies van dit proefschrift samengevat, in perspectief geplaatst en besproken wat betreft hun belangrijkste implicaties. Tevens worden enkele onbeantwoorde vragen aangestipt die als suggesties voor toekomstig onderzoek kunnen worden gezien.

Bibliography

- [1] M.B. Abbott, J.C. Bathurst, J.A. Cunge, P.E. O'Connell, and J. Rasmussen. An introduction to the European Hydrologic System - Systeme Hydrologique Europeen (SHE), 2: Structure of a physically-based distributed modelling system. *J. Hydrol.*, 87:60-79, 1986.
- [2] M. Abramowitz and I.A. Stegun. *Handbook of Mathematical functions*. Dover Publications, Inc., New York, New York, ninth edition, 1970. pp. 1046.
- [3] J.C. André, J.P. Goutorbe, and A. Perrier. A hydrologic atmospheric experiment for the study of water budget and evaporation flux at the climate scale. *Bull. Am. Meteorol. Soc.*, 67:138-144, 1986.
- [4] P. Baveye and G. Sposito. The operational significance of the continuum hypothesis in the theory of water movement through soils and aquifers. *Water Resour. Res.*, 20(5):521-530, 1984.
- [5] C. Belmans, J.G. Wesseling, and R.A. Feddes. Simulation model of the water balance of a cropped soil: SWATRE. *J. Hydrol.*, 63:271-286, 1983.
- [6] K.J. Beven and M.J. Kirkby. A physically based variable contributing area model of basin hydrology. *Hydrol. Sci. Bull.*, 24:43-69, 1979.
- [7] M.F.P. Bierkens. *Complex confining layers; a stochastic analysis of hydraulic properties at various scales*. PhD thesis, Faculteit Ruimtelijke Wetenschappen, Utrecht University, Netherlands, 1994. pp. 263.
- [8] H.J. Bolle, J.C. André, J.L. Arrue, H.K. Barth, P. Bessemoulin, A. Brasa, H.A.R. de Bruin, G. Dugdale, E.T. Engman, D.L. Evans, R. Fantechi, F. Fiedler, A. Van de Griend, A.C. Imeson, A.M. Jochum, P. Kabat, T. Kratzsch, J.P. Lagouarde, I. Langer, R. Llamas, E. Lopes-Baeza, J. Meli Miralles, L.S. Mubox, J. Munniosguren, F. Nerry, J. Noilhan, H.R. Oliver, R. Roth, J. Sanchez Diaz, M. de Sante Ollala, W.J. Shuttleworth, H. Sogaard, H. Stricker, J. Thornes, M. Vauclin, and D. Wickland. EFEDA: European Field Experiment in a Desertification threatened Area. *Ann. Geophysicae*, 11:173-189, 1993.
- [9] D.L. Brakensiek, R.L. Engleman, and W.J. Rawls. Variation within texture classes of soil water parameters. *Trans. Am. Soc. Agric. Eng.*, 24(2):335-339, 1981.

- [10] R.L. Bras. *Hydrology, an introduction to hydrologic science*. Addison-Wesley Publishing Inc., Reading, Massachusetts, 1990. pp. 643.
- [11] E. Bresler and G. Dagan. Unsaturated flow in spatially variable fields, 2, Application of water flow models to various fields. *Water Resour. Res.*, 19(2):421-428, 1983.
- [12] R.H. Brooks and A.T. Corey. Properties of porous media affecting fluid flow. *J. Irrig. Drain. Div. Am. Soc. Civil Eng.*, 92(IR2):61-88, 1966.
- [13] K.L. Brubaker and D. Entekhabi. Nonlinear dynamics of water and energy balance in land-atmosphere interaction. Technical Report 341, Dept. of Civil Engineering, Mass. Inst. of Tech., Cambridge, Massachusetts, 1994. pp. 147.
- [14] W. Brutsaert. Catchment scale evaporation and the atmospheric boundary layer. *Water Resour. Res.*, 22(9):39S-45S, 1986.
- [15] Z. Chen, R.S. Govindaraju, and M.L. Kavvas. Spatial averaging of unsaturated flow equations under infiltration conditions over areally heterogeneous fields 1. Development of models. *Water Resour. Res.*, 30(2):523-533, 1994.
- [16] Z. Chen, R.S. Govindaraju, and M.L. Kavvas. Spatial averaging of unsaturated flow equations under infiltration conditions over areally heterogeneous fields 2. Numerical simulations. *Water Resour. Res.*, 30(2):535-548, 1994.
- [17] V. Clapp and G.M. Hornberger. Empirical equations for some soil hydraulic properties. *Water Resour. Res.*, 14(4):601-604, 1978.
- [18] V. Clausnitzer, J.W. Hopmans, and D.R. Nielsen. Simultaneous scaling of soil water retention and soil hydraulic properties. *Water Resour. Res.*, 28(1):19-31, 1992.
- [19] C.G. Collier. The application of a continental-scale radar database to hydrological process parameterization within atmospheric general circulation models. *J. Hydrol.*, 142:301-318, 1993.
- [20] G. Dagan. Analysis of flow through heterogeneous random aquifers, 2, insteady flow in confined formations. *Water Resour. Res.*, 18(5):1571-1585, 1982.
- [21] G. Dagan and E. Bresler. Unsaturated flow in spatially variable fields, 1, Derivation of models for infiltration and redistribution. *Water Resour. Res.*, 19(2):413-420, 1983.
- [22] J.W. Deardorff. A parameterization of ground-surface moisture content for use in atmospheric prediction models. *J. Atmos. Sci.*, 16:1182-1185, 1977.
- [23] J.W. Deardorff. Efficient prediction of ground surface temperature and moisture, with inclusion of a layer of vegetation. *J. Geophys. Res.*, 83(C4):1889-1903, 1978.
- [24] T.L. Delworth and S. Manabe. The influence of soil wetness on near-surface atmospheric variability. *J. Clim.*, 2:1447-1462, 1989.
- [25] R.E. Dickinson, A. Henderson-Sellers, P.J. Kennedy, and M.F. Wilson. Biosphere-Atmosphere Transfer Scheme (BATS) for the NCAR Commu-

- nity Climate Model. Technical Report TN-275+STR, NCAR, Boulder, Colorado, 1986. pp. 69.
- [26] C. Dirksen, J.B. Kool, P. Koorevaar, and M.Th. Van Genuchten. Simulation model of hysteretic water and solute transport in the root zone. In D. Russo and G. Dagan, editors, *Water Flow and Solute Transport in Soils.*, pages 99–122, Berlin, 1993. Springer Verlag.
- [27] J.C.I. Dooge. Linear theory of hydrologic systems. Technical Report 1468, Agricultural Research Service, U.S. Department of Agriculture, Washington, D.C., 1973.
- [28] J.C.I. Dooge, M. Bruen, and A. Dowley. Spatial variability of land surfaces processes. Technical Report LSP/94/19, Centre for Water Resources Research, University College Dublin, Ireland, 1994. pp. 141.
- [29] J.C.I. Dooge and Q.J. Wang. Comment on "An investigation of the relation between ponded and constant flux rainfall infiltration by A. Poulouvalis *et al.*". *Water Resour. Res.*, 29(4):1335–1337, 1993.
- [30] R. Dubayah, J. Dozier, and F.W. Davis. Topographic distribution of clear-sky radiation over the Konza prairie, Kansas. *Water Resour. Res.*, 26(4):679–690, 1990.
- [31] P.S. Eagleson. Climate, soil and vegetation 1. Introduction to water balance dynamics. *Water Resour. Res.*, 14(5):705–712, 1978.
- [32] P.S. Eagleson. Climate, soil and vegetation 2. The distribution of annual precipitation derived from observed storm sequences. *Water Resour. Res.*, 14(5):713–721, 1978.
- [33] P.S. Eagleson. The distribution of catchments coverage by stationary rainstorms. *Water Resour. Res.*, 20(5):581–590, 1984.
- [34] D. Entekhabi. A simple model of the hydrologic cycle and climate: 1. model construct and sensitivity to the land surface boundary. *Adv. Water Resour.*, 17:79–91, 1994.
- [35] D. Entekhabi and P.S. Eagleson. Land surface hydrology parameterization for atmospheric general circulation models including subgrid scale variability. *J. Clim.*, 2(8):816–831, 1989.
- [36] J.S. Famiglietti and E.F. Wood. Evapotranspiration and runoff from large land areas. In E.F. Wood, editor, *Land Surface-Atmosphere Interaction: Observations, Models and Analysis.*, pages 179–204, Dordrecht, The Netherlands, 1991. Kluwer Academic Publishers.
- [37] R.A. Feddes, G.H. de Rooij, J.C. van Dam, P. Kabat, P. Droogers, and J.N.M. Stricker. Estimation of regional effective soil hydraulic parameters by inverse modeling. In D. Russo and G. Dagan, editors, *Water Flow and Solute Transport in Soils.*, pages 211–231, Berlin, 1993. Springer Verlag.
- [38] R.A. Feddes, P.J. Kowalik, and H. Zaradny. *Simulation model of the water balance of a cropped soil.* Simulation Monograph. PUDOC, Wageningen, The Netherlands, 1978. pp. 189.

- [39] R.A. Freeze. Three-dimensional, transient, saturated-unsaturated flow in a groundwater basin. *Water Resour. Res.*, 7(2):347-366, 1971.
- [40] L.M. Glymph and H.N. Holtan. Land treatment in agricultural watershed hydrology research. In W.L. Moore and C.W. Morgan, editors, *Effects of Watershed Changes on Streamflow.*, pages 44-68, Austin, Texas, 1969. Univ. Texas Press. pp. 289.
- [41] J.P. Goutorbe, T. Lebel, A. Tinga, P. Bessemoulin, J. Brouwer, A.J. Dolman, E.T. Engman, J.H.C. Gash, M. Hoepffner, P. Kabat, Y.H. Kerr, B. Monteny, S. Prince, F. Said, P. Sellers, and J.S. Wallace. HAPEX-Sahel: a large-scale study of land-atmosphere interactions in the semi-arid tropics. *Ann. Geophysicae*, 12:53-64, 1994.
- [42] W.H. Green and G.A. Ampt. Studies in soil physics, i, flow of air and water through soils. *J. Agric. Sci.*, 4:1-24, 1911.
- [43] R. Haverkamp, J.Y. Parlange, J.L. Starr, G. Schmitz, and C. Fuentes. Infiltration under ponded conditions: 3. A predictive equation based on physical parameters. *Soil Sci.*, 149(5):292-300, 1990.
- [44] K.L. Hawk and P.S. Eagleson. Climatology of station storm rainfall in the continental United States: Parameters of the Bartlett-Lewis and Poisson rectangular pulses models. Technical Report 336, Dept. of Civil Engineering, Mass. Inst. of Tech., Cambridge, Massachusetts, 1992.
- [45] J.W. Hopmans. A comparison of various methods to scale soil hydraulic properties. *J. Hydrol.*, 105:57-84, 1987.
- [46] J.W. Hopmans and Stricker J.N.M. Stochastic analysis of soil water regime in a watershed. *J. Hydrol.*, 105:57-84, 1989.
- [47] K.D. Johnson, D. Entekhabi, and P.S. Eagleson. The implementation and validation of improved landsurface hydrology in an atmospheric circulation model. Technical Report 334, Dept. of Civil Engineering, Mass. Inst. of Tech., Cambridge, Massachusetts, 1991. pp. 192.
- [48] R.D. Koster and M.J. Suarez. Modeling the land surface boundary in climate models as a composite of independent vegetation stands. *J. Geophys. Res.*, 97(D3):2697-2715, 1992.
- [49] V. Kühnel, J.C.I. Dooge, J.P.J. O'Kane, and R.J. Romanowicz. Partial analysis applied to scale problems in surface soil moisture fluxes. In E.F. Wood, editor, *Land Surface - Atmosphere Interaction for Climate Modeling.*, pages 221-247, Dordrecht, The Netherlands, 1991. Kluwer Academic Publishers.
- [50] J. Lean. A guide to the uk meteorological office single column model. Technical report, Hadley Centre for Climate Prediction and Research, Meteorological Office., Bracknell, United Kingdom, 1992. pp. 36.
- [51] E.N. Lorenz. The predictability of a flow which possesses many scales of motion. *Tellus*, 21:289-307, 1969.

- [52] J.F. Mahfouf, E. Richard, and P. Mascart. The influence of soil and vegetation on the development of mesoscale circulations. *J. Clim. Appl. Meteorol.*, 26:1483-1495, 1987.
- [53] R.A. Maller and M.L. Sharma. An analysis of areal infiltration considering spatial variability. *J. Hydrol.*, 52:25-37, 1981.
- [54] R.A. Maller and M.L. Sharma. Aspects of rainfall excess from spatially varying hydrological parameters. *J. Hydrol.*, 67:115-127, 1984.
- [55] S. Manabe. Climate and the ocean circulation. i. The atmospheric circulation and the hydrology of the earth's surface. *Mon. Weather Rev.*, 97:739-774, 1969.
- [56] S. Manabe and J.L. Jr. Holloway. Seasonal variation of hydrologic cycle as simulated by a global model of the atmosphere. *J. Geophys. Res.*, 80:1617-1649, 1975.
- [57] J.J. McDonnell. A rationale for old water discharge through macropores in a steep, humid catchment. *Water Resour. Res.*, 26(11):2821-2832, 1990.
- [58] A.L. McNab. Climate and drought. *EOS, Am. Geophys. Union.*, 70(40):873, 1989.
- [59] G.A. Meehl and W.M. Washington. A comparison of soil moisture sensitivity in two climate models. *J. Atmos. Sci.*, 45:1476-1492, 1988.
- [60] R.G. Mein and C.L. Larson. Modeling infiltration during a steady rain. *Water Resour. Res.*, 9(2):384-394, 1973.
- [61] E.E. Miller and R.D. Miller. Physical theory for capillary flow phenomena. *J. Appl. Phys.*, 27:324-332, 1956.
- [62] P.C.D. Milly and P.S. Eagleson. Effects of spatial variability on annual average water balance. *Water Resour. Res.*, 23(11):2135-2142, 1987.
- [63] M.A. Mood, F.A. Graybill, and D. Boes. *Introduction to the theory of statistics*. McGraw-Hill, Singapore, third edition, 1974. pp. 564.
- [64] M.P. Mosley. Steramflow generation in a forested watershed, New Zealand. *Water Resour. Res.*, 15(4):795-806, 1979.
- [65] Y. Mualem. A new model for predicting the hydraulic conductivity of unsaturated porous media. *Water Resour. Res.*, 12, 1976.
- [66] J. Noilhan and S. Planton. A simple parameterization of land-surface processes for meteorological models. *Mon. Weather Rev.*, 117:536-549, 1989.
- [67] C. Paniconi and E.F. Wood. A detailed model for simulation of catchment scale subsurface hydrologic processes. *Water Resour. Res.*, 29(6):1601-1620, 1993.
- [68] A. Papoulis. *Probability, Random Variables and Stochastic Processes*. McGraw-Hill, Inc, Singapore, third edition, 1991. pp. 666.
- [69] J.Y. Parlange, I. Lisle, R.D. Braddock, and R.E. Smith. The three parameter infiltration equation. *Soil Sci.*, 133:337-341, 1982.
- [70] A.J. Pearce, M.K. Stewart, and M.G. Sklash. Storm runoff generation in humid headwater catchments 1. Where does the water come from? *Water Resour. Res.*, 22(8):1263-1272, 1986.

- [71] J.P. Peixoto. Atmospheric energetics and the water cycle. In E. Raschke and D. Jacob, editors, *Energy and Water Cycles in the Climatic System.*, pages 1–42, Berlin, Germany, 1993. NATO Advanced Study Institute, Springer Verlag. pp. 467.
- [72] J.P. Peixoto and A.H. Oort. *Physics of climate.* American Institute of Physics, New York, New York, 1993. pp. 520.
- [73] H.L. Penman. Vegetation and hydrology. Technical Report 53, Commonwealth Bureau of Soils, Harpenden, 1951.
- [74] J.R. Philip. The theory of infiltration, 4, sorptivity and algebraic infiltration equations. *Soil Sci.*, 84:257–264, 1957.
- [75] N.A. Phillips. The general circulation of the atmosphere: a numerical experiment. *Quart. J. Roy. Meteor. Soc.*, 82:123–164, 1956.
- [76] W.H. Press, B.P. Flannery, S.A. Teukolsky, and W.T. Vetterling. *Numerical Recipes.* Cambridge University Press, Cambridge, United Kingdom, 1986. pp. 818.
- [77] I. Rodriguez-Iturbe, D. Entekhabi, and R.L. Bras. Nonlinear dynamics of soil moisture at climate scales: 1. Stochastic analysis. *Water Resour. Res.*, 27(8):1899–1906, 1991.
- [78] I. Rodriguez-Iturbe and J.M. Mejia. The design of rainfall networks in time and space. *Water Resour. Res.*, 10(4):713–728, 1974.
- [79] I. Rodriguez-Iturbe and J.B. Valdès. The geomorphologic structure of hydrologic response. *Water Resour. Res.*, 15(6):1409–1429, 1979.
- [80] L.K. Rowe. Rainfall interception by a beech-podocarp-hardwood forest near Reefton, North Westland, New Zealand. *J. Hydrol. N.Z.*, 18:63–72, 1979.
- [81] P.R. Rowntree. Review of General Circulation Models for predicting the effects of vegetation change. In E.R.C. Reynolds and F.B. Thompson, editors, *Forests, Climate and Hydrology: Regional Impacts*, pages 162–196, Oxford, 1988. United Nations University.
- [82] D. Russo and E. Bresler. Soil hydraulic properties as stochastic processes: I. An analysis of field spatial variability. *Soil Sci. Soc. Am. J.*, 45:682–687, 1981.
- [83] G.D. Salvucci. *Hillslope and climatic controls on hydrologic fluxes.* PhD thesis, Mass. Inst. Tech., Cambridge, Massachusetts, 1994. pp. 246.
- [84] P.J. Sellers, F.G. Hall, F.G. Asrar, D.E. Strebel, and R.E. Murphy. The First ISLSCP Field Experiment (FIFE). *Bull. Amer. Meteor. Soc.*, 69(1):22–67, 1988.
- [85] P.J. Sellers, Y. Mintz, Y.C. Sud, and A. Dalcher. A Simple Biosphere model (SiB) for use within General Circulation Models. *J. Atmos. Sci.*, 43(6):305–331, 1986.
- [86] M.L. Sharma and R.J. Luxmoore. Soil spatial variability and its consequences on simulated water balance. *Water Resour. Res.*, 15(6):1567–1573, 1979.

- [87] M.L. Sharma, R.J. Luxmoore, R. DeAngelis, R.C. Ward, and G.T. Yeh. Subsurface water flow simulated for hillslopes with spatially dependent soil hydraulic characteristics. *Water Resour. Res.*, 23(8):1523-1530, 1987.
- [88] L.K. Sherman. Stream flow from rainfall by the unit-graph method. *Eng. News Rec.*, 108:501-505, 1932.
- [89] L.K. Sherman. Comparison of f-curves derived by the method of Sharp and Holtan and of Sherman and Mayer. *Trans. Amer. Geophys. Union*, 24:465-467, 1943.
- [90] J. Shukla and Y. Mintz. Influence of land-surface evapotranspiration on the earth's climate. *Science*, 215:1498-1500, 1982.
- [91] W.J. Shuttleworth. Macrohydrology - the new challenge for process hydrology. *J. Hydrol.*, 100:31-56, 1988.
- [92] W.J. Shuttleworth. The Soil-Vegetation-Atmosphere interface. In E. Raschke and D. Jacob, editors, *Energy and Water Cycles in the Climate System*, pages 365-418, Berlin, Germany, 1993. NATO Advance Study Institute, Springer Verlag. pp. 467.
- [93] M. Sivapalan and P.C.D. Milly. On the relation between the time condensation approximation and the flux-concentration relation. *J. Hydrol.*, 105:357-367, 1989.
- [94] M. Sivapalan and E.F. Wood. Spatial heterogeneity and scale in the infiltration response of catchments. In V.K. Gupta, I. Rodriguez-Iturbe, and E.F. Wood, editors, *Scale Problems in Hydrology*, pages 81-106, The Netherlands, 1986. D. Reidel publishing company. pp. 246.
- [95] M.G. Sklash, M.K. Stewart, and A.J. Pearce. Storm runoff generation in humid headwater catchments 2. A case study of hillslope and low-order stream response. *Water Resour. Res.*, 22(8):1273-1282, 1986.
- [96] R.E. Smith, C. Corradini, and F. Melone. Modeling infiltration for multi-storm runoff events. *Water Resour. Res.*, 29(1):133-143, 1993.
- [97] R.E. Smith and R.H.B. Hebbert. Mathematical simulation of interdependent surface and subsurface hydrological processes. *Water Resour. Res.*, 19(4):987-1001, 1983.
- [98] R.E. Smith and J.Y. Parlange. A parameter-efficient hydrologic infiltration model. *Water Resour. Res.*, 14(3):533-538, 1978.
- [99] G.R. Stephenson and R.A. Freeze. Mathematical simulation of subsurface flow contributions to snowmelt runoff, reynolds creeak watershed, idaho. *Water Resour. Res.*, 10(2):284-298, 1974.
- [100] A.S. Thom and H.R. Oliver. On penman's equation for estimating regional evaporation. *Quart. J. Roy. Meteorol. Soc.*, 103:345-357, 1977.
- [101] J.C. Van Dam, J.N.M. Stricker, and P. Droogers. Inverse method to determine soil hydraulic functions from multistep outflow experiments. *Soil Sci. Soc. Am. J.*, 58:647-652, 1994.
- [102] M.Th. Van Genuchten. A closed-form equation for predicting the hydraulic conductivity of unsaturated soil. *Soil Sci. Soc. Am. J.*, 44:892-898, 1980.

- [103] A.W. Warrick, G.J. Mullen, and D.R. Nielsen. Scaling field-measured soil hydraulic properties using a similar media concept. *Water Resour. Res.*, 13(2):355-362, 1977.
- [104] D.A. Warrilow. Indications of the sensitivity of european climate to land use variation using a one-dimensional model. In *Proceedings ISLSCP Conference, Rome, Italy.*, pages 159-156. ESA SP-248, 1986.
- [105] E. Waymire and V.K. Gupta. The mathematical structure of rainfall representations, 1, a review of the stochastic rainfall models. *Water Resour. Res.*, 17(5):1261-1272, 1981.
- [106] J.V. Witter. *Heterogeneity of Dutch rainfall.* PhD thesis, Wageningen Agricultural University, Wageningen, The Netherlands, 1984. pp. 304.
- [107] J. Zaidel and D. Russo. Estimation of finite difference interblock conductivities for simulation of infiltration into initially dry soils. *Water Resour. Res.*, 29:2285-2295, 1993.
- [108] Y.B. Zecharias and W. Brutsaert. The influence of basin morphology on groundwater outflow. *Water Resour. Res.*, 24(10):1645-1650, 1988.
- [109] Y.B. Zecharias and W. Brutsaert. Recession characteristics of groundwater outflow and base flow from mountainous watersheds. *Water Resour. Res.*, 24(10):1651-1658, 1988.

Curriculum Vitae

Cornelis Pieter Kim, 14 september 1966, Den Ham (Ov.)

- juni 1984 : Atheneum diploma, scholengemeenschap 'Revius', Deventer.
- augustus 1990 : Bul Cultuurtechniek, specialisatie Hydrologie en waterbeheer, Landbouwniversiteit Wageningen, Afstudeervakken in de Hydrologie en de Hydraulica.
- januari 1991 : Aanvang promotieonderzoek, vakgroep Waterhuishouding, Landbouwniversiteit Wageningen, Gastverblijf van september 1993 - juni 1994, Ralph M. Parsons Laboratory, Massachusetts Institute of Technology.
- oktober 1995 : Post Doctoral onderzoeker, Ralph M. Parsons Laboratory, Massachusetts Institute of Technology.